SENSOR FUSION BY BAYESIAN FILTERING FOR SEAMLESS PEDESTRIAN NAVIGATION

SENSOR-FUSION MITTELS BAYESSCHER FILTERUNG FÜR DIE NAHTLOSE FUSSGÄNGER-NAVIGATION

Der Technischen Fakultät der
Universität Erlangen-Nürnberg
zur Erlangung des Grades

DOKTOR-INGENIEUR

vorgelegt von

Bernhard Krach

Erlangen - 2010

Als Dissertation genehmigt von
der Technischen Fakultät der
Universität Erlangen-Nürnberg

Tag der Einreichung: 29.05.2009
Tag der Promotion: 25.11.2009
Dekan: Prof. Dr. Reinhard German
Berichterstatter: Prof. Dr. Robert Weigel
Prof. Dr. Jörn Thielecke

May all your ships sail safely through the night

Farewell of The Miserable Rich

Acknowledgement

This thesis results from 4 years of research as scientific staff of the Institute of Communications and Navigation at the German Aerospace Center (DLR) in Oberpfaffenhofen, Germany.

Foremost I would like to thank my advisor Prof. Robert Weigel for his guidance, thrust and encouragement over the past years. I also wish to thank Prof. Jörn Thielecke for acting as the co-advisor for this thesis.

My special thanks I want to express to Dr. Patrick Robertson for his inspiring ideas and for many fruitful discussions. I also like to thank Dr. Uwe-Carsten Fiebig for his support during the last years. As well many thanks to all my colleagues at DLR, I'm grateful for the time we worked together.

Oberpfaffenhofen, May 2009

Abstract

Seamless pedestrian navigation in both indoor and outdoor environments is an unsolved challenge today. Though various navigation systems and sensors exist which are suitable in terms of size, cost, and power consumption, today none of these systems is expected to serve as a sole means for personal navigation in the mid-term future. In particular the characteristic drawbacks of today's systems in specific environments prevent their successful use. This work shows how to solve the problem by the rigorous application of a sound theoretically motivated approach: The combination of various sensors and the optimal joint processing of their provided data by a Bayesian filter algorithm, which optimally takes into account the uncertainty inherently included in each sensor's data and which exploits optimally all available knowledge about the movement of the navigating individual, such that in the end no information is lost during the processing of the data. After an introduction to personal navigation systems and sensors, particularly focusing on satellite and inertial navigation, and a summary on the concept and the implementation of Bayesian filters, the thesis addresses the application of Bayesian filtering to enhance the performance of satellite navigation receivers in urban multipath environments. The results confirm the benefit of the Bayesian approach, which is shown to outperform a conventional navigation receiver significantly. Subsequently a novel integration scheme for inertial sensors is proposed based on the concept of foot-mounted inertial sensing. Thereby particular emphasis is put on the incorporation of an adequate map-based pedestrian mobility model in order to reduce the heavy drift of today's small-scale and low-cost micro-electro-mechanical inertial sensor platforms. The results show that the combination of inertial navigation with a map-based pedestrian mobility model can achieve a fully autonomous drift-free navigation in indoor environments. Finally it is shown how seamless pedestrian navigation systems can be designed successfully by the use of Bayesian filtering algorithms. The design of the filter algorithms is addressed and depending on the employed and available sensors the suitable filter implementation is chosen, including an extended Kalman filter for the combination of fingerprinting via a wireless local area network and foot-mounted inertial sensors and a particle filter for the integration of a satellite navigation receiver, a radio-frequency identification unit, a compass, a baro-altimeter, a foot-mounted inertial platform, and a map-based pedestrian mobility model.

Zusammenfassung

Das Problem der nahtlos und kontinuierlich verfügbaren Fußgänger-Navigation ist heute noch weitgehend ungelöst, insbesondere innerhalb von Gebäuden. Obgleich heute eine Vielzahl von Systemen und Sensoren zur Verfügung steht, die aufgrund ihrer Merkmale wie Größe, Kosten und Stromverbrauch als geeignet erscheinen, ist es doch mittelfristig nicht zu erwarten, dass eine der bereits exisitierenden Lösungen das alleinige Mittel der Wahl sein wird, um die Probleme der Fußgänger-Navigation zu lösen, da dem insbesondere die jeweils systemspezifischen Schwächen der einzelnen Systeme und Sensoren in unterschiedlichen Szenarien entgegenstehen. Im Rahmen dieser Arbeit wird aufgezeigt wie dort bestehende Probleme durch die strikte Anwendung eines theoretisch solide motivierten Ansatzes gelöst werden können: Die Kombination verschiedener Sensoren und die optimale Verarbeitung ihrer Daten mittels eines Bayes'schen Filters, das in optimaler Weise die Unsicherheiten in den Sensordaten berücksichtigt und welches optimal alles verfügbare Wissen über die Bewegung der navigierenden Person miteinbezieht, so dass letztendlich keinerlei Information bei der Verarbeitung der Daten verloren geht. Nach einer Einleitung zu Systemen und Sensoren der Fußgänger-Navigation, die speziell die Grundlagen der Satelliten- und Trägheitsnavigation adressiert, und einer Zusammenfassung der Prinzipien und Implementierungen der Bayes'schen Filter, wird in der vorliegenden Arbeit die Anwendung der Bayes'schen Filterung bei der Signalverabeitung in Satellitennavigationsempfängern untersucht, insbesondere mit dem Ziel, deren Genauigkeit in städtischen Mehrwegeumgebungen zu verbessern. Die dort präsentierten Resultate bestätigen den Vorteil der Bayes'schen Filterkonzepte, die verglichen mit konventionellen Empfängeralgorithmen eine deutlich höhere Genauigkeit erzielen. Basierend auf dem Konzept einer Fuß-montierten Sensorplattform wird nachfolgend eine neue Integrationsmethode für die Nutzung von Trägheitssensoren vorgeschlagen, wobei im Speziellen die Berücksichtigung von geeigneten kartenbasierten Fußgänger-spezifischen Bewegungmodellen im Vordergrund steht, mit dem Ziel die bei der Verwendung der heute verfügbaren miniaturisierten und kostengünstigen mikro-elektro-mechanischen Sensoren entstehende Drift zu vermindern. In diesem Zusammenhang wird gezeigt, dass durch die Kombination von Trägheitssensoren und kartenbasierten Bewegungsmodellen eine voll autonome und Drift-freie Navigation innerhalb von Gebäuden erzielt werden kann. Schließlich wird diskutiert, wie nahtlose Fußgänger-Navigationssysteme mittels Bayes'scher Filter realisiert werden können. Dabei wird gezeigt, wie ein geeignetes Filter in Abhängigkeit von den verwendeten und verfügbaren Sensoren entworfen und implementiert werden kann. Im Speziellen wird dabei der Entwurf eines erweiterten Kalman-Filters zur Fusion einer Feldstärke-basierten Ortung mittels eines lokalen Funknetzwerkes und Fuß-montierten Trägheitssensoren behandelt und der Entwurf eines Partikel-Filters zur Fusion von Satellitennavigation, Funkidentifikation, Kompass, Höhenmesser, Fuß-montierten Trägheitssensoren und eines kartenbasierten Fußgänger-Bewegungsmodells.

Contents

Abstract i

Zusammenfassung iii

Table of Contents v

1 Introduction 1
- 1.1 The Need for Pedestrian Navigation . . . 2
- 1.2 Combining Sensors for Pedestrian Navigation . . . 3
- 1.3 Objectives of the Thesis . . . 7
- 1.4 Structure of the Thesis . . . 7

2 Fundamentals 9
- 2.1 Satellite Navigation . . . 9
  - 2.1.1 Synchronization of Navigation Signals . . . 10
  - 2.1.2 The Problem of Multipath . . . 12
- 2.2 Inertial Navigation . . . 15
  - 2.2.1 Inertial Sensors and Platforms . . . 15
  - 2.2.2 Inertial Navigation Computations . . . 15
- 2.3 Optimal Estimation . . . 19
  - 2.3.1 Algorithm Implementation . . . 22
  - 2.3.2 Application to Joint Satellite and Inertial Navigation . . . 28

3 Pedestrian Satellite Navigation 33
- 3.1 Multipath Signal Model . . . 35
  - 3.1.1 Discrete Time Model . . . 36
  - 3.1.2 The Likelihood Function . . . 37
- 3.2 Bayesian Estimation in the Pseudorange Domain . . . 40
  - 3.2.1 Choice of Channel Process . . . 40
  - 3.2.2 Filter Implementation . . . 42
- 3.3 Bayesian Estimation in the Position Domain . . . 47
  - 3.3.1 Choice of System Process . . . 47
  - 3.3.2 Filter Implementation . . . 49
- 3.4 Comparison of Approaches . . . 53
  - 3.4.1 Equivalent Dynamic Modeling . . . 54
  - 3.4.2 Estimator Complexity . . . 55

3.4.3 A Posteriori Cramer-Rao Bounds 55
3.5 Results 55
3.5.1 AWGN Channel 56
3.5.2 Static Multipath Channel 57
3.5.3 Pedestrian Channel Model 59
3.5.4 Measured Pedestrian Channel 61

4 Pedestrian Inertial Navigation 69
4.1 Motivation of a Novel Approach 70
4.2 Cascaded Implementation 71
4.2.1 Upper Filter 71
4.2.2 Lower Filter 74
4.2.3 Choice of an Appropriate Proposal Density 81
4.2.4 Integration of a Pair of Platforms 83
4.2.5 Joint System Error Analysis 84
4.2.6 Integration of Additional Sensors 86
4.3 Results 86
4.3.1 Simulation 86
4.3.2 Experiment 87

5 Application Examples 91
5.1 A Joint WLAN/INS Pedestrian Positioning System 91
5.1.1 WLAN Fingerprinting 92
5.1.2 Inertial Step Sensing 93
5.1.3 Main Integration Filter 94
5.1.4 System Evaluation 96
5.2 A Multi-Sensor Framework for Pedestrian Navigation 100
5.2.1 Incorporation of Sensors 100
5.2.2 Characterization of Sensors 101
5.2.3 Movement Model 104
5.2.4 Performance Evaluation 104

6 Conclusions 113
6.1 Summary of Contributions 113
6.2 Future Work 115

A Proof of the Factorized Bayesian Estimator 117

B Simulation Parameters 119
B.1 Chapter 3 119
B.1.1 Section 3.4.3: PCRB Computation 119
B.1.2 Section 3.5.1: AWGN Channel 119
B.1.3 Section 3.5.2: Static Multipath Channel 120
B.1.4 Section 3.5.3: Pedestrian Channel Model 120
B.1.5 Section 3.5.4: Measured Pedestrian Channel 125
B.2 Chapter 4 125

B.2.1 Section 4.2.3: Proposal Density 125
B.2.2 Section 4.3.1: Error Analysis 125
B.2.3 Section 4.3.2: Experiment 125
B.3 Chapter 5 125
B.3.1 Section 5.1: Filter Settings 125
B.3.2 Section 5.2: Filter Settings 126

C Sensors and Devices **127**

Bibliography **127**

List of Abbreviations **141**

List of Symbols **143**

List of Figures **146**

List of Tabels **154**

Chapter 1

Introduction

The term *navigation*, which originates from the Latin verb *navigare*, denotes the art of orientation in a topographic space with the objective to reach a specific destination. It comprises basically two operations: The determination of position and course and the control of the movement to the destination. The early fundamentals of navigation have been developed by ancient sailors millennia ago and have evolved continuously to this day. Today the term navigation is used not only in nautics but more generally for space, aeronautical, and land navigation as well. Apart from suitable guidance to the destination a crucial step in the process of navigation is the retrieval of the required information, i.e. basically the actual position and course of the navigating object. This information can usually not be determined directly, and thus there is the need to infer it indirectly from observations of physical effects, which are somehow related to the place of their observation and/or to the movement of the navigating object. The capability to perform orientation and navigation is a fundamental property of intelligent life-forms. Humans and animals own sense organs, which enable them to orientate, e.g. through visual perception. The most intuitive method of human orientation and navigation is via landmarks: The direct orientation by the recognition of already known or pre-described places or objects. Nevertheless not all physical effects that can be exploited for navigation are directly perceivable by the human senses. The rise of natural sciences and the technical advances through the past centuries enabled the development of tools and instruments, which could make previously unexploitable physical effects properly perceptible to humans or man-made apparatuses. Such instruments, which are denoted as sensors, are key components of modern navigation systems. Historically sailors used compass and sextant as sensors. The sensing of the earth's magnetic field by the compass allowed to determine north direction and bearing, whereas the sextant was used to determine the position based on the observation of the elevation angle of a star with respect to the horizon. Today the by far most important sensing principle has become the reception of electromagnetic waves, which are emitted from sources of known location, such that their power, their direction of arrival, their time of arrival, their Doppler shift, and their distortion is characteristic for the place of reception and thus can be used to derive information about the receiver's position. In this context global satellite navigation systems (GNSS) like the Global Positioning System (GPS) [PS96] or the future European satellite navigation system Galileo have today become the most important radio-based navigation systems. The successful deployment of a fully operational constellation of dedicated navigation radio-transmitters in space and the establishment of an associated ground infrastructure in terms of the GPS space and ground segments represents a unique advance in the history of navigation, since the world's first world-wide available radio-based navigation system has become available. Whereas satellite navigation was formerly restricted and limited to military and professional applications, it is currently firmly established in the mass market. Satellite-based navigation systems for private cars have become a standard during the last decade. A still increasing percentage of mobile phones is packaged with satellite navigation receivers, making personal navigation an established mass market application. Although GPS and the Russian GLONASS system still are the two only operational GNSS, the fact that in the near future two further GNSS in terms of the European Galileo system and the Chinese Compass system will be available, shows the importance of satellite navigation today. A quite complementary sensing principle is the concept of inertial navigation [TW04], since it is based on body-mounted sensors only and does not require any additional infrastructure. As expressed by Newton's law of motion any navigating object experiences characteristic accelerations and turn rates during its movement. In inertial navigation these quantities are sensed via an assembly of accelerometers and gyroscopes. Mathematical integration of the observed quantities allows to compute continuously position and attitude by the concept of dead-reckoning. Inertial navigation systems (INS) became standard in aircraft, ships and submarines during the 1960s using the stable platform technology. Since then the increasing performance of micro-computers and advances in gyroscope technology allowed for the realization of strapdown inertial navigation systems, which has lead to decreased size, complexity, power consumption, and cost of such systems [Kin98]. Within the past few years micro-electro-mechanical (MEMS) inertial sensors have been developed significantly and are about to replace conventional mechanical and optical inertial sensors in many classical applications as well as to open new fields of application for inertial navigation systems due to further reduced size and cost. In particular personal navigation is about to take benefit of these technological advances, since power consumption, size, and cost of the latest MEMS inertial sensors have reached a scale which allows to integrate them into mobile devices and wearables.

1.1 The Need for Pedestrian Navigation

Though there are various sensors and systems available which today work properly for many pedestrian navigation applications, there is still a large need for seamless pedestrian navigation systems, i.e. for systems that still operate under conditions which may be regarded as harsh for the existing systems and which may even cause them to fail. For instance satellite based navigation works properly in free field conditions but usually fails in dense urban canyons or indoor environments. Consequently, satellite navigation does not provide a seamless solution covering both indoor and outdoor scenarios. But specifically for pedestrian navigation a key issue is the capability to operate also accurately in dense urban environments or indoor, since these adverse scenarios are the most relevant ones for navigating persons. Thus there is still an unmet demand for seamless solutions, and the current world-wide efforts in research and development of such systems confirm this need. Applications that will take benefit of such solutions are numerous: localization, monitoring and guidance of first responders, firefighters, relief units, and special forces in the professional sector, and, amongst many others, mass market applications such as guidance and assistance of tourists and travelers, general location-based and context-aware services, sports applications, and assisted living for the elderly.

1.2 Combining Sensors for Pedestrian Navigation

Each navigation method has its individual advantages and drawbacks which are determined mainly due to the characteristic properties of the employed sensors. Actually, it can be shown that the integration of complementary navigation sensors or systems into a joint multi-sensor navigation system is advantageous, since the adverse properties of the individual sensors or sub-system can be compensated in the joint system. In particular the combination of GNSS and INS, which is well-established in aerospace applications [KF97], is a famous example, as both system have quite complementary characteristics: An INS is fully self-contained, very accurate in the short term, even under highly dynamic conditions, but does degrade in the long term, mainly due to instrument imperfections. In contrast the GNSS solution is generally rather inaccurate in short term, but does not degrade in the long term. The synergy of both systems allows for an improved calibration of the INS instrument errors along with a reduction of the GNSS receiver noise susceptibility, which leads to mutual advantage. Thus the shortcomings of the INS are compensated by the GNSS and vice versa, such that the joint system achieves a significantly improved performance. They key for a successful integration of complementary sensors and systems is the use of an optimal sensor data fusion algorithm. Since it is not possible to manufacture perfect sensors, each real-world sensor data does inherently not represent the truth, but is disturbed somehow, so that there is always a specific amount of uncertainty in the provided data. Thus an optimal fusion of sensor data is achieved only if the information within the components of the joint system is represented and exchanged in association with reliability measures, i.e. in particular by a representation via probability density functions (PDFs) instead of fixed data values. If each of the components exploits the provided probabilistic information adequately, no information is lost during the interaction of the systems components and thus the overall system performance is increased up to the theoretical thresholds. The probabilistic concept has already been applied successfully in communication systems [Hag94] and has an even longer history in navigation [May79], where the optimal algorithm can be circumscribed as follows: It uses all available sensors to compute position and course by ensuring that the accuracy of each sensor is taken into account in an optimal way. Furthermore, the optimal algorithm makes use of any a priori knowledge about the evolution of position and course, which is given due to physical constraints in the movement of the navigating object. In this context it is well known that the framework of Bayesian filtering allows to implement the desired optimal probabilistic solution. Since the introduction of the Kalman filter [Kal60], which optimally solves the problem of Bayesian filtering for the special class of Gaussian and linear dynamic systems, the theory on Bayesian filter implementations has evolved significantly to this day. Specifically the increase in computational power in digital signal processors and computers in combination with the development of the Particle filtering algorithms [AMGC02] during the last decade allows us today to solve general nonlinear Bayesian filtering problems, which could not be solved adequately in the past. In particular the field of personal navigation, which is today still more a subject of research than a mature technology, is expected to reap a large benefit from both the recent developments in the field of signal processing capabilities as well as the recent developments in sensor technology. Specifically, for personal navigation applications there are certain restrictions on the sensors that can be used: Personal navigation sensors need to be light-weight, small-scale, low-power and low-priced, which prevents the use of some existing navigation sensor technologies. In Figure 1.1 various sensors that are suitable for personal

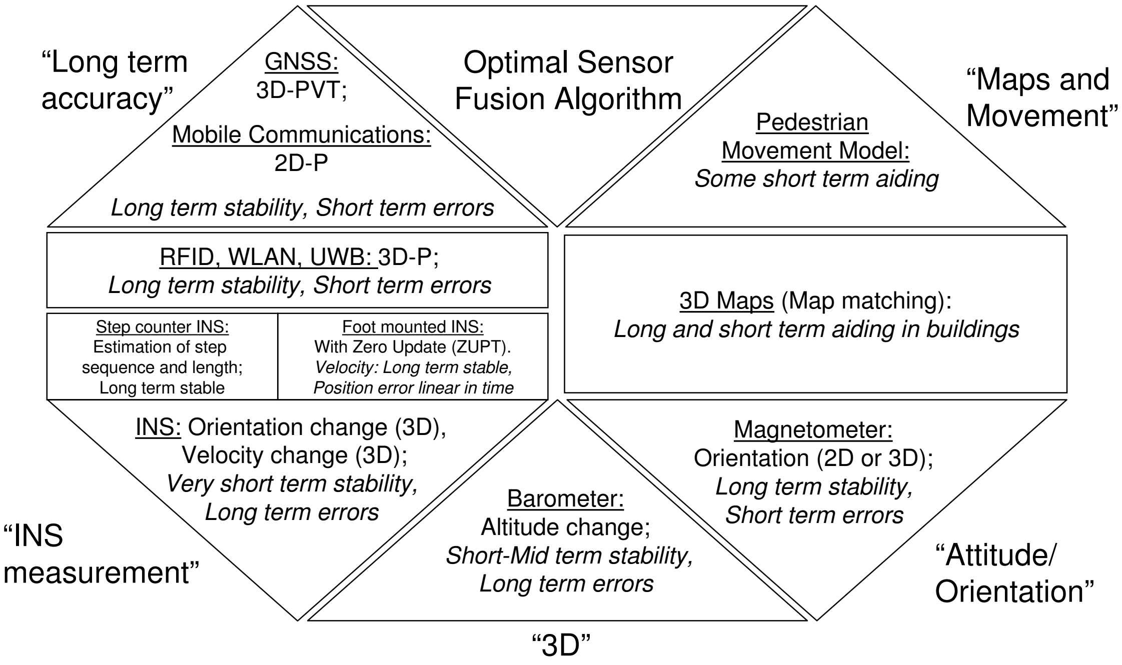
"Long term accuracy"
GNSS:
3D-PVT;
Mobile Communications:
2D-P
Long term stability, Short term errors
Optimal Sensor Fusion Algorithm
Pedestrian Movement Model:
Some short term aiding
"Maps and Movement"
RFID, WLAN, UWB: 3D-P;
Long term stability, Short term errors
3D Maps (Map matching):
Long and short term aiding in buildings
Step counter INS:
Estimation of step sequence and length;
Long term stable
Foot mounted INS:
With Zero Update (ZUPT).
Velocity: Long term stable,
Position error linear in time
INS: Orientation change (3D),
Velocity change (3D);
Very short term stability,
Long term errors
"INS measurement"
Barometer:
Altitude change;
Short-Mid term stability,
Long term errors
Magnetometer:
Orientation (2D or 3D);
Long term stability,
Short term errors
"Attitude/ Orientation"
"3D"

Figure 1.1: Personal navigation sensors and their properties: Each sensor has its individual characteristics. The combination of complementary sensors via an optimal sensor fusion algorithm allows to exploit synergetic effects and improves the overall navigation performance.

navigation are summarized along with their individual properties and characteristics, which are discussed in more detail in the following.

Satellite Navigation

Satellite navigation offers the major advantage of world-wide availability. A complete GNSS constellation enables the user device to continuously determine its three-dimensional position at any time and at any place in the world, given that a sufficient number of operating satellites can be received properly. Satellite navigation receivers are today available in the form of integrated circuits, which makes it possible to integrate them into small-scale mobile devices such as mobile phones or personal digital assistants (PDA). The accuracy with latest mass market receivers approaches to 1-2 meters in free field conditions. When the acquisition is assisted by mobile communication systems the time-to-first-fix (TTFX), the period from switching on the receiver to the first position fix, is today only a few seconds. A major remaining problem in GNSS is the performance degradation in urban or indoor environments, where the reception of multipath can cause errors up to 100 meters and more [SL03]. In some harsh indoor environments satellite navigation is even completely unavailable.

Mobile Communications

Positioning via mobile communication signals benefits from higher reception power compared to GNSS, leading to a significantly increased availability in adverse urban and indoor environments. Nevertheless the achievable accuracy with today's standardized second and third generation mobile communication signals, such as the Global System for Mobile Communications (GSM) or the Universal Mobile Telecommunications System (UMTS), is in the order of 50-300 meters or even worse, depending on the concentration of available base stations and the positioning method used [DMS98]. It is usually accurate enough for a coarse orientation and beneficial when used to assist the acquisition of GNSS, but due to its limited accuracy it can not serve as a sole means for all personal navigation applications.

Radio Frequency Identification

Localization via radio frequency identification (RFID) is highly valuable whenever it is possible to distribute infrastructure. Depending on the employed standard RFID can provide an accuracy in the order of few meters [WRK$^+$07] or even less, which allows to maintain accurate positioning indoors, whenever other sensors or systems like GNSS are inaccurate or even completely unavailable. There are two basic approaches of RFID-based positioning: Either the RFID readers are deployed and the users carry the tags or the other way round with the users being equipped with RFID readers and distributed tags. The positioning via RFID systems can be done either based on the received signal strength (RSS) or based on the identification number (ID) of the received tag only.

Wireless Local Area Network

The localization via wireless local area networks (WLANs) [ISO99, IEE99] is comparable to the RFID approach with respect to the system characteristics. The achievable accuracy is in the same order and both approaches require a deployed infrastructure. A major advantage of the WLAN approach is that today in the majority of buildings in which people require personal navigation, for example in airports, public buildings, and company premises there already exists a dense installation of WLAN infrastructure. In WLAN positioning commonly the RSS of the received base stations is used to determine the user location. For this purpose the RSS characteristics of each base station, the so-called RSS fingerprints, need to be known at regularly distributed reference locations, which is a major drawback, as it usually requires to carry out extensive calibrations. In some advanced WLAN positioning systems the signal timing information is exploited to derive the location information.

Ultra-Wideband Systems

Ultra-Wideband (UWB) systems [GTG$^+$05] require the deployment of infrastructure as well but offer several major benefits compared to RFID- and WLAN-based positioning. Due to the high bandwidth of the UWB pulses, whose travel time is commonly used to determine the user position, the achievable accuracy is much higher and can reach to the millimeter range. In particular for first responder applications UWB is a favorable alternative, since on site mobile UWB transmitters can be deployed quickly around any building and the emitted UWB signals can penetrate the walls of a building to a certain extent.

Inertial Sensors

Basically two approaches for the use of inertial sensors in personal navigation can be distinguished. The pedometer approach employs an accelerometer for detecting individual steps whilst the stride length and stride direction are themselves estimated using additional sensors or a priori information [GM99]. Given a detected step, its length and its direction, a person's position can be determined by dead-reckoning. The latest approaches are based on full six degree of freedom (6DOF) inertial navigation. A foot-mounted 6DOF strapdown inertial platform comprising triads of accelerometers and gyroscopes is used to dead reckon via a conventional inertial navigation algorithm. Rest phases of the foot, which are detected from the accelerometer signals, trigger zero-velocity updates (ZUPTs), which allow for the compensation of the drift errors, which accumulate in the inertial navigation solution. It was shown in [Fox05] that this approach can achieve a performance down to one percent of the traveled distance or less even with today's low-cost MEMS inertial sensors, because the ZUPTs are usually so frequent that errors build up only slowly during each step a pedestrian makes.

Baro-Altimeter

Baro-altimeters are widely used in airborne navigation [KF97] and for sports applications such as hiking or skydiving. Once calibrated for the local air pressure, baro-altimeters usually maintain sub-meter accuracy for intermediate-term periods. Baro-altimeters can be used to sense changes in the floor level indoors and thus are valuable when extending personal navigation towards the vertical dimension. A typical problem is the susceptibility to changes in the surrounding temperature, which may occur when entering rooms and buildings and the long-term stability, which is degraded by the natural variations of the local atmospheric pressure.

Magnetic Compass

The natural magnetic field of the earth is a valuable indicator of local bearing and thus the compass is today still an important navigation sensor, which is used in many navigation applications such as attitude and heading reference systems (AHRS). Though traditional mechanical compasses are more and more becoming replaced by electronic magnetometers, the principle has remained the same: The compass aligns with respect to the local magnetic field of the earth and, given that the local magnetic declination (the deviation between the magnetic and the actual north direction) is known, the actual heading with respect to north direction can be determined. A characteristic problem of the magnetic compass is its susceptibility to local external disturbances, which may be caused by surrounding magnetic materials and by any nearby current-carrying structures. In particular in indoor environments this can cause a serious performance degradation.

Movement Models and Maps

A movement model characterizes the constraints in the dynamics of a navigating object, e.g. the maximum speed and the inertia of a pedestrian. Even though it is not possible to predict the movement of a navigating object completely accurate, it is still possible to predict its movement in a probabilistic fashion with a specific amount of uncertainty. Actually maps can be regarded as a part of general movement models. The topology of the map affects the movement [KKRA08], since given the actual position and course of an object, and the map layout, some new positions and directions may be considered to be more likely than others, e.g. it is unlikely that a pedestrian will attempt to cross a building wall. In the simple use of map information the user position and direction is just matched via a map-matching algorithm onto the map. For many applications, e.g. car navigation, this is sufficient, given the map is up to date and the matching algorithm converges properly. In more elaborated models the movement is explicitly characterized by a map-dependent probabilistic model [KKRA08].

1.3 Objectives of the Thesis

Seamless personal navigation is an unsolved challenge today. The key motivation of this thesis is to address this challenge by applying the concept of sensor fusion and to show that optimally fusing complementary sensors and sources of information can be highly beneficial, even if the sensors are either rather simple or seem to be only of little value, at least when used stand-alone. Specifically the formulation of suitable Bayesian filter implementations is addressed, with the objective to quasi-optimally fuse satellite navigation, inertial sensors, and further navigation sensors as illustrated in Figure 1.1, in order to achieve seamless personal navigation in indoor and outdoor environments. Although in particular the integration of GNSS and INS is already a well established field in engineering science, which was driven in particular by aerospace applications, the boundary conditions are quite different for personal navigation. Firstly, size, weight, and power consumption of the sensors must meet the needs of a personal navigation system, which imposes stringent restrictions on the quality and thus on the performance of the sensors. Secondly, the dynamics of a pedestrian differ significantly from those of an aircraft, ship, or land vehicle and thirdly the user environment is much more challenging. In particular in urban or indoor environments the propagation conditions for electromagnetic waves are adverse due to the crucial problems of signal blockage, attenuation and multipath propagation, which degrade the nominal performance of radio-based navigation seriously. Thus the thesis focuses on the handling of these adverse propagation environments and on the incorporation of pedestrian movement models into inertial navigation. A further motivation is thereby not only to make personal navigation in these environments feasible, robust, and precise, but also to accompany the navigation with information that informs the user about the current reliability and precision of the system.

1.4 Structure of the Thesis

The thesis is structured as follows: After the introduction in Chapter 2 the fundamentals of satellite navigation, inertial navigation, and optimal filtering are reviewed as far as they are relevant for the scope of the thesis. In Chapter 3 the problem of personal satellite navigation is addressed, in particular focusing the problem of multipath and non line-of-sight (LOS) reception and its successful mitigation via sequential Bayesian estimation. Thereby emphasis is placed on time-variant dynamic multipath channels, which are characteristic for urban environments. Subsequently Chapter 4 deals with the efficient integration of inertial sensors. The central issue of this chapter is the proper combination of conventional foot-mounted inertial navigation, which lacks an adequate pedestrian movement model, with elaborated map-based movement models. In Chapter 5 two real-world implementation examples for personal navigation systems are presented and evaluated: first a joint WLAN fingerprinting and inertial positioning system based on two federated extended Kalman filters, and second an experimental multi-sensor fusion platform, which integrates satellite navigation, inertial sensors, compass, RFID, baro-altimeter, map information, and a pedestrian movement model via a cascade of an extended Kalman filter and a particle filter algorithm. Chapter 6 concludes the thesis by summarizing the main contributions of the presented work and gives an outlook to possible future work in the context of this thesis.

Chapter 2

Fundamentals

2.1 Satellite Navigation

Within global navigation satellite systems, such as the Global Positioning System (GPS) or the future European satellite navigation system Galileo, the user position is determined based upon the code division multiplex access (CDMA) navigation signals received from different satellites using the time-of-arrival (TOA) method. A constellation of orbiting satellites transmits continuously navigation signals. Each of the satellites transmits its own unique CDMA code sequence, which is modulated by a stream of navigation data. The signal travel time from the satellite to the receiver is measured at the receiver for each of the received satellites. For that purpose the provided navigation data includes for each satellite the relevant information to retrieve the position of the satellite at the time of transmission as well as the time of transmission itself. Since the receiver clock is not synchronized to the system time, the measured travel time at the receiver has a common error for all received satellites. This error is referred to as the receiver clock offset and has to be estimated in addition to the three-dimensional receiver position. Thus once the travel time is measured for at least four received satellites, the receiver position and the receiver clock offset can be determined geometrically as illustrated in Figure 2.1. Since the measured travel time is not equal to the true travel time due to the receiver clock offset, the distance measure at the receiver is commonly referred to as pseudorange. The pseudorange for satellite j, $j = 1, \ldots, M$, with M being the number of received satellites, is according to [Kap96]

$$\rho_j = \left|\mathbf{r}_j^t - \mathbf{r}^r\right| c^{-1} + \tau^r \ , \tag{2.1}$$

with the pseudorange ρ_j, the position of the transmitting satellite $\mathbf{r}_j^t$, the receiver position $\mathbf{r}^r$, the receiver clock bias τ^r, and the speed of light c. The observable pseudorange measure is affected by several systematic errors, for which corrections can be retrieved from the received navigation data. These errors include the transmitter clock offset τ_j^t and, due to the signal propagation through the atmosphere, the ionospheric delay τ_j^{iono} as well as the tropospheric delay τ_j^{tropo} [PS96]. Considering these additional error terms the actually measured travel time τ_j at the receiver is finally

$$\tau_j = \rho_j + \tau_j^t + \tau_j^{\text{iono}} + \tau_j^{\text{tropo}} + \varepsilon_j \ . \tag{2.2}$$

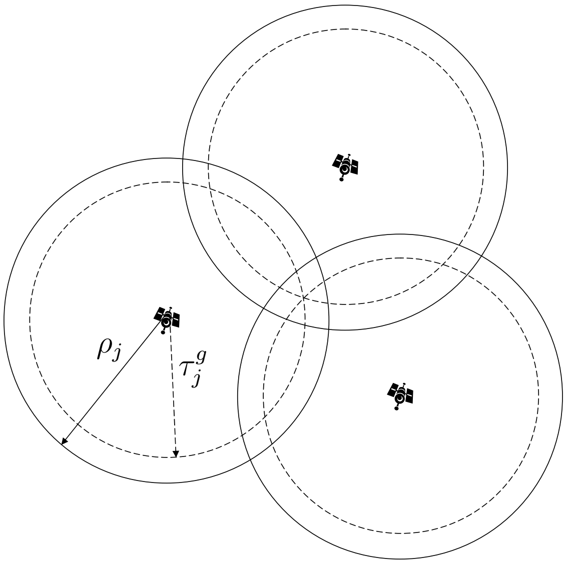

Figure 2.1: 2D illustration of TOA positioning: The measured travel time ρ_j is different from the true geometrical travel time $\tau_j^g = \left|\mathbf{r}_j^t - \mathbf{r}^r\right| c^{-1}$ due to the asynchronous receiver clock. The receiver position is at the intersection of the three dashed circles.

Further unknown errors, e.g. the random error due to the receiver noise, are taken into account by the residual error term ε_j. To obtain a position from the TOA measurements the parameters $\mathbf{r}_j^t$, τ_j^t, τ_j^{iono},τ_j^{tropo} and ε_j are considered as known values and a linearized approximation of (2.1) and (2.2) is commonly used to solve the non-linear system of pseudorange equations iteratively [Kap96]. For this procedure the unknowns are collected in the vector $\mathbf{x} = [\mathbf{r}^r, \tau^r]$ and the system of equations is expressed by the truncated Taylor series expansion

$$\underbrace{\begin{bmatrix}\tau_1(\mathbf{x})\\ \vdots \\ \tau_M(\mathbf{x})\end{bmatrix}}_{\boldsymbol{\tau}} = \begin{bmatrix}\tau_1(\mathbf{x}_0+\delta\mathbf{x})\\ \vdots \\ \tau_M(\mathbf{x}_0+\delta\mathbf{x})\end{bmatrix} = \underbrace{\begin{bmatrix}\tau_1(\mathbf{x}_0)\\ \vdots \\ \tau_M(\mathbf{x}_0)\end{bmatrix}}_{\boldsymbol{\tau}_0} + \underbrace{\frac{\partial}{\partial \mathbf{x}}\begin{bmatrix}\tau_1(\mathbf{x})\\ \vdots \\ \tau_M(\mathbf{x})\end{bmatrix}\Bigg|_{\mathbf{x}_0}}_{\mathbf{D}} \delta\mathbf{x}\ . \tag{2.3}$$

The solution obtains a refined position and clock bias estimate $\hat{\mathbf{x}} = \mathbf{x}_0 + \delta\hat{\mathbf{x}}$ based on an initial hypothesis $\mathbf{x}_0$, where the refined value is computed via the weighted least squares (LS) estimate

$$\delta\hat{\mathbf{x}} = \left(\mathbf{D}^T\mathbf{W}^{-1}\mathbf{D}\right)^{-1}\mathbf{D}^T\mathbf{W}^{-1}(\hat{\boldsymbol{\tau}} - \boldsymbol{\tau}_0)\ , \tag{2.4}$$

with the diagonal weighting matrix $\mathbf{W} = \mathrm{diag}([\sigma_1^2, \ldots, \sigma_M^2])$ and the satellite geometry matrix $\mathbf{D}$. In the weighting matrix the element σ_j^2 refers to the variance of the delay estimate $\hat{\tau}_j$. In the iterative solution of (2.4) the actual point of linearization $\mathbf{x}_0$ is set equal to the estimate $\hat{\mathbf{x}}$ from the previous iteration. For a receiver located on the surface of the earth the solution usually converges quickly after few cycles of iteration [EM06a].

2.1.1 Synchronization of Navigation Signals

Unlike communication signals, navigation signals are designed and optimized in particular with respect to synchronization performance instead of data transmission performance, as the precise synchronization at the receiver is crucial to provide accurate time delay estimates for the subsequent position computation. In particular the synchronization of the CDMA code sequence is important, as it provides (unlike the phase synchronization) an unambiguous measure of signal travel time [Kap96]. According to [PS96] the complex valued baseband-equivalent received signal in a navigation receiver for satellite j is equal to

$$z_j(t) \;=\; a_j(t)s_j\left(t-\tau_j(t)\right)+n(t)\ , \tag{2.5}$$

where $s_j(t)$ is the CDMA navigation signal, $a_j(t)$ is its complex amplitude, and $\tau_j(t)$ the time delay of the signal according to (2.2). The signal is assumed to be received superimposed by white Gaussian noise, which is represented through $n_j(t)$. The signal is sampled at times $(m+kL)T_s$, $m=0,\dots,L-1$ and grouped in blocks of L samples together into vectors $\mathbf{z}_{j,k}$, $k=0,1,\dots,$. Assuming the parameter functions $\tau_j(t)$ and $a_j(t)$ to be constant and equal to $\tau_{j,k}$ and $a_{j,k}$ during the corresponding time interval, the discrete-time signal for satellite j at time index k may be written in the compact form

$$\mathbf{z}_{j,k} \;=\; \mathbf{s}_j(\tau_{j,k})a_{j,k}+\mathbf{n}_{j,k}\ . \tag{2.6}$$

In a conventional navigation receiver a combination of a delay lock loop (DLL) and a frequency/phase lock loop (FLL/PLL) is used to estimate signal delays. The DLL is designed to keep track of the maximum of the correlation of the received and a local replica signal [PS96] and thus implements an approximation to the maximum likelihood (ML) time delay estimator [Kay93]. The FLL/PLL is used to counter the variations of the complex amplitude of the received signal [Kap96]. The DLL estimation is based on a sequence of coherent observations of the received signal, with the LT_s being the so-called coherent integration time of the receiver, and a local linear approximation of the cross-correlation function $\mathbf{s}^H(\tau)\mathbf{z}_{j,k}$, where at each time step the delay estimate $\hat{\tau}_k$ is obtained through refining a delay hypothesis $\tau^0_{j,k}$ by the estimate of the actual timing mismatch $\tau_{\epsilon,j,k}$, i.e.:

$$\hat{\tau}_{j,k}=\tau^0_{j,k}+\hat{\tau}_{\epsilon,j,k}\ . \tag{2.7}$$

The timing mismatch is obtained via the linear approximation

$$\hat{\tau}_{\epsilon,j,k}=\left(\left.\frac{\mathrm{d}D(\tau_{j,k})}{\mathrm{d}\tau_{j,k}}\right|_{\tau^0_{j,k}}\right)^{-1} D(\tau_{j,k})\ , \tag{2.8}$$

with the function $D(\bullet)$ being the timing error detector (TED) of the DLL, e.g. a non-coherent unnormed early/late discriminator [PS96]

$$D(\tau_{j,k}) \;=\; \left|\mathbf{z}^e_{c,j,k}\right|^2-\left|\mathbf{z}^l_{c,j,k}\right|^2\ , \tag{2.9}$$

with the early and late correlation values

$$\mathbf{z}^e_{c,j,k} \;=\; \mathbf{s}^H_j(\tau^e_{j,k})\mathbf{z}_{j,k}\ , \tag{2.10}$$

$$\mathbf{z}^l_{c,j,k} \;=\; \mathbf{s}^H_j(\tau^l_{j,k})\mathbf{z}_{j,k}\ . \tag{2.11}$$

The computation of the correlation values $\mathbf{s}^H_j(\bullet)\mathbf{z}_{j,k}$ is done by receiver components that are denoted as correlators. The slope of the function $D(\bullet)$ is designed to be an approximation

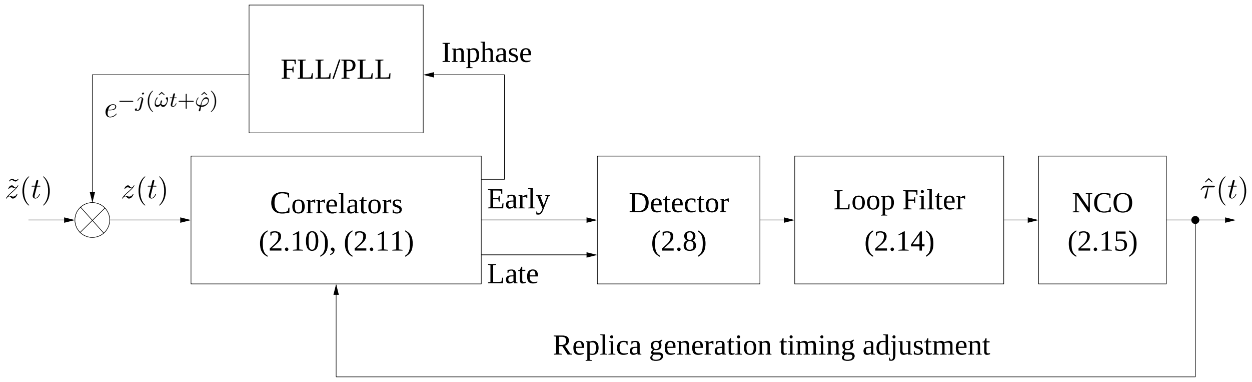

Figure 2.2: Synchronization in a navigation receiver: A combination of a DLL and a FLL/PLL is used to track the delay of the received signal with respect to a local replica signal.

to the derivative of the correlation function $\mathbf{s}_j^H(\tau)\mathbf{z}_{j,k}$, which is according to (2.9) achieved by subtracting the squared results of the correlation of the received signal $\mathbf{z}_{j,k}$ with two local replica, one in advance (early) and one delayed (late) by $\frac{\Delta\tau}{2}$. The individual delays of the two correlators are thus given by

$$\tau_{j,k}^{e} = \tau_{j,k}^{0} + \frac{\Delta\tau}{2} \quad , \tag{2.12}$$

$$\tau_{j,k}^{l} = \tau_{j,k}^{0} - \frac{\Delta\tau}{2} \quad . \tag{2.13}$$

Other types of TED functions are also used in practice [BvD99], e.g. the narrow correlator [vDFF92], where $\Delta\tau$ is much smaller than the chip duration, or the double-delta correlator [GvDR96], which uses an additional pair of correlators to form the TED. The DLL in a navigation receiver is a sequential implementation of a snapshot TED, since the estimates of the timing mismatch are low-pass filtered to reduce the noise

$$\hat{\tau}_{\epsilon,j,k}^{f} = \sum_{n=1}^{N_{lp}} a_n \hat{\tau}_{\epsilon,j,k-n}^{f} + \sum_{m=0}^{M_{lp}} b_m \hat{\tau}_{\epsilon,j,k-m} \quad , \tag{2.14}$$

and the filtered estimates are used to obtain the actual delay estimate,

$$\hat{\tau}_{j,k} = \hat{\tau}_{j,k-1} + \hat{\tau}_{\epsilon,j,k}^{f} \quad , \tag{2.15}$$

which is used in turn in the next cycle as new reference delay value by setting $\tau_{j,k}^{0} = \hat{\tau}_{j,k-1}$. The filter coefficients a_n, b_m of the low-pass filter depend on the specific DLL implementation [PS96]. Figure 2.2 illustrates the DLL concept. An inphase/prompt correlation

$$\mathbf{z}_{c,j,k}^{0} = \mathbf{s}^{H}(\tau_{j,k}^{0})\mathbf{z}_{j,k} \tag{2.16}$$

is commonly used to feed the frequency/phase estimation of the FLL/PLL.

2.1.2 The Problem of Multipath

A major error source for positioning in GNSS comes from multipath, the reception of additional signal replica due to reflections caused by the receiver environment, which is illustrated

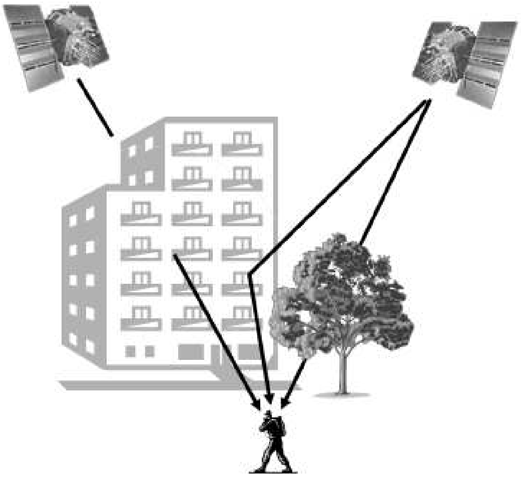

Figure 2.3: Illustration of multipath due to a reflection at a house front. The LOS path may be shadowed or even blocked simultaneously.

in Figure 2.3. The reception of multipath leads to a distortion of the TED of the DLL, which introduces a bias into the time delay estimate, which finally leads to a bias in the position estimate. In a multipath environment the line-of-sight (LOS) signal is superimposed by additional replica and the generalized multipath signal model becomes

$$z_j(t) \ = \ \sum_{i=0}^{N_m} a_{i,j}(t) s_j\left(t - \tau_{i,j}(t)\right) + n_j(t) \ , \tag{2.17}$$

where $\tau_{0,j}(t)$ and $a_{0,j}(t)$ corresponds to the delay and the complex amplitude of the LOS signal and $\tau_{i,j}(t)$ and $a_{i,j}(t)$ with $i = 1, \ldots, N_m$ to the respective time delays and complex amplitudes of the N_m considered multipath replica. Following the discrete time notation used in Section 2.1.1 the signal is sampled and grouped into blocks, with the parameter functions $\tau_{i,j}(t)$ and $a_{i,j}(t)$ that are assumed to be constant and equal to $\tau_{i,j,k}$ and $a_{i,j,k}$ during the corresponding time intervals. In the concise notation the signal vectors are stacked together as columns of the matrix $\mathbf{S}_j(\boldsymbol{\tau}_{j,k}) = [\mathbf{s}_j(\tau_{0,j,k}), \ldots, \mathbf{s}_j(\tau_{N_m,j,k})]$ and the amplitudes are collected in the vector $\mathbf{a}_{j,k} = [a_{1,j,k}, \ldots, a_{N_m,j,k}]^T$ such that the discrete-time multipath-affected signal may now be written in the compact form

$$\mathbf{z}_{j,k} \ = \ \mathbf{S}_j(\boldsymbol{\tau}_{j,k})\mathbf{a}_{j,k} + \mathbf{n}_{j,k} \ . \tag{2.18}$$

The multipath performance is commonly assessed using the multipath error function [PS96], which gives the estimation bias of the TED for a LOS signal superimposed by a single additional path as a function the relative delay of the replica. Parameters of the multipath error function are the signal-to-multipath ratio (SMR) $20\log_{10}\left(|a_{0,j,k}||a_{1,j,k}|^{-1}\right)$ and the relative phase $\delta\varphi = \arctan\left(a_{0,j,k}\right) - \arctan\left(a_{1,j,k}\right)$. The error envelope function relates to the inphase ($\delta\varphi_{j,k} = 0$) and antiphase ($\delta\varphi_{j,k} = \pi$) scenario, which represent the two worst-case situations that form the positive and negative upper error bound with respect to the estimation bias due to the variation of the relative phase. Details on the calculation of the bias functions can be found in [PS96]. The magnitude of the multipath bias varies with the relative phase and delay

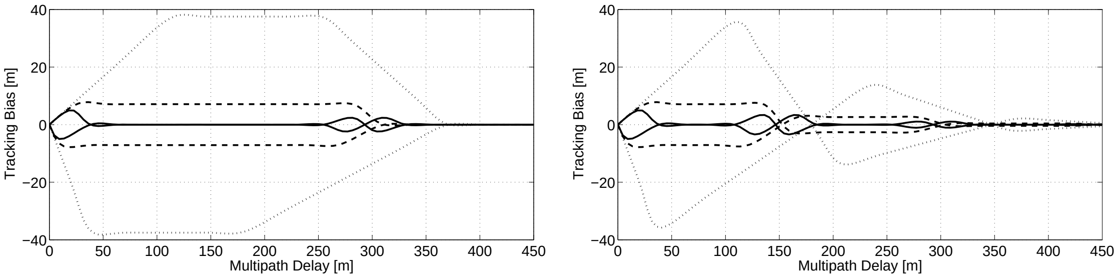

(a) BPSK (b) BOC(1,1)

Figure 2.4: Tracking bias envelopes for BPSK (2.4(a)) and BOC(1,1) (2.4(b)) modulation, early/late TED with $\Delta\tau = 0.5$ chips (outer dotted line), $\Delta\tau = 0.1$ chips (middle dashed line), and double-delta TED with $\Delta\tau = 0.1$ chips (inner solid line), SMR=6 dB, rectangular modulation pulses, 16 MHz two-sided precorrelation signal bandwidth, chip rate 1023 MHz, Gold code of length 1023. As evident the DLL suffers much less from the multipath when the BOC(1,1) modulation is used. Additionally the advantage of the more complex TED functions becomes obvious.

of the multipath replica, the TED used and the shape of the navigation signal. Various adaptations of the TED have been proposed to reduce the multipath errors, including the Narrow Correlator [vDFF92], the Strobe Correlator [GvDR96], the Gated Correlator [MB99], or the Pulse Aperture Correlator [JFS04]. The Narrow correlator is an efficient mitigation technique, which enhances the multipath robustness by a simple adjustment of the correlator spacing $\Delta\tau$ towards values smaller than the duration of a chip. The Double-Delta correlator concept, for instance implemented by the Strobe correlator, uses an additional pair of correlators to calculate the detector function. The additional early/late correlators are placed at

$$\begin{aligned} \tau_{j,k}^{2e} &= \tau_{j,k}^{0} + \Delta\tau \ , && (2.19) \\ \tau_{j,k}^{2l} &= \tau_{j,k}^{0} - \Delta\tau \ , && (2.20) \end{aligned}$$

and a combination of the inner and outer detector function

$$\begin{aligned} D_i(\tau_{0,j,k,l}) &= \left|\mathbf{s}^H(\tau_{j,k}^{e})\mathbf{z}_{j,k,l}\right|^2 - \left|\mathbf{s}^H(\tau_{j,k}^{l})\mathbf{z}_{j,k,l}\right|^2 \ , && (2.21) \\ D_o(\tau_{0,j,k,l}) &= \left|\mathbf{s}^H(\tau_{j,k}^{2e})\mathbf{z}_{j,k,l}\right|^2 - \left|\mathbf{s}^H(\tau_{j,k}^{2l})\mathbf{z}_{j,k,l}\right|^2 && (2.22) \end{aligned}$$

yields the TED for the Double-Delta correlator

$$D(\tau_{0,j,k,l}) = D_i(\tau_{0,j,k,l}) - 0.5 D_o(\tau_{0,j,k,l}) \ . \qquad (2.23)$$

To enhance the receiver robustness against multipath in future satellite navigation systems, multipath performance has become an important criteria in the design of future navigation signals [ARHW$^+$07]. An illustration of multipath error envelopes is shown in Figure 2.4 for a conventional binary phase shift keying (BPSK) signal, which is currently transmitted by the GPS system, and a binary offset carrier (BOC) (1,1) signal, which represents the concept of offset carrier signals that is pursued for future satellite navigation signals.

2.2 Inertial Navigation

Inertial navigation is based on the sensing of acceleration and rotational speed. Using the mathematical formulation of Newton's law of motion, which expresses the physical dependencies between mass, force, acceleration, velocity, position, attitude, and rotational speed, it is possible to derive position, velocity and attitude from the measured acceleration and rotational speed, given initial values of position, velocity, and attitude are available. The procedure of obtaining these initial values is termed alignment [TW04]. After the alignment has been performed, an inertial navigation system (INS) provides fully self-contained autonomous navigation capabilities. Characteristic for inertial navigation is the degradation of the navigation accuracy over time, often referred to as the drift, which arises amongst other effects mainly due to instrument errors, i.e. the noise and imperfections of the inertial sensors. An INS comprises basically two components: A sensor cluster, which is commonly termed inertial measurement unit (IMU), and an inertial navigation computer (INC), which performs the necessary computations to derive position, velocity and attitude from the sensor data.

2.2.1 Inertial Sensors and Platforms

The sensor cluster of a conventional IMU comprises three accelerometers and three gyroscopes, which are mounted onto a common platform such that their sensitive axes are mutually orthogonal. Though the basic concept has remained the same since the initial days of inertial navigation, technological advances and innovation had a big impact on the evolution of inertial navigation during the last 50 years [Kin98]. Whereas formerly the sensor platform was mounted within a set of gimbals, which kept the cluster aligned to the navigation frame and thus independent from the vehicle attitude, today strapdown sensor clusters have become the preferred type of IMUs (see Figure 2.5). In a strapdown IMU the sensor cluster is attached directly to the host vehicle and the resolution of the accelerometers measurements to the navigation frame is done in a computer. The advantage of the strapdown approach is that no complex mechanical gimbals are required. Strapdown systems became feasible during the 1970s due to the advances in gyroscopes technology, which allowed to sense a larger dynamic range of rotational speed and the advances in micro-electronics, which enabled digital computers that were capable of performing the computationally demanding strapdown attitude computations.

2.2.2 Inertial Navigation Computations

Though the concept of inertial navigation is rather simple, the implementation of the navigation algorithm can indeed be complex [TW04]. This is mainly due to fact that inertial sensors sense their measures with respect to the pure inertial space, whereas the coordinate system in which the navigation takes place is usually attached to the spheric rotating earth. Additionally accelerometers are not able to differentiate between gravitational and dynamic acceleration. Since this thesis focuses on the navigation of individuals using low-cost MEMS inertial sensors, Schuler and Coriolis effects will be neglected. A flat non-rotating earth is assumed, which is adequate when considering a moving pedestrian within a limited local area. In this case the navigation coordinate frame equals the inertial coordinate frame. As it is commonly known the

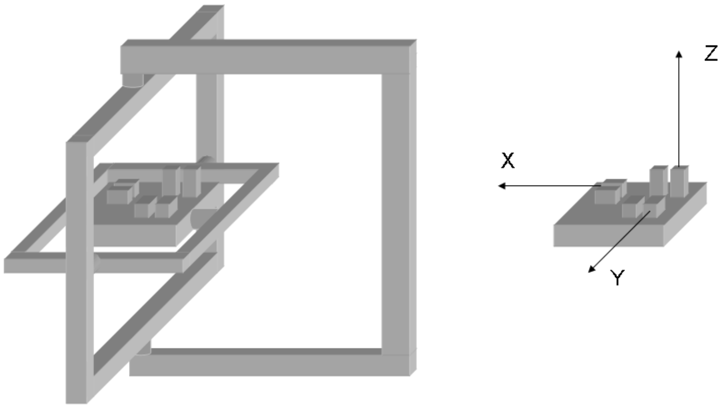

Figure 2.5: Principle of a gimbaled platform (left) and a strapdown platform (right). In the gimbaled variant the gimbals keep the platform leveled and aligned with respect to the navigation coordinate frame. The strapdown platform is attached rigidly to the host vehicle.

acceleration is the second temporal derivative of the position

$$\mathbf{a}^i = \frac{d^2}{dt^2}\mathbf{r}^i \ , \tag{2.24}$$

The superscript i indicates thereby that the vectors are given in the representation of the inertial frame. The triad of acceleration sensors of the IMU provides a measure of the specific force

$$\mathbf{f}^i = \frac{d^2}{dt^2}\mathbf{r}^i - \mathbf{g}^i \ , \tag{2.25}$$

in which $\mathbf{g}^i$ is the gravitation vector due to the gravitational acceleration of the earth. As the inertial platform is not necessarily aligned to the inertial coordinate frame, the forces $\mathbf{f}^i$ are actually measured in the sensor platform or so-called body frame via the force vector $\mathbf{f}^b$. To resolve the body frame measurements to the inertial frame, a transformation according to

$$\mathbf{f}^i = \mathbf{C}_b^i\mathbf{f}^b \tag{2.26}$$

is required, in which $\mathbf{C}_b^i$ is the rotation matrix that relates the attitude of the body frame with respect to the inertial frame [TW04]. Figure 2.6 illustrates such a transformation for two coordinate systems. Inserting (2.26) into (2.25) and rearranging leads to the differential equations

$$\frac{d^2}{dt^2}\mathbf{r}^i \quad = \quad \mathbf{C}_b^i\mathbf{f}^b + \mathbf{g}^i \ , \tag{2.27}$$

$$\frac{d}{dt}\mathbf{v}^i \quad = \quad \mathbf{C}_b^i\mathbf{f}^b + \mathbf{g}^i \ . \tag{2.28}$$

The solution of (2.27) and (2.28) allows to calculate position and velocity. Usually this solution is performed numerically in a dedicated navigation computer. For that purpose the exact value of the gravitational acceleration $\mathbf{g}^i$ needs to be known. Since usually the exact value is not known, an average value is often used. For some special high precision applications also gravitational maps are employed. Furthermore the navigation computer has to continuously

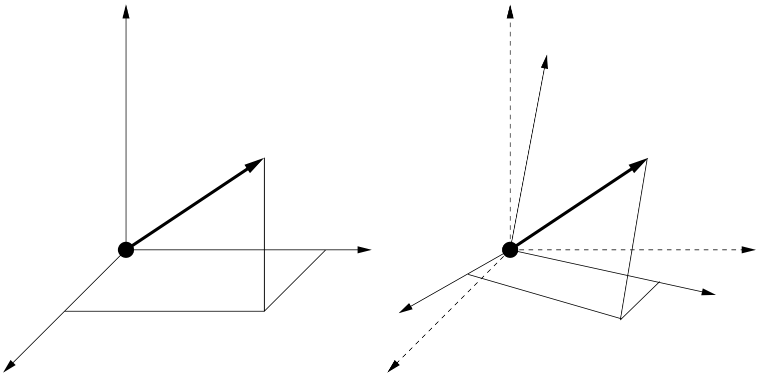

Figure 2.6: Tilt of two coordinate systems. The transformation of a vector from one into another coordinate system is performed through a multiplication of the vector with a rotation matrix.

update the attitude matrix based on the turn rate measurements $\boldsymbol{\omega}_{ib}^{b}$, which are obtained by the gyroscope triad. According to [TW04] thus an attitude computer has to implement a solution for the differential equation

$$\frac{d}{dt}\mathbf{C}_b^i = \mathbf{C}_b^i \boldsymbol{\Omega}_{ib}^b \ \ , \tag{2.29}$$

in which $\boldsymbol{\Omega}_{ib}^b$ is a skew symmetric form

$$\boldsymbol{\Omega}_{ib}^b = \begin{pmatrix} 0 & -\omega_z & \omega_y \\ \omega_z & 0 & -\omega_x \\ -\omega_y & \omega_x & 0 \end{pmatrix} \tag{2.30}$$

of the turn rate vector $\boldsymbol{\omega}_{ib}^b = [\omega_x, \omega_y, \omega_z]^T$, or in alternative notation $\boldsymbol{\Omega}_{ib}^b = [\boldsymbol{\omega}_{ib}^b \times]$. The concept of a complete strapdown navigation and attitude computation algorithm is illustrated in Figure 2.7.

Implementation Example

Various numerical integration schemes are appropriate to solve (2.27), (2.28), and (2.29). The most simple implementation is the approximation of the integrals by a sum of rectangles. Given that the discrete time equivalents $\mathbf{r}_k^i$, $\mathbf{v}_k^i$, $\mathbf{f}_k^b$, $\boldsymbol{\omega}_{ib,k}^b$, $\mathbf{C}_{b,k}^i$, and $\mathbf{g}_k^i$ are constant during the observation interval T_s, position and velocity can be computed via

$$\mathbf{r}_k^i = \mathbf{r}_{k-1}^i + \mathbf{v}_{k-1}^i T_s \ \ , \tag{2.31}$$

$$\mathbf{v}_k^i = \mathbf{v}_{k-1}^i + \mathbf{a}_{k-1}^i T_s \ \ , \tag{2.32}$$

with $\mathbf{a}_{k-1}^i = \mathbf{C}_{b,k-1}^i \mathbf{f}_{k-1}^b + \mathbf{g}_{k-1}^i$. Following [TW04] the attitude matrix is computed in accordance via

$$\mathbf{C}_{b,k}^i = \mathbf{C}_{b,k-1}^i (\mathbf{I} + [\boldsymbol{\omega}_{ib,k-1}^b \times] T_s) \ \ . \tag{2.33}$$

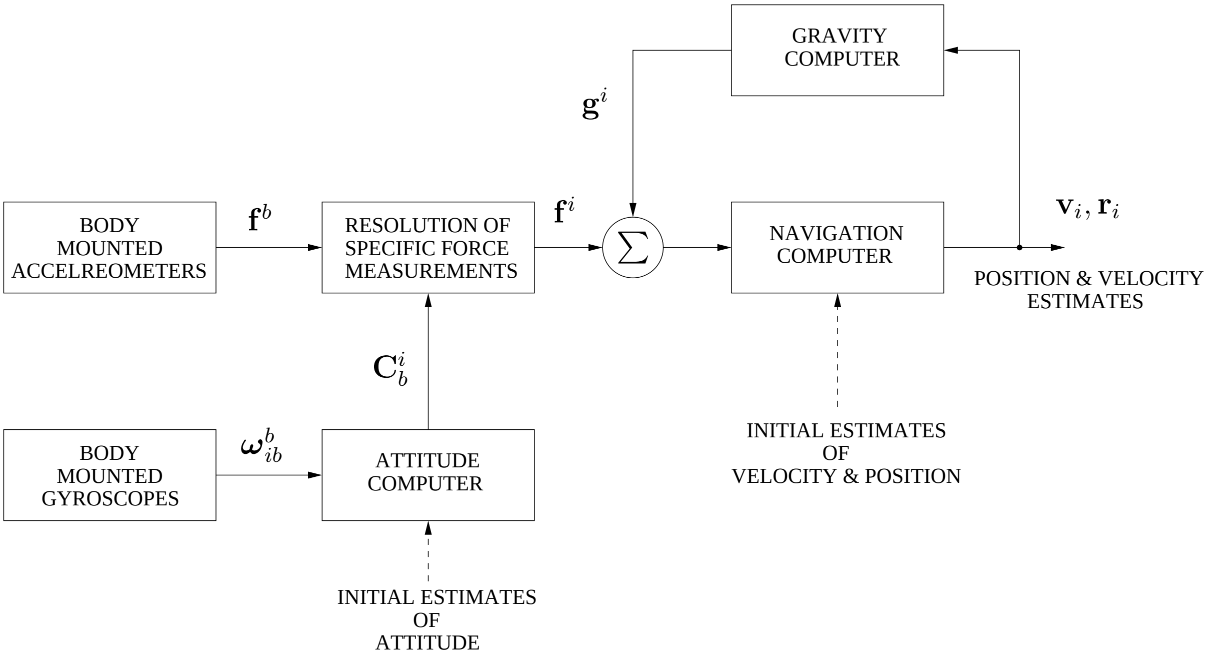
GRAVITY COMPUTER
$\mathbf{g}^i$
BODY MOUNTED ACCELREOMETERS
$\mathbf{f}^b$
RESOLUTION OF SPECIFIC FORCE MEASUREMENTS
$\mathbf{f}^i$
$\sum$
NAVIGATION COMPUTER
$\mathbf{v}_i, \mathbf{r}_i$
POSITION & VELOCITY ESTIMATES
$\mathbf{C}_b^i$
BODY MOUNTED GYROSCOPES
$\boldsymbol{\omega}_{ib}^b$
ATTITUDE COMPUTER
INITIAL ESTIMATES OF VELOCITY & POSITION
INITIAL ESTIMATES OF ATTITUDE

Figure 2.7: Illustration of the strapdown navigation computer in inertial frame mechanization. For each set of arriving gyroscope measurements the attitude computer is updated. The latest attitude matrix is used to resolve the measured accelerations from the vehicle's body frame to the inertial navigation frame. After subtraction of the earth acceleration position and velocity are computed by numerical integration.

2.3 Optimal Estimation

Common to all navigation, positioning, and localization systems is the principle of deriving navigational information from the observation of physical effects which are somehow related to this information. To observe the effects physical sensors are needed, whose output corresponds in a characteristics manner to the physical effect and the navigational information that is of interest finally. E.g. a compass senses the magnetic field of the earth, which allows to derive its orientation, or an antenna receives a signal whose travel time is of interest. Due to imperfections the output of a sensor is not only depending on the quantity of interest, but also on other disturbing quantities and effects. To infer the quantity of interest accurately on principle all other relevant disturbing factors have to be known. Since this is not the case in practice, the output of a sensor is always disturbed by a noise quantity, which cumulates the unknown contributions in the sensor output. Practically this error can be characterized by a random process, which is characteristic for each sensor. So even if the exact realization of the disturbance is unknown, the quantity of interest can be inferred with a specific uncertainty, which can be quantified by the characteristics of the random process. Necessarily the task of any navigation system is thus to derive information about specific navigational quantities, which here will be referred to as the hidden state $\mathbf{x}_k$, based on an evolving sequence of noisy measurements $\mathbf{z}_k$ (over the temporal index k). Since the measurements depend on the hidden state $\mathbf{x}_k$ and on a random process $\mathbf{n}_k^{\mathrm{m}}$ that cumulates all unknown impacting factors, the measurements can be expressed generally via the function

$$\mathbf{z}_k = \mathbf{h}_k(\mathbf{x}_k, \mathbf{n}_k^{\mathrm{m}}) \ . \tag{2.34}$$

Given the process underlying $\mathbf{n}_k^{\mathrm{m}}$ is specified, an alternative probabilistic representation of (2.34) is the *likelihood function* $p(\mathbf{z}_k|\mathbf{x}_k)$, the probability density function that characterizes the likelihood of the observed measurement conditional on the unknown state. The optimal inferred knowledge about the state is then the *a posteriori probability density function* $p(\mathbf{x}_k|\mathbf{z}_k)$, which is obtained by applying the Bayes rule:

$$p(\mathbf{x}_k|\mathbf{z}_k) = \frac{p(\mathbf{z}_k|\mathbf{x}_k)p(\mathbf{x}_k)}{p(\mathbf{z}_k)} \ . \tag{2.35}$$

The function $p(\mathbf{x}_k)$ thereby represents the *a priori probability density function*, which includes all the knowledge about the state, that was available before the measurement was observed. The *evidence* term $p(\mathbf{z}_k)$ is a constant for a given observation and normalizes the product of the likelihood function and the a priori PDF in the numerator of (2.35). This way of inference is optimal and no other estimator can outperform this approach, in particular since all the remaining uncertainty is kept in the a posteriori PDF. The preservation of this information is a key paradigm to reach optimal performance and has been very successful in the field communications engineering [Hag94]. Specifically the paradigm can be adapted to navigation and localization problems under the term *Soft-Location* (SoLo) [AKR$^+$01]. Nevertheless, as will be shown later, Soft-Location has a far reaching history in the design of multi-sensor navigation systems.

Since the measurement noise is limiting the inferable knowledge through the likelihood function, the only remaining way to improve in (2.35) is to use more sensors, more observations, or to use a refined a priori knowledge. The benefit of additional sensors and additional measurements from the same sensors is implicitly given by the Soft-Location paradigm. For that purpose the vector of measurements is grouped into sub-vectors according to

$$\mathbf{z}_k \widehat{=} \{\mathbf{z}_{j,k}, j = 1, \ldots, M\} \ , \tag{2.36}$$

and the vectors $\mathbf{z}^-_{j,k}$ are introduced for $\mathbf{z}_k$ after omitting $\mathbf{z}_{j,k}$, i.e. $\mathbf{z}^-_{j,k} = \mathbf{z}_k \backslash \mathbf{z}_{j,k}$. If now independent noise perturbations on the sub-vectors are assumed, i.e. that the actual error affecting the observation $\mathbf{z}_{j,k}$ is statistically independent from the errors that affect all other current observation (and generally also from all disturbances, which have affected any previous observations), the likelihood function for sensor j may be written as

$$p(\mathbf{z}_{j,k}|\mathbf{x}_k, \mathbf{z}^-_{j,k}) = p(\mathbf{z}_{j,k}|\mathbf{x}_k) \ , \tag{2.37}$$

so that given the actual state, the measurements $\mathbf{z}^-_{j,k}$ will not affect the measurement $\mathbf{z}_{j,k}$. In this case the overall likelihood function can be written in product form according to the factorization of Bayes' rule [AKR$^+$01] as

$$p(\mathbf{z}_k|\mathbf{x}_k) = C \prod_{j=1}^{M} p(\mathbf{z}_{j,k}|\mathbf{x}_k) \ , \tag{2.38}$$

with C being a normalizing constant. In other words, the sensors can be incorporated by simple multiplication of their likelihood functions. A proof of this fundamental equation can be found in Appendix A. Since the information that is comprised in each factor of the overall likelihood function is always positive [Kay93], each additional sensor or or observation contributes necessarily beneficial, at least theoretically. In practice the measurement model is often slightly mismatched to the real world situation, which deteriorates the theoretically expected performance, as the assumptions taken in the derivation of (2.38) are violated. Furthermore the amount of available sensors is usually limited due to the system design: The performance advance with additional sensors does not always justify the increase in power consumption, system cost and size. On the other hand the number of observation per sensor can not increased arbitrarily, since the underlying state that biases the measurement is changing over time, e.g. a pedestrian is moving and in consequence the measurements alter. Thus a set of taken measurements is only sufficient to infer the state during a specific period of time. At this point the refinement of the a priori knowledge comes into play. Though an observation is only valid for a limited time two successive observations are certainly somehow related to each other, since the dynamics of a moving individual or generally any state evolution are practically limited due to physical constraints. Although the exact evolution is generally unknown, at least a statistical characterization of the temporal dependencies can help to obtain a refined a priori knowledge from any past observations. In particular if the future state given the current state and all its past states depends only on the previous state (and not on any past states), the temporal evolution of state parameters can be modeled as a first-order *Markov process* as illustrated in Figure 2.8. The process is characterized by the function

$$\mathbf{x}_k = \mathbf{f}_{k-1}(\mathbf{x}_{k-1}, \mathbf{n}^{\mathrm{d}}_{k-1}) \ , \tag{2.39}$$

with the uncertainty in the evolution being characterized by the process noise $\mathbf{n}^{\mathrm{d}}_{k-1}$. As a consequence equation (2.39) can for a specified process underlying $\mathbf{n}^{\mathrm{d}}_{k-1}$ also be expressed probabilistically in terms of the *transition density* $p(\mathbf{x}_k|\mathbf{x}_{k-1})$. If it is furthermore assumed that the

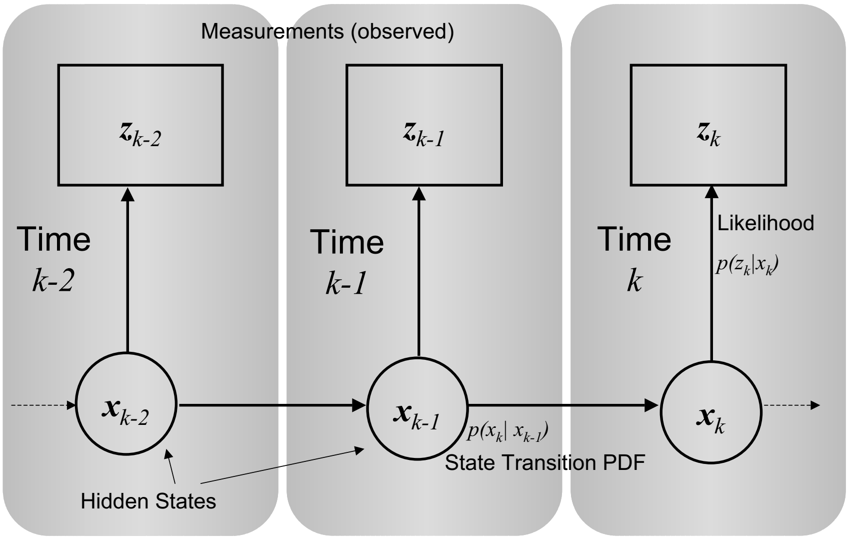

Figure 2.8: Illustration of the hidden Markov estimation process for three time instances. The measurements are the sequence $\mathbf{z}_q, q = 0, \ldots, k\}$, and the parameters to be estimated are $\mathbf{x}_q, q = 0, \ldots, k\}$

noise affecting successive measurements is independent of the past noise values, such that each observation depends only on the present state, the optimal solution is given by the application of the well-known framework of *sequential Bayesian estimation*. A detailed derivation of the general framework for optimal estimation of temporally evolving (Markovian) parameters by means of inference is given in [AMGC02]; and here a similar notation is chosen. The entire history of observations can be written as

$$\mathbf{Z}_k \widehat{=} \{\mathbf{z}_q, q = 1, \ldots, k\} \ . \tag{2.40}$$

It can be shown that the sequential estimation algorithm is recursive as illustrated in Figure 2.9, as it uses the a posteriori PDF computed for time instance $k-1$ to compute the a posteriori PDF for instance k . For a given a posteriori PDF at time instance $k-1$, $p(\mathbf{x}_{k-1}|\mathbf{Z}_{k-1})$, the a priori PDF $p(\mathbf{x}_k|\mathbf{Z}_{k-1})$ is calculated in the so-called *prediction step* by applying the Chapman-Kolmogorov equation:

$$p(\mathbf{x}_k|\mathbf{Z}_{k-1}) = \int p(\mathbf{x}_k|\mathbf{x}_{k-1}) p(\mathbf{x}_{k-1}|\mathbf{Z}_{k-1}) \mathrm{d}\mathbf{x}_{k-1} \ , \tag{2.41}$$

with $p(\mathbf{x}_k|\mathbf{x}_{k-1})$ being the state transition PDF of the Markov process according to (2.39). In the *update step* the new a posteriori PDF for step k is obtained by applying Bayes' rule to $p(\mathbf{x}_k|\mathbf{z}_k, \mathbf{Z}_{k-1})$ yielding the normalized product of the likelihood function $p(\mathbf{z}_k|\mathbf{x}_k)$ and the a priori PDF:

$$\begin{aligned} p(\mathbf{x}_k|\mathbf{Z}_k) &= p(\mathbf{x}_k|\mathbf{z}_k, \mathbf{Z}_{k-1}) \\ &= \frac{p(\mathbf{z}_k|\mathbf{x}_k, \mathbf{Z}_{k-1}) p(\mathbf{x}_k|\mathbf{Z}_{k-1})}{p(\mathbf{z}_k|\mathbf{Z}_{k-1})} \\ &= \frac{p(\mathbf{z}_k|\mathbf{x}_k) p(\mathbf{x}_k|\mathbf{Z}_{k-1})}{p(\mathbf{z}_k|\mathbf{Z}_{k-1})} \ , \end{aligned} \tag{2.42}$$

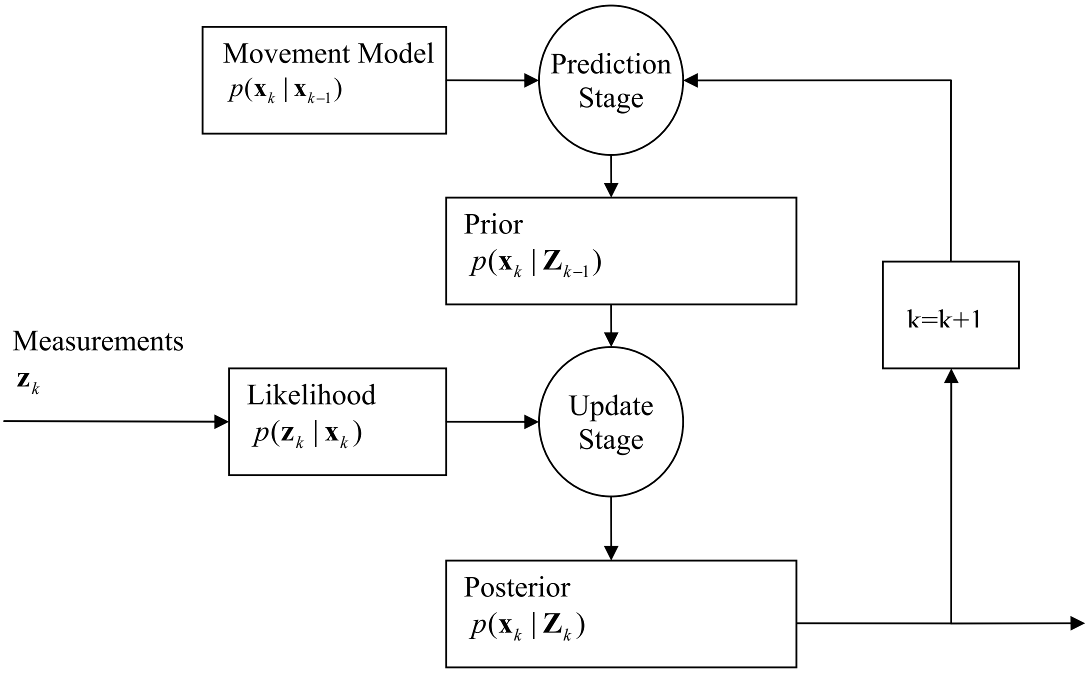
Movement Model
$p(\mathbf{x}_k \mid \mathbf{x}_{k-1})$
Prediction Stage
Prior
$p(\mathbf{x}_k \mid \mathbf{Z}_{k-1})$
k=k+1
Measurements
$\mathbf{z}_k$
Likelihood
$p(\mathbf{z}_k \mid \mathbf{x}_k)$
Update Stage
Posterior
$p(\mathbf{x}_k \mid \mathbf{Z}_k)$

Figure 2.9: Illustration of the recursive Bayesian estimator. The operations prediction and update can be carried recursively, since the computation of the a posteriori PDF $p(\mathbf{x}_k|\mathbf{Z}_k)$ requires beside the likelihood function $p(\mathbf{z}_k|\mathbf{x}_k)$ as well the a priori PDF $p(\mathbf{x}_k|\mathbf{Z}_{k-1})$, which can be computed from the previous a posteriori PDF $p(\mathbf{x}_{k-1}|\mathbf{Z}_{k-1})$.

which is actually a more general formulation of (2.35). Once the a posteriori PDF has been evaluated either that parameter configuration that maximizes it can be determined - the so called maximum a posteriori (MAP) estimate; or expectation can be chosen - equivalent to the minimum mean square error (MMSE) estimate:

$$\hat{\mathbf{x}}_k^{\mathrm{MAP}} = \arg\max_{\mathbf{x}_k} p(\mathbf{x}_k|\mathbf{Z}_k) \ , \tag{2.43}$$

$$\hat{\mathbf{x}}_k^{\mathrm{MMSE}} = \int\limits_{\mathbf{x}_k} \mathbf{x}_k p(\mathbf{x}_k|\mathbf{Z}_k) \mathrm{d}\mathbf{x}_k \ . \tag{2.44}$$

For the scope of this thesis, unless stated otherwise, always the MMSE estimate will be used. Note that for the important case of a Gaussian a posteriori PDF both criteria are equivalent. In addition, the a posteriori PDF itself contains all uncertainty information about the current state and is thus the optimal reliability measure.

2.3.1 Algorithm Implementation

The optimal Bayesian filtering algorithm relies on evaluating the integral (2.41), which is usually a very difficult task, except for the measurement model (2.34) and the dynamic model (2.39) have certain restrictive properties. Beside few restricted optimal algorithms a large number of suboptimal approximations to the optimal Bayesian framework exist. In the following those filter implementations that are relevant for the scope of this thesis are discussed: The optimal grid-based filter (GBF), the conventional and the extended variant of the Kalman filter (KF/EKF), the particle filter (PF), and a general marginalized filter (MF), which may consist of any nested combination of Bayesian filters.

Grid-Based Filter

If the state space is discrete and finite the Bayesian recursion can be carried out analytically. The associated computations are referred to as the grid-based filter algorithm [RAG04]. In a discrete and finite state space of dimension N the a posteriori PDF at time $k-1$ can be represented as the sum

$$p(\mathbf{x}_{k-1}|\mathbf{Z}_{k-1}) = \sum_{\mu=1}^{N} w_{k-1}^{\mu} \delta(\mathbf{x}_{k-1} - \mathbf{x}_{k-1}^{\mu}) \ . \tag{2.45}$$

Using (2.41) the GBF algorithm computes the a priori PDF with

$$p(\mathbf{x}_{k}|\mathbf{Z}_{k-1}) = \sum_{\mu=1}^{N} w_{k}^{\mu-} \delta(\mathbf{x}_{k} - \mathbf{x}_{k}^{\mu}) \ , \tag{2.46}$$

in which the predicted weights are computed via

$$w_{k}^{\mu-} = \sum_{\nu=1}^{N} w_{k-1}^{\nu} p(\mathbf{x}_{k}^{\mu}|\mathbf{x}_{k-1}^{\nu}) \ . \tag{2.47}$$

In this case the transition PDF $p(\mathbf{x}_k|\mathbf{x}_{k-1})$ may be any regular PDF. The likelihood function $p(\mathbf{z}_k|\mathbf{x}_k)$ can be any regular PDF as well and the use of (2.42) gives

$$p(\mathbf{x}_{k}|\mathbf{Z}_{k}) = \sum_{\mu=1}^{N} w_{k}^{\mu} \delta(\mathbf{x}_{k} - \mathbf{x}_{k}^{\mu}) \ , \tag{2.48}$$

and the updated weight becomes

$$w_{k}^{\mu} = \frac{w_{k}^{\mu-} p(\mathbf{z}_k|\mathbf{x}_{k}^{\mu})}{\sum_{\nu=1}^{N} w_{k}^{\nu-} p(\mathbf{z}_k|\mathbf{x}_{k}^{\nu})} \ . \tag{2.49}$$

Kalman Filter

The Kalman filter [Kal60] is an optimal implementation of the Bayesian recursion for the important case of linear state dynamics and linear measurement equations, in which the dynamic and measurement noise processes are given by additive Gaussian noise respectively. The process dynamics (2.39) are restricted to the class of problems that can be expressed in the form of $\mathbf{x}_k = \mathbf{F}_{k-1}\mathbf{x}_{k-1} + \mathbf{n}_{k-1}^{\mathrm{d}}$, in which the realization of the random process follows $\mathbf{n}_{k-1}^{\mathrm{d}} \sim \mathcal{N}(\mathbf{0}, \mathbf{Q}_{k-1})$. The measurement relation (2.34) is required to be representable via the function $\mathbf{z}_k = \mathbf{H}_k\mathbf{x}_k + \mathbf{n}_k^{\mathrm{m}}$, with the measurement noise according to $\mathbf{n}_k^{\mathrm{m}} \sim \mathcal{N}(\mathbf{0}, \mathbf{R}_k)$. Additionally the a posteriori PDF is restricted to be a Gaussian density, and thus

$$p(\mathbf{x}_{k-1}|\mathbf{Z}_{k-1}) = \mathcal{N}(\hat{\mathbf{x}}_{k-1}, \mathbf{P}_{k-1}) \ , \tag{2.50}$$

Due to the imposed restrictions the transition PDF can be expressed as

$$p(\mathbf{x}_k|\mathbf{x}_{k-1}) = \mathcal{N}(\mathbf{F}_{k-1}\mathbf{x}_{k-1}, \mathbf{Q}_{k-1}) \ . \tag{2.51}$$

The term $\mathbf{F}_{k-1}$ denotes the transition matrix, which characterizes the deterministic dynamics of the state $\mathbf{x}$. Since (2.50) and (2.51) are both Gaussian, inserting in (2.41) leads to an integral, which can be tracted analytically and it can be shown that the resulting a priori PDF is a Gaussian as well:

$$p(\mathbf{x}_k|\mathbf{Z}_{k-1}) = \mathcal{N}(\hat{\mathbf{x}}_k^-, \mathbf{P}_k^-) \ , \tag{2.52}$$

with mean $\hat{\mathbf{x}}_k^-$ and covariance $\mathbf{P}_k^-$ according to

$$\begin{aligned} \hat{\mathbf{x}}_k^- &= \mathbf{F}_{k-1}\hat{\mathbf{x}}_{k-1} \ , && (2.53) \\ \mathbf{P}_k^- &= \mathbf{F}_{k-1}\mathbf{P}_{k-1}\mathbf{F}_{k-1}^T + \mathbf{Q}_{k-1} \ . && (2.54) \end{aligned}$$

As mentioned above the measurement model is linear and the likelihood function can be expressed due to the Gaussian measurement noise in terms of

$$p(\mathbf{z}_k|\mathbf{x}_k) = \mathcal{N}(\mathbf{H}_k\mathbf{x}_k, \mathbf{R}_k) \ , \tag{2.55}$$

where $\mathbf{H}_k$ is the so-called measurement matrix. Since (2.52) and (2.55) are both Gaussian, it can be shown that inserting in (2.42) leads to an expression, which can be solved analytically and that the resulting a posteriori PDF is again Gaussian:

$$p(\mathbf{x}_k|\mathbf{Z}_k) = \mathcal{N}(\hat{\mathbf{x}}_k, \mathbf{P}_k) \ , \tag{2.56}$$

in which mean $\hat{\mathbf{x}}_k$ and covariance $\mathbf{P}_k$ are given by

$$\begin{aligned} \hat{\mathbf{x}}_k &= \hat{\mathbf{x}}_k^- + \mathbf{K}_k(\mathbf{z}_k - \mathbf{H}_k\hat{\mathbf{x}}_k^-) \ , && (2.57) \\ \mathbf{P}_k &= (\mathbf{I} - \mathbf{K}_k\mathbf{H}_k)\mathbf{P}_k^- \ , && (2.58) \end{aligned}$$

where the so-called Kalman gain $\mathbf{K}_k$ computes with

$$\mathbf{K}_k = \mathbf{P}_k^-\mathbf{H}_k^T(\mathbf{H}_k\mathbf{P}_k^-\mathbf{H}_k^T + \mathbf{R}_k)^{-1} \ . \tag{2.59}$$

Extended Kalman Filter

A suboptimal implementation for more general non-linear problems is the extended Kalman filter [May79]. For the EKF (2.39) can be of the form

$$\mathbf{x}_k = \mathbf{f}_{k-1}(\mathbf{x}_{k-1}) + \mathbf{n}_{k-1}^{\mathrm{d}} \ , \tag{2.60}$$

and (2.34) of the form

$$\mathbf{z}_k = \mathbf{h}_k(\mathbf{x}_k) + \mathbf{n}_k^{\mathrm{m}} \ . \tag{2.61}$$

The random processes follow thereby the Gaussian restriction of the KF, such that the transition PDF is for the EKF

$$p(\mathbf{x}_k|\mathbf{x}_{k-1}) = \mathcal{N}(\mathbf{f}_{k-1}(\mathbf{x}_{k-1}), \mathbf{Q}_{k-1}) \ . \tag{2.62}$$

The a priori PDF is a Gaussian approximation of the true a priori PDF

$$p(\mathbf{x}_k|\mathbf{Z}_{k-1}) \approx \mathcal{N}(\hat{\mathbf{x}}_k^-, \mathbf{P}_k^-) \ , \tag{2.63}$$

with mean

$$\hat{\mathbf{x}}_k^- = \mathbf{f}_{k-1}(\hat{\mathbf{x}}_{k-1}) \tag{2.64}$$

and the Jacobian approximation of the transition matrix

$$\mathbf{F}_{k-1} = \left.\frac{\partial \mathbf{f}_{k-1}(\mathbf{x}_{k-1})}{\partial \mathbf{x}_{k-1}}\right|_{\hat{\mathbf{x}}_{k-1}} \ , \tag{2.65}$$

which is used according to the generic KF equation (2.54) for the calculation of the predicted covariance $\mathbf{P}_k^-$. Due to the non-linear measurement equation the likelihood function becomes

$$p(\mathbf{z}_k|\mathbf{x}_k) = \mathcal{N}(\mathbf{h}_k(\mathbf{x}_k), \mathbf{R}_k) \ , \tag{2.66}$$

and the a posteriori PDF is approximated through the Gaussian PDF

$$p(\mathbf{x}_k|\mathbf{Z}_k) \approx \mathcal{N}(\hat{\mathbf{x}}_k, \mathbf{P}_k) \ , \tag{2.67}$$

with mean

$$\hat{\mathbf{x}}_k = \hat{\mathbf{x}}_k^- + \mathbf{K}_k(\mathbf{z}_k - \mathbf{h}_k(\hat{\mathbf{x}}_k^-)) \ . \tag{2.68}$$

The calculation of the a posteriori covariance and the Kalman gain follow thereby the generic KF equations (2.58) and (2.59) respectively, in which the Jacobian approximation

$$\mathbf{H}_k = \left.\frac{\partial \mathbf{h}_k(\mathbf{x}_k)}{\partial \mathbf{x}_k}\right|_{\hat{\mathbf{x}}_k^-} \tag{2.69}$$

is used for the measurement matrix. An alternative equivalent formulation of the EKF is the small-signal space filter, which computes the large-signal trajectory $\mathbf{X}_k^r \widehat{=} \{\mathbf{x}_q^r, q = 0, \ldots, k\}$ independently from the small-signal perturbations $\delta\mathbf{x}_k$. The transition PDF in the small-signal space EKF is with using $\mathbf{x}_k = \mathbf{x}_k^r + \delta\mathbf{x}_k$

$$p(\mathbf{x}_k|\mathbf{x}_{k-1}) \approx \mathcal{N}(\mathbf{f}_{k-1}(\mathbf{x}_{k-1}^r) + \mathbf{F}_{k-1}\delta\mathbf{x}_{k-1}, \mathbf{Q}_{k-1}) \ . \tag{2.70}$$

The a priori PDF follows from (2.63) with mean $\hat{\mathbf{x}}_k^- = \mathbf{x}_k^r + \delta\hat{\mathbf{x}}_k^-$, in which $\mathbf{x}_k^r = \mathbf{f}_{k-1}(\mathbf{x}_{k-1}^r)$ and $\delta\hat{\mathbf{x}}_k^- = \mathbf{F}_{k-1}\delta\hat{\mathbf{x}}_{k-1}$. The likelihood function in this formulation is approximated by

$$p(\mathbf{z}_k|\mathbf{x}_k) \approx \mathcal{N}(\mathbf{h}_k(\mathbf{x}_k^r) + \mathbf{H}_k\delta\mathbf{x}_k, \mathbf{R}_k) \ , \tag{2.71}$$

and thus after the update the a posteriori PDF follows from (2.67) with mean $\hat{\mathbf{x}}_k = \mathbf{x}_k^r + \delta\hat{\mathbf{x}}_k = \mathbf{x}_k^r + \delta\hat{\mathbf{x}}_k^- + \mathbf{K}_k(\mathbf{z}_k^\delta - \mathbf{H}_k\delta\hat{\mathbf{x}}_k^-)$, with the small-signal space measurement $\mathbf{z}_k^\delta = \mathbf{z}_k - \mathbf{h}_k(\mathbf{x}_k^r)$. It can be derived from (2.70) and (2.71) that this formulation allows to decouple the computation of $\mathbf{x}_k^r$ and $\delta\hat{\mathbf{x}}_k$ (except for the computation of $\mathbf{F}_k$ and $\mathbf{H}_k$). A correction of the large-signal trajectory may be performed each filter cycle by adding the estimated small-signal deviations via $\mathbf{x}_k^{r,\mathrm{cal}} = \mathbf{x}_k^r + \delta\hat{\mathbf{x}}_k$. The calibration is considered in the filter by using the new small signal mean $\delta\hat{\mathbf{x}}_k^{\mathrm{cal}} = \mathbf{0}$. After correction the previous state equals the calibrated previous state, namely $\mathbf{x}_{k-1}^r = \mathbf{x}_{k-1}^{r,\mathrm{cal}}$, and the filter prediction uses $\delta\hat{\mathbf{x}}_{k-1} = \delta\hat{\mathbf{x}}_{k-1}^{\mathrm{cal}}$. If a correction is applied after each filter update, the small-signal formulation of the EKF is fully equivalent to the direct EKF formulation. In some implementations the sign of the small-signal space is inverted. The implementation with the inverted sign is referred to as the error space implementation of the EKF, since the filter tracks the errors of the large-signal trajectory, which are subtracted to give the total mean. Due to the inverted sign the effective error space measurement is $\mathbf{z}_k^\epsilon = -\mathbf{z}_k^\delta = \mathbf{h}_k(\mathbf{x}_k^r) - \mathbf{z}_k$. The error space implementation can be found often in the integration of satellite and inertial navigation systems [Nat04], since the decoupled computation of $\mathbf{x}_k^r$ and $\delta\mathbf{x}_k$ allows to perform the filter computations at lower rate than those of the reference trajectory. E.g. in an integrated satellite and inertial navigation system the reference trajectory is computed at the high rate of the inertial sensor data, whereas the filter update is executed only once per each incoming satellite measurement.

Particle Filter

Another important class of Bayesian filters are those belonging to the family of sequential Monte Carlo (SMC) filters [AMGC02] [DdFG01]. SMC filters, which are also referred to as particle filters, solve the Bayesian filtering equations based on the principle of *importance sampling* and thus inherently implement only a suboptimal approximation of the optimal Bayesian solution. In a SMC filter the a posteriori PDF at step k is represented as a sum, and is specified by a set of N_p particles:

$$p(\mathbf{x}_k|\mathbf{Z}_k) \approx \sum_{\mu=1}^{N_p} w_k^\mu \delta(\mathbf{x}_k - \mathbf{x}_k^\mu) \quad , \tag{2.72}$$

where each particle with index μ has a state $\mathbf{x}_k^\mu$ and has a weight w_k^μ. The sum over all particles' weights is one. The SMC filters are not restricted with respect to the class of the model and the noise process, but the number of employed particles is a crucial parameter, as only for $N_p \to \infty$ the approximate a posteriori PDF approaches the true PDF (Strictly speaking only the expectations on the discrete approximation converge to the expectations on the true PDF). The particles are drawn according to the concept of importance sampling from a so-called proposal density $q(\mathbf{x}_k|\mathbf{x}_{k-1}^\mu, \mathbf{z}_k)$, such that their respective weight is calculated via

$$w_k^\mu \propto w_{k-1}^\mu \frac{p(\mathbf{z}_k|\mathbf{x}_k^\mu)p(\mathbf{x}_k^\mu|\mathbf{x}_{k-1}^\mu)}{q(\mathbf{x}_k^\mu|\mathbf{x}_{k-1}^\mu, \mathbf{z}_k)} \quad . \tag{2.73}$$

The selection of the proposal density is crucial for the performance of the particle filter. Although the optimal proposal density can be derived theoretically [AMGC02], it is in practice often impossible or at least very difficult to actually draw from this density and to compute the corresponding weight according to (2.73). Consequently the choice of the proposal density is characteristic for the specific realization of the filtering algorithm. The most common choice is the so-called sequential importance resampling particle filter (SIR-PF) [AMGC02]. In the SIR-PF the proposal density is chosen to be $p(\mathbf{x}_k|\mathbf{x}_{k-1} = \mathbf{x}^{\mu}_{k-1})$, and with resampling [AMGC02] at every time step. The key step in which the measurement for instance k is incorporated, is in the calculation of the weight w^{μ}_k, which for the SIR-PF can be shown to be the likelihood function: $p(\mathbf{z}_k|\mathbf{x}^{\mu}_k)$. The characterization of the dynamic process enters in the algorithm when at each time instance k, the state of each particle $\mathbf{x}^{\mu}_k$ is drawn randomly from the proposal distribution; i.e. from $p(\mathbf{x}_k|\mathbf{x}^{\mu}_{k-1})$.

Marginalized Filter

In a marginalized filter [SGN05], which is also often referred to as Rao-Blackwellized filter [DdFMR00] the state space is separated into W sub-state vectors according to $\mathbf{x}_k = [\mathbf{x}^1_k, \ldots, \mathbf{x}^W_k]$. Often the state space is separated into two groups: Linear Gaussian and non-linear states. Thereby KFs are used to estimate the linear and Gaussian states analytically whereas the non-linear states are tracked by the sub-optimal and computationally more complex PF. Though the term marginalized filter is often used as synonym for the combination KF/PF, a marginalized filter can actually comprise any nested combination of Bayesian filters. A general marginal filter factorizes the a posteriori PDF according to

$$\begin{aligned} p(\mathbf{x}^1_k, \ldots, \mathbf{x}^W_k|\mathbf{Z}_k) &= \frac{p(\mathbf{z}_k|\mathbf{x}^1_k, \ldots, \mathbf{x}^W_k)}{p(\mathbf{z}_k|\mathbf{Z}_{k-1})} p(\mathbf{x}^1_k, \ldots, \mathbf{x}^W_k|\mathbf{Z}_{k-1}) \\ &= \frac{p(\mathbf{z}_k|\mathbf{x}^1_k, \ldots, \mathbf{x}^W_k)}{p(\mathbf{z}_k|\mathbf{Z}_{k-1})} \prod_{w=1}^{W} p(\mathbf{x}^w_k|\mathbf{Z}_{k-1}, \mathbf{x}^{w+1}_k, \ldots, \mathbf{x}^W_k) \\ &= \prod_{w=1}^{W} \frac{p(\mathbf{z}_k|\mathbf{Z}_{k-1}, \mathbf{x}^w_k, \ldots, \mathbf{x}^W_k)}{p(\mathbf{z}_k|\mathbf{Z}_{k-1}, \mathbf{x}^{w+1}_k, \ldots, \mathbf{x}^W_k)} p(\mathbf{x}^w_k|\mathbf{Z}_{k-1}, \mathbf{x}^{w+1}_k, \ldots, \mathbf{x}^W_k) \\ &= \prod_{w=1}^{W} p(\mathbf{x}^w_k|\mathbf{Z}_k, \mathbf{x}^{w+1}_k, \ldots, \mathbf{x}^W_k) \;, \end{aligned} \tag{2.74}$$

in which a specific filter is associated to each conditional a posteriori PDF $p(\mathbf{x}^w_k|\mathbf{Z}_k, \mathbf{x}^{w+1}_k, \ldots, \mathbf{x}^W_k)$. To factorize the a posteriori PDF according to (2.74) several conditions must hold [DdFG01]. It was shown that the MF approach can significantly improve the filtering performance compared to an equivalent PF implementation for a given number of particles (which is not necessarily a reasonable criteria under all circumstances, since in an MF that combines KF/PF each particle carries commonly its own KF, and the complexity of several hundreds of KFs could be higher than that of a sufficient number of additional computational efficient particles in some cases).

A crucial step in any MF is the computation of the marginal likelihood functions that are used to update the nested filters. The marginal likelihood function can be computed recursively via

$$\begin{aligned} & p(\mathbf{z}_k|\mathbf{Z}_{k-1}, \mathbf{x}^w_k, \ldots, \mathbf{x}^W_k) = \\ & \quad \int\limits_{\mathbf{x}^{w-1}_k} p(\mathbf{z}_k|\mathbf{Z}_{k-1}, \mathbf{x}^{w-1}_k, \ldots, \mathbf{x}^W_k) p(\mathbf{x}^{w-1}_k|\mathbf{Z}_{k-1}, \mathbf{x}^w_k, \ldots, \mathbf{x}^W_k) \mathrm{d}\mathbf{x}^{w-1}_k \;. \end{aligned} \tag{2.75}$$

A Posteriori Cramer-Rao Lower Bound

The a posteriori Cramer-Rao lower bound (CRLB/PCRB) is the theoretical performance bound of an *unbiased* sequential Bayesian estimator. As it was shown in [vT68] the variance of any unbiased estimator must be larger than the CRLB. A detailed summary on the derivation and the computation of the CRLB is available in [RAG04]. In the scope of this thesis the CRLB is used to compare the performance of the derived algorithms against the theoretically achievable limits whereas in difference to the general filtering information matrix notation the bound is calculated via the EKF approximation, which is viable whenever the process and measurement noise models are Gaussian and when a unique system trajectory is used instead of an ensemble.

Model Matching

It is important to point out that the Bayesian estimators are only as good as their system models match the real world situation. The state model needs to capture *all* relevant hidden states with memory and needs to correctly model their dependencies, while adhering to the first order Markov condition. Furthermore, any memory of the measurement noise affecting the likelihood function $p(\mathbf{z}_k|\mathbf{x}_k)$ must be explicitly contained as additional states of the model $\mathbf{x}$, so that the measurement noise is i.i.d.. Practically there will be always a mismatch between the assumptions taken in the estimation algorithm and the real world situation. Nevertheless if the mismatch is reduced as much as possible, it may be expected that the estimation accuracy is increased.

2.3.2 Application to Joint Satellite and Inertial Navigation

The standard algorithm to combine a satellite navigation system and an inertial navigation system is the EKF, whose dynamic and measurement model is adapted to the joint system. Unlike the GNSS measurements the acceleration and gyroscope measurements are not treated as regular measurements in the standard implementation of a conventional GNSS/INS EKF. This is due to the fact that the standard EKF algorithm for the integration of inertial sensors indeed follows Bayesian philosophy, but assumes uniform and thus non-informative priors on accelerations and turn rates, which transforms the transition model from a dynamic to a pure kinematic one. This is a crucial point, since in this case there is no more benefit of the transition model with respect to the inertial measurement. This leads to the consequence, that the algorithm formulation is completely independent of the navigating vehicle or individual, e.g. though an aircraft and a pedestrian have obviously quite different dynamics the conventional EKF integration algorithm [TW04] does not consider this. The lack of an adequate dynamic model is the major drawback of todays standard integration approach.

Depending on the level of integration three basic types of integration approaches can be found in the literature [Nat04]:

- **Loose Coupling**: In a loosely coupled GNSS/INS the fusion filter combines the position estimates of the GNSS receiver with the inertial solution.
- **Tight Coupling**: In a tightly coupled GNSS/INS fusion the inertial solution is joined directly with the delay estimates of the GNSS receiver, which has the advantage that a

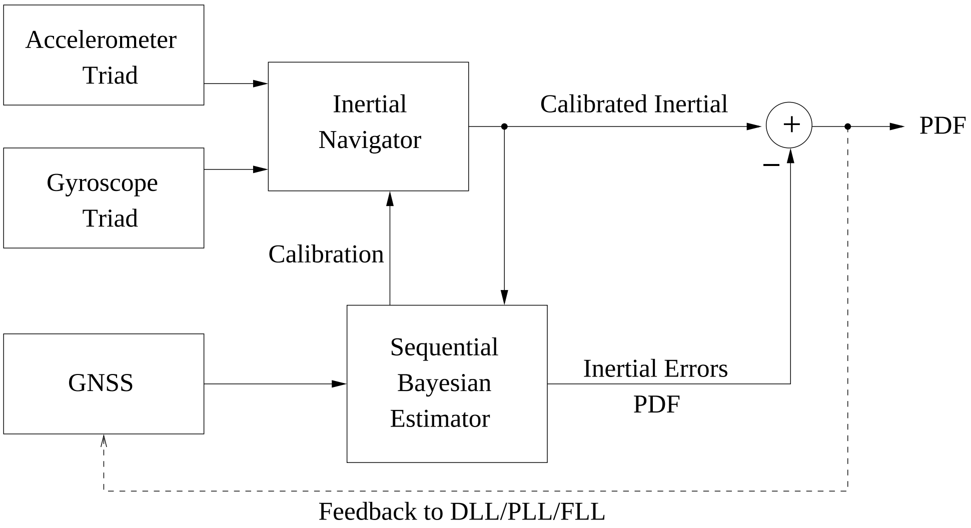

Figure 2.10: State-of-the-art implementation of the Bayesian estimator for a joint satellite and inertial navigation system. The inertial navigation computations are performed in parallel to a Bayesian estimator, commonly an EKF, which estimates the errors of the inertial navigation.

filter update is not restricted to the case that at least four or more delay estimates are available at the GNSS receiver.

- **Ultra-Tight Coupling/Deep Integration**: In a ultra-tightly coupled GNSS/INS, which is also referred to as deeply integrated GNSS/INS, the fusion filter aids the DLL/PLL/FLL circuitry of the GNSS receiver. Depending on the implementation also correlator outputs are used as measurements instead of the time delay estimates.

As illustrated in 2.10 commonly an error state space formulation is used for a GNSS/INS filter [May79]. The error state space formulation, which is also referred to as indirect estimation, arises due to the linearization in the EKF. As addressed briefly in Section 2.3.1 the error state space implementation allows to use the navigation solution of the INS to obtain the large-signal system trajectory, upon which the linearization is performed, which enables the estimation of the small-signal error dynamics. The error estimates are in turn used to correct the solution of the INS and thus the large-signal system trajectory as well. In the error space implementation of the EKF the INS serves as reference system. The general concept of how the information is joined in a combined GNSS/INS navigation system is shown in Figure 2.11.

Loose Coupling

The state vector in a loosely coupled system comprises position, velocity and attitude

$$\mathbf{x}_k^{\mathrm{lc}} = [\mathbf{r}_k, \mathbf{v}_k, \boldsymbol{\psi}_k] \ . \tag{2.76}$$

Using (2.31), (2.32), and (2.33) the position is assumed to follow the process

$$\mathbf{r}_k = \mathbf{r}_{k-1} + \mathbf{v}_{k-1} T_s + \mathbf{n}_{r,k}^{\mathrm{d}} \ , \tag{2.77}$$

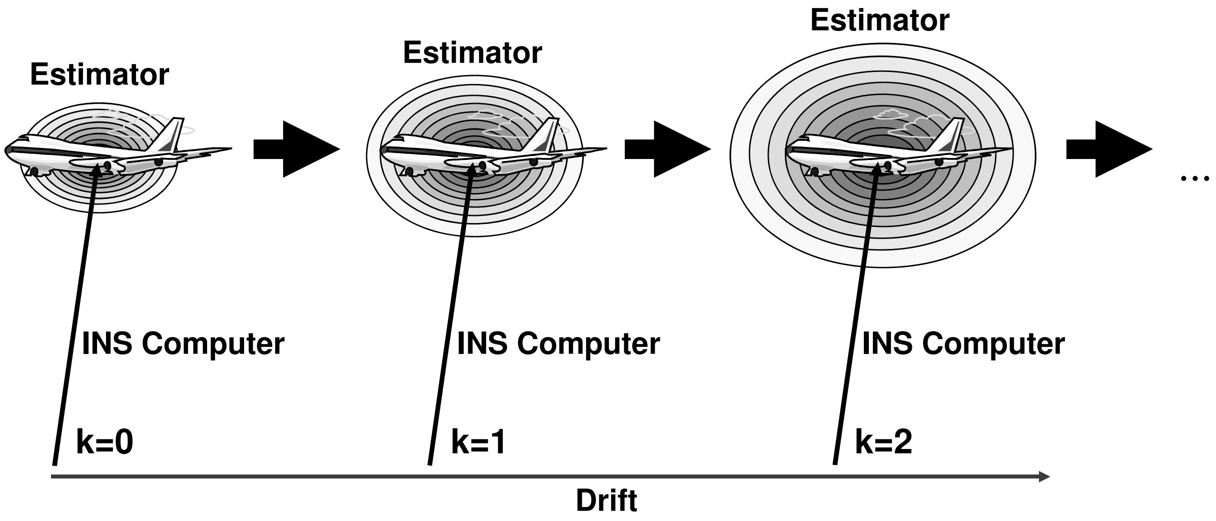
Estimator
Estimator
Estimator
...
INS Computer
INS Computer
INS Computer
k=0
k=1
k=2
Drift

(a) Free running INS

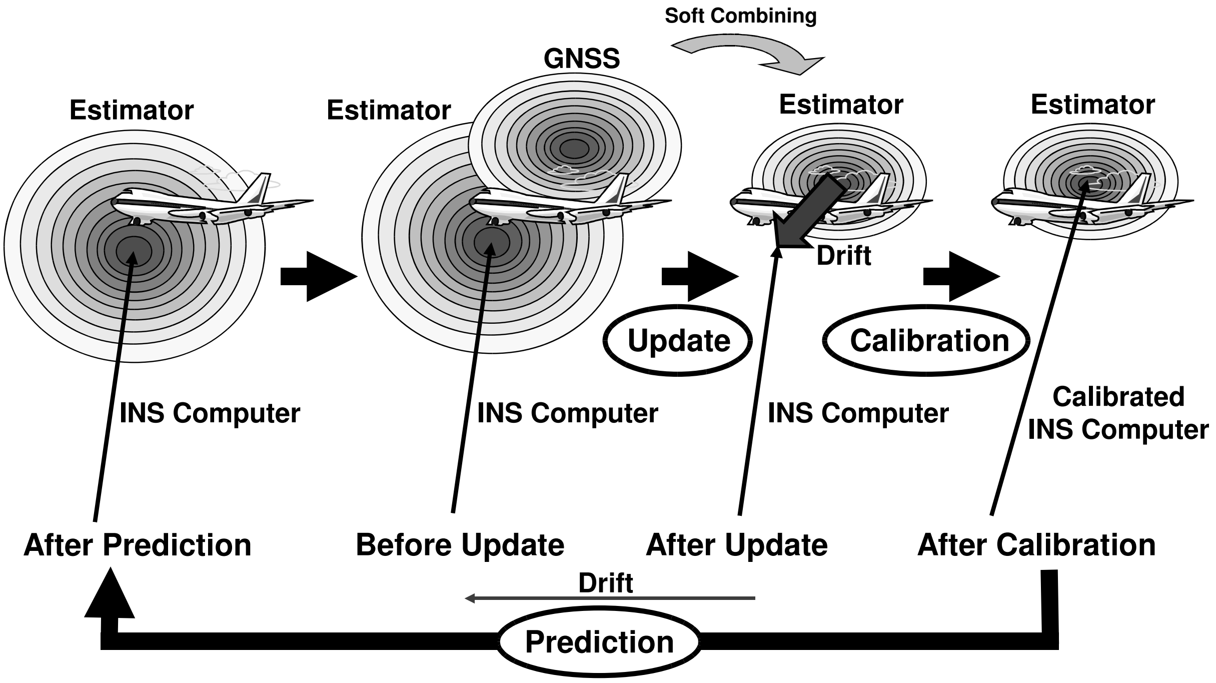
Soft Combining
GNSS
Estimator
Estimator
Estimator
Estimator
Drift
Update
Calibration
INS Computer
INS Computer
INS Computer
Calibrated
INS Computer
After Prediction
Before Update
After Update
After Calibration
Drift
Prediction

(b) INS updated by GNSS

Figure 2.11: Information fusion in a GNSS/INS navigation system as it is used in aeronautics. Since there is no information that constrains the movement of the vessel a sole INS solution degrades over time, thus the uncertainty about its location increases continuously (2.11(a)). The information provided by the GNSS constrains the possible locations, which allows to correct the joint estimate (Figure 2.11(b)).

the velocity is assumed to follow

$$\mathbf{v}_k = \mathbf{v}_{k-1} + \mathbf{a}^i_{k-1} T_s + \mathbf{n}^{\mathrm{d}}_{v,k} \quad , \tag{2.78}$$

the attitude is assumed to follow

$$\boldsymbol{\psi}_k = \boldsymbol{\psi}_{k-1} + \mathbf{n}^{\mathrm{d}}_{\psi,k} \quad , \tag{2.79}$$

and the Jacobian system matrix becomes for the EKF according to [TW04]:

$$\mathbf{F}_{k-1} = \left. \begin{pmatrix} \mathbf{I}_{3\times3} & \mathbf{I}_{3\times3} T_s & \mathbf{0}_{3\times3} \\ \mathbf{0}_{3\times3} & \mathbf{I}_{3\times3} & [\mathbf{f}^i_{k-1} \times] T_s \\ \mathbf{0}_{3\times3} & \mathbf{0}_{3\times3} & \mathbf{I}_{3\times3} \end{pmatrix} \right|_{\hat{\mathbf{x}}_{k-1}} \quad . \tag{2.80}$$

The measurement that is used to update the filter is the position estimate of the GNSS receiver $\mathbf{z}^{\mathrm{lc}}_k = \hat{\mathbf{r}}^r_k$. Thus the effective measurement for the error space EKF is the difference of the INS position and the computed position of the GNSS receiver:

$$\mathbf{z}^{\epsilon,\mathrm{lc}}_k = \mathbf{r}^i_k - \hat{\mathbf{r}}^r_k \quad . \tag{2.81}$$

The measurement matrix is thus

$$\mathbf{H}^{\mathrm{lc}}_k = \begin{pmatrix} \mathbf{I}_{3\times3} & \mathbf{0}_{3\times3} & \mathbf{0}_{3\times3} \end{pmatrix} \quad . \tag{2.82}$$

Tight Coupling

In a tightly coupled system the state space is extended by the receiver clock bias and clock drift to allow for the direct incorporation of range measurements. Using the clock bias τ^r_k and the clock drift $\dot{\tau}^r_k$ the state vector for the tightly coupled integration is

$$\mathbf{x}^{\mathrm{tc}}_k = [\mathbf{x}^{\mathrm{lc}}_k, \tau^r_k, \dot{\tau}^r_k] \quad . \tag{2.83}$$

The clock bias is assumed to follow the process

$$\tau^r_k = \tau^r_{k-1} + \dot{\tau}^r_{k-1} T_s + n^{\mathrm{d}}_{\tau,k} \quad , \tag{2.84}$$

and the clock drift the process

$$\dot{\tau}^r_k = \dot{\tau}^r_{k-1} + n^{\mathrm{d}}_{\dot{\tau},k} \quad . \tag{2.85}$$

The extended system matrix is thus

$$\mathbf{F}^{\mathrm{tc}}_{k-1} = \begin{pmatrix} \mathbf{F}^{\mathrm{lc}}_{k-1} & \mathbf{0}_{9\times1} & \mathbf{0}_{9\times1} \\ \mathbf{0}_{1\times9} & 1 & T_s \\ \mathbf{0}_{1\times9} & 0 & 1 \end{pmatrix} \quad . \tag{2.86}$$

The measurements are now the range estimates of the GNSS receiver $\mathbf{z}^{\mathrm{tc}}_k = \hat{\boldsymbol{\tau}}_k$. Consequently the error space measurements are the difference of the predicted ranges and the estimated ranges of the GNSS receiver

$$\mathbf{z}^{\epsilon,\mathrm{tc}}_k = \hat{\boldsymbol{\tau}}_{0,k} - \hat{\boldsymbol{\tau}}_k \quad , \tag{2.87}$$

where $\hat{\boldsymbol{\tau}}_{0,k} = \hat{\boldsymbol{\tau}}_0([\hat{\mathbf{r}}^i_k, 0])$ according to Section 2.1. The measurement matrix is thus

$$\mathbf{H}^{\mathrm{tc}}_k = \begin{pmatrix} \tilde{\mathbf{D}}_k & \mathbf{0}_{M\times3} & \mathbf{0}_{M\times3} & \mathbf{1}_{M\times1} & \mathbf{0}_{M\times1} \end{pmatrix} \quad , \tag{2.88}$$

in which $\tilde{\mathbf{D}}_k = \mathbf{D}_{[:,1:3],k}$ according to (2.3).

Ultra-Tight Coupling

In a ultra-tightly coupled integration the signal tracking circuitry of the GNSS receiver is aided by the output of the integration filter. The state space in such a filter equals that of a tightly coupled system and thus $\mathbf{x}_k^{\mathrm{utc}} = \mathbf{x}_k^{\mathrm{tc}}$ and $\mathbf{F}_{k-1}^{\mathrm{utc}} = \mathbf{F}_{k-1}^{\mathrm{tc}}$. To aid the DLLs the linearization point for the TED is adjusted based on the predicted state of the joint GNSS/INS. Introducing a vector notation for the TED linearization points $\boldsymbol{\tau}_k^0 = [\tau_{1,k}^0, \dots, \tau_{M,k}^0]^T$ and the filtered version of the timing mismatch $\hat{\boldsymbol{\tau}}_{\epsilon,k}^f = [\hat{\tau}_{\epsilon,1,k}^f, \dots, \hat{\tau}_{\epsilon,M,k}^f]^T$ according to Section 2.1.1, the point of linearization is obtained via

$$\begin{aligned} \boldsymbol{\tau}_k^0 &= \hat{\boldsymbol{\tau}}_{0,k}^- && (2.89) \\ &= \boldsymbol{\tau}_0\big([\hat{\mathbf{r}}_k^{i-}, \hat{\tau}_k^{r-}]\big) \ , && (2.90) \end{aligned}$$

in which the function $\boldsymbol{\tau}_0(\bullet)$ follows from (2.3). The delay estimates are then obtained via

$$\hat{\boldsymbol{\tau}}_k = \hat{\boldsymbol{\tau}}_{0,k}^- + \hat{\boldsymbol{\tau}}_{\epsilon,k}^f \qquad (2.91)$$

Beside the aiding of the tracking loops an alternative formulation of the measurement equations is characteristic for some implementations of the ultra-tightly coupled concept, e.g. the deeply integrated system analyzed in [Nat04], which is based on the direct observation of the early/late and prompt correlator outputs.

Chapter 3

Pedestrian Satellite Navigation

As the need for personal localization and navigation systems is emerging, pedestrian navigation is today a rapidly growing market. Location- and context-aware applications are mainly driving the evolution in the mass market sector. In the professional sector fire fighters and other relief units have the still unmet want for a system allowing the precise and seamless localization and tracking of operating individuals. Indeed standardization has already taken place for positioning via mobile radio signals and positioning capabilities are becoming a design criteria for future mobile radio communication systems. GPS receivers are today integrated in many types of mobile phones and PDAs, hence world-wide positioning of individuals is feasible. In particular the synergies between communication and navigation systems are exploited in assisted GPS (AGPS) applications. An initial coarse fix and further assistance data is provided by the mobile radio communication system, which allows to reduce the search space in the acquisition for the satellite signals significantly, resulting in a time-to-first-fix (TTFF) of few seconds or even less. Furthermore high sensitivity navigation receivers allow the processing of heavily attenuated signals using long periods of coherent reception. Geodetic applications can reach centimeter or even millimeter accuracy by the processing of carrier phase measurements [Ver05]. Despite these advances todays existing systems don’t meet the accuracy and availability criteria of many future personal navigation applications. A crucial problem seizing these applications is the impact of the user dynamics and the user environment on the availability and accuracy of satellite-based positioning. Though satellite navigation works very accurate in free field conditions with todays latest mass market receivers, their performance gets degraded heavily in those environments, where accurate and reliable localization of individuals is of particular interest: Environments where people usually move most frequently, like dense urban environments or even inside of buildings. The physics are thereby the limiting factor, since in these scenarios the local environment causes diffraction and attenuation of the direct satellite-to-user propagation path. The signal is diffracted at edges of obstacles like buildings or trees and the signal power gets reduced due to propagation through foliage, walls, roofs or windows. Additionally multipath, the reception of additional signal replica due to reflections caused by the receiver environment, worsens the situation significantly. The reception of multipath introduces a bias into the time delay estimate of the delay lock loop of a conventional navigation receiver, which finally leads to a bias in the receiver’s position estimate. Multipath is today still one of the most crucial problems in GNSS, as the error is caused locally and can not be corrected through the use of conventional correction data, which is provided by differential

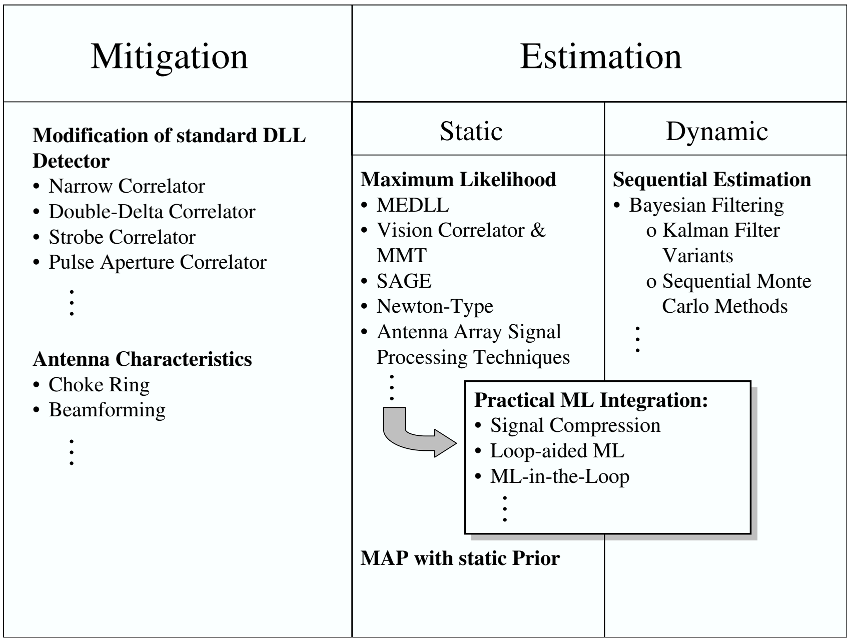
Mitigation
Estimation
Modification of standard DLL Detector
• Narrow Correlator
• Double-Delta Correlator
• Strobe Correlator
• Pulse Aperture Correlator
Antenna Characteristics
• Choke Ring
• Beamforming
Static
Maximum Likelihood
• MEDLL
• Vision Correlator & MMT
• SAGE
• Newton-Type
• Antenna Array Signal Processing Techniques
Practical ML Integration:
• Signal Compression
• Loop-aided ML
• ML-in-the-Loop
MAP with static Prior
Dynamic
Sequential Estimation
• Bayesian Filtering
o Kalman Filter Variants
o Sequential Monte Carlo Methods

Figure 3.1: Classification of multipath mitigation approaches. The genuine mitigation approaches actually mitigate the impact of multipath, whereas the estimation approaches estimate and compensate the multipath at a later processing stage.

augmentation systems. Examples are the differential GPS (DGPS) systems EGNOS, a satellite-based augmentation system (SBAS), or SAPOS, a ground-based augmentation system (GBAS). In particular for personal navigation multipath is a critical problem, since the pedestrian user dynamics do not allow for the use of geodetic measurement principles. Nevertheless the dynamics are smaller compared to those of vehicles, leading to less variation in the propagation channel and thus increased impact of multipath.

The need to cope with the multipath problem has led to the development of various signal processing techniques for multipath mitigation. Their evolution to this day reaches back almost twenty years. During that period the advances in that field have led to a continuous improvement of performance. As illustrated in Figure 3.1 basically two major approaches can be distinguished: The class of techniques that actually *mitigate* the effect of multipath by modifications of the antenna pattern (either by means of hardware design or with signal processing techniques) or by aligning the more or less traditional receiver components (e.g. the early/late correlator) and the class of multipath *estimation* techniques, which treat multipath (in particular the delay of the paths) as something to be estimated from the received signal, so that its effects can be trivially removed at a later processing stage. Most of the conventional mitigation techniques are in some way aligning the discriminator of the DLL to the signal received in the multipath environment. Well-known examples of this category are amongst others the Narrow Correlator [vDFF92] and the Strobe Correlator [GvDR96]. For the estimation techniques *static* and *dynamic* approaches can be distinguished, according to the underlying assumption of the channel dynamics. Examples for static multipath estimation are those belonging to the family of maximum likelihood (ML) estimators, where the probably best-known technique is the multipath estimating delay lock loop (MEDLL) [vNSFT94]. Dynamic algorithms for estimation of time-varying synchronization parameters in spread spectrum systems have been suggested in the field of communications using the extended Kalman filter [Ilt90] as well as the sequential Monte Carlo approach [PDF04, BRPT04]. For navigation systems estimators based on sequential importance sampling methods (particle filtering) have been considered for static [CFPFR06] and dynamic scenarios [LKRT07, LKR08, KW09]. Aside from the aforementioned mitigation techniques various other concepts have been shown to improve the multipath mitigation performance in navigation systems, including the use of antenna arrays and array processing techniques for multipath and interference mitigation [SGFRFP05, HKDA08], and concepts which are based on the exploitation of the mutual dependencies of the signal delays through the common position parameters like the vector DLL (VDLL) [PS96], including the position domain ML estimator [CFPFR07a] and joint positioning and mitigation tracking algorithms [GT05, KLR08a, KLR08b].

The objective of this chapter is the application of the Bayesian approach to the problem of multipath mitigation, which thus becomes now a problem of channel estimation. Apart from the required complexity, which may indeed be high, the advantage of Bayesian approach is obviously the fact, that it is an optimal approach, at least conceptually. In other words, no other algorithm can outperform the optimal Bayesian filter, given the same premises and assumptions. Starting from the conventional approach to apply the channel estimation separately per each received satellite, the multipath problem is subsequently embedded into a superior estimation problem: The direct estimation of the relevant states of a individual, in particular its position and speed, and all other states affecting the received signals, e.g. the state of the receiver clock and the realization of the particular channel responses. Unlike other algorithms the Bayesian filtering approach allows thereby to exploit the probabilistic dependencies between the user and the channel dynamics [LS05] and is thus foreseen to reach better performance compared to other methods.

3.1 Multipath Signal Model

A crucial problem in Bayesian filtering is to model all relevant observations, states and their temporal dependencies properly by means of a probabilistic system model. Only if these models are correct the Bayesian approach is optimal. To adequately model the observations and measurements that are performed in a navigation receiver, the receiver is assumed to provide M parallel channels to simultaneously process the signals arriving from the available satellites [PS96]. After coarse removal of the Doppler shifts, e.g. through a conventional PLL, the complex valued baseband-equivalent received signal for the receiver channel $j = 1, ..., M$, is expressed as

$$z_j(t) = \sum_{i=0}^{N_m} e_{i,j}(t) a_{i,j}(t) s_j(t - \tau_{i,j}(t)) + n_j(t) \quad , \tag{3.1}$$

where $s_j(t)$ is the CDMA navigation signal, N_m is the maximum number of considered multipath replica reaching the receiver (to restrict the modeling complexity), $e_{i,j}(t)$ is a binary function that controls the activity of the i'th path and $a_{i,j}(t)$ and $\tau_{i,j}(t)$ are their individual complex amplitudes and time delays, respectively. The signal is disturbed by additive white Gaussian noise $n_j(t)$.

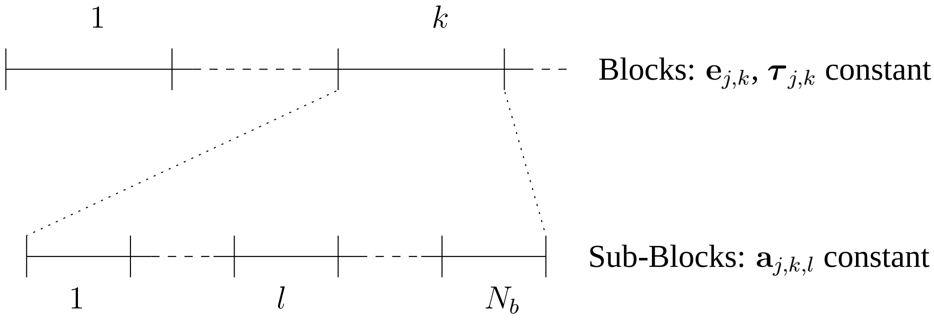
1
k
Blocks: $\mathbf{e}_{j,k}$, $\boldsymbol{\tau}_{j,k}$ constant
Sub-Blocks: $\mathbf{a}_{j,k,l}$ constant
1
l
N_b

Figure 3.2: Signal model using blocks and sub-blocks. The complex amplitudes $\mathbf{a}$ are allowed to vary with a higher rate than the path activity indicators $\mathbf{e}$ and the delays $\boldsymbol{\tau}$.

Usually signal models in this context, e.g. the ones used in [Sel04b] or [SGFRFP05] consider a fixed known number of replica. The benefit of the model proposed here is that it incorporates the commonly unknown number of received replica implicitly through the parameter functions $e_{i,j}(t)$.

3.1.1 Discrete Time Model

As common in satellite navigation a block fading process for the complex amplitudes is assumed, which has higher dynamics compared to the other signal parameters, and as consequence a discrete time signal model comprising blocks and coherent sub-blocks is used [Sel04c]. The concept of the signal model is shown in Figure 3.2. The signal is sampled at times $(m+(l-1)L+kLN_b)T_s$, $m=0,\ldots,L-1$ and grouped in sub-blocks of L samples together into vectors $\mathbf{z}_{j,k,l}$, $\mathbf{s}_j(\tau_{i,j,k,l})$, and $\mathbf{n}_{j,k,l}$, with the block index $k=0,1,\ldots,$ and the sub-block index $l=1,\ldots,N_b$, with N_b being the number of sub-blocks in each block k. The parameter functions $e_{i,j}(t)$ and $\tau_{i,j}(t)$ are assumed to be constant and equal to $e_{i,j,k}$ and $\tau_{i,j,k}$ for the duration of an entire block, thus $e_{i,j,k,l}=e_{i,j,k}$ and $\tau_{i,j,k,l}=\tau_{i,j,k}$. The functions $a_{i,j}(t)$ are assumed to be constant and equal to $a_{i,j,k,l}$ during a coherent sub-block interval only. Furthermore the vector $\mathbf{e}_{j,k,l}=\mathbf{e}_{j,k}=[e_{0,j,k,l},\ldots,e_{N_m,j,k,l}]^T$ is used, with $e_{i,j,k,l}\in[0,1]$ to determine whether the i'th path is active or not by being either $e_{i,j,k,l}=1$ corresponding to an active path or $e_{i,j,k,l}=0$ for a path that is currently not active. Note that the notation with the binary path activity parameters $e_{i,j,k,l}$ is used to address the estimation of the commonly unknown number of impinging replica. For concise notation the signal and amplitude vectors are stacked together as columns of the matrices $\mathbf{S}_j(\boldsymbol{\tau}_{j,k,l})=[\mathbf{s}_j(\tau_{0,j,k,l}),\ldots,\mathbf{s}_j(\tau_{N_m,j,k,l})]$ and the discrete-time signal for the sub-block l in block k may be written in the compact form

$$\begin{aligned} \mathbf{z}_{j,k,l} &= \mathbf{S}_j(\boldsymbol{\tau}_{j,k,l})\mathbf{E}_{j,k,l}\mathbf{a}_{j,k,l}+\mathbf{n}_{j,k,l} \\ &\mathrel{\widehat{=}} \mathbf{y}_{j,k,l}+\mathbf{n}_{j,k,l} \ , \end{aligned} \tag{3.2}$$

with $\mathbf{E}_{j,k,l}=\operatorname{diag}\left([e_{0,j,k,l},\ldots,e_{N_m,j,k,l}]\right)$. The delays and amplitudes are collected in the parameter vectors $\boldsymbol{\tau}_{j,k,l}=[\tau_{0,j,k,l},\ldots,\tau_{N_m,j,k,l}]^T$ and $\mathbf{a}_{j,k,l}=[a_{0,j,k,l},\ldots,a_{N_m,j,k,l}]^T$.

3.1.2 The Likelihood Function

The likelihood function plays a central role for the parametric channel estimation algorithms. Its purpose is to quantify the conditional probability of the received signal conditioned on the unknown signal (specifically the channel parameters). The term $\mathbf{y}_{j,k,l}$ denotes the signal hypothesis and is according to (3.2) completely determined by the channel parameters $\mathbf{a}_{j,k,l}$, $\mathbf{e}_{j,k,l}$, and $\boldsymbol{\tau}_{j,k,l}$. Using the signal model according to (3.2) and assuming that $\mathbf{n}_{j,k,l}$ is a vector of zero-mean element-wise uncorrelated white Gaussian noise of variance σ_j^2 the associated *likelihood function* for a sub-block can be written as

$$p(\mathbf{z}_{j,k,l}|\{\mathbf{a},\mathbf{e},\boldsymbol{\tau}\}_{j,k,l}) = \frac{1}{(2\pi)^L\sigma_j^{2L}} \cdot \exp\left[-\frac{1}{2\sigma_j^2}\left(\mathbf{z}_{j,k,l}-\mathbf{y}_{j,k,l}\right)^H\left(\mathbf{z}_{j,k,l}-\mathbf{y}_{j,k,l}\right)\right] \ . \tag{3.3}$$

Efficient Computation

The use of likelihood measures or other types of cost functions has become widespread in navigation receivers implementing high performance multipath mitigation algorithms. Since the data size in navigation receivers is typically quite large due to the bandwidth of the navigation signals, reduced complexity techniques are employed in all real-time implementations such as [vNSFT94, FJ05]. In [Sel04b] a general theory for the efficient representation of the likelihood function was presented. The key idea of this concept is to formulate (3.3) through a vector $\mathbf{z}_{c,j,k,l}$ resulting from an orthonormal projection of the observed signal $\mathbf{z}_{j,k,l}$ onto a smaller vector space, so that $\mathbf{z}_{c,j,k,l}$ is a sufficient statistic according to the Neyman-Fisher factorization [Kay93] and hence suitable for estimating $\{\mathbf{a},\mathbf{e},\boldsymbol{\tau}\}_{j,k,l}$. In other words the reduced signal comprises the same information as the original signal itself. In practice this concept becomes relevant as the projection can be achieved by processing the received signal with a bank of correlators. A variant of this very general concept has also been referred to as the *Signal Compression Theorem* in [Wei06]. The large vector containing the received signal samples $\mathbf{z}_{j,k,l}$ is linearly transformed into a vector $\mathbf{z}_{c,j,k,l}$ of much smaller size. Following this approach the likelihood function according to (3.3) can be rewritten as

$$\begin{aligned}
&p(\mathbf{z}_{j,k,l}|\{\mathbf{a},\mathbf{e},\boldsymbol{\tau}\}_{j,k,l}) \approx \\
&\qquad \frac{1}{(2\pi)^L\sigma_j^{2L}}\exp\left[-\frac{\mathbf{z}_{j,k,l}^H\mathbf{z}_{j,k,l}}{2\sigma_j^2}+\frac{\Re\{\mathbf{z}_{j,k,l}^H\mathbf{Q}_{c,j}\mathbf{Q}_{c,j}^H\mathbf{y}_{j,k,l}\}}{\sigma_j^2}-\frac{\mathbf{y}_{j,k,l}^H\mathbf{Q}_{c,j}\mathbf{Q}_{c,j}^H\mathbf{y}_{j,k,l}}{2\sigma_j^2}\right] \\
&= \quad \frac{1}{(2\pi)^L\sigma_j^{2L}}\exp\left[-\frac{\mathbf{z}_{j,k,l}^H\mathbf{z}_{j,k,l}}{2\sigma_j^2}+\frac{\Re\{\mathbf{z}_{c,j,k,l}^H\mathbf{y}_{c,j,k,l}\}}{\sigma_j^2}-\frac{\mathbf{y}_{c,j,k,l}^H\mathbf{y}_{c,j,k,l}}{2\sigma_j^2}\right] \\
&\propto \quad \exp\left[\frac{\Re\{\mathbf{z}_{c,j,k,l}^H\mathbf{y}_{c,j,k,l}\}}{\sigma_j^2}-\frac{\mathbf{y}_{c,j,k,l}^H\mathbf{y}_{c,j,k,l}}{2\sigma_j^2}\right] \ ,
\end{aligned} \tag{3.4}$$

with the compressed received vector $\mathbf{z}_{c,j,k,l}$ and the compressed signal hypothesis $\mathbf{y}_{c,j,k,l}$:

$$\mathbf{z}_{c,j,k,l} = \mathbf{Q}_{c,j}^H\mathbf{z}_{j,k,l}, \quad \mathbf{y}_{c,j,k,l} = \mathbf{Q}_{c,j}^H\mathbf{y}_{j,k,l} \ , \tag{3.5}$$

and the orthonormal compression matrix $\mathbf{Q}_{c,j}$, which needs to fulfill

$$\mathbf{Q}_{c,j}\mathbf{Q}_{c,j}^H\mathbf{S}_j(\boldsymbol{\tau}) \approx \mathbf{S}_j(\boldsymbol{\tau}), \quad \mathbf{Q}_{c,j}^H\mathbf{Q}_{c,j} \approx \mathbf{I} \ , \tag{3.6}$$

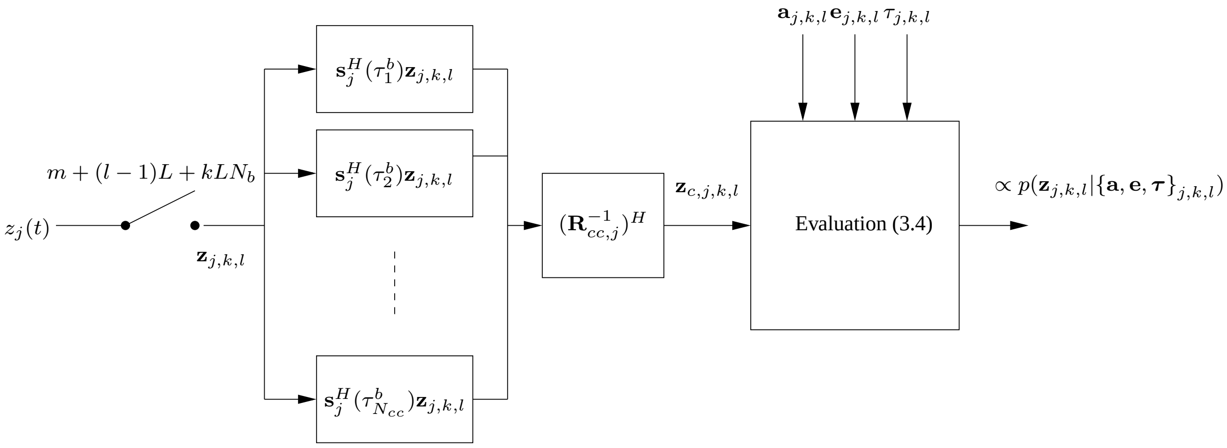
$\mathbf{a}_{j,k,l}\,\mathbf{e}_{j,k,l}\,\tau_{j,k,l}$
$\mathbf{s}_j^H(\tau_1^b)\mathbf{z}_{j,k,l}$
$m+(l-1)L+kLN_b$
$\mathbf{s}_j^H(\tau_2^b)\mathbf{z}_{j,k,l}$
$(\mathbf{R}_{cc,j}^{-1})^H$
$\mathbf{z}_{c,j,k,l}$
$\propto p(\mathbf{z}_{j,k,l}|\{\mathbf{a},\mathbf{e},\boldsymbol{\tau}\}_{j,k,l})$
$z_j(t)$
Evaluation (3.4)
$\mathbf{z}_{j,k,l}$
$\mathbf{s}_j^H(\tau_{N_{cc}}^b)\mathbf{z}_{j,k,l}$

Figure 3.3: Architecture for efficient evaluation of the likelihood function in navigation receivers [Sel04c]. A bank of conventional correlators provides the reduced data set $\mathbf{z}_{c,j,k,l}$, which is sufficient to compute the likelihood function and to estimate the signal parameters.

to minimize the compression loss. According to [Sel04c] the compression can be two-fold so that it can be factorized according to

$$\mathbf{Q}_{c,j} = \mathbf{Q}_{cc,j}\mathbf{Q}_{pc,j} \tag{3.7}$$

into a *canonical component decomposition*, given by an $L \times N_{cc}$ matrix $\mathbf{Q}_{cc,j}$, and a *principal component decomposition*, given by an $N_{cc} \times N_{pc}$ matrix $\mathbf{Q}_{pc,j}$. In [Sel04c] two choices for $\mathbf{Q}_{cc,j}$ are proposed, which correspond to the correlator bank implementations found in [vNSFT94] and [FJ05]. In this thesis the compression through

$$\mathbf{Q}_{cc,j} = \mathbf{S}_j(\boldsymbol{\tau}^b)\mathbf{R}_{cc,j}^{-1} \tag{3.8}$$

is considered, with $\mathbf{S}_j(\boldsymbol{\tau}^b) = [\mathrm{s}_j(\tau_1^b), \ldots, \mathrm{s}(\tau_{N_{cc}}^b)]$, as it does not require a factorization of the signal into a code sequence and a modulation pulse, which is not necessarily unique, in particular for novel modulation schemes [Wei06]. In (3.8) the elements of the vector $\boldsymbol{\tau}^b = [\tau_1^b, \ldots, \tau_{N_{cc}}^b]^T$ define the positions of the individual correlators. To project the bank outputs $(\mathbf{S}_j(\boldsymbol{\tau}^b))^H\mathbf{z}_{j,k,l}$ onto a vector space of uncorrelated noise the whitening matrix $\mathbf{R}_{cc,j}$ can be obtained from a QR decomposition of $\mathbf{S}_j(\boldsymbol{\tau}^b)$, such that

$$\mathbf{z}_{c,j,k,l} = (\mathbf{R}_{cc,j}^{-1})^H(\mathbf{S}_j(\boldsymbol{\tau}^b))^H\mathbf{z}_{j,k,l} \ . \tag{3.9}$$

The implementation is illustrated in Figure 3.3. Details on the compression through $\mathbf{Q}_{pc,j}$ are available in [Sel04c].

A crucial parameter for the complexity of the hardware implementation of the compression through the canonical components is the minimum number of required complex correlators N_{cc}. According to [Sel04c] it is sufficient to place the individual correlators with a delay spacing that corresponds to the Nyquist-rate associated to the received signal $z_j(t)$. Furthermore it is recommended to have at least the main correlation peak covered by the correlators as illustrated in Figure 3.4. Thus given a chip rate of T_c for the CDMA signal and a pre-correlation reception bandwidth of B_{pre} the minimum number of required correlators computes with

$$N_{cc} > 4T_cB_{\text{pre}} \ . \tag{3.10}$$

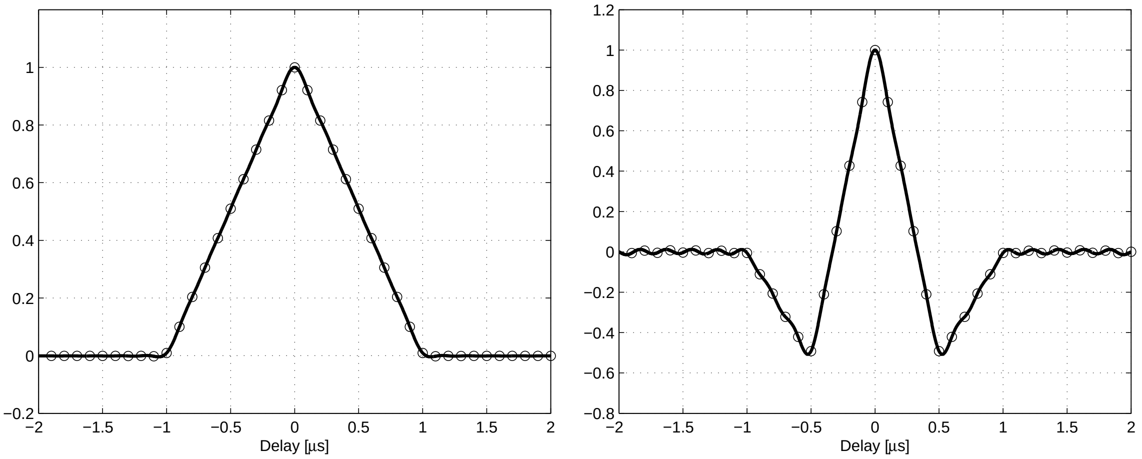

(a) BPSK signal matched (b) BOC(1,1) signal matched

Figure 3.4: Output of correlator banks that can be used for data size reduction in navigation receivers for a BPSK and a BOC(1,1) signal with 1.023 MChips/s respectively. The obtained samples need to cover at least a chip interval around the main peak.

Hence for processing the GPS C/A signal (Chip rate f_c = 1.023 MChips/s) with e.g. a one-sided receiver bandwidth of B_{pre} = 8 MHz at least $N_{cc} = 33$ correlators are required.

Interpolation

In [Sel04c] it was proposed to compute (3.4) independently of the sampling grid by making use of interpolation techniques [Sel06]. For this purpose the signal is factorized into

$$\mathbf{s}_j(\tau_{i,j,k,l}) \quad = \quad \mathbf{S}_j^d \boldsymbol{\delta}(\tau_{i,j,k,l}) \ , \tag{3.11}$$

where $\boldsymbol{\delta}$ is e.g. a sampled SI-pulse of length N_g and $\mathbf{S}_j^d$ a matrix representing the signal. Using (3.11) and the discrete Fourier transformation (DFT), with $\boldsymbol{\Psi}$ being the DFT matrix and $\boldsymbol{\Psi}^{-1}$ its inverse (IDFT), the compressed signal may be written as

$$\begin{aligned} \mathbf{y}_{c,j,k,l} &= \mathbf{Q}_{c,j}^H \mathbf{S}_j^d \boldsymbol{\Psi}^{-1} \text{diag}\left[\boldsymbol{\Psi}\boldsymbol{\delta}(0)\right] \boldsymbol{\Omega}(\boldsymbol{\tau}_{j,k,l}) \mathbf{E}_{j,k,l} \mathbf{a}_{j,k,l} \\ &\mathrel{\widehat{=}} \mathbf{M}_{s_c,j} \boldsymbol{\Omega}(\boldsymbol{\tau}_{j,k,l}) \mathbf{E}_{j,k,l} \mathbf{a}_{j,k,l} \ , \end{aligned} \tag{3.12}$$

with $\boldsymbol{\Omega}(\boldsymbol{\tau}_{j,k,l}) = [\boldsymbol{\Omega}(\tau_{0,j,k,l}), \ldots, \boldsymbol{\Omega}(\tau_{N_m,j,k,l})]$ being a matrix of column-wise stacked vectors with Vandermonde structure [Sel04c], such that the element at row g and column i (corresponding to path i) computes with

$$\Re\left\{[\boldsymbol{\Omega}(\boldsymbol{\tau}_{j,k,l})]_{[g,i]}\right\} \quad = \quad \cos\Big(2\pi(g-1)\tau_{i,j,k,l}/(N_g T_s)\Big) \ , \tag{3.13}$$

$$\Im\left\{[\boldsymbol{\Omega}(\boldsymbol{\tau}_{j,k,l})]_{[g,i]}\right\} \quad = \quad -\sin\Big(2\pi(g-1)\tau_{i,j,k,l}/(N_g T_s)\Big) \ . \tag{3.14}$$

The advantage of the interpolation is that it can take place in the reduced space. The most costly computations in (3.12) can be carried out in precalculation, as the matrix $\mathbf{M}_{s_c,j}$ is constant. The row dimension of $\mathbf{M}_{s_c,j}$ corresponds to the dimension of the reduced space and the column dimension is the pulse length N_g. The interpolation exploits that fact that a delayed version of the signal can be obtained by delaying the pulse component $\boldsymbol{\delta}$, which is achieved through a transformation into the frequency domain, a subsequent multiplication with complex exponentials, and a transformation back to temporal domain finally. In the following sections always the uncompressed signal notation will be used without loss of generality regarding the use of compressed signals.

3.2 Bayesian Estimation in the Pseudorange Domain

As addressed in Section 2.3 the concept of sequential Bayesian estimation allows to consider statistical dependencies between successive observation intervals, given that the evolution of the estimated parameters can be modeled as a first order Markov process, which holds if future parameters given the present state of the channel and all its past states, depend only on the present channel state (and not on any past states), and if the noise affecting successive channel outputs is independent of the past noise values; so each observation depends only on the present channel state. The objective of this section is to apply the sequential Bayesian approach to the multipath problem while considering the requirement that the mitigation is applied independently per each received satellite as it is done in conventional navigation receivers. In this case the problem of multipath mitigation becomes one of sequential channel estimation, in particular one of the estimation of a hidden Markov process: The unknown channel parameters are estimated based on an evolving sequence of received noisy channel outputs $\mathbf{z}_{j,k,l}$. Intuitively the optimal sequential algorithm exploits thereby not only the channel observations to estimate the hidden channel parameters (via the likelihood function), but also exploits the a priori knowledge about the statistical dependencies between successive sets of channel parameters, which is very promising for practical reasons, as real world navigation channels are temporally and spatially constrained through the dynamics of the user [SL04].

3.2.1 Choice of Channel Process

To exploit the advantages of sequential estimation the actual channel characteristics (channel parameters) must be described so that these are captured by $p(\mathbf{x}_k|\mathbf{x}_{k-1})$. In other words, the model must be a first order Markov model and all transition probabilities, i.e. the system dynamics must be known. Recalling the general notation (2.39)

$$\mathbf{x}_k = \mathbf{f}_{k-1}(\mathbf{x}_{k-1}, \mathbf{n}^{\mathrm{d}}_{k-1}) \ , \tag{3.15}$$

the channel dynamics are approximated as follows: The channel is totally characterized by a direct LOS path (index $i = 0$) and at most N_m echoes. Each path has complex amplitude $a_{i,j,k,l}$, $l = 1, \ldots, N_b$, activity $e_{i,j,k}$, delay $\tau_{i,j,k}$, and delay rate $\dot{\tau}_{i,j,k}$, where echoes are constrained to have delay $\tau_{i,j,k} \geq \tau_{0,j,k}$, $i = 1, \ldots, N_m$, to reflect that multipath replica are physically constrained to arrive later at the receiver than the LOS path. Furthermore the echoes are constrained to have delay $\tau_{i,j,k} < \tau_{0,j,kT_c} + T_c$, $i = 1, \ldots, N_m$, with T_c being the chip duration of the CMDA code, in order to consider only those replica which have actually an impact on the receiver behavior.

Characterization of Delays and Delay Rates

The delay of each path is assumed to follow the process

$$\tau_{i,j,k} \quad = \tau_{i,j,k-1} + \dot{\tau}_{i,j,k-1}\Delta t + n_{i,j,\tau} + n_{\tau} \quad , \tag{3.16}$$

with $\Delta t = LN_bT_s$ and where $n_{i,j,\tau}$ and n_τ is white Gaussian noise with n_τ being the same value for all indices i, in order to model the impact of the receiver clock, which is the same on all replica. Each parameter $\dot{\tau}_{i,j,k}$ that specifies the rate of the change of the path delay follows its own process:

$$\dot{\tau}_{i,j,k} = \dot{\tau}_{i,j,k-1} + n_{i,j,\dot{\tau}} + n_{\dot{\tau}} \quad , \tag{3.17}$$

with white Gaussian noise $n_{i,j,\dot{\tau}}$ and $n_{\dot{\tau}}$. Thereby $n_{\dot{\tau}}$ is again the same value for all indices i, in order to model the impact of the receiver clock drift that is jointly affecting all observed delay rates.

Characterization of Path Activity

Since the number of impinging multipath replica is unknown, each echo is either ”on” or ”off”, as defined by the channel parameter $e_{i,j,k} \in \{1 \equiv \text{”on”}, 0 \equiv \text{”off”}\}$, where $e_{i,j,k}$, $i = 1, \ldots, N_m$ follows a simple two-state Markov process with a-symmetric crossover and same-state probabilities:

$$\begin{aligned} p(e_{i,j,k} = 0|e_{i,j,k-1} = 1) \quad &= p_{\text{onoff}} \qquad i = 1, \ldots, N_m \quad , \\ p(e_{i,j,k} = 1|e_{i,j,k-1} = 0) \quad &= p_{\text{offon}} \qquad i = 1, \ldots, N_m \quad . \end{aligned} \tag{3.18}$$

The LOS component is assumed to be always present and consequently $e_{0,j,k} = 1$ for all k. Appearing echoes ($e_{i,j,k} = 1$ and $e_{i,j,k-1} = 0$) are initialized according to [CFPFR06] with

$$\tau_{i,j,k} = \tau_{0,j,k} + |\tau_m + n_{j,\tau_0}| \quad , \tag{3.19}$$

with white Gaussian noise n_{j,τ_0} and the characteristic mean value τ_m. Additionally persisting echoes are allowed to jump with a small probability of p_{jump}. In this case a new echo delay is drawn from (3.19). This scenario is considered to model abrupt changes in the echo delay that are due discontinuities on the surface of a reflector, e.g. a house front.

Characterization of Amplitudes

The complex amplitudes $a_{i,j,k,l}$ are assumed to depend on the amplitudes of the previous sub-block $a_{i,j,k,l-1}$ through

$$a_{i,j,k,l} = a_{i,j,k,l-1}e^{-j2\pi f_0 LT_s \dot{\tau}_{i,j,k,l}} + n_{i,j,a_i} \quad . \tag{3.20}$$

Thus the rate of change in the delay affects the evolution of the complex amplitude through a phase shift according to the current Doppler frequency and an additional white Gaussian noise term n_{i,j,a_i}. This allows to consider the physical relations between phase, Doppler-frequency, and time delay adequately. Blockage and shadowing of the LOS signal is considered through variations of the LOS amplitude $a_{0,j,k,l}$.

Model Summary

The model implicitly incorporates nine i.i.d. noise sources within the process noise vector $\mathbf{n}^{\mathrm{d}}$: Gaussian $n_{i,j,\tau} \sim \mathcal{N}(0, \sigma^2_{i,j,\tau})$, $n_{i,j,\dot{\tau}} \sim \mathcal{N}(0, \sigma^2_{i,j,\dot{\tau}})$, $n_\tau \sim \mathcal{N}(0, \sigma^2_\tau)$, $n_{\dot{\tau}} \sim \mathcal{N}(0, \sigma^2_{\dot{\tau}})$, $n_{j,\tau_0} \sim \mathcal{N}(\tau_m, \sigma^2_{j,\tau_0})$, and complex Gaussian $n_{i,j,a_i} \sim \mathcal{N}(0, \sigma^2_{i,j,a_i})$, as well as the noise process driving the state changes for $e_{i,j,k}$ and the process for drawing samples according to the probability p_{jump}. These sources provide the randomness of the model. The noise sources n_τ and $n_{\dot{\tau}}$ are included to model the impact of the receiver clock on the individual delays and delay rates, since at the receiver they are actually affected simultaneously by the same clock random process. Finally, $\Delta t = N_b L T_s$ is the time between instances $k-1$ and k. It is assumed that all model parameters (i.e. Δt, noise variances, and the "on"/"off" Markov model) are independent of k. Note that the model implicitly represents the number of paths through the time variant parameter

$$N_{m,j,k,l} = \sum_{i=0}^{N_m} e_{i,j,k,l} \quad . \tag{3.21}$$

The hidden channel state vector $\mathbf{x}_{j,k,l}$ of the range-based channel model is thus represented as

$$\mathbf{x}_{j,k,l} \quad \widehat{=} \quad \{\mathbf{a}, \mathbf{e}, \boldsymbol{\tau}, \dot{\boldsymbol{\tau}}\}_{j,k,l} \quad . \tag{3.22}$$

The channel state model used here is motivated by channel modeling work for multipath prone environments such as the urban satellite navigation channel [LS05, SL04]. In fact the process of constructing a channel model in order to characterize the channel for signal level simulations and receiver evaluation comes close to the task of building a first order Markov process for sequential estimation. For the algorithm implementation, the model needs to satisfy the condition that one can carry out the Bayesian recursion with relatively low computational complexity, e.g. that some calculations can be performed analytically by Kalman or grid-based filters and that one can draw states with low computational effort in a particle filter. Adapting the model structure and the model parameters to the real channel environment is a task that is not addressed in detail here. It may even be possible to envisage hierarchical models in which the selection of the current model itself follows a process. In this case e.g. a sequential estimator will automatically choose the correct weighting of these models according to their ability to fit the received signal.

3.2.2 Filter Implementation

Different families of algorithms are known to implement the Bayesian recursion (2.41) and (2.42), including amongst others the well-known Kalman filter as well as the particle filtering algorithms. Certain restrictions are imposed on the use of these algorithms. The objective here is to estimate the channel parameters (3.22) using the likelihood function (3.3) and the process defined in 3.2.1, which makes the estimation complex: The amplitude parameters $a_{i,j,k,l}$ are continuous and the measurement depends linearly on them like the activity parameters $e_{i,j,k}$, which are discrete and thus follow a discrete evolution. In difference the observations depend nonlinearly on the continuous delays $\tau_{i,j,k}$, which are also nonlinear with respect to their dynamics. A straightforward way would be to implement the estimation algorithm completely with a particle filter, which is the most general method with respect to system nonlinearities, but depending on the considered number of paths N_m the state space in such a filter becomes large and it becomes difficult to cover the entire space with a reasonable number of particles.

To consider the nonlinearities while keeping the state space to be covered by the particles as small as possible, it was proposed to reduce the computational complexity of the filter by means of marginalization over the linear state variables, a technique also known as Rao-Blackwellization. In a marginalized filter, particles are still used to estimate the non-linear states, while for each of the particles the linear states can be estimated analytically. A marginalized filter was already proposed in [CFPFR08], and here the concept is extended towards the use of path activity estimation, resulting finally in a two-fold marginalization. The novel two-fold marginalized estimator factorizes the a posteriori PDF according to

$$\begin{aligned} &p(\{\mathbf{a},\mathbf{e},\boldsymbol{\tau},\dot{\boldsymbol{\tau}}\}_{j,k,l}|\mathbf{Z}_{j,k,l}) = \\ &\quad \underbrace{p(\mathbf{a}_{j,k,l}|\mathbf{Z}_{j,k,l},\{\mathbf{e},\boldsymbol{\tau},\dot{\boldsymbol{\tau}}\}_{j,k,l})}_{\text{Kalman filter}}\underbrace{p(\mathbf{e}_{j,k,l}|\mathbf{Z}_{j,k,l},\{\boldsymbol{\tau},\dot{\boldsymbol{\tau}}\}_{j,k,l})}_{\text{Grid-based filter}}\underbrace{p(\{\boldsymbol{\tau},\dot{\boldsymbol{\tau}}\}_{j,k,l}|\mathbf{Z}_{j,k,l})}_{\text{Particle filter}} \ . \end{aligned} \tag{3.23}$$

Kalman filters are used to estimate the amplitudes $\mathbf{a}_{j,k,l}$ analytically conditional on the parameters $\{\mathbf{e},\boldsymbol{\tau},\dot{\boldsymbol{\tau}}\}_{j,k,l}$. The discrete path activity parameters are in turn estimated conditionally on the delays and delay rates $\{\boldsymbol{\tau},\dot{\boldsymbol{\tau}}\}_{j,k,l}$ using a grid based method [AMGC02], which is appropriate to optimally estimate their discrete state space. Finally the delays and delay rates $\{\boldsymbol{\tau},\dot{\boldsymbol{\tau}}\}_{j,k,l}$ are the only remaining parameters to be estimated by the sub-optimal particle filtering algorithm. Using

$$\begin{aligned} &p(\{\mathbf{a},\mathbf{e},\boldsymbol{\tau},\dot{\boldsymbol{\tau}}\}_{j,k,l}|\mathbf{Z}_{j,k,l-1}) = \\ &\quad p(\mathbf{a}_{j,k,l}|\mathbf{Z}_{j,k,l-1},\{\mathbf{e},\boldsymbol{\tau},\dot{\boldsymbol{\tau}}\}_{j,k,l})p(\mathbf{e}_{j,k,l}|\mathbf{Z}_{j,k,l-1},\{\boldsymbol{\tau},\dot{\boldsymbol{\tau}}\}_{j,k,l})p(\{\boldsymbol{\tau},\dot{\boldsymbol{\tau}}\}_{j,k,l}|\mathbf{Z}_{j,k,l-1}) \ , \end{aligned} \tag{3.24}$$

the update step (2.42) of the marginalized filter can be expressed as

$$\begin{aligned} &p(\{\mathbf{a},\mathbf{e},\boldsymbol{\tau},\dot{\boldsymbol{\tau}}\}_{j,k,l}|\mathbf{Z}_{j,k,l}) = \\ &\quad \frac{p(\mathbf{z}_{j,k,l}|\{\mathbf{a},\mathbf{e},\boldsymbol{\tau},\dot{\boldsymbol{\tau}}\}_{j,k,l})}{p(\mathbf{z}_{j,k,l}|\mathbf{Z}_{j,k,l-1})}p(\{\mathbf{a},\mathbf{e},\boldsymbol{\tau},\dot{\boldsymbol{\tau}}\}_{j,k,l}|\mathbf{Z}_{j,k,l-1}) \\ &= \underbrace{\frac{p(\mathbf{z}_{j,k,l}|\{\mathbf{a},\mathbf{e},\boldsymbol{\tau},\dot{\boldsymbol{\tau}}\}_{j,k,l})}{p(\mathbf{z}_{j,k,l}|\mathbf{Z}_{j,k,l-1},\{\mathbf{e},\boldsymbol{\tau},\dot{\boldsymbol{\tau}}\}_{j,k,l})}p(\mathbf{a}_{j,k,l}|\mathbf{Z}_{j,k,l-1},\{\mathbf{e},\boldsymbol{\tau},\dot{\boldsymbol{\tau}}\}_{j,k,l})}_{\text{Amplitude estimator: Kalman filter}} \\ &\quad \underbrace{\frac{p(\mathbf{z}_{j,k,l}|\mathbf{Z}_{j,k,l-1},\{\mathbf{e},\boldsymbol{\tau},\dot{\boldsymbol{\tau}}\}_{j,k,l})}{p(\mathbf{z}_{j,k,l}|\mathbf{Z}_{j,k,l-1},\{\boldsymbol{\tau},\dot{\boldsymbol{\tau}}\}_{j,k,l})}p(\mathbf{e}_{j,k,l}|\mathbf{Z}_{j,k,l-1},\{\boldsymbol{\tau},\dot{\boldsymbol{\tau}}\}_{j,k,l})}_{\text{Path activity estimator: Grid-based filter}} \\ &\quad \underbrace{\frac{p(\mathbf{z}_{j,k,l}|\mathbf{Z}_{j,k,l-1},\{\boldsymbol{\tau},\dot{\boldsymbol{\tau}}\}_{j,k,l})}{p(\mathbf{z}_{j,k,l}|\mathbf{Z}_{j,k,l-1})}p(\{\boldsymbol{\tau},\dot{\boldsymbol{\tau}}\}_{j,k,l}|\mathbf{Z}_{j,k,l-1})}_{\text{Delay and delay rate estimator: Particle filter}} \\ &= p(\mathbf{a}_{j,k,l}|\mathbf{Z}_{j,k,l},\{\mathbf{e},\boldsymbol{\tau},\dot{\boldsymbol{\tau}}\}_{j,k,l})p(\mathbf{e}_{j,k,l}|\mathbf{Z}_{j,k,l},\{\boldsymbol{\tau},\dot{\boldsymbol{\tau}}\}_{j,k,l})p(\{\boldsymbol{\tau},\dot{\boldsymbol{\tau}}\}_{j,k,l}|\mathbf{Z}_{j,k,l}) \ . \end{aligned} \tag{3.25}$$

The details of the filter computations are discussed now.

Estimation of Amplitudes From (3.25) follows the implementation of the conditional amplitude filter. The conditional a posteriori PDF with respect to the complex amplitudes is given by

$$\begin{aligned} & p(\mathbf{a}_{j,k,l}|\mathbf{Z}_{j,k,l},\{\mathbf{e},\boldsymbol{\tau},\dot{\boldsymbol{\tau}}\}_{j,k,l}) = \\ & \quad \frac{p(\mathbf{z}_{j,k,l}|\{\mathbf{a},\mathbf{e},\boldsymbol{\tau},\dot{\boldsymbol{\tau}}\}_{j,k,l})}{p(\mathbf{z}_{j,k,l}|\mathbf{Z}_{j,k,l-1},\{\mathbf{e},\boldsymbol{\tau},\dot{\boldsymbol{\tau}}\}_{j,k,l})} p(\mathbf{a}_{j,k,l}|\mathbf{Z}_{j,k,l-1},\{\mathbf{e},\boldsymbol{\tau},\dot{\boldsymbol{\tau}}\}_{j,k,l}) \ . \end{aligned} \tag{3.26}$$

Recalling the structure of the amplitude system model, i.e. (3.3) and (3.20), the observed signal $\mathbf{z}_{j,k,l}$ depends linearly on the amplitudes $\mathbf{a}_{j,k,l}$ and the amplitude dynamics are linear conditional on the delay rates. Hence the Rao-Blackwellization can be applied directly [DdFMR00, SGN05] and the a priori PDF is given by the Gaussian

$$p(\mathbf{a}_{j,k,l}|\mathbf{Z}_{j,k,l-1},\{\mathbf{e},\boldsymbol{\tau},\dot{\boldsymbol{\tau}}\}_{j,k,l}) = \mathcal{N}\left(\hat{\mathbf{a}}^{-}_{j,k,l},\tilde{\mathbf{P}}^{-}_{j,k,l}\right) \ , \tag{3.27}$$

with mean and covariance that are obtained in the prediction step from the previous time instance $l-1$ through the framework of the Kalman filter equations

$$\hat{\mathbf{a}}^{-}_{j,k,l} = \tilde{\mathbf{F}}_{j,k,l}\hat{\mathbf{a}}_{j,k,l-1} \ , \tag{3.28}$$

$$\tilde{\mathbf{P}}^{-}_{j,k,l} = \tilde{\mathbf{F}}_{j,k,l}\tilde{\mathbf{P}}_{j,k,l-1}\tilde{\mathbf{F}}^{T}_{j,k,l} + \tilde{\mathbf{Q}}_{j} \ . \tag{3.29}$$

In this case the matrices $\mathbf{F}_{j,k,l}$ and $\mathbf{Q}_j$ follow directly from (3.20) and compute with

$$\mathbf{F}_{j,k,l} = \mathrm{diag}\left([e^{-j2\pi f_0 L T_s \dot{\tau}_{0,j,k,l}},\ldots,e^{-j2\pi f_0 L T_s \dot{\tau}_{N_m,j,k,l}}]\right) \ , \tag{3.30}$$

$$\mathbf{Q}_{j} = \mathrm{diag}\left([\sigma^2_{0,j,a_i},\ldots,\sigma^2_{N_m,j,a_i}]\right) \ . \tag{3.31}$$

The notation $\tilde{\bullet}$ indicates thereby that dimension and values of the respective matrices correspond to the active paths as given by $\mathbf{e}_{j,k,l}$. The notation $\hat{\bullet}$ used for the mean vector implies this as well. Due to the conditional linear Gaussian model the evaluation of (3.26) is feasible through the application of the Kalman filter update equations and the a posteriori PDF becomes

$$p(\mathbf{a}_{j,k,l}|\mathbf{Z}_{j,k,l},\{\mathbf{e},\boldsymbol{\tau},\dot{\boldsymbol{\tau}}\}_{j,k,l}) = \mathcal{N}\left(\hat{\mathbf{a}}_{j,k,l},\tilde{\mathbf{P}}_{j,k,l}\right) \ , \tag{3.32}$$

in which mean and covariance are given by

$$\hat{\mathbf{a}}_{j,k,l} = \hat{\mathbf{a}}^{-}_{j,k,l} + \tilde{\mathbf{K}}_{j,k,l}\left(\mathbf{z}_{j,k,l} - \tilde{\mathbf{S}}_{j,k,l}\hat{\mathbf{a}}^{-}_{j,k,l}\right) \ , \tag{3.33}$$

$$\tilde{\mathbf{P}}_{j,k,l} = \left(\mathbf{I} - \tilde{\mathbf{K}}_{j,k,l}\tilde{\mathbf{S}}_{j,k,l}\right)\tilde{\mathbf{P}}^{-}_{j,k,l} \ , \tag{3.34}$$

with the concise notation $\mathbf{S}_{j,k,l} = \mathbf{S}_j(\boldsymbol{\tau}_{j,k,l})$ and the Kalman gain

$$\tilde{\mathbf{K}}_{j,k,l} = \tilde{\mathbf{P}}^{-}_{j,k,l}\tilde{\mathbf{S}}^{T}_{j,k,l}\left(\tilde{\mathbf{S}}_{j,k,l}\tilde{\mathbf{P}}^{-}_{j,k,l}\tilde{\mathbf{S}}^{T}_{j,k,l} + \mathbf{R}_j\right)^{-1} \ . \tag{3.35}$$

The value of $\mathbf{R}_j = \sigma^2_j \cdot \mathbf{I}$ follows directly from (3.3).

Estimation of Path Activity The estimation of the path activity $\mathbf{e}_{j,k,l}$ follows (3.25) and thus the conditional a posteriori PDF for the activity state is given by

$$\begin{aligned} &p(\mathbf{e}_{j,k,l}|\mathbf{Z}_{j,k,l},\{\boldsymbol{\tau},\dot{\boldsymbol{\tau}}\}_{j,k,l}) = \\ &\quad \frac{p(\mathbf{z}_{j,k,l}|\mathbf{Z}_{j,k,l-1},\{\mathbf{e},\boldsymbol{\tau},\dot{\boldsymbol{\tau}}\}_{j,k,l})}{p(\mathbf{z}_{j,k,l}|\mathbf{Z}_{j,k,l-1},\{\boldsymbol{\tau},\dot{\boldsymbol{\tau}}\}_{j,k,l})} p(\mathbf{e}_{j,k,l}|\mathbf{Z}_{j,k,l-1},\{\boldsymbol{\tau},\dot{\boldsymbol{\tau}}\}_{j,k,l}) \ . \end{aligned} \tag{3.36}$$

The activity state space is discrete and thus can be estimated optimally using a grid-based filter [AMGC02]. In this case the prediction (2.41) simplifies to the evaluation of the sum

$$\begin{aligned} &p(\mathbf{e}_{j,k,l}|\mathbf{Z}_{j,k,l-1},\{\boldsymbol{\tau},\dot{\boldsymbol{\tau}}\}_{j,k,l}) = \\ &\quad \sum_{\mathbf{e}_{j,k,l-1}} p(\mathbf{e}_{j,k,l}|\mathbf{e}_{j,k,l-1},\mathbf{Z}_{j,k,l-1},\{\boldsymbol{\tau},\dot{\boldsymbol{\tau}}\}_{j,k,l}) p(\mathbf{e}_{j,k,l-1}|\mathbf{Z}_{j,k,l-1},\{\boldsymbol{\tau},\dot{\boldsymbol{\tau}}\}_{j,k,l}) \ . \end{aligned} \tag{3.37}$$

The transition density with respect to the activity states is given by (3.18) and (3.19) and depends therefore on the realization of the path transition according to

$$\begin{aligned} &p(\mathbf{e}_{j,k,l}=\bar{\mathbf{e}}_{j,k,l}|\mathbf{e}_{j,k,l-1}=\bar{\mathbf{e}}_{j,k,l-1},\mathbf{Z}_{j,k,l-1},\boldsymbol{\tau}_{j,k,l},\dot{\boldsymbol{\tau}}_{j,k,l}) = \\ &\quad (p_{\text{offon}})^{N_{\text{offon}}} \cdot (p_{\text{onoff}})^{N_{\text{onoff}}} \cdot (1-p_{\text{offon}})^{N_{\text{offoff}}} \cdot (1-p_{\text{onoff}})^{N_{\text{onon}}} \ , \end{aligned} \tag{3.38}$$

where N_{offon} is the number of paths switching from ”off” to ”on”, N_{onoff} is the number of paths switching from ”on” to ”off”, N_{offoff} is the number of paths remaining ”off”, and N_{onon} is the number of paths remaining ”on” during the transition from $\bar{\mathbf{e}}_{j,k-1}$ to $\bar{\mathbf{e}}_{j,k,l}$. Note that there are 2^{N_m+1} discrete states and 2^{2N_m+2} transitions to be covered by the grid based filter. The marginal likelihood value used in the update step is given by the solution of the integral

$$\begin{aligned} &p(\mathbf{z}_{j,k,l}|\mathbf{Z}_{j,k,l-1},\{\mathbf{e},\boldsymbol{\tau},\dot{\boldsymbol{\tau}}\}_{j,k,l}) = \\ &\quad \int\limits_{\mathbf{a}_{j,k,l}} p(\mathbf{z}_{j,k,l}|\mathbf{Z}_{j,k,l-1},\{\mathbf{a},\mathbf{e},\boldsymbol{\tau},\dot{\boldsymbol{\tau}}\}_{j,k,l}) p(\mathbf{a}_{j,k,l}|\mathbf{Z}_{j,k,l-1},\{\mathbf{e},\boldsymbol{\tau},\dot{\boldsymbol{\tau}}\}_{j,k,l}) \mathrm{d}\mathbf{a}_{j,k,l} \ , \end{aligned} \tag{3.39}$$

which equals the Gaussian density

$$p(\mathbf{z}_{j,k,l}|\mathbf{Z}_{j,k,l-1},\{\mathbf{e},\boldsymbol{\tau},\dot{\boldsymbol{\tau}}\}_{j,k,l}) = \mathcal{N}\left(\tilde{\mathbf{S}}_{j,k,l}\hat{\mathbf{a}}^-_{j,k,l}, \tilde{\mathbf{S}}_{j,k,l}\tilde{\mathbf{P}}^-_{j,k,l}\tilde{\mathbf{S}}^T_{j,k,l} + \mathbf{R}_j\right) \ . \tag{3.40}$$

Since the somewhat lengthy derivation of (3.40) in its general form is well-established in the context of marginalized Bayesian filters, it is omitted here. For a detailed proof the interested reader is referred to [Sch03].

Estimation of Path Delays Due to the nonlinearity in the system model the remaining parts of the state vector, namely the delays and the delay rates, are to be estimated by a particle filter. According to (3.25) the a posteriori PDF with respect to the path delays and delay rates computes with

$$p(\{\boldsymbol{\tau},\dot{\boldsymbol{\tau}}\}_{j,k,l}|\mathbf{Z}_{j,k,l}) = \frac{p(\mathbf{z}_{j,k,l}|\mathbf{Z}_{j,k,l-1},\{\boldsymbol{\tau},\dot{\boldsymbol{\tau}}\}_{j,k,l})}{p(\mathbf{z}_{j,k,l}|\mathbf{Z}_{j,k,l-1})} p(\{\boldsymbol{\tau},\dot{\boldsymbol{\tau}}\}_{j,k,l}|\mathbf{Z}_{j,k,l-1}) \ . \tag{3.41}$$

Here a simple SIR-PF according to [DdFG01] is proposed to implement the marginalized delay and delay rate estimator. In the SIR-PF algorithm the a posteriori PDF at step k is represented as a sum, and is specified by a set of N_p particles:

$$p(\{\boldsymbol{\tau},\dot{\boldsymbol{\tau}}\}_{j,k,l}|\mathbf{Z}_{j,k,l}) \approx \sum_{\mu=1}^{N_p} w^{\mu}_{j,k,l}\delta(\{\boldsymbol{\tau},\dot{\boldsymbol{\tau}}\}_{j,k,l} - \{\boldsymbol{\tau},\dot{\boldsymbol{\tau}}\}^{\mu}_{j,k,l}) \ , \tag{3.42}$$

where each particle with index j has a state $\{\boldsymbol{\tau},\dot{\boldsymbol{\tau}}\}^{\mu}_{j,k,l}$ and has a weight $w^{\mu}_{j,k,l}$. The key step in which the measurement for instance k is incorporated, is in the calculation of the weight $w^{\mu}_{j,k,l}$, which for the SIR-PF and the given implementation is the marginalized likelihood function: $p(\mathbf{z}_{j,k,l}|\mathbf{Z}_{j,k,l-1},\{\boldsymbol{\tau},\dot{\boldsymbol{\tau}}\}^{\mu}_{j,k,l})$. The characterization of the channel process, which is given by (3.16), (3.17), and (3.19), enters in the algorithm when at each time instance k the state of each particle $\{\boldsymbol{\tau},\dot{\boldsymbol{\tau}}\}^{\mu}_{j,k,l}$ is drawn randomly from the proposal distribution; i.e. from $p(\{\boldsymbol{\tau},\dot{\boldsymbol{\tau}}\}_{j,k,l}|\{\boldsymbol{\tau},\dot{\boldsymbol{\tau}}\}^{\mu}_{j,k,l-1})$, which corresponds to drawing values for $n_{j,\tau}$, $n_{j,\dot{\tau}}$, n_{τ}, $n_{\dot{\tau}}$, and n_{j,τ_i}. The marginal likelihood value, which is required to update the marginal particle filter, is given by summing up the weighted marginal likelihood values of all path activity hypotheses

$$\begin{aligned} &p(\mathbf{z}_{j,k,l}|\mathbf{Z}_{j,k,l-1},\{\boldsymbol{\tau},\dot{\boldsymbol{\tau}}\}_{j,k,l}) = \\ &\quad \sum_{\mathbf{e}_{j,k,l}} p(\mathbf{z}_{j,k,l}|\mathbf{Z}_{j,k,l-1},\{\mathbf{e},\boldsymbol{\tau},\dot{\boldsymbol{\tau}}\}_{j,k,l})p(\mathbf{e}_{j,k,l}|\mathbf{Z}_{j,k,l-1},\{\boldsymbol{\tau},\dot{\boldsymbol{\tau}}\}_{j,k,l}) \ . \end{aligned} \tag{3.43}$$

Estimation of Position and Clock Recalling that the final objective in a navigation receiver is to determine the position based on the obtained delay estimates through the relation (2.1), the joint a posteriori PDF of $\boldsymbol{\xi}_{k,l} = [\mathbf{r}^r_{k,l}, \tau^r_{k,l}]$ with respect to all received satellites signals $\mathbf{Z}_{k,l} = [\mathbf{Z}_{1,k,l},\ldots,\mathbf{Z}_{M,k,l}]$ is given according to the Soft-Location concept [AKR$^+$01] by the product of the range-wise a posteriori PDFs, including the transformation from the range parameters into their position-domain equivalents:

$$p(\boldsymbol{\xi}_{k,l}|\mathbf{Z}_{k,l}) = C\prod_{j=1}^{M}\left\|\frac{\partial\boldsymbol{\tau}_{j,k,l}(\boldsymbol{\xi}_{k,l})}{\partial\boldsymbol{\xi}_{k,l}}\right\| p(\boldsymbol{\tau}_{j,k,l}(\boldsymbol{\xi}_{k,l})|\mathbf{Z}_{j,k,l}) \ . \tag{3.44}$$

Using the approximation $\left\|\frac{\partial\boldsymbol{\tau}_{j,k,l}(\boldsymbol{\xi}_{k,l})}{\partial\boldsymbol{\xi}_{k,l}}\right\| p(\boldsymbol{\tau}_{j,k,l}(\boldsymbol{\xi}_{k,l})|\mathbf{Z}_{j,k,l}) \approx \mathcal{N}(\hat{\tau}_{0,j,k,l},\hat{\sigma}^2_{j,k,l})$ with the estimates for mean and covariance

$$\hat{\tau}_{0,j,k,l} = \int \tau_{0,j,k,l}\,p(\tau_{0,j,k,l}|\mathbf{Z}_{j,k,l})\mathrm{d}\tau_{0,j,k,l} \ , \tag{3.45}$$

$$\hat{\sigma}^2_{j,k,l} = \int (\tau_{0,j,k,l}-\hat{\tau}_{0,j,k,l})^2 p(\tau_{0,j,k,l}|\mathbf{Z}_{j,k,l})\mathrm{d}\tau_{0,j,k} \ , \tag{3.46}$$

the state $\boldsymbol{\xi}_{k,l}$ can be computed according to (2.3) via the system of equations

$$\underbrace{\begin{bmatrix}\hat{\tau}_{0,1,k,l}\\ \vdots \\ \hat{\tau}_{0,M,k,l}\end{bmatrix}}_{\hat{\boldsymbol{\tau}}_{k,l}} = \underbrace{\begin{bmatrix}\tau_{0,1,k,l}(\boldsymbol{\xi}_{0,k,l})\\ \vdots \\ \tau_{0,M,k,l}(\boldsymbol{\xi}_{0,k,l})\end{bmatrix}}_{\boldsymbol{\tau}_{0,k,l}} + \underbrace{\frac{\partial}{\partial\boldsymbol{\xi}}\begin{bmatrix}\tau_{0,1,k,l}(\boldsymbol{\xi})\\ \vdots \\ \tau_{0,M,k,l}(\boldsymbol{\xi})\end{bmatrix}\Bigg|_{\boldsymbol{\xi}_{0,k,l}}}_{\mathbf{D}_{k,l}} \delta\boldsymbol{\xi}_{k,l} \ . \tag{3.47}$$

Analogously to the conventional approach $\hat{\boldsymbol{\xi}}_{k,l} = \boldsymbol{\xi}_{0,k,l} + \delta\hat{\boldsymbol{\xi}}_{k,l}$ can be computed iteratively using the weighted least squares estimate

$$\delta\hat{\boldsymbol{\xi}}_{k,l} = \left(\mathbf{D}_{k,l}^T \mathbf{W}_{k,l}^{-1} \mathbf{D}_{k,l}\right)^{-1} \mathbf{D}_{k,l}^T \mathbf{W}_{k,l}^{-1} (\hat{\boldsymbol{\tau}}_{k,l} - \boldsymbol{\tau}_{0,k,l}) \ , \tag{3.48}$$

with the weighting matrix $\mathbf{W}_{k,l} = \mathrm{diag}[\hat{\sigma}_{1,k,l}^2, \ldots, \hat{\sigma}_{M,k,l}^2]$. Consequently the Gaussian approximation of the position domain density becomes

$$\tilde{p}(\boldsymbol{\xi}_{k,l}|\mathbf{Z}_{k,l}) \approx \mathcal{N}\left(\hat{\boldsymbol{\xi}}_{k,l}, (\mathbf{D}_{k,l}^T \mathbf{W}_{k,l}^{-1} \mathbf{D}_{k,l})^{-1}\right) \ . \tag{3.49}$$

3.3 Bayesian Estimation in the Position Domain

In the preceding section the concept of sequential Bayesian estimation applied on a single-range basis was introduced. A two-fold marginalized estimator was proposed, in which the delays and delay rates are estimated by a particle filter, and where path activity and complex amplitudes are estimated optimally using conditional grid-based and Kalman filters. Actually, given that the individual LOS delays and delay rates of each received satellite signal are not independent from each other, since they are mutually dependent on the common user and clock parameters through (2.2), the range-based approach is not yet the optimal solution, as the mutual correlation between these states is not exploited. In order to exploit these dependencies the optimal estimator has to consider the actual relevant states and processes, which are finally causing the dynamics of each of the received satellite signals, namely the user and receiver clock parameters. Given these parameters are included in the system, the delays and delay rates for each received satellite can be directly expressed in terms of (2.2), and there is no need to consider independently evolving processes and states for them. In the following this approach is referred to as the position-based method. An advantage of the position-based approach is that the resulting estimator is able to provide directly an a posteriori PDF of the user position instead of the indirection via the conventional solution through (3.48).

3.3.1 Choice of System Process

Compared to the range-based approach the formulation of the dynamic processes is much more straightforward in the position-based approach. The process model includes beside the receiver clock model directly a statistical characterization of the user dynamics and incorporates thus a true user movement model, i.e. a direct probabilistic characterization of the dynamics of the receiver expressed with respect to the position domain, which is thus equivalent to the dynamics of the navigating user or vehicle.

User Model

As mentioned before the temporal evolution of the receiver position can be characterized by a physical movement model of the user or vehicle that carries the receiver. Though this model could be any Markovian model of user movement, e.g. as given by [KKRA08], here a simple model is proposed, which represents the user movement just by the states position and velocity, which both are related linearly over time and which are driven by Gaussian noise processes according to

$$\mathbf{r}_k^r = \mathbf{r}_{k-1}^r + \mathbf{v}_{k-1}^r \Delta t + \mathbf{n}_r \ , \tag{3.50}$$

$$\mathbf{v}_k^r = \mathbf{v}_{k-1}^r + \mathbf{n}_v \ , \tag{3.51}$$

with the velocity $\mathbf{v}_k^r = [v_{x,k}^r, v_{y,k}^r, v_{z,k}^r]^T$ as the temporal derivative of $\mathbf{r}_k^r = [r_{x,k}^r, r_{y,k}^r, r_{z,k}^r]^T$, and $\mathbf{n}_r = [n_x, n_y, n_z]^T$, $\mathbf{n}_v = [n_{\dot{x}}, n_{\dot{y}}, n_{\dot{z}}]^T$ being vectors of element-wise uncorrelated zero-mean white Gaussian noise, whose elements have a given variance of σ_x^2, σ_y^2, σ_z^2 and $\sigma_{\dot{x}}^2$, $\sigma_{\dot{y}}^2$, $\sigma_{\dot{z}}^2$, respectively. As will be shown later the simple linear Gaussian model eases the theoretical analysis of the estimator.

Clock Model

The clock model is used to characterize the receiver clock, in particular the evolution of the user clock offset τ_k^r and the user clock drift $\dot{\tau}_k^r$. Here the following simple model is used:

$$\tau_k^r = \tau_{k-1}^r + \dot{\tau}_{k-1}^r \Delta t + n_\tau \ , \tag{3.52}$$

$$\dot{\tau}_k^r = \dot{\tau}_{k-1}^r + n_{\dot{\tau}} . \tag{3.53}$$

The noise terms n_τ and $n_{\dot{\tau}}$ are realizations of a zero-mean white Gaussian noise process of variance σ_τ^2 and $\sigma_{\dot{\tau}}^2$ respectively.

Model Summary

Since the position-based formulation does affect only the LOS components, the modeling of the multipath channel, i.e. specifically the process driving of the complex amplitudes, the path activity parameters, and the multipath delays and delay rates, remain the same as the ones introduced in Section 3.2. Actually the only crucial difference between both models is that the LOS delays and delay rates are in the position-domain approach expressed via

$$\tau_{0,j} = \left|\mathbf{r}_j^t - \mathbf{r}^r\right| c^{-1} + \tau^r + \tau_j^t + \tau_j^{\text{iono}} + \tau_j^{\text{tropo}} + \varepsilon_j \ , \tag{3.54}$$

$$\dot{\tau}_{0,j} = \left|\mathbf{v}_j^t - \mathbf{v}^r\right| c^{-1} + \dot{\tau}^r + \dot{\tau}_j^t + \dot{\tau}_j^{\text{iono}} + \dot{\tau}_j^{\text{tropo}} + \dot{\varepsilon}_j \ , \tag{3.55}$$

according to (2.1) and (2.2) and thus follow the previously introduced position domain processes. To achieve in the following a convenient notation the delays of the multipath delays and delay rates for each satellite are grouped into vectors

$$\boldsymbol{\tau}_{j,k,l}^{\text{mp}} = \left[\tau_{1,j,k,l}, \ldots, \tau_{N_m,j,k,l}\right]^T \ , \tag{3.56}$$

$$\dot{\boldsymbol{\tau}}_{j,k,l}^{\text{mp}} = \left[\dot{\tau}_{1,j,k,l}, \ldots, \dot{\tau}_{N_m,j,k,l}\right]^T \ , \tag{3.57}$$

and the amplitude, path activity, multipath delay, and multipath delay rate vectors associated to the respective satellites are collected in the super-vectors

$$\mathbf{a}_{k,l} \mathrel{\widehat{=}} \left\{\mathbf{a}_{1,k,l}, \ldots, \mathbf{a}_{M,k,l}\right\} \ , \tag{3.58}$$

$$\mathbf{e}_{k,l} \mathrel{\widehat{=}} \left\{\mathbf{e}_{1,k,l}, \ldots, \mathbf{e}_{M,k,l}\right\} \ , \tag{3.59}$$

$$\boldsymbol{\tau}_{k,l}^{\text{mp}} \mathrel{\widehat{=}} \left\{\boldsymbol{\tau}_{1,k,l}^{\text{mp}}, \ldots, \boldsymbol{\tau}_{M,k,l}^{\text{mp}}\right\} \ , \tag{3.60}$$

$$\dot{\boldsymbol{\tau}}_{k,l}^{\text{mp}} \mathrel{\widehat{=}} \left\{\dot{\boldsymbol{\tau}}_{1,k,l}^{\text{mp}}, \ldots, \dot{\boldsymbol{\tau}}_{M,k,l}^{\text{mp}}\right\} \ . \tag{3.61}$$

Using the previously introduced notations the relevant parameters can be combined into the overall state vector of the position-based model. Using the concise notation

$$\boldsymbol{\xi}_{k,l} \;\widehat{=}\; \{\mathbf{r}^r_{k,l}, \mathbf{v}^r_{k,l}, \tau^r_{k,l}, \dot{\tau}^r_{k,l}, \boldsymbol{\tau}^{\mathrm{mp}}_{k,l}, \dot{\boldsymbol{\tau}}^{\mathrm{mp}}_{k,l}\} \;, \tag{3.62}$$

the state vector of the position-based model becomes finally

$$\mathbf{x}_{k,l} \;\widehat{=}\; \{\mathbf{a}, \mathbf{e}, \boldsymbol{\xi}\}_{k,l} \;. \tag{3.63}$$

3.3.2 Filter Implementation

The previously introduced range-based concept requires a Bayesian estimator per each received satellite and the navigation computation is performed subsequently. This concept is comparable to a conventional receiver, where the DLLs are replaced by Bayesian estimators. For that reason the range-based Bayesian estimation concept has also been referred to as *Bayesian DLL* in the literature [CFPFR06]. In difference the position-based approach requires to estimate the navigational parameters directly along with the channel realizations. This unfortunately leads to an increase of the state space of the joint estimator, since all channel parameters, which have previously been estimated range-wise in separated estimators, are now to be estimated jointly in a single estimator. Nevertheless, for the implementation of the joint estimator, fortunately advantage can be taken of the distributed structure of the estimation problem, which allows to keep some of the structures used in the range-based approach. This finally allows to preserve at least the overall number of conditional estimators, i.e. the Kalman and grid-based filters, and to keep their number equal to the one, which is required in the range-based formulation. This can be achieved, since given the position, velocity, multipath delays, and their rates the path activity and complex amplitude densities for all satellites can be estimated conditionally independent, such that the a posteriori PDF of the partially separable estimator can be expressed in the product form

$$\begin{aligned} &p(\{\mathbf{a}, \mathbf{e}, \boldsymbol{\xi}\}_{k,l}|\mathbf{Z}_{k,l}) = \\ &\left[\prod_{j=1}^{M} \underbrace{p(\mathbf{a}_{j,k,l}|\mathbf{Z}_{k,l}, \{\mathbf{e}, \boldsymbol{\xi}\}_{k,l})}_{\text{Kalman filter}} \underbrace{p(\mathbf{e}_{j,k,l}|\mathbf{Z}_{k,l}, \boldsymbol{\xi}_{k,l})}_{\text{Grid-based filter}}\right] \underbrace{p(\boldsymbol{\xi}_{k,l}|\mathbf{Z}_{k,l})}_{\text{Particle filter}} \;. \end{aligned} \tag{3.64}$$

Comparing (3.64) to (3.23), the factorization of the a posteriori PDF leads to a quite similar structure with respect to the conditional a posteriori PDFs for the path activity states and the complex amplitudes. As an important consequence still Kalman filters can be used to estimate the amplitudes $\mathbf{a}_{j,k,l}$ analytically conditional on the parameters $\mathbf{e}_{j,k,l}$ and $\boldsymbol{\xi}_{j,k,l}$. In a similar fashion the discrete path activity parameters are estimated conditionally on the parameters $\boldsymbol{\xi}_{k,l}$ using the optimal grid-based filter. Actually these estimators remain of the same structure as in the range-wise separated range-based estimators. In difference only the states $\boldsymbol{\xi}_{k,l}$ are estimated jointly by the particle filtering algorithm, instead of estimating $\{\boldsymbol{\tau}, \dot{\boldsymbol{\tau}}\}_{j,k,l}$ independently per each received satellite. Assuming the joint a priori PDF can be written in a product comparable to (3.64), the a priori PDF can be expressed as

$$\begin{aligned} &p(\{\mathbf{a}, \mathbf{e}, \boldsymbol{\xi}\}_{k,l}|\mathbf{Z}_{k,l-1}) = \\ &\left[\prod_{j=1}^{M} p(\mathbf{a}_{j,k,l}|\mathbf{Z}_{k,l-1}, \{\mathbf{e}, \boldsymbol{\xi}\}_{k,l}) p(\mathbf{e}_{j,k,l}|\mathbf{Z}_{k,l-1}, \boldsymbol{\xi}_{k,l})\right] p(\boldsymbol{\xi}_{k,l}|\mathbf{Z}_{k,l-1}) \;, \end{aligned} \tag{3.65}$$

which is viable, if the evolution of the complex amplitudes and path activities depends for satellite j only on $\boldsymbol{\xi}_{k,l}$ and on its own amplitudes $\mathbf{a}_{j,k,l-1}$ and activity $\mathbf{e}_{j,k,l-1}$ for each received satellite respectively. As for the dynamics of complex amplitudes and path activities the models introduced in Section 3.2.1 are reused, this condition holds. Furthermore it is assumed that the overall likelihood function can be factorized according to (2.38) into the the contributions of each of the received satellite signals respectively via

$$p(\mathbf{z}_{k,l}|\{\mathbf{a},\mathbf{e},\boldsymbol{\xi}\}_{k,l}) = \prod_{j=1}^{M} p(\mathbf{z}_{j,k,l}|\{\mathbf{a},\mathbf{e}\}_{j,k,l},\boldsymbol{\xi}_{k,l}) \ . \tag{3.66}$$

Applying the Bayes rule to (3.65) and (3.66), it can be shown now that (3.64) holds, as the update step of the joint filter can be expressed as

$$\begin{aligned} & p(\{\mathbf{a},\mathbf{e},\boldsymbol{\xi}\}_{k,l}|\mathbf{Z}_{k,l}) = \\ & \quad \frac{p(\mathbf{z}_{k,l}|\{\mathbf{a},\mathbf{e},\boldsymbol{\xi}\}_{k,l})}{p(\mathbf{z}_{k,l}|\mathbf{Z}_{k,l-1})} p(\{\mathbf{a},\mathbf{e},\boldsymbol{\xi}\}_{k,l}|\mathbf{Z}_{k,l-1}) \\ = & \left[\prod_{j=1}^{M} \underbrace{\frac{p(\mathbf{z}_{j,k,l}|\{\mathbf{a},\mathbf{e}\}_{j,k,l},\boldsymbol{\xi}_{k,l})}{p(\mathbf{z}_{j,k,l}|\mathbf{Z}_{k,l-1},\mathbf{e}_{j,k,l},\boldsymbol{\xi}_{k,l})} p(\mathbf{a}_{j,k,l}|\mathbf{Z}_{k,l-1},\mathbf{e}_{j,k,l},\boldsymbol{\xi}_{k,l})}_{\text{Amplitude estimator: Kalman filter}} \right. \\ & \quad \left. \underbrace{\frac{p(\mathbf{z}_{j,k,l}|\mathbf{Z}_{k,l-1},\mathbf{e}_{j,k,l},\boldsymbol{\xi}_{k,l})}{p(\mathbf{z}_{j,k,l}|\mathbf{Z}_{k,l-1},\boldsymbol{\xi}_{k,l})} p(\mathbf{e}_{j,k,l}|\mathbf{Z}_{k,l-1},\boldsymbol{\xi}_{k,l})}_{\text{Path activity estimator: Grid-based filter}} \right] \\ & \quad \underbrace{\frac{\prod_{j=1}^{M} p(\mathbf{z}_{j,k,l}|\mathbf{Z}_{k,l-1},\boldsymbol{\xi}_{k,l})}{p(\mathbf{z}_{k,l}|\mathbf{Z}_{k,l-1})} p(\boldsymbol{\xi}_{k,l}|\mathbf{Z}_{k,l-1})}_{\text{Position, velocity, delay and delay rate estimator: Particle filter}} \\ = & \left[\prod_{j=1}^{M} p(\mathbf{a}_{j,k,l}|\mathbf{Z}_{k,l},\mathbf{e}_{j,k,l},\boldsymbol{\xi}_{k,l}) p(\mathbf{e}_{j,k,l}|\mathbf{Z}_{k,l},\boldsymbol{\xi}_{k,l})\right] p(\boldsymbol{\xi}_{k,l}|\mathbf{Z}_{k,l}) \ . \end{aligned} \tag{3.67}$$

The details of the filter computations are discussed now.

Estimation of Amplitudes From (3.67) follows the implementation of the conditional amplitude filter. The conditional a posteriori PDF with respect to the complex amplitudes is thus given by

$$\begin{aligned} & p(\mathbf{a}_{j,k,l}|\mathbf{Z}_{j,k,l},\mathbf{e}_{j,k,l},\boldsymbol{\xi}_{k,l}) = \\ & \quad \frac{p(\mathbf{z}_{j,k,l}|\{\mathbf{a},\mathbf{e}\}_{j,k,l},\boldsymbol{\xi}_{k,l})}{p(\mathbf{z}_{j,k,l}|\mathbf{Z}_{j,k,l-1},\mathbf{e}_{j,k,l},\boldsymbol{\xi}_{k,l})} p(\mathbf{a}_{j,k,l}|\mathbf{Z}_{j,k,l-1},\mathbf{e}_{j,k,l},\boldsymbol{\xi}_{k,l}) \ . \end{aligned} \tag{3.68}$$

Recalling the structure of the amplitude system model, i.e. (3.3) and (3.20), the observed signal $\mathbf{z}_{j,k,l}$ depends linearly on the amplitudes $\mathbf{a}_{j,k,l}$ and the amplitude dynamics are linear conditional on the delay rates. Hence a marginalization can be applied in the same manner as done for the range-based approach and the a priori PDF of the amplitudes is given by the Gaussian

$$p(\mathbf{a}_{j,k,l}|\mathbf{Z}_{j,k,l-1}, \mathbf{e}_{j,k,l}, \boldsymbol{\xi}_{k,l}) = \mathcal{N}\left(\hat{\mathbf{a}}^{-}_{j,k,l}, \tilde{\mathbf{P}}^{-}_{j,k,l}\right) \quad , \tag{3.69}$$

in which mean and covariance are obtained in the prediction step from the previous time instance $l-1$ through the prediction in the Kalman filter

$$\begin{aligned} \hat{\mathbf{a}}^{-}_{j,k,l} &= \tilde{\mathbf{F}}_{j,k,l}\hat{\mathbf{a}}_{j,k,l-1} \quad , & (3.70)\\ \tilde{\mathbf{P}}^{-}_{j,k,l} &= \tilde{\mathbf{F}}_{j,k,l}\tilde{\mathbf{P}}_{j,k,l-1}\tilde{\mathbf{F}}^{T}_{j,k,l} + \tilde{\mathbf{Q}}_{j} \quad . & (3.71) \end{aligned}$$

The matrices $\mathbf{F}_{j,k,l}$ and $\mathbf{Q}_j$ follow directly from (3.20) and compute with

$$\begin{aligned} \mathbf{F}_{j,k,l} &= \operatorname{diag}\left([e^{-j2\pi f_0 L T_s \dot{\tau}_{0,j,k,l}}, \ldots, e^{-j2\pi f_0 L T_s \dot{\tau}_{N_m,j,k,l}}]\right) \quad , & (3.72)\\ \mathbf{Q}_{j} &= \operatorname{diag}\left([\sigma^2_{0,j,a_i}, \ldots, \sigma^2_{N_m,j,a_i}]\right) \quad . & (3.73) \end{aligned}$$

In difference to the range-based approach the delay rate of the LOS path is expressed via the geometry-weighted superposition of the position-domain equivalents

$$\dot{\tau}_{0,j,k,l} = d_{j,1}v^{r}_{x,k,l} + d_{j,2}v^{r}_{y,k,l} + d_{j,3}v^{r}_{z,k,l} + \dot{\tau}^{r}_{k,l} \quad , \tag{3.74}$$

where according to (2.3) $d_{m,n}$ corresponds to the matrix element a row m and column n of the satellite geometry matrix $\mathbf{D}$. In accordance to the range-based formulation the evaluation of (3.26) is performed through the Kalman filter update equations and the a posteriori PDF becomes

$$p(\mathbf{a}_{j,k,l}|\mathbf{Z}_{j,k,l}, \mathbf{e}_{j,k,l}, \boldsymbol{\xi}_{k,l}) = \mathcal{N}\left(\hat{\mathbf{a}}_{j,k,l}, \tilde{\mathbf{P}}_{j,k,l}\right) \quad , \tag{3.75}$$

with mean and covariance according to

$$\begin{aligned} \hat{\mathbf{a}}_{j,k,l} &= \hat{\mathbf{a}}^{-}_{j,k,l} + \tilde{\mathbf{K}}_{j,k,l}\left(\mathbf{z}_{j,k,l} - \tilde{\mathbf{S}}_{j,k,l}\hat{\mathbf{a}}^{-}_{j,k,l}\right) \quad , & (3.76)\\ \tilde{\mathbf{P}}_{j,k,l} &= \left(\mathbf{I} - \tilde{\mathbf{K}}_{j,k,l}\tilde{\mathbf{S}}_{j,k,l}\right)\tilde{\mathbf{P}}^{-}_{j,k,l} \quad , & (3.77) \end{aligned}$$

with the Kalman gain

$$\tilde{\mathbf{K}}_{j,k,l} = \tilde{\mathbf{P}}^{-}_{j,k,l}\tilde{\mathbf{S}}^{T}_{j,k,l}\left(\tilde{\mathbf{S}}_{j,k,l}\tilde{\mathbf{P}}^{-}_{j,k,l}\tilde{\mathbf{S}}^{T}_{j,k,l} + \mathbf{R}_j\right)^{-1} \quad , \tag{3.78}$$

the measurement noise matrix $\mathbf{R}_j = \sigma^2_j \cdot \mathbf{I}$, and $\mathbf{S}_{j,k,l} = \mathbf{S}_j(\boldsymbol{\tau}_{j,k,l})$.

Estimation of Path Activity Since the estimation of the path activity $\mathbf{e}_{j,k,l}$ follows (3.67), the conditional a posteriori PDF with respect of the path activity states is given by

$$\begin{aligned} &p(\mathbf{e}_{j,k,l}|\mathbf{Z}_{j,k,l}, \boldsymbol{\xi}_{k,l}) = \\ &\qquad \frac{p(\mathbf{z}_{j,k,l}|\mathbf{Z}_{j,k,l-1}, \mathbf{e}_{j,k,l}, \boldsymbol{\xi}_{k,l})}{p(\mathbf{z}_{j,k,l}|\mathbf{Z}_{j,k,l-1}, \boldsymbol{\xi}_{k,l})} p(\mathbf{e}_{j,k,l}|\mathbf{Z}_{j,k,l-1}, \boldsymbol{\xi}_{k,l}) \quad . \end{aligned} \tag{3.79}$$

In accordance to the range-based approach the discrete activity state space is estimated by an optimal grid-based filter. Hence the prediction (2.41) simplifies to the evaluation of the sum

$$\begin{aligned} &p(\mathbf{e}_{j,k,l}|\mathbf{Z}_{j,k,l-1},\boldsymbol{\xi}_{k,l}) = \\ &\quad \sum_{\mathbf{e}_{j,k,l-1}} p(\mathbf{e}_{j,k,l}|\mathbf{e}_{j,k,l-1},\mathbf{Z}_{j,k,l-1},\boldsymbol{\xi}_{k,l})p(\mathbf{e}_{j,k,l-1}|\mathbf{Z}_{j,k,l-1},\boldsymbol{\xi}_{k,l}) \ . \end{aligned} \tag{3.80}$$

The transition density with respect to the activity states is given by (3.18) and (3.19) and depends therefore on the realization of the path transition according to

$$\begin{aligned} &p(\mathbf{e}_{j,k,l}=\bar{\mathbf{e}}_{j,k,l}|\mathbf{e}_{j,k,l-1}=\bar{\mathbf{e}}_{j,k,l-1},\mathbf{Z}_{j,k,l-1},\boldsymbol{\xi}_{k,l}) = \\ &\quad (p_{\text{offon}})^{N_{\text{offon}}} \cdot (p_{\text{onoff}})^{N_{\text{onoff}}} \cdot (1-p_{\text{offon}})^{N_{\text{offoff}}} \cdot (1-p_{\text{onoff}})^{N_{\text{onon}}} \ , \end{aligned} \tag{3.81}$$

where N_{offon}, N_{onoff}, N_{offoff}, and N_{onon} follow from the number of switching paths as defined in Section 3.2.2. The marginal likelihood value used in the update step is given by the solution of the integral

$$\begin{aligned} &p(\mathbf{z}_{j,k,l}|\mathbf{Z}_{j,k,l-1},\mathbf{e}_{j,k,l},\boldsymbol{\xi}_{k,l}) = \\ &\quad \int_{\mathbf{a}_{j,k,l}} p(\mathbf{z}_{j,k,l}|\mathbf{Z}_{j,k,l-1},\mathbf{a}_{j,k,l},\mathbf{e}_{j,k,l},\boldsymbol{\xi}_{k,l})p(\mathbf{a}_{j,k,l}|\mathbf{Z}_{j,k,l-1},\mathbf{e}_{j,k,l},\boldsymbol{\xi}_{k,l})d\mathbf{a}_{j,k,l} \ , \end{aligned} \tag{3.82}$$

which equals in correspondence to (3.40) the Gaussian density

$$p(\mathbf{z}_{j,k,l}|\mathbf{Z}_{j,k,l-1},\mathbf{e}_{j,k,l},\boldsymbol{\xi}_{k,l}) = \mathcal{N}\left(\tilde{\mathbf{S}}_{j,k,l}\hat{\mathbf{a}}^{-}_{j,k,l},\tilde{\mathbf{S}}_{j,k,l}\tilde{\mathbf{P}}^{-}_{j,k,l}\tilde{\mathbf{S}}^{T}_{j,k,l}+\mathbf{R}_j\right) \ . \tag{3.83}$$

Joint Estimation of Receiver and Channel Parameters So far the estimation has been quite similar to the range-based approach. In accordance the remaining parts of the state vector in the form of $\boldsymbol{\xi}_{k,l}$ are now estimated by a particle filter. Corresponding to (3.67) the a posteriori PDF with respect to $\boldsymbol{\xi}_{k,l}$ computes with

$$p(\boldsymbol{\xi}_{k,l}|\mathbf{Z}_{j,k,l}) = \frac{\prod_{j=1}^{M} p(\mathbf{z}_{j,k,l}|\mathbf{Z}_{k,l-1},\boldsymbol{\xi}_{k,l})}{p(\mathbf{z}_{k,l}|\mathbf{Z}_{k,l-1})} p(\boldsymbol{\xi}_{k,l}|\mathbf{Z}_{k,l-1}) \ . \tag{3.84}$$

Again the SIR-PF algorithm is proposed to implement the estimator, where the a posteriori PDF at step k is represented as a sum, and is specified by a set of N_p particles:

$$p(\boldsymbol{\xi}_{k,l}|\mathbf{Z}_{k,l}) \approx \sum_{\mu=1}^{N_p} w^{\mu}_{k,l}\delta(\boldsymbol{\xi}_{k,l}-\boldsymbol{\xi}^{\mu}_{k,l}) \ , \tag{3.85}$$

where each particle with index μ has a state $\boldsymbol{\xi}^{\mu}_{k,l}$ and has a weight $w^{\mu}_{k,l}$. The key step in which the measurement for instance k is incorporated, is in the calculation of the weight $w^{\mu}_{k,l}$, which for the position domain SIR-PF is the product of the marginalized likelihood functions:

$$w^{\mu}_{k,l} \propto w^{\mu}_{k,l-1} \prod_{j=1}^{M} p(\mathbf{z}_{j,k,l}|\mathbf{Z}_{j,k,l-1},\boldsymbol{\xi}^{\mu}_{k,l}) \ . \tag{3.86}$$

The characterization of the system process enters in the algorithm when at each time instance k, the state of each particle $\boldsymbol{\xi}^{\mu}_{k,l}$ is drawn randomly from the proposal distribution; i.e. from $p(\boldsymbol{\xi}_{k,l}|\boldsymbol{\xi}^{\mu}_{k,l-1})$, which corresponds to drawing values for $\mathbf{n}_r$, $\mathbf{n}_v$, n_τ, $n_{\dot{\tau}}$, $n_{j,\tau}$, $n_{j,\dot{\tau}}$ and n_{j,τ_i}. The marginal likelihood values, which are required to update the particle filter, are given by summing up the weighted marginal likelihood values of all path activity hypotheses:

$$\begin{aligned} p(\mathbf{z}_{j,k,l}|\mathbf{Z}_{j,k,l-1},\boldsymbol{\xi}_{k,l}) = \\ \sum_{\mathbf{e}_{j,k,l}} p(\mathbf{z}_{j,k,l}|\mathbf{Z}_{j,k,l-1},\mathbf{e}_{j,k,l},\boldsymbol{\xi}_{k,l})p(\mathbf{e}_{j,k,l}|\mathbf{Z}_{j,k,l-1},\boldsymbol{\xi}_{k,l}) \ . \end{aligned} \tag{3.87}$$

Modified Proposal Density Since the number of dimensions that are to be covered by the position-based estimator can be quite large, the proposal density used in the SIR-PF, i.e. in the given implementation the density $p(\boldsymbol{\xi}_{k,l}|\boldsymbol{\xi}^{\mu}_{k,l-1})$, is only a weak choice. Though the selection of a better proposal is generally difficult, the previously introduced range-based approach may be exploited for that purpose. The basic idea is to employ the set of range-based estimators in order to construct an improved proposal density for the high-dimensional position-domain estimator. Given the approximate a posteriori PDF $\tilde{p}(\boldsymbol{\xi}_{k,l}|\mathbf{Z}_{k,l})$ according to (3.49), an improved proposal density is given by the function

$$q(\boldsymbol{\xi}_{k,l}|\boldsymbol{\xi}^{\mu}_{k,l-1},\mathbf{Z}_{k,l}) \propto p(\boldsymbol{\xi}_{k,l}|\boldsymbol{\xi}^{\mu}_{k,l-1})\tilde{p}(\boldsymbol{\xi}_{k,l}|\mathbf{Z}_{k,l}) \ . \tag{3.88}$$

In this case the update of the particle filter computes according to (2.73) with

$$w^{\mu}_{k,l} \propto w^{\mu}_{k,l-1}\frac{p(\boldsymbol{\xi}^{\mu}_{k,l}|\boldsymbol{\xi}^{\mu}_{k,l-1})\prod_{j=1}^{M}p(\mathbf{z}_{j,k,l}|\mathbf{Z}_{j,k,l-1},\boldsymbol{\xi}^{\mu}_{k,l})}{q(\boldsymbol{\xi}^{\mu}_{k,l}|\boldsymbol{\xi}^{\mu}_{k,l-1},\mathbf{Z}_{k,l})} \ . \tag{3.89}$$

3.4 Comparison of Approaches

The complexity of the estimator is a crucial criterion for implementation. Though the Rao-Blackwellized formulation allows to cover some states with optimal analytical estimators, each particle in the superordinate particle filter has to carry its own conditional estimators. In particular the proposed two-fold Rao-Blackwelization that is illustrated for both approaches in Figure 3.5 requires a large number of Kalman filters, which grows exponentially with the number of considered multipath replica. Another relevant parameter with respect to the complexity is the number of states that are to be covered by the particle filter, since the number of required particles is coarsely growing exponentially with the number of states. Nevertheless state dimensions with little dynamics, limited range, or those states, which can be inferred accurately, usually require only a smaller number of hypotheses to be covered. The advantage in the channel estimation for navigation is that the region in which the multipath delays are of interest due to their impact on the receiver is commonly limited to the duration of a chip of the CDMA signal. Thus the state space for a GPS C/A multipath signal can be limited from the LOS delay up to 1 μs after the LOS delay, which corresponds to 300 m. Furthermore for a fair comparison of the range- and position-based method it is crucial to compare both estimators under the same conditions, i.e. the assumptions that are taken on the process dynamics must be equivalent for both approaches.

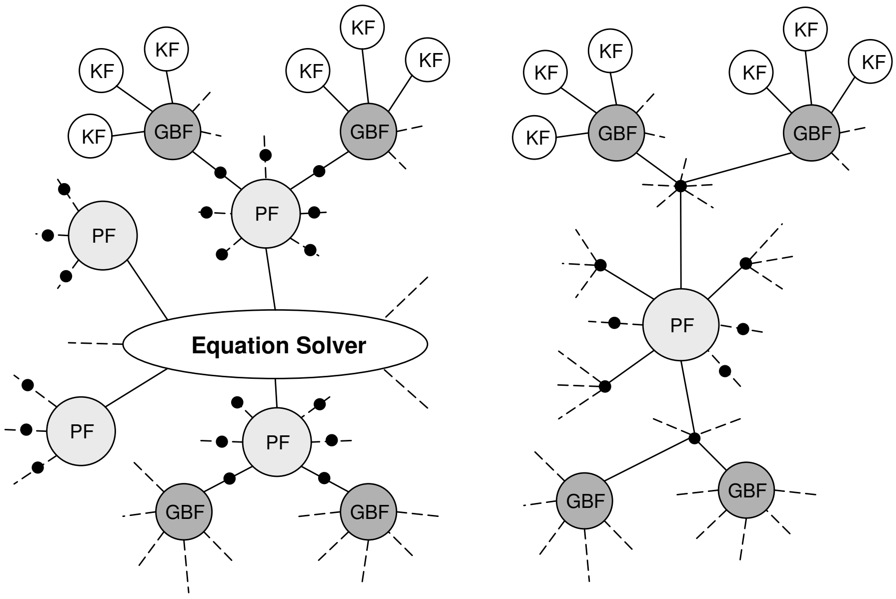

(a) Range-based (b) Position-based

Figure 3.5: Structure of the range-based (3.5(a)) and the position-based estimator (3.5(b)). In the range-based formulation there is a separate particle filter for each received satellite, and each particle (black dots) carries a grid-based filter and several Kalman filters. In the position-based formulation there is only a single particle filter, in which each of the particles carries several grid-based filters with associated Kalman filters.

3.4.1 Equivalent Dynamic Modeling

In the range-based approach the LOS delay dynamics are driven by the noise sources $n_{0,j,\tau}$ and $n_{0,j,\dot{\tau}}$, whereas in the position-based approach the movement is driven by the noise processes $\mathbf{n}_r$ and $\mathbf{n}_v$. Since the common clock process is already adequately considered in both models through the noise processes n_τ and $n_{\dot{\tau}}$ the remaining task is to obtain an equivalent model for the LOS dynamics in the range-based approach, given the the position-based characterization of (3.50) and (3.51). An equivalent formulation is now possible thanks to (2.3), since the dynamics may be linearized locally. Using the satellite geometry matrix $\mathbf{D}$, where $d_{m,n}$ corresponds to the matrix element at row m and column n, the noise processes at the range-based model are a superposition of the noise processes driving the evolution of the position-based model and may thus be expressed as

$$n_{0,j,\tau} = d_{j,1}n_x + d_{j,2}n_y + d_{j,3}n_z \ , \tag{3.90}$$
$$n_{0,j,\dot{\tau}} = d_{j,1}n_{\dot{x}} + d_{j,2}n_{\dot{y}} + d_{j,3}n_{\dot{z}} \ , \tag{3.91}$$

and the variances of the Gaussian noise sources $n_{0,j,\tau}$ and $n_{0,j,\dot{\tau}}$ can be computed accordingly via

$$\sigma^2_{0,j,\tau} = d^2_{j,1}\sigma^2_x + d^2_{j,2}\sigma^2_y + d^2_{j,3}\sigma^2_z \ , \tag{3.92}$$
$$\sigma^2_{0,j,\dot{\tau}} = d^2_{j,1}\sigma^2_{\dot{x}} + d^2_{j,2}\sigma^2_{\dot{y}} + d^2_{j,3}\sigma^2_{\dot{z}} \ . \tag{3.93}$$

3.4.2 Estimator Complexity

For the pseudorange-based estimation the number of required particle filters corresponds to the number of received satellites M, as for each received satellite signal a separate particle filter is required. The dimension of the particle filter is then given by the maximum number of required multipath replica. For the LOS path and each replica delay and delay rate are to be estimated. Thus the dimension to be covered by each particle filter is $2N_m + 2$. Thereby at least the state space with respect to the multipath delays is limited. In difference the position-based estimator has to consider at least eight states: three-dimensional position and velocity, the receiver clock bias and the receiver's clock drift. Additionally the multipath delays and and their rates need to be estimates for each of the received satellites, which requires the high number of $8 + 2MN_m$ states to be covered by the central particle filter. In both approaches each particle needs to carry its grid-based filters to estimate the path activities. In the range-based approach there is only a single grid-based filter per particle, whereas in the position-based estimator there are M grid-based filters per each particle. Hence the overall number of required grid-based filters in the receiver equals MN_p in both approaches. Their respective dimension is 2^{N_m}, because the LOS path is assumed to be always active. The number of Kalman filters computes accordingly with $MN_p2^{N_m}$, since each activity hypothesis is required to carry its own Kalman filter, and consequently the overall number of required Kalman filters is the same for the range- and the position-based formulation. The dimension of the Kalman filters depends thereby on the number of active paths and is in the range of $1, \ldots, N_m + 1$. In the overall implementation at each dimension there are $MN_p\begin{pmatrix} N_m \\ m \end{pmatrix}$ Kalman filters of dimension $m + 1$, where m corresponds to the number of active paths. Actually both approaches, range-based and position-based estimation, have a quite similar structure, which is highlighted by the illustration in Figure 3.5.

3.4.3 A Posteriori Cramer-Rao Bounds

The position-based estimator seems to be the favorable approach from the theoretical point of view, since it implements straightforwardly the Bayesian approach to estimate the position directly from the received signals instead of estimating the time delays and the position separately. Thus it is expected that the position-based estimator is superior, which is confirmed when calculating the PCRB as illustrated in Figure 3.6. In the investigated scenario the estimation performance is more than doubled when using the position-based formulation.

3.5 Results

To assess the introduced algorithms computer simulations were carried out for different propagation conditions. For conceptual verification and for comparison of the range-based and the position-based approach these scenarios include the simple additive white Gaussian noise (AWGN) channel and the static multipath channel, which is typically used to assess the performance of multipath mitigation algorithms for GNSS receivers. In difference to well-known earlier introduced algorithms [vDFF92, vNSFT94, SA06a, CFPFR06] the accompanying results presented here include a performance analysis for realistic propagation conditions, which

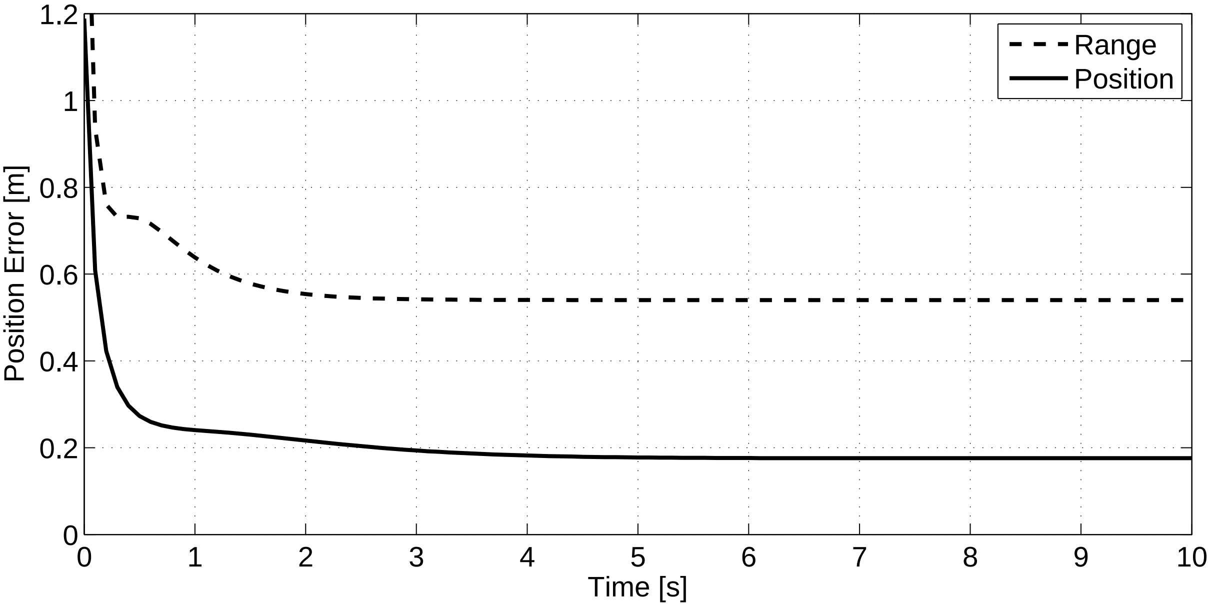

Figure 3.6: PCRB of the range-based and the position-based estimator. The position-based approach outperforms the range-based approach, since it omits the intermediate step of range-wise independent time delay estimation before the position computation.

are resembled by the latest available cutting-edge highly realistic pedestrian navigation channel model [LS09] as well as by sequences of real measured channel data [SL04].

3.5.1 AWGN Channel

The AWGN channel is the by far simplest channel model. Assuming that the received signal is the result of the convolution of the transmitted signal with the channel impulse response (CIR) $h(t)$ superimposed by white Gaussian noise, the CIR of the AWGN channel is given by

$$h(t) = a_0 \cdot e^{-j2\pi f_0 \tau_0(t)} \delta(t - \tau_0(t)) \ , \tag{3.94}$$

in which the complex amplitude of the channel response is determined by the nominal amplitude a_0 and the phase rotation due to the channel delay, which follows from the basics of electromagnetic wave propagation. Though the AWGN channel is not representative for typical pedestrian propagation environments such as urban scenarios, which are addressed specifically in this thesis, an assessment of the introduced estimation algorithms based on the AWGN channel is still highly valuable. The AWGN channel represents the standard environment, for which conventional navigation receivers are designed for, and represents, since it is actually based on quite optimistic assumptions, the mildest propagation conditions a receiver algorithm has to cope with. In particular for theoretical analysis the well-defined and simple channel offers various advantages, including the feasibility of the calculation of accuracy bounds such as the CRLB or the PCRB. As pointed out in section 3.4.3 the position-based estimator is favorable from the theoretically point of view, since it optimally takes into account the mutual correlations of the received signals. Nevertheless the complexity of the position-based approach tends to be higher, since more states have to be estimated simultaneously. This has a serious impact on the

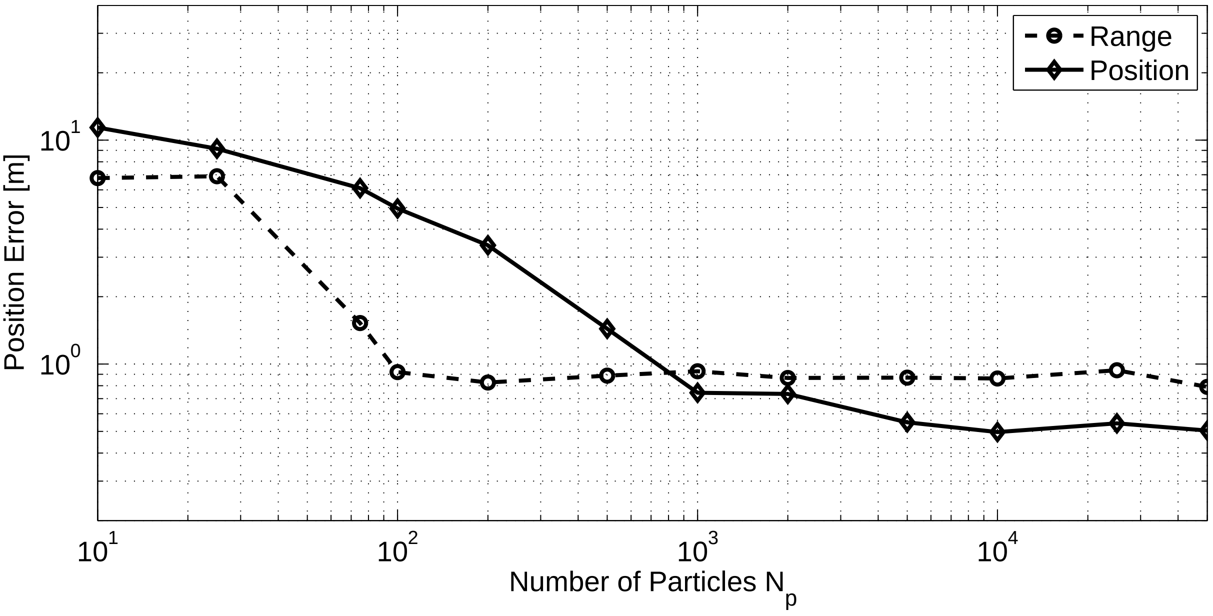

Figure 3.7: Performance comparison of the range-based and the position-based approach in a four satellite scenario. Due to the smaller state space only few (≈100) particles are needed for the range-based approach to reach convergence, since with more particles its performance does not improve further. Nevertheless for more than 1.000 particles the position-based approach is able to outperform the range-based estimator as it is expected theoretically by the PCRB (see Figure 3.6). With more than 10.000 particles there is no further improvement for the position-based estimator.

number of particles that are required to implement the estimator, as the discrete particles need to cover the high-dimensional state-space properly to minimize the error due to the sub-optimal particle filter implementation of the Bayesian recursion. The expected behavior is confirmed by the result of the computer simulations, which are shown in Figure 3.7. The performance of the range-based estimator tends to saturate already for more than 100 particles, since a further increase in the number of particles does not improve the performance any more. Since for a small amount of particles the position-based approach lacks of a sufficient number of particles its performance is even worse than the range-based approach. The results reveal that at least 1000 particles are required for the position-based estimator to achieve a performance improvement compared to the range-based estimator, as it is predicted by the theoretical performance bounds (see Figure 3.6). Thus the theoretically feasible advance is subject to a trade-off between estimator performance and complexity (in terms of the required number of particles).

3.5.2 Static Multipath Channel

A further common channel for the assessment of satellite navigation receiver signal processing algorithms is the static multipath (SMP) channel. In the simple form of the SMP channel the CIR of the conventional AWGN channel is extended by an additional delayed echo tap, such that the CIR of the SMP channel becomes

$$h(t) = a_0 e^{-j2\pi f_0 \tau_0(t)} \delta(t - \tau_0(t)) + a_1 e^{-j2\pi f_0 (\tau_0(t) + \tau_{\mathrm{mp}})} \delta(t - \tau_0(t) - \tau_{\mathrm{mp}}) \ , \tag{3.95}$$

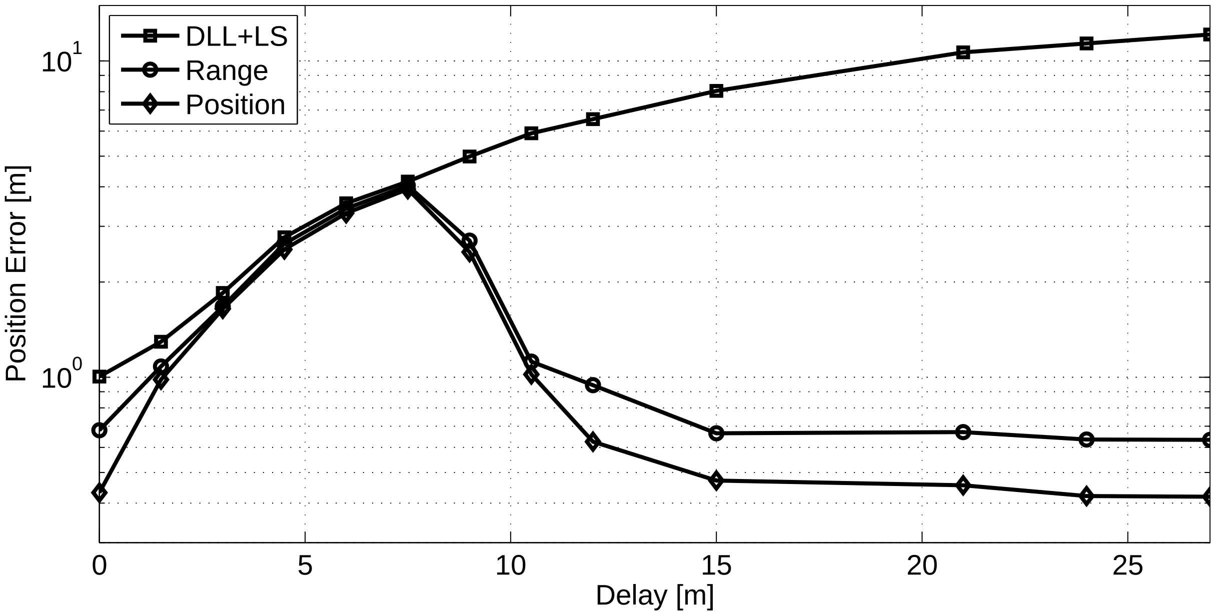

Figure 3.8: Positioning error for the conventional receiver using narrow spaced DLLs and LS estimation, the range-based and the position-based estimator in a static multipath scenario with four received satellites. For very short echoes ($\tau_{\mathrm{m}p} < 7$ m) the mitigation algorithms are not able to resolve the two paths any more. Once the paths can be resolved the advanced estimation methods perform much better than the conventional approach. Thereby the position-based estimator is superior with respect to the error performance.

with the nominal multipath amplitude a_1 and the static multipath delay $\tau_{\mathrm{m}p}$. For the simulations presented in the following a four satellite scenario is assumed, in which only one of the four ranges is assumed to be affected by the multipath channel and the others are received in AWGN conditions. According to the conventional error envelope function the results presented in Figure 3.8 are shown for a fixed SMR in terms of the positioning error versus the relative delay of the multipath component. The error behavior illustrated in Figure 3.8 reveals the benefit of the advanced estimation algorithms compared to the position estimation in a conventional receiver. For multipath delays that are larger than 15 m, which corresponds to the 20th part of a chip for the simulated GPS C/A signal, the sequential estimators mitigate the impact of the multipath replica to a large extent. Thereby the position-based approach is slightly superior compared to the range-based approach. As illustrated in Figure 3.9 for delays in the region between 7 m and 15 m the estimators are operating in the region, where a distinct detection of the multipath component is not entirely feasible, and thus the error is increased. For delays smaller than 7 m the estimation algorithms are not capable to resolve the two separate paths any more and thus the average a posteriori detection probability is almost zero. Interestingly in the investigated four-satellite scenario the average a posteriori detection probabilities of the range- and the position-based estimator almost coincide, which leads to the conclusion that, though it is expected generally, the multipath detection in the position-based estimator benefits only to a negligible extent from the other received signals in the addressed scenario.

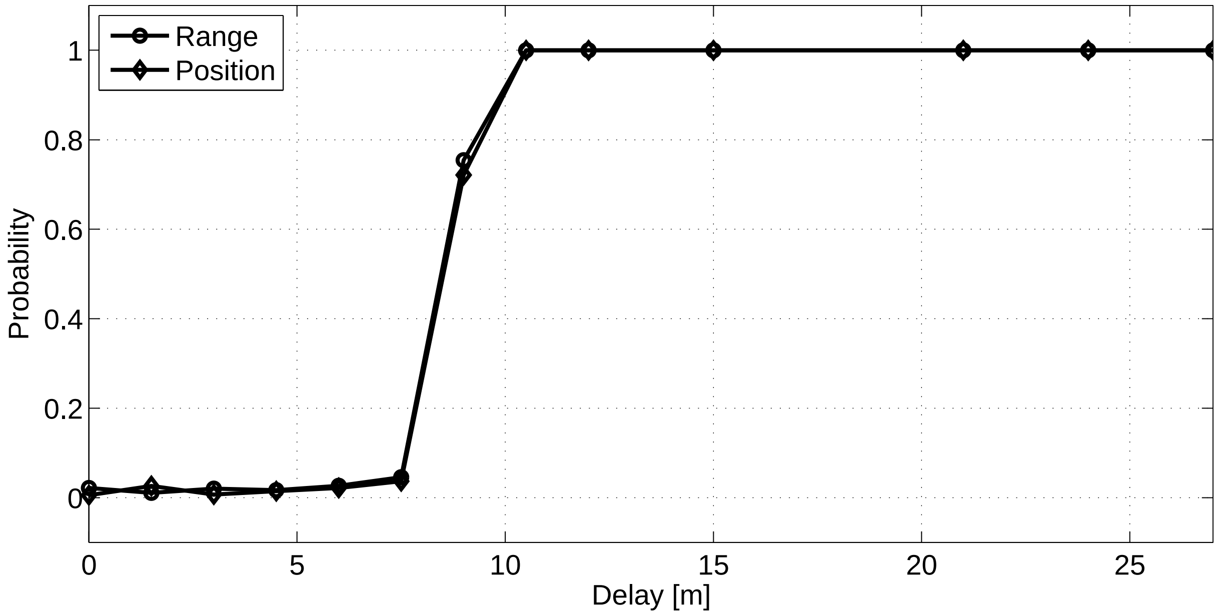

Figure 3.9: Average a posteriori multipath detection probability $p(e_{1,1,k}|\mathbf{Z}_k)$ for the the range-based and the position-based estimator in a static multipath scenario with four received satellites. For very short echoes ($\tau_{\mathrm{m}p} < 7$ m) the mitigation algorithms are not able to detect the multipath component any more.

3.5.3 Pedestrian Channel Model

During the last decade the German Aerospace Center (DLR) has derived and published several satellite navigation channel models based on the detailed analysis of measurement data [SL03, SL04, SLF^{+}04, LS05]. These models represent the latest state of research in this field and have already or are about to become standardized reference models at the International Telecommunication Union (ITU) [IR03, IR07]. Whereas the initial models were devoted to aeronautical, land mobile and vehicular scenarios the latest extensions are capable of emulating propagation conditions that are typical for pedestrian applications [LS09]. To assess the performance of the introduced algorithms under realistic conditions computer simulations have been carried out. The used multipath channel was generated from the public available channel model published in [LS09]. The channel model is composed of a stochastic and a deterministic part. The simulated user moves within an artificial scenery that is generated from statistical processes. The deterministic scenery comprises obstacles such as house fronts, trees, and lamp posts, which are used to compute the blockage and shadowing of the LOS path based upon geometrical considerations and statistical processes. The multipath components of the channel model are generated from statistical processes that place reflectors at positions whose statistical distributions have been determined empirically from the measured data. The overall structure of the model is illustrated in Figure 3.10. The mixed statistical and deterministic modeling leads to a highly realistic modeling of the channel dynamics, since the impact of the user's movement profile on the channel dynamics (e.g. the Doppler bandwidth) and on the LOS obtrusion by obstacles is reflected adequately. Very characteristic for this highly realistic channel model is the high number of reflectors that may occur simultaneously, which can reach up to fifty si-

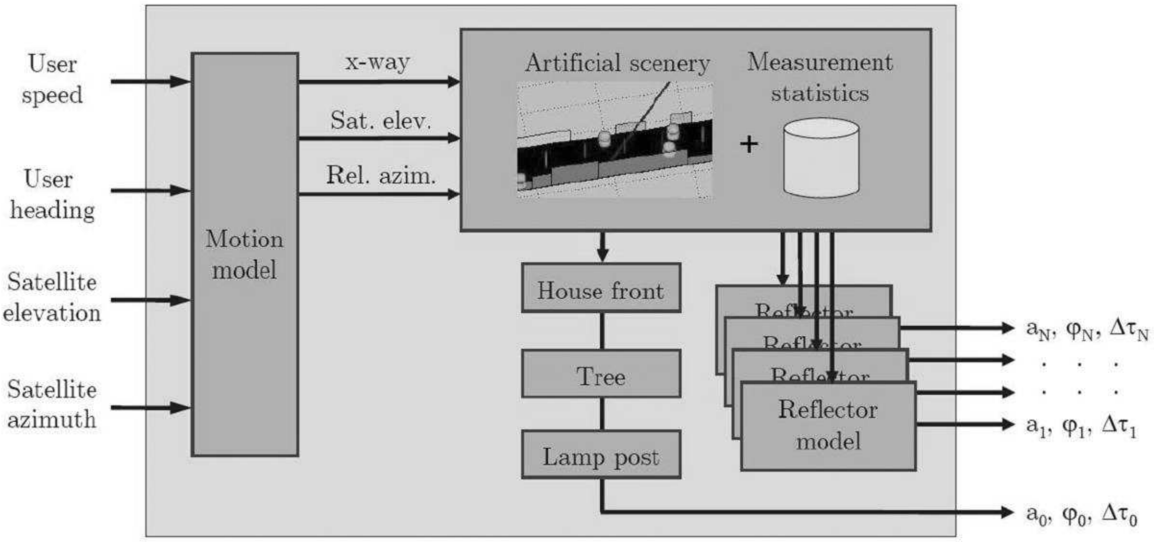

Figure 3.10: Structure of the pedestrian channel model according to [LS09]

multaneous echoes and more. Since most of these echoes have short life cycles and are very weak in power, it is of particular interest how many multipath components an advanced channel estimating receiver will have to take into account in order to reach its optimal performance. For that reason in the following simulations the introduced algorithms have not been compared only to the conventional DLL receiver, but also the impact of the parameter N_m has been studied. For the scope of this analysis at first only simulations on a single range-level have been carried out. The user movement profiles used for the simulation are given in the Appendix in Section B.1.4. The results of the simulations are illustrated in Figure 3.11 in terms of the cumulative density function (CDF) of the LOS estimation error. Due to LOS blockage and shadowing large errors can occur occasionally for the conventional DLL receiver. It can be seen clearly that the use of the sequential estimation algorithm enhances the performance significantly, even if only a single LOS path ($N_m = 0$) is considered by the estimation algorithm. This is due to the dynamic model that underlies the recursive estimation procedure and which prohibits the LOS estimate to have errors that become on average as large as those of the conventional DLL receiver. For the actual mitigation algorithms ($N_m > 0$), which are capable of detecting and tracking multipath and which thus are able to remove the estimation bias due to multipath, it can be observed that the estimation performance tends to saturate quickly for $N_m > 1$. Thus the additional complexity that is needed by considering more simultaneous paths may not be justified, given the amount of performance gain. Furthermore the quick performance saturation for $N_m > 1$ shows that the presence of more than a single relevant multipath component tends to happen only rarely and if so, that the simultaneous tracking of two or more multipath replica leads only to a small amount of performance improvement in the average error statistics.

As addressed in the previous sections the position-based approach can achieve theoretically better performance compared to the range-based approach, given a sufficient number of particles and thus complexity is spent on its implementation. To quantify the benefit under environments that are more realistic than the AWGN or SMP channel, the results illustrated in Figure 3.12 present a comparison of the position- and range based estimator under the propagation condi-

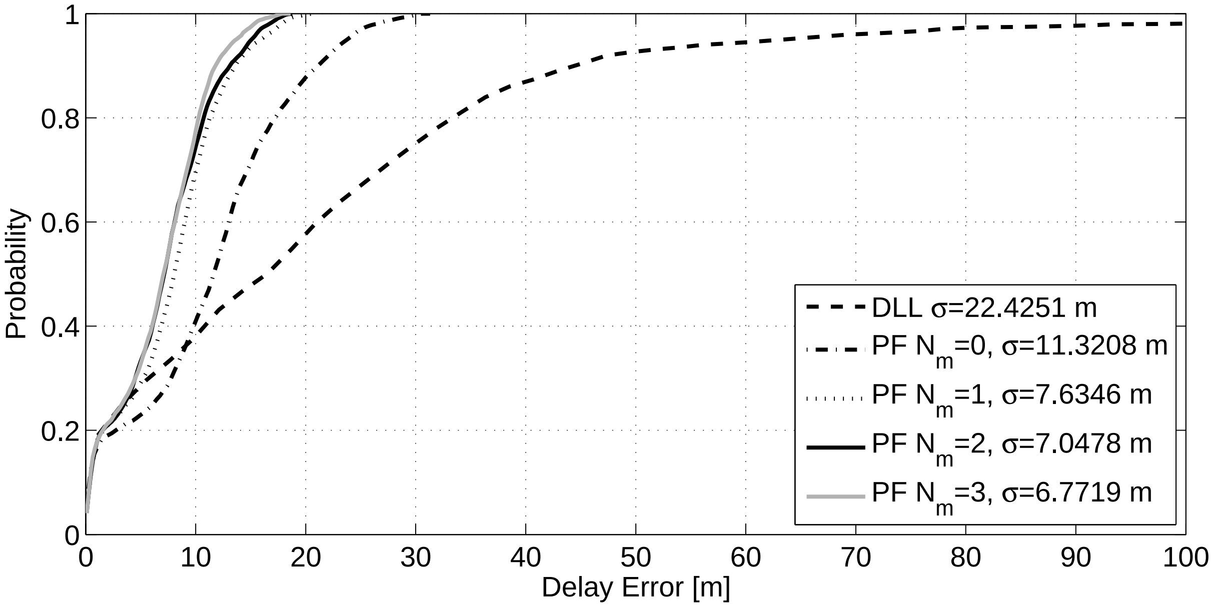

Figure 3.11: Cumulative normalized histogram of the LOS delay estimation error of the range-based approach in comparison with a conventional narrow correlator DLL using the pedestrian channel model. Already without considering multipath the advanced approach is significantly superior. Considering more simultaneously echoes (via N_m) leads to a further improved performance, which tends to saturate rapidly for more than one additional path.

tions that are given by the previously introduced pedestrian channel model. Basically the results confirm the previous ones. Occasionally large errors happen in a conventional receiver, which uses DLLs and a LS position estimator. Due to the exploited dynamic models and the multipath tracking capabilities the two introduced advanced estimators are both superior to the conventional approach. Similar to the AWGN and SMP scenario the results reveal that compared to the range-based estimator the position-based estimator remains still the more elaborated approach, even for the realistic propagation conditions that are given by the pedestrian channel model.

3.5.4 Measured Pedestrian Channel

So far results for the AWGN, SMP, and the DLR pedestrian channel model have been presented to validate the concept of the introduced sequential estimation algorithms. A remaining validation method is the simulation with measured CIRs, which is also known as the concept of the *stored channel*: A channel profile is recorded during a measurement campaign and the stored profile is fed back into the simulation. Though the statistical significance of such simulations is limited, it is the most realistic simulation approach, since the employed channel corresponds to a real world scenario. In Figure 3.13(b) such a recorded channel profile is illustrated [SL04]. It represents the CIR that affects the propagation from a satellite at 10 degrees elevation to a pedestrian user that moves in an urban environment. The profile clearly motivates the pursued algorithmic approach. Discrete echoes due to reflectors such as house fronts are clearly visible. Thereby each echo experiences a typical life-cycle, which is basically determined by the dynamics of the user. The simulations with the stored channel have been carried out for differ-

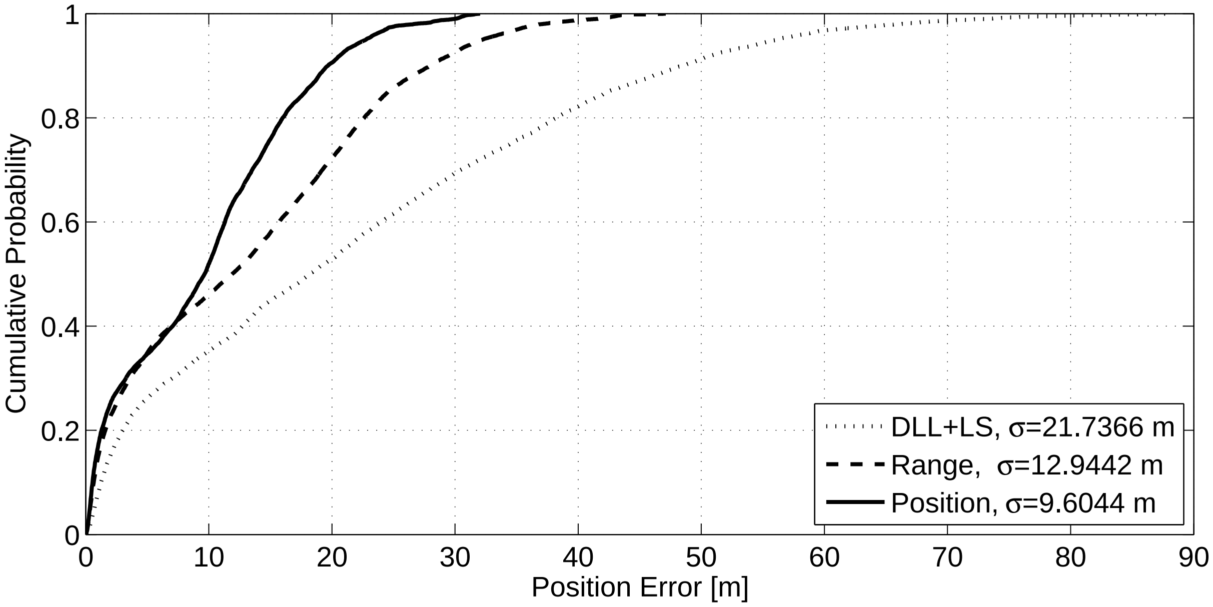

Figure 3.12: Comparison of a conventional narrow correlation receiver and the range- and position-based estimator in a four satellite scenario using the pedestrian channel model. The advanced algorithms allow for a significant improvement of accuracy. The position-based implementation is even more advanced than the range-based approach, in particular for errors that are larger than 10 m.

ent types of modulation schemes that are typical for satellite navigation signals, including the conventional BPSK modulation, which is used for the GPS L1 C/A signal, and the BOC and the composite BOC (CBOC) modulation, which are both candidates for the future European satellite navigation system Galileo [ARHW$^+$07] and the modernization of the GPS navigation signals. The results of the simulations are shown in Figure 3.14. As already observed for the pedestrian channel model the DLL shows occasionally large errors. The performance of the sequential estimation algorithm tends to saturate for $N_m > 1$, irrespective of the signal modulation. Compared to the BPSK signal (Figure 3.14(a)) the BOC(1,1) and CBOC signals (Figures 3.14(b) and 3.14(c)) show improved performance for both the DLL and the estimation algorithm. The detailed comparison of the BOC(1,1) and CBOC performance does not reveal significant differences. Interestingly the results show that the performance gain due to the advanced signals is much smaller for the estimation algorithms. The DLL receiver is able to take large benefit of the BOC(1,1) or CBOC signal. In difference the performance of the estimation algorithms is much more influenced by the channel itself and not by the used modulation, such that the performance is rather independent of the signal waveform.

To illustrate the operation of the sequential estimation algorithm its MMSE estimates of the LOS and multipath delays are depicted in Figure 3.15 and Figure 3.16, which correspond to two typical scenarios a navigation receiver has to cope with in urban environments. The scenario shown in Figure 3.15 corresponds to a situation where several simultaneous echoes arrive at the receiver. The evolution of these echoes shows the typical behavior that can be observed in urban environments, including echoes that are approaching and other echoes that are departing due to the movement of the receiver toward to or away from the reflector. The scenario

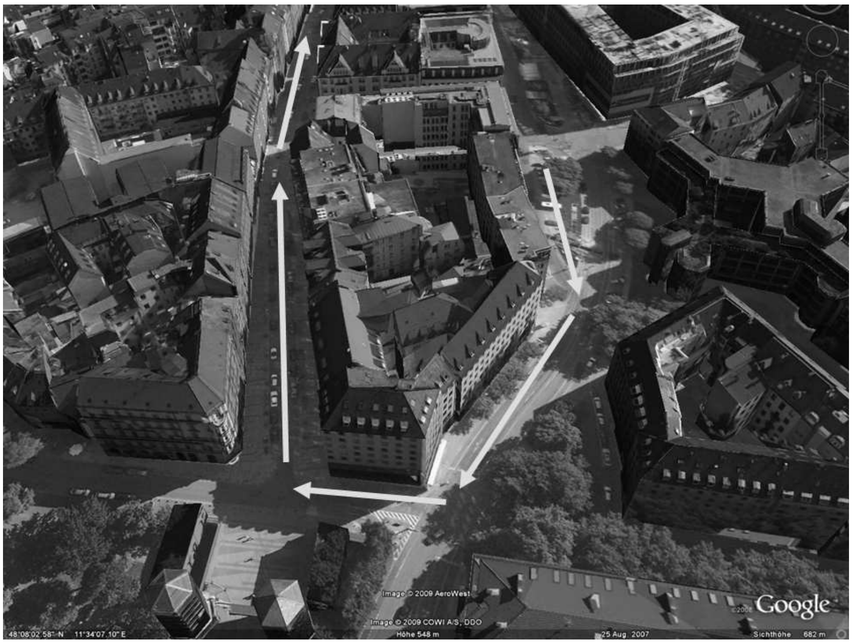

(a) Environment

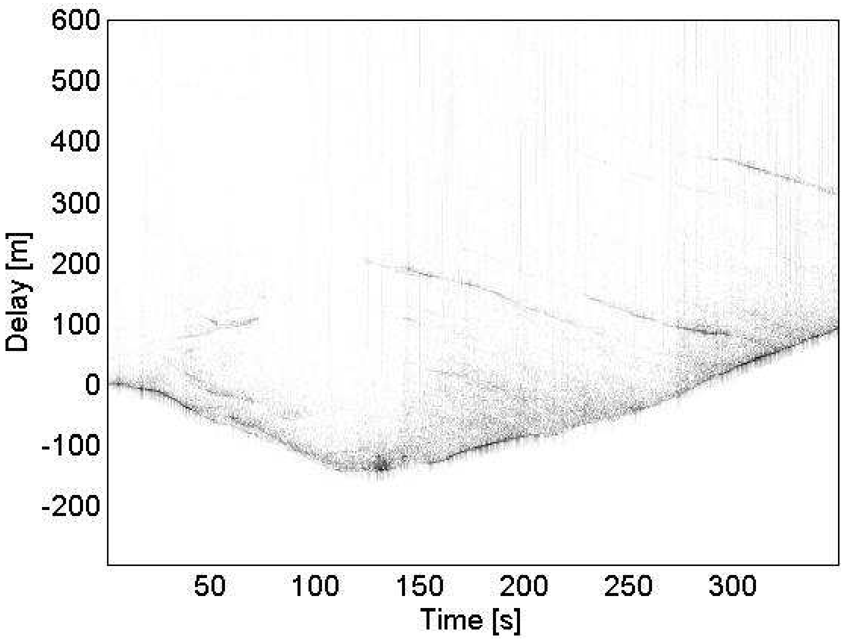

(b) Channel

Figure 3.13: Figure 3.13(b) illustrates the impulse response of a channel, which was measured for a pedestrian moving in the urban environment shown in Figure 3.13(a), where the pedestrian's track is indicated by the arrows (Picture by Google Earth). The view on the scenery corresponds to the direction of the transmitter station. Typical properties of the channel are the long correlation times in the multipath echoes and their clearly observable binding to the user dynamics and the surrounding environment, where reflections at house fronts cause echo traces that persist, approach and depart along with the occasionally shadowed LOS path.

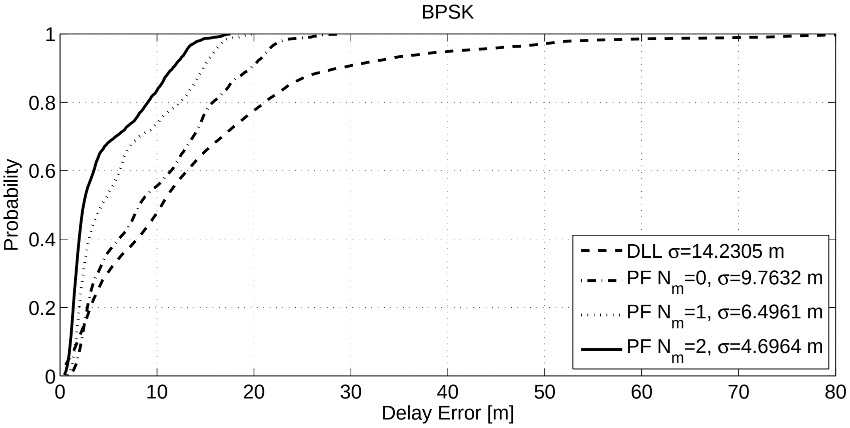

(a) BPSK

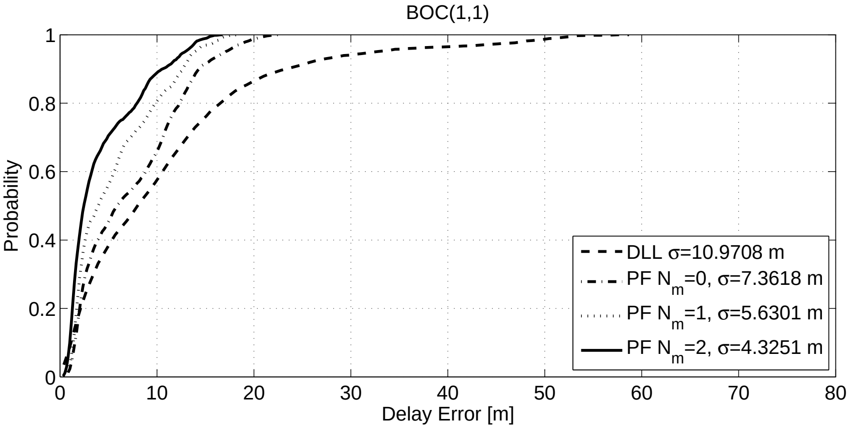

(b) BOC(1,1)

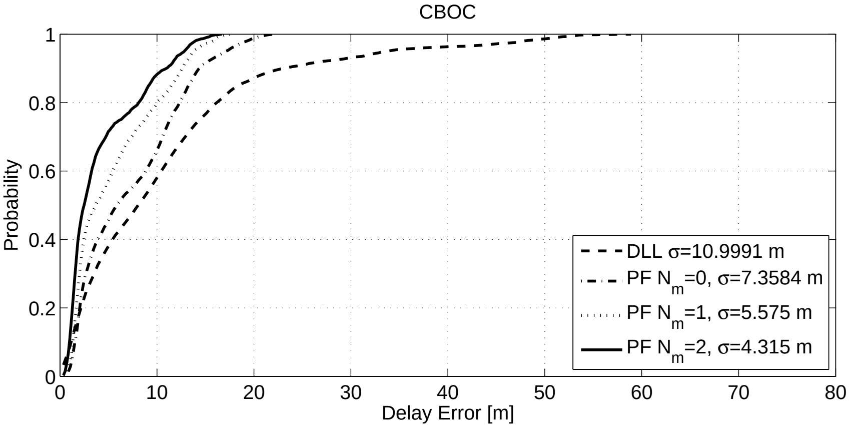

(c) CBOC

Figure 3.14: Comparison of LOS delay estimation error for the BPSK signal 3.14(a), the BOC(1,1) signal 3.14(b) and the CBOC signal 3.14(c) for the measured pedestrian channel scenario corresponding to Figure 3.13(b). The advanced modulations significantly outperform the conventional BPSK signal and the range-based estimators are superior compared to the narrow correlator DLL. As already observed for the channel model an increase of the number of considered paths N_m improves the performance.

illustrated in Figure 3.16 represents a situation where a partially shadowed LOS component is superimposed by a strong multipath signal. Both scenarios reveal the general benefit of the sequential estimation approach compared to the conventional DLL. On the one hand the explicit consideration of the multipath replica in the signal model at the receiver allows to mitigate the multipath errors successfully, on the other hand the exploitation of the constrained dynamic model allows to obtain more smooth and realistic estimates, which do not follow the abrupt changes in the channel such as the DLL does occasionally, e.g. in Figure 3.16 during the period from 275 s to 295 s, which are quite unlikely given the limited dynamics of the pedestrian. In particular this period shows the major drawback of the conventional DLL: Though the DLL implements a low-pass characteristic and thus limits the dynamics it is not able to take into account a real probabilistic and physical model of the receiver dynamics and thus tends to track immediately the strongest present path while neglecting any weaker earlier paths, which are much more likely to be the actual LOS path due to the recent channel history and the limited user dynamics.

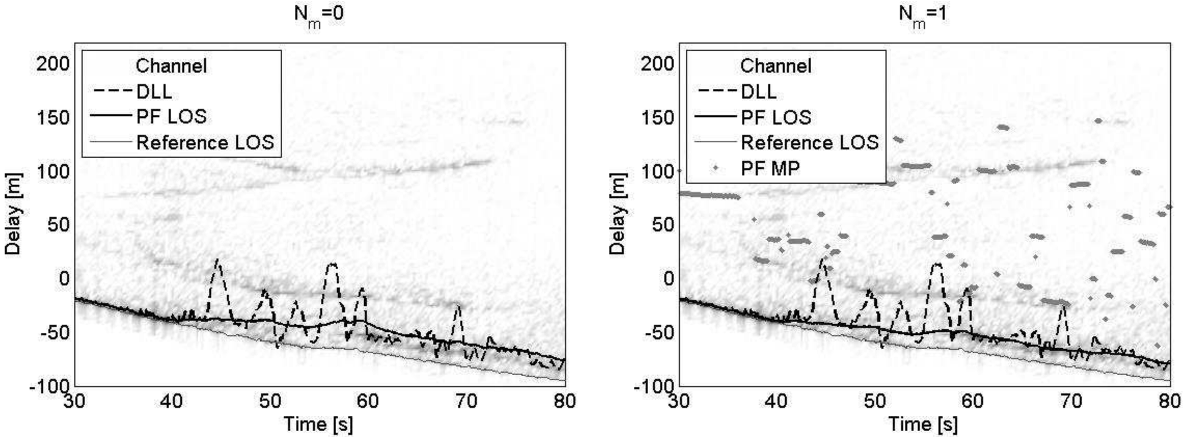

(a) $N_m = 0$ (b) $N_m = 1$

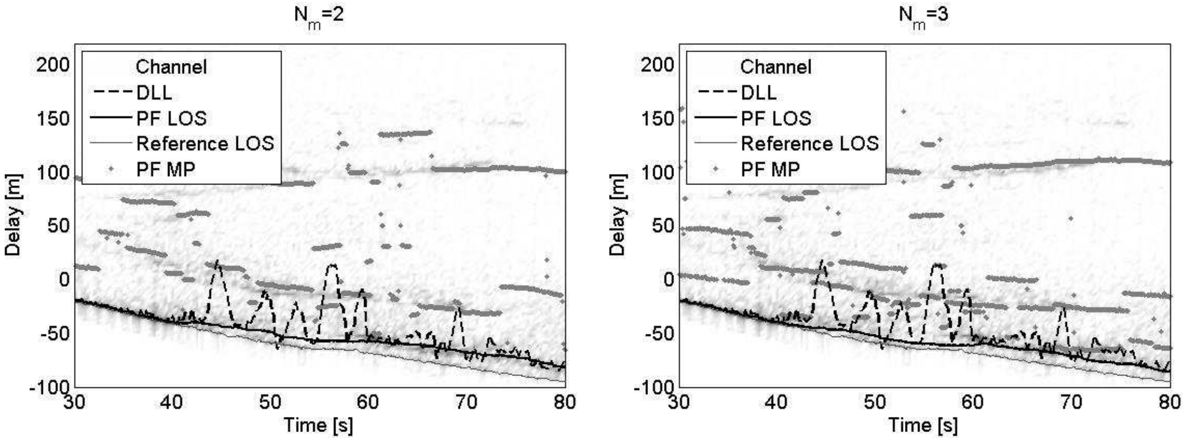

(c) $N_m = 2$ (d) $N_m = 3$

Figure 3.15: The channel estimation algorithm has to cope with several simultaneous multipath replica. The DLL receiver shows the typical multipath errors, whose magnitude varies due to the fading processes of the path amplitudes. If the multipath replica are not taken account by the estimator ($N_m = 0$, Figure 3.15(a)), there are still significant errors, but their magnitude is smaller than the DLL errors, since the dynamic model used in the estimator helps to constrain variation of the LOS estimate. With $N_m = 1$ (Figure 3.15(b)) the number of considered paths is to small to track all replica and thus the multipath delay estimates tend to jump between the respective multipath signals. Once the number of considered replica is sufficient to take into account all present signals ($N_m > 1$, Figures 3.15(c) and 3.15(d)), the estimation algorithm detects and tracks properly the channel.

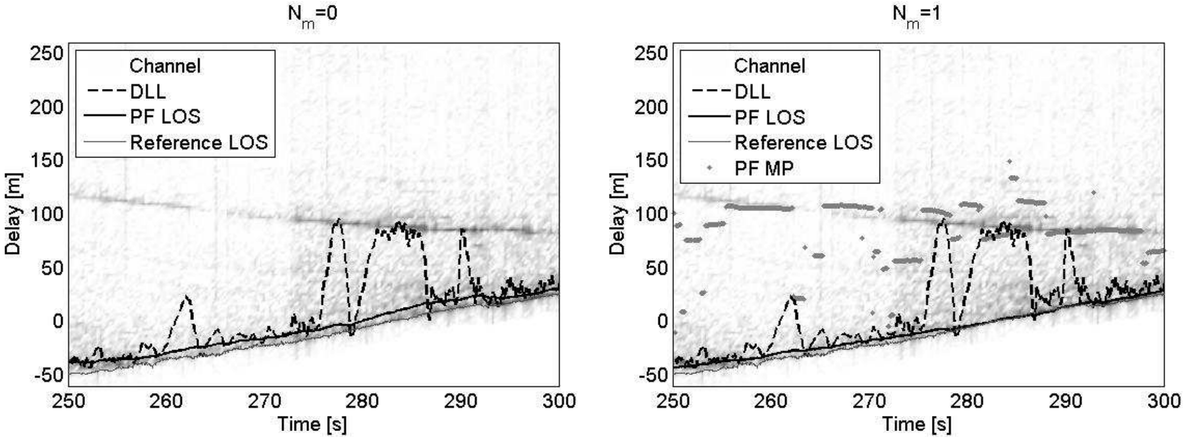

(a) $N_m = 0$ (b) $N_m = 1$

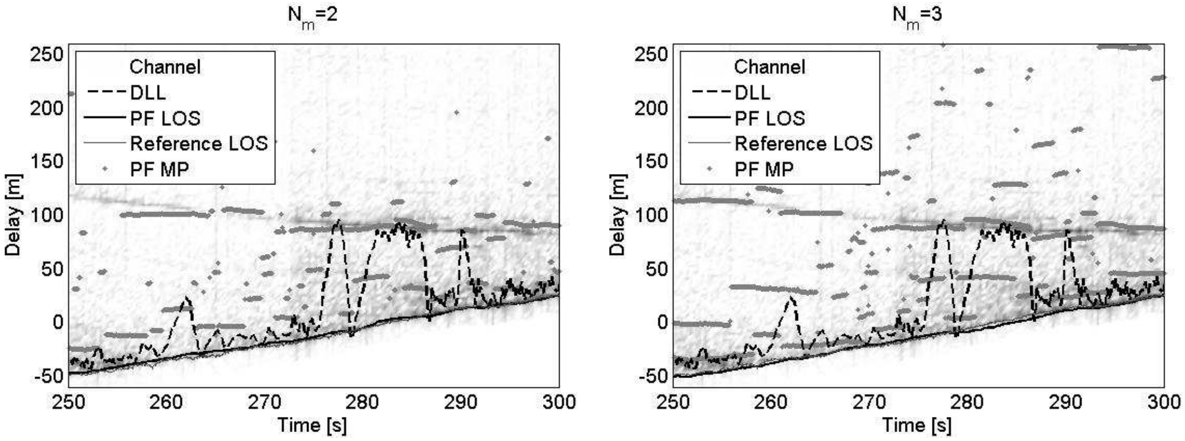

(c) $N_m = 2$ (d) $N_m = 3$

Figure 3.16: In the illustrated scenario there is a partially shadowed LOS path that is superimpose by a heavy multipath component. During some periods with weak LOS the DLL receiver tracks the multipath signal instead of the true LOS, which leads to high errors in the order of 100 meters. Comparable to the scenario shown in Figure 3.15 the estimation algorithm is still slightly biased, if the multipath replica is not taken account by the estimator ($N_m = 0$, Figure 3.16(a)). Nevertheless the magnitude of the errors is much smaller than the DLL errors, since the dynamic model of the estimator prevents fast variations of the LOS estimate. Once the number of considered replica is sufficient to take into account both present signals ($N_m > 0$, Figures 3.16(b), 3.16(c), and 3.16(d)), the estimation algorithm detects and tracks properly the additional replica and thus successfully mitigates the multipath errors.

Chapter 4

Pedestrian Inertial Navigation

During the last century the development of inertial navigation systems was mainly driven by military applications. Today their use has become widespread also in various fields of civil applications, including commercial and private aviation, naval, and land vehicle navigation. In the past size, cost, and power consumption of inertial platforms was preventing their use for pedestrian navigation. During the last decade the technical advances in the implementation of mechanical structures along with miniaturized integrated circuits have led to the maturity of micro-electro-mechanical inertial sensors. Today inertial MEMS are produced in high quantity with significantly reduced cost, mainly induced by automotive applications. The reduced size and power consumption of these novel sensors allows to integrate them into small-scale personal mobile devices and wearable ubiquitous computing systems. Consequently inertial sensors are about to be considered and applied for pedestrian navigation, especially for indoor applications, since they can provide autonomous navigation, where other systems like satellite navigation fail. For the use of inertial sensors in personal navigation basically two approaches can be distinguished. The pedometer-approach employs an accelerometer for detecting individual steps whilst the stride length and stride direction are themselves estimated using additional sensors, such as GNSS, or a priori information. Given a detected step, its length and its direction, a person's position can be determined by dead-reckoning [GM99, Lad00]. In a more advanced approach a complete foot-mounted strapdown inertial platform comprising triads of accelerometers and gyroscopes is used to dead reckon via a conventional strapdown navigation algorithm. An extended Kalman filter runs in parallel to the strapdown algorithm, where rest phases of the foot, which are detected from the accelerometer signals, trigger zero-velocity (virtual) measurements that are used to update the filter (ZUPT). Due to the regular ZUPT measurements the drift errors, which accumulate in the strapdown solution, can be estimated and corrected [Fox05]. It was revealed that this approach can achieve very good performance even with today's low-cost MEMS sensors, because the ZUPTs are so frequent that errors build up only slowly during each step the pedestrian makes. Since the foot-mounted INS approach is more flexible and performs much better than the pedometer approach [GPL$^+$07], it is expected that future high-performance pedestrian navigation will rely on foot-mounted INS, at least for professional applications such as localization and guidance of firefighters and other relief units. For that reason the enhancement of the integration of foot-mounted inertial sensors is addressed within the scope of this chapter, specifically because the state-of-the-art integration approach for foot-mounted INS is not optimal, as the algorithm does not take into account any a priori knowledge about the motion of the pedestrian or the motion of her foot and there is no mathematically sound procedure when considering the incorporation of nonlinear map-matching techniques or additional non-linear / non-Gaussian sensors typically used in an indoor scenario. To address this problem a cascaded estimation architecture is proposed in this chapter: To estimate the foot's navigation parameters a state-of-the-art integration filter is proposed, which comprises a conventional strapdown navigation computer, an extended Kalman filter, and a ZUPT detection algorithm for the foot that is suitably equipped with the inertial sensor suite. In the novel approach for each step the foot displacement and heading changes from the foot's filter are computed and exploited as measurements within a higher-level main fusion (particle) filter, which is able to consider the nonlinear dynamics of the human by means of a dedicated pedestrian movement model, including also maps and building constraints. This approach, which operates at a much lower sampling rate, is shown to be highly valuable, in particular in an indoor scenario. Based on a simple mechanical pedestrian model interconnecting the pedestrian's body and her feet it is shown additionally that the same approach is still viable when integrating a pair of platforms that are mounted on each of the pedestrians' feet respectively. It is shown that in this case the accuracy of the dead-reckoning is doubled.

4.1 Motivation of a Novel Approach

The state-of-the-art approach to integrate strapdown inertial sensors into a navigation system is to use an extended Kalman filter together with a strapdown navigation computer [GWA01]. The combination of the two algorithms may be interpreted as a ”probabilistic” inertial navigation system (INS) and allows to calculate an approximation of the a posteriori PDF of position, velocity, attitude, and sensor errors based on the sequence of measurement received from the sensors of the inertial platform. The approximated a posteriori and a priori PDFs are Gaussian densities, whose mean is given by the strapdown solution corrected by the Kalman filter state vector and whose covariance matrix is given by the covariance matrix of the Kalman filter. The major advantage of this approach is that the resulting Gaussian PDFs can be joined analytically with linear/linearized Gaussian likelihood functions of further sensors during the filter update step (2.73). Despite the fact that the Kalman filter implements a Bayesian filter, the conventional integration approach suffers from the major drawback that it does not follow (2.41) and (2.42) straightforwardly for two reasons:

- The Kalman filter indeed uses a probabilistic state transition model, but this model is based solely on pure kinematic relations between velocity, position, attitude, and sensor errors rather than on a true probabilistic characterization of the dynamics of the tracked object (e.g. a person traveling by foot)

- No likelihood function and no a priori knowledge is used to incorporate the accelerometer and gyroscope measurements into the algorithm. Accelerometer and gyroscope measurements enter the algorithm directly via the strapdown computations and no explicit use is made of any a priori knowledge about the object's dynamics. As a consequence the performance of a conventional INS is mainly determined by the quality of the inertial sensors.

To overcome this drawback it would indeed be optimal to formulate a Bayesian estimator whose dynamic model characterizes - besides position, velocity, attitude, and sensor errors - also accelerations and turn rates of the navigating individual using a Markov chain whose state transitions occur at the sensor measurement rate, which is relatively high for inertial sensors. Due to nonlinear constraints this is a very difficult task, especially when considering a Markov-chain characterization of a pedestrian and the motion of her foot. Because of this problem the conventional integration approach is the only appropriate one to estimate the movement of a pedestrian's foot. Indeed, for the considered application this is not a major drawback, as the inertial drift errors can be constrained efficiently through the use of ZUPT measurements. However, it is generally desirable to consider further a priori knowledge about the pedestrian's dynamics in an overall navigation filter. To take benefit of both the accurate foot-mounted inertial system and a dedicated pedestrian movement model including nonlinear effects such as building plans a cascaded estimation architecture is introduced in the following.

4.2 Cascaded Implementation

Due to the requirement to be flexible with respect to the incorporation of sensors and process models (movement or mobility models) that are nonlinear and which may have non-Gaussian noise models, it is required to employ a particle filter framework for the main fusion filter. In particular the movement model shall be flexible to incorporate a building map based mobility model whenever available, which may be nonlinear. Thus it is proposed here to use a Kalman filter to provide stepwise computed values of foot displacement and heading change, here referred to as the step-measurement, which in turn can be treated as measurements within the particle filter algorithm, where they enter via a Gaussian likelihood function along with the measurements and likelihood functions of further available sensors. The particle filter is designed to perform sensor fusion roughly every second or when triggered to do so by a specific sensor - specifically an update cycle is performed approximately at the latest once every second and also upon each received step-measurement. To distinguish in the following the low rate operations of the ”upper” particle filter from the high rate operations of the ”lower” Kalman filter, the terms k*-rate* and l*-rate* are introduced. The upper filter is associated to the k-rate, which is approximately the step-rate, and the lower filter is associated to the l-rate, which is given by the rate of the inertial sensors. Corresponding variables are indicated by the subscripts $(\bullet)_k$ and $(\bullet)_l$. The overall architecture of the two-layered fusion algorithm is illustrated in 4.1. The details on the computations that are performed in both layers and their interaction is addressed in the subsequent sections.

4.2.1 Upper Filter

As already mentioned a particle filter is selected for the main fusion filter, since it is a quite flexible implementation with respect to nonlinearities. With exception of the step-measurement it adopts according to the standard SIR formulation [AMGC02] the state transition probabilities as proposal function (2.73) and uses the product of the sensors' likelihood functions in the weight computation (2.38). The incorporation of the INS-step-measurement, however, does not follow this approach, as outlined later.

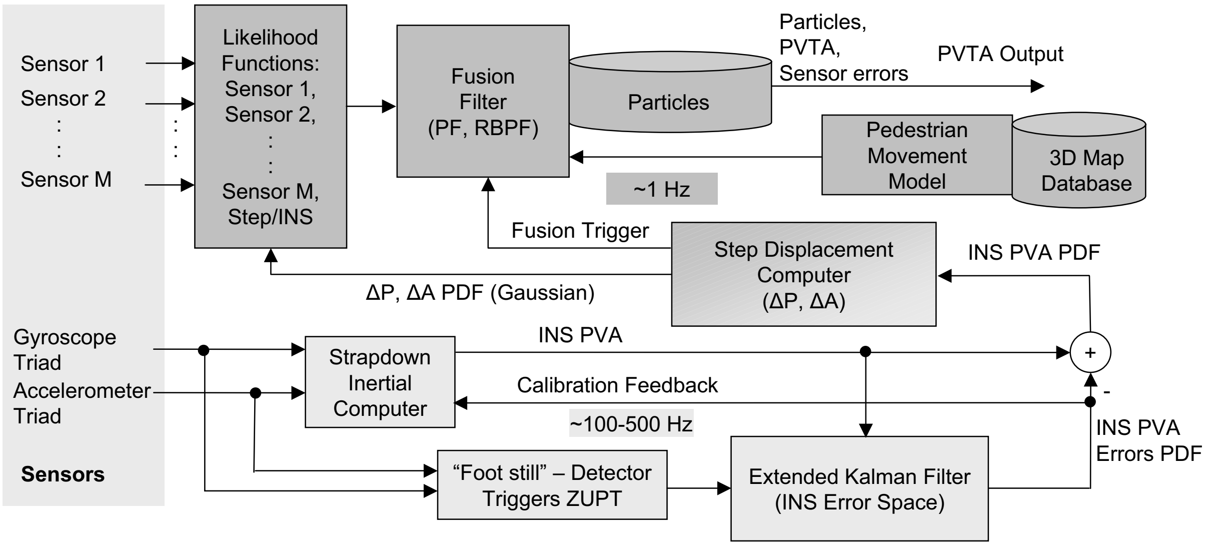
Sensor 1
Sensor 2
Sensor M
Likelihood Functions: Sensor 1, Sensor 2, Sensor M, Step/INS
Fusion Filter (PF, RBPF)
Particles
Particles, PVTA, Sensor errors
PVTA Output
Pedestrian Movement Model
3D Map Database
~1 Hz
Fusion Trigger
Step Displacement Computer (ΔP, ΔA)
INS PVA PDF
ΔP, ΔA PDF (Gaussian)
Gyroscope Triad
Accelerometer Triad
Sensors
Strapdown Inertial Computer
INS PVA
+
Calibration Feedback
-
~100-500 Hz
INS PVA Errors PDF
"Foot still" – Detector Triggers ZUPT
Extended Kalman Filter (INS Error Space)

Figure 4.1: Illustration of the cascaded estimator: The high rate inertial computations for the stride estimation are performed in the lower extended Kalman filter (light gray). For each step the pedestrian makes the displacement computer calculates a displacement estimate, which is used at a reduced rate along with all other measurements in the upper main particle filter (dark gray).

State Model

The particle filter is designed to track the pedestrian's position $\mathbf{r}_k$ and her heading Ψ_k. To allow the incorporation of the step-measurement the state vector is extended by the step-states $\Delta\mathbf{r}_k$ and $\Delta\Psi_k$, which relate $\mathbf{r}_k$ and Ψ_k to the time index $k-1$ as illustrated in Figure 4.2. Hence the overall state vector becomes

$$\mathbf{x}_k = \begin{pmatrix} \mathbf{r}_k \\ \Psi_k \\ \Delta\mathbf{r}_k \\ \Delta\Psi_k \end{pmatrix} \quad . \tag{4.1}$$

Measurement Model

The step-measurement $\mathbf{z}_k$, which will be the only used measurement within the scope of this chapter, is assumed to depend only on the current state $\mathbf{x}_k$ and a noise term $\mathbf{n}_\Delta$ via the function

$$\mathbf{z}_k = h(\mathbf{x}_k, \mathbf{n}_\Delta) \quad . \tag{4.2}$$

In particular it is assumed that

$$\mathbf{z}_k = \begin{pmatrix} \Delta\mathbf{r}_k \\ \Delta\Psi_k \end{pmatrix} + \mathbf{n}_\Delta \quad , \tag{4.3}$$

with $\mathbf{n}_\Delta$ being zero-mean element-wise uncorrelated Gaussian noise. The underlying variances $\sigma^2_{\Delta x}$, $\sigma^2_{\Delta y}$, and $\sigma^2_{\Delta\Psi}$ are adjusted to reflect the uncertainty of the step-measurement.

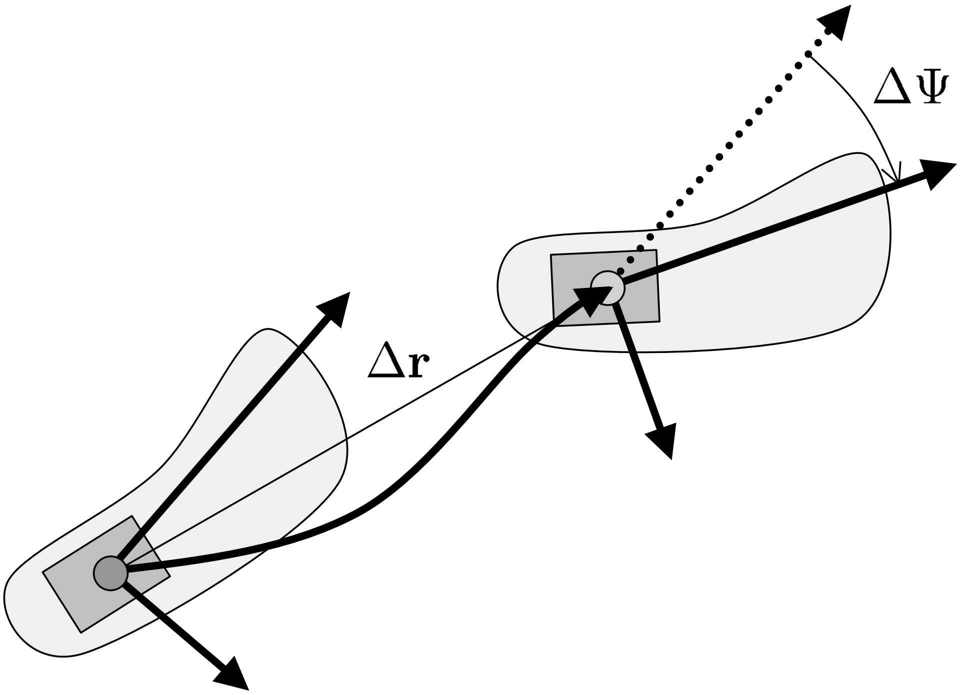

Figure 4.2: Illustration of the foot displacement vector $\Delta\mathbf{r}$ and the change in heading $\Delta\Psi$ for each step the pedestrian makes.

Movement Model

A probabilistic movement model is used to characterize the temporal evolution of the state $\mathbf{x}_k$. Given that this evolution can be characterized by a transitional density $p(\mathbf{x}_k|\mathbf{x}_{k-1})$, the model follows the Markovian approach. The movement model used here aims to reflect the physical constraints that are imposed on the movement of a pedestrian, in particular in an indoor scenario, where the layout of the building restricts the dynamics. Formally, the new state $\mathbf{x}_k$ is assumed to depend only on the previous state $\mathbf{x}_{k-1}$ and a noise term $\mathbf{n}_d$ through

$$\mathbf{x}_k = f(\mathbf{x}_{k-1}, \mathbf{n}_d) \ . \tag{4.4}$$

It is assumed that the new location and heading depend deterministically on the past state (and on the current state through the Δ-states) according to

$$\begin{aligned} \mathbf{r}_k &= \mathbf{r}_{k-1} + \mathbf{C}(\Psi_\varepsilon)\mathbf{C}(\Psi_{k-1})\Delta\mathbf{r}_k \ , \quad (4.5) \\ \Psi_k &= \Psi_{k-1} + \Delta\Psi_k \ , \quad (4.6) \end{aligned}$$

where $\mathbf{C}(\Psi_{k-1})$ is the rotation matrix

$$\mathbf{C}(\bullet) = \begin{pmatrix} \cos(\bullet) & -\sin(\bullet) & 0 \\ \sin(\bullet) & \cos(\bullet) & 0 \\ 0 & 0 & 1 \end{pmatrix} \ , \tag{4.7}$$

and where the average heading misalignment of the inertial sensor platform with respect to the pedestrian's heading is given by the angle Ψ_ε, which can either be set to a fixed value or which can be modeled as a random process as addressed subsequently. The probabilistic part of the movement model is incorporated into the temporal evolution of the displacement states $\Delta\mathbf{r}_k$ and $\Delta\Psi_k$ via

$$\begin{aligned} \Delta\mathbf{r}_k &= \mathbf{f}_r(\mathbf{x}_{k-1}, \mathbf{n}_r) \ , && (4.8) \\ \Delta\Psi_k &= \mathbf{f}_\Psi(\mathbf{x}_{k-1}, \mathbf{n}_\Psi) \ , && (4.9) \end{aligned}$$

which depend only on the past state $\mathbf{x}_{k-1}$ and the noise terms $\mathbf{n}_r$ and $\mathbf{n}_\Psi$. The constraints that are imposed by the building layout are included in (4.8) in that the displacement of the location $\Delta\mathbf{r}_k$ depends on the presence of nearby walls and obstacles. A very simple movement model is proposed here: Given that a displacement $\Delta\mathbf{r}_k$ intersects with one of the walls that are stored in the map database, the probability $p(\mathbf{x}_k|\mathbf{x}_{k-1}) = p_{\text{cross}}$ is assigned [EM06b], where p_{cross} is a small probability that takes into account that the stored building data may be erroneous. In other situations, if a wall has not been crossed, the displacement is assumed to follow

$$\begin{aligned} \Delta\mathbf{r}_k &= \mathbf{n}_r \ , && (4.10) \\ \Delta\Psi_k &= n_\Psi \ , && (4.11) \end{aligned}$$

where $\mathbf{n}_r$ and n_Ψ are drawn from mutually uncorrelated zero-mean white Gaussian noise processes, whose variances σ_x^2, σ_y^2, and σ_Ψ^2 are adapted to the movement of a pedestrian. Despite the fact that this model is suitable for the case of a wall crossing, it is quite coarse otherwise, as it does not adequately represent the probability with which a pedestrian will move, given a known building layout or map [KKRA08]. To alleviate this, more accurate movement models could be used as well. An illustration of the pedestrian model used here in terms of a dynamic Bayesian network is shown in Figure 4.3, where at each step the change in position and the change in heading is observable through the step-measurement (4.3).

The relation between the measurement (4.3) and the movement (4.5), (4.6) is illustrated in Figure 4.4. Specifically the actual displacement with respect to the navigation coordinate system is given according to (4.5) by $\Delta\mathbf{r}'_k = \mathbf{C}(\Psi_\varepsilon)\mathbf{C}(\Psi_{k-1})\Delta\mathbf{r}_k$, which is a rotated version of the displacement state $\Delta\mathbf{r}_k$.

Modeling of Angular Drift

When modeling the evolution Ψ_ε by a random process the state vector (4.1) can be extended by the time-variant misalignment $\Psi_{\varepsilon,k}$ and the heading drift rate $\dot{\Psi}_{\varepsilon,k}$, for which the following simple Gaussian linear models are assumed:

$$\begin{aligned} \Psi_{\varepsilon,k} &= \Psi_{\varepsilon,k-1} + \dot{\Psi}_{\varepsilon,k-1}\Delta t + n_{\Psi,\varepsilon} \ , && (4.12) \\ \dot{\Psi}_{\varepsilon,k} &= \dot{\Psi}_{\varepsilon,k-1} + n_{\dot{\Psi},\varepsilon} \ , && (4.13) \end{aligned}$$

with $n_{\Psi,\varepsilon}$ and $n_{\dot{\Psi},\varepsilon}$ being zero-mean white Gaussian noise of variance $\sigma^2_{\Psi,\varepsilon}$ and $\sigma^2_{\dot{\Psi},\varepsilon}$ respectively and Δt being the time elapsed during the interval between k and $k-1$.

4.2.2 Lower Filter

As the integration method proposed in [Fox05] was shown to have both good performance and low complexity, this approach is followed for the step estimation algorithm. The lower filter

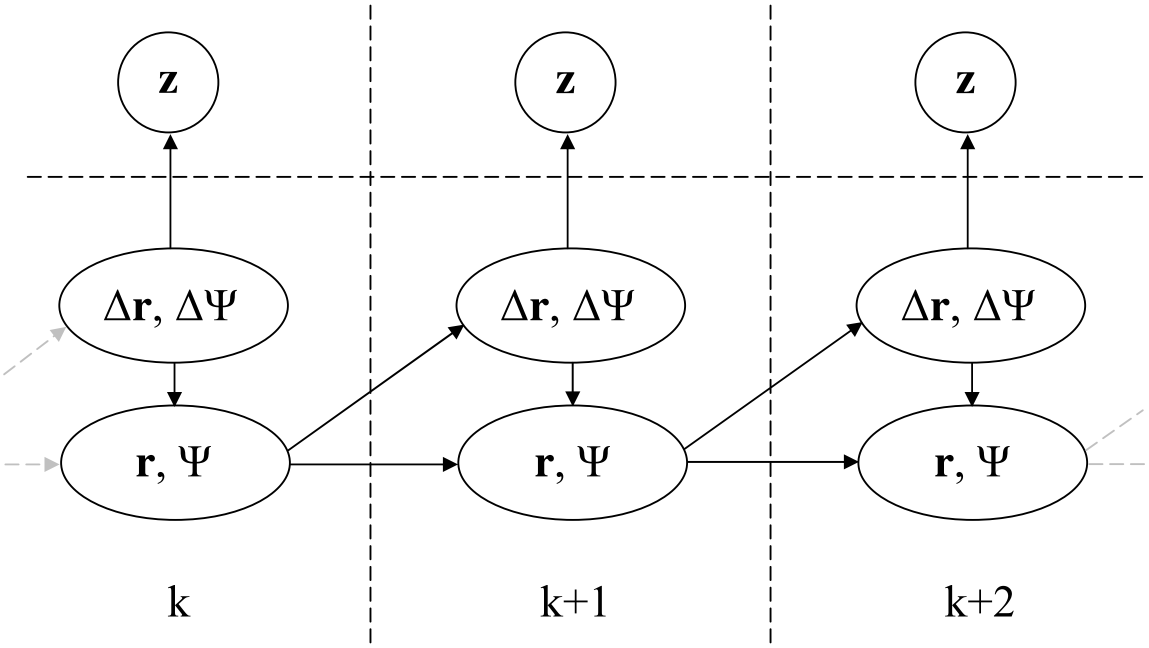

Figure 4.3: Dynamic Bayesian network illustration of the pedestrian model used in the upper particle filter. The current position depends on the previous position and the current displacement, which is observable through the measurement (4.3).

operates at the rate given by the output of the inertial sensor suite, which is in the range of 100–500 Hz, depending on the hardware settings.

Implementation

A strapdown navigation algorithm [TW04] processes the vector of acceleration and turn rate measurements $\mathbf{z}_l^{\mathrm{INS}} = [\mathbf{f}_l^b, \boldsymbol{\omega}_l^b]^T$, which is provided by the inertial sensors, to compute position $\mathbf{r}_l$, velocity $\mathbf{v}_l$, and attitude $\boldsymbol{\Psi}_l$. In parallel an extended Kalman filter is used to estimate the errors of the strapdown calculations. Typically at least 9 states are estimated by the filter [GWA01]: position errors $\delta\mathbf{r}_l$, velocity errors $\delta\mathbf{v}_l$, and attitude errors $\delta\boldsymbol{\Psi}_l$. Additionally sensor imperfections like accelerometer biases $\delta\mathbf{f}_l$, and gyroscopic biases $\delta\boldsymbol{\omega}_l$ may be estimated along. The error estimates $\delta\mathbf{r}_l$, $\delta\mathbf{v}_l$, and $\delta\boldsymbol{\Psi}_l$ are perturbations around the filter operating point $\mathbf{r}_l$, $\mathbf{v}_l$, $\boldsymbol{\Psi}_l$ that is calculated by the strapdown algorithm. The purpose of the lower filter architecture is to provide step-wise estimates of position and attitude. Therefore a conventional strapdown computation according to Section 2.2.2 is carried out:

$$
\begin{aligned}
\mathbf{r}_l^i &= \mathbf{r}_{l-1}^i + \mathbf{v}_{l-1}^i T_s \ , && (4.14)\\
\mathbf{v}_l^i &= \mathbf{v}_{l-1}^i + \left(\mathbf{C}_{b,l-1}^i \mathbf{f}_{l-1}^b + \mathbf{g}_{l-1}^i\right) T_s \ , && (4.15)\\
\mathbf{C}_{b,l}^i &= \mathbf{C}_{b,l-1}^i (\mathbf{I} + [\boldsymbol{\omega}_{ib,l-1}^b \times] T_s) \ . && (4.16)
\end{aligned}
$$

For concise notation the large-scale state is written as $\mathbf{x}_l \mathrel{\widehat{=}} [\mathbf{r}_l, \mathbf{v}_l, \boldsymbol{\Psi}_l]$. To estimate the drift errors of the inertial navigator an extended Kalman filter in the error space formulation is used, where the small-scale error state $\delta\mathbf{x}_l \mathrel{\widehat{=}} [\delta\mathbf{r}_l, \delta\mathbf{v}_l, \delta\boldsymbol{\Psi}_l]$ is estimated. Starting with an initial state

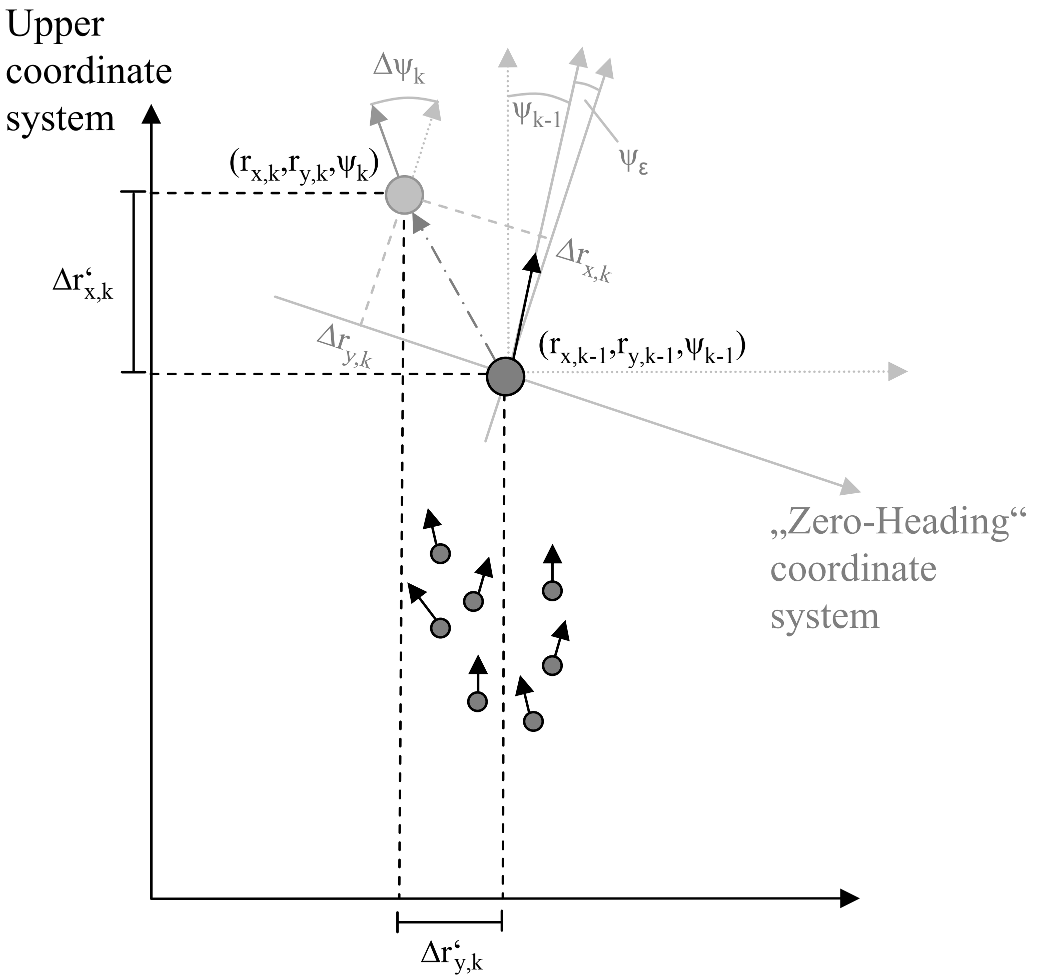
Upper coordinate system
Δψk
ψk-1
ψε
(rx,k,ry,k,ψk)
Δrx,k
Δr'x,k
Δry,k
(rx,k-1,ry,k-1,ψk-1)
„Zero-Heading“ coordinate system
Δr'y,k

Figure 4.4: Movement of particles in the upper filter. The displacement $\Delta\mathbf{r}_k = [\Delta r_{x,k}, \Delta r_{y,k}]^T$ corresponds to the movement with respect to the ”Zero-Heading” coordinate system that is associated to each particle according to its heading. The particle movement with respect to the upper filter navigation coordinate system is thus for each particle given by the vector $\Delta\mathbf{r}'_k = [\Delta r'_{x,k}, \Delta r'_{y,k}]^T$, which is according to (4.5) just the result of a rotational transformation on $\Delta\mathbf{r}_k$.

$\delta\mathbf{x}_0 = \delta\bar{\mathbf{x}}_0$ and an associated initial covariance $\mathbf{P}_0 = \bar{\mathbf{P}}_0$, the linearized dynamics (cf. Section 2.3.2) allow the prediction of the mean via

$$\delta\hat{\mathbf{x}}_l^- = \underbrace{\begin{pmatrix} \mathbf{I}_{3\times3} & \mathbf{I}_{3\times3}T_s & \mathbf{0}_{3\times3} \\ \mathbf{0}_{3\times3} & \mathbf{I}_{3\times3} & [\mathbf{f}_{l-1}^i\times]T_s \\ \mathbf{0}_{3\times3} & \mathbf{0}_{3\times3} & \mathbf{I}_{3\times3} \end{pmatrix}}_{\mathbf{F}_{l-1}} \delta\hat{\mathbf{x}}_{l-1} \ . \tag{4.17}$$

The covariance is predicted with

$$\mathbf{P}_l^- = \mathbf{F}_{l-1}\mathbf{P}_{l-1}\mathbf{F}_{l-1}^T + \mathbf{Q} \ . \tag{4.18}$$

The system noise matrix $\mathbf{Q}$ is adjusted to the quality of the inertial sensor according to

$$\mathbf{Q} \;=\; \begin{pmatrix} \mathbf{0}_{3x3} & \mathbf{0}_{3x3} & \mathbf{0}_{3x3} \\ \mathbf{0}_{3x3} & \mathbf{C}_{b,l}^i\boldsymbol{\Sigma}_a^2\mathbf{C}_{i,l}^bT_s^2 & \mathbf{0}_{3x3} \\ \mathbf{0}_{3x3} & \mathbf{0}_{3x3} & \mathbf{C}_{b,l}^i\boldsymbol{\Sigma}_\omega^2\mathbf{C}_{i,l}^bT_s^2 \end{pmatrix} \ , \tag{4.19}$$

with the direction cosine matrix $\mathbf{C}_{b,l}^i$, the sampling interval T_s and the vectors comprising the noise variances of the accelerometer and gyroscope triads:

$$\boldsymbol{\Sigma}_a^2 \;=\; \mathrm{diag}([\sigma_{a,x}^2, \sigma_{a,y}^2, \sigma_{a,z}^2]^T) \ , \tag{4.20}$$

$$\boldsymbol{\Sigma}_\omega^2 \;=\; \mathrm{diag}([\sigma_{\omega,x}^2, \sigma_{\omega,y}^2, \sigma_{\omega,z}^2]^T) \ . \tag{4.21}$$

Depending on the detection of zero-velocity updates the a posteriori mean of the INS errors computes in the EKF's update step with

$$\delta\hat{\mathbf{x}}_l = \begin{cases} \delta\hat{\mathbf{x}}_l^- + \mathbf{K}_k(\mathbf{z}_l^\epsilon - \mathbf{H}\delta\hat{\mathbf{x}}_l^-) & \text{if ZUPT} \\ \delta\hat{\mathbf{x}}_l^- & \text{otherwise} \end{cases} \ , \tag{4.22}$$

with the error space ZUPT measurement $\mathbf{z}_k^\epsilon = \mathbf{h}_l(\mathbf{x}_l) - \mathbf{z}_l = \mathbf{v}_{l-1}^i$, since $\mathbf{h}_l(\mathbf{x}_l) = \mathbf{v}_{l-1}^i$ and $\mathbf{z}_l = \mathbf{0}$ for the zero velocity measurement. In accordance the corresponding covariance computes with

$$\mathbf{P}_l = \begin{cases} (\mathbf{I} - \mathbf{K}_l\mathbf{H})\mathbf{P}_l^- & \text{if ZUPT} \\ \mathbf{P}_l^- & \text{otherwise} \end{cases} \ , \tag{4.23}$$

with the Kalman gain

$$\mathbf{K}_l = \mathbf{P}_l^-\mathbf{H}^T(\mathbf{H}\mathbf{P}_l^-\mathbf{H}^T + \mathbf{R}_l)^{-1} \ . \tag{4.24}$$

Since for the analysis of the lower filter the only used measurements are the ZUPTs, which correspond to conventional velocity measurements, the measurement matrix $\mathbf{H}$ is given by

$$\mathbf{H} \;=\; \begin{bmatrix} \mathbf{0}_{3\times3} & \mathbf{I}_{3\times3} & \mathbf{0}_{3\times3} \end{bmatrix} \ . \tag{4.25}$$

To ensure a smooth zero-velocity updating it was proposed in [Fox05] to adjust the measurement noise of the zero-velocity updates to the current covariance of the estimated velocities. In this case the estimated covariance of the velocities and the ZUPT measurement covariance are

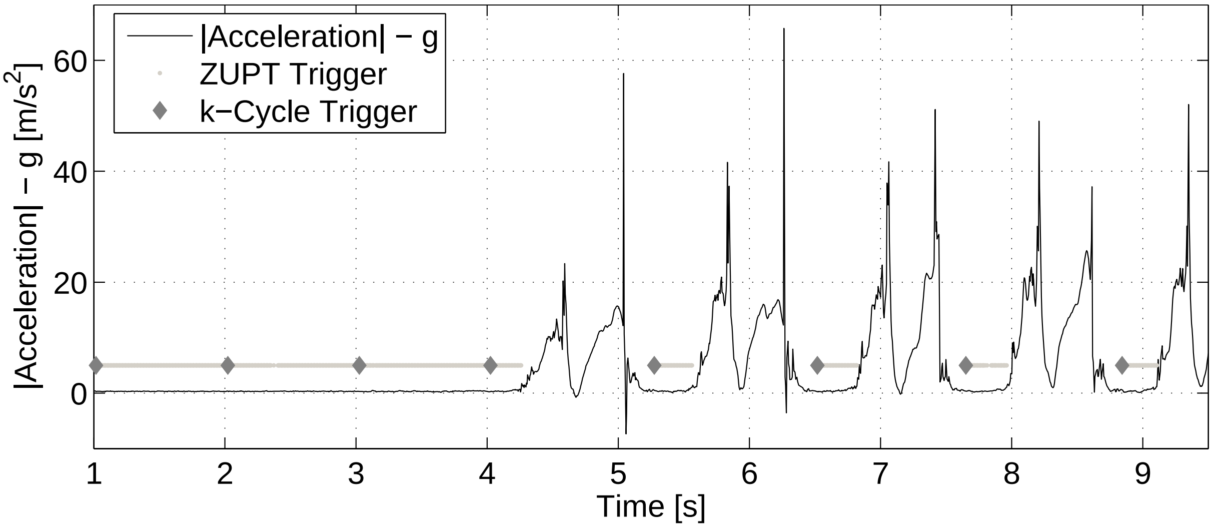

Figure 4.5: Magnitude of acceleration vector subtracted by gravity g during the beginning of a walk sequence. ZUPT triggers and k-cycle triggers are shown along. Each time a novel step is detected a fusion at the upper filter is triggered.

always in the same order of magnitude, which prevents numerical problems during the update of the Kalman filter. Following this approach the measurement noise matrix $\mathbf{R}_l$ equals the corresponding covariance of the predicted velocity:

$$\mathbf{R}_l = \mathbf{P}^-_{l,[4:6,4:6]} \ . \tag{4.26}$$

In the subsequent processing only position and heading are states of interest and can be expressed in concise notation as

$$\bar{\mathbf{x}}^{\mathrm{s}}_l = \begin{pmatrix} \mathbf{r}_l \\ \Psi_l \end{pmatrix} \ , \tag{4.27}$$

with the yaw angle Ψ_l that is derived from $\mathbf{\Psi}_l$. From the a posteriori PDF of the lower filter the (marginalized) a posteriori PDF $p(\mathbf{x}^{\mathrm{s}}_l|\mathbf{Z}_l)$ can be derived straightforwardly.

Rest Phase Detection

The reliable identification of the foot's rest phases is crucial for the update of the lower filter. Different approaches have been proposed to trigger the ZUPT measurement [Fox05, GLC06]. Here these ideas are adopted basically and the magnitude of the acceleration vector, which is sensed by the accelerometer triad, is monitored [GLC06]. If the signal remains within a threshold interval around earth gravity for a certain time interval ZUPTs are triggered until the threshold condition is violated. In the cascaded approach the ZUPT detection is also used to trigger the update of the upper filter. Each time a ZUPT is triggered in the lower filter the elapsed time since the last update of the upper filter is checked. If this time exceeds a certain threshold, for instance one second as illustrated in Figure 4.5, a new update of the upper filter is initiated.

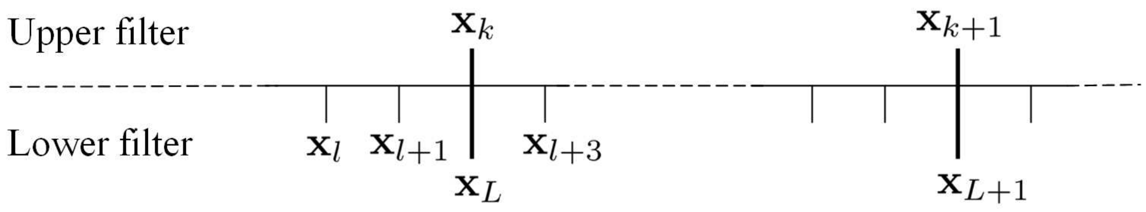

Figure 4.6: Relation between upper and lower filter scheduling. The time instances where the lower index l corresponds to the index L indicate a cycle a the k-rate.

The Step Sensor

The lower filter is used to process the high rate inertial measurements. To exploit them in the upper filter a (virtual) step sensor is derived from the lower filter in order to provide a measure of the traveled distance and the change in heading for each step the pedestrian makes. As the step sensor does not provide absolute position and heading information the inertial navigator of the lower filter can be aligned with arbitrary position and heading, which eases the alignment procedure. To provide the step measurements the following operations are performed at the interface between the lower filter and the virtual step sensor: As illustrated in Figure 4.6 each time a new upper filter cycle (k-cycle) is triggered the expectation of the lower filter $\hat{\mathbf{x}}^{\mathrm{s}}_l$ is stored in the variable $\hat{\mathbf{x}}^{\mathrm{s}}_L \hat{=} \hat{\mathbf{x}}^{\mathrm{s}}_l$ with $L = k$. Please note that variables associated to the lower filter are indicated by the subscript $(\bullet)_L$ for those time instances l for which k-cycles are triggered. Introducing the step displacement variable $\Delta\mathbf{x}^{\mathrm{s}}_L = \mathbf{x}^{\mathrm{s}}_L - \mathbf{x}^{\mathrm{s}}_{L-1}$ its expectation is almost independent from previous steps due to the ZUPTs that are applied. Thus there is $\Delta\hat{\mathbf{x}}^{\mathrm{s}}_L = \mathbb{E}(\Delta\mathbf{x}^{\mathrm{s}}_L|\mathbf{Z}_L)) \approx \mathbb{E}(\Delta\mathbf{x}^{\mathrm{s}}_L|\mathbf{Z}_L \backslash \mathbf{Z}_{L-1})$ and the displacement with respect to the coordinate system of the lower filter may be expressed as

$$\begin{aligned} \Delta\hat{\mathbf{x}}^{\mathrm{s}}_L &= \hat{\mathbf{x}}^{\mathrm{s}}_L - \hat{\mathbf{x}}^{\mathrm{s}}_{L-1} && (4.28) \\ &= \begin{pmatrix} \hat{\mathbf{r}}_L \\ \hat{\Psi}_L \end{pmatrix} - \begin{pmatrix} \hat{\mathbf{r}}_{L-1} \\ \hat{\Psi}_{L-1} \end{pmatrix} && (4.29) \\ &= \begin{pmatrix} \Delta\hat{\mathbf{r}}_L \\ \Delta\hat{\Psi}_L \end{pmatrix} \quad . && (4.30) \end{aligned}$$

Finally the displacement with respect to the heading at the previous k-cycle is computed according to

$$\mathbf{z}_k = \begin{pmatrix} \mathbf{C}^T(\Psi_{L-1})\Delta\hat{\mathbf{r}}_L \\ \Delta\hat{\Psi}_L \end{pmatrix} \quad , \tag{4.31}$$

such that the displacement with respect to the zero-heading coordinate system that is actually reported as measurement to the upper filter is given by $\Delta\hat{\mathbf{r}}^0_L = \mathbf{C}^T(\hat{\Psi}_{L-1})\Delta\hat{\mathbf{r}}_L$ according to (4.31). In Figure 4.7 the relations between the coordinate systems are illustrated. The so-called ”Zero-Heading” coordinate system, which is used to provide the displacement measurement, is spanned by the heading at time $L-1$ respectively.

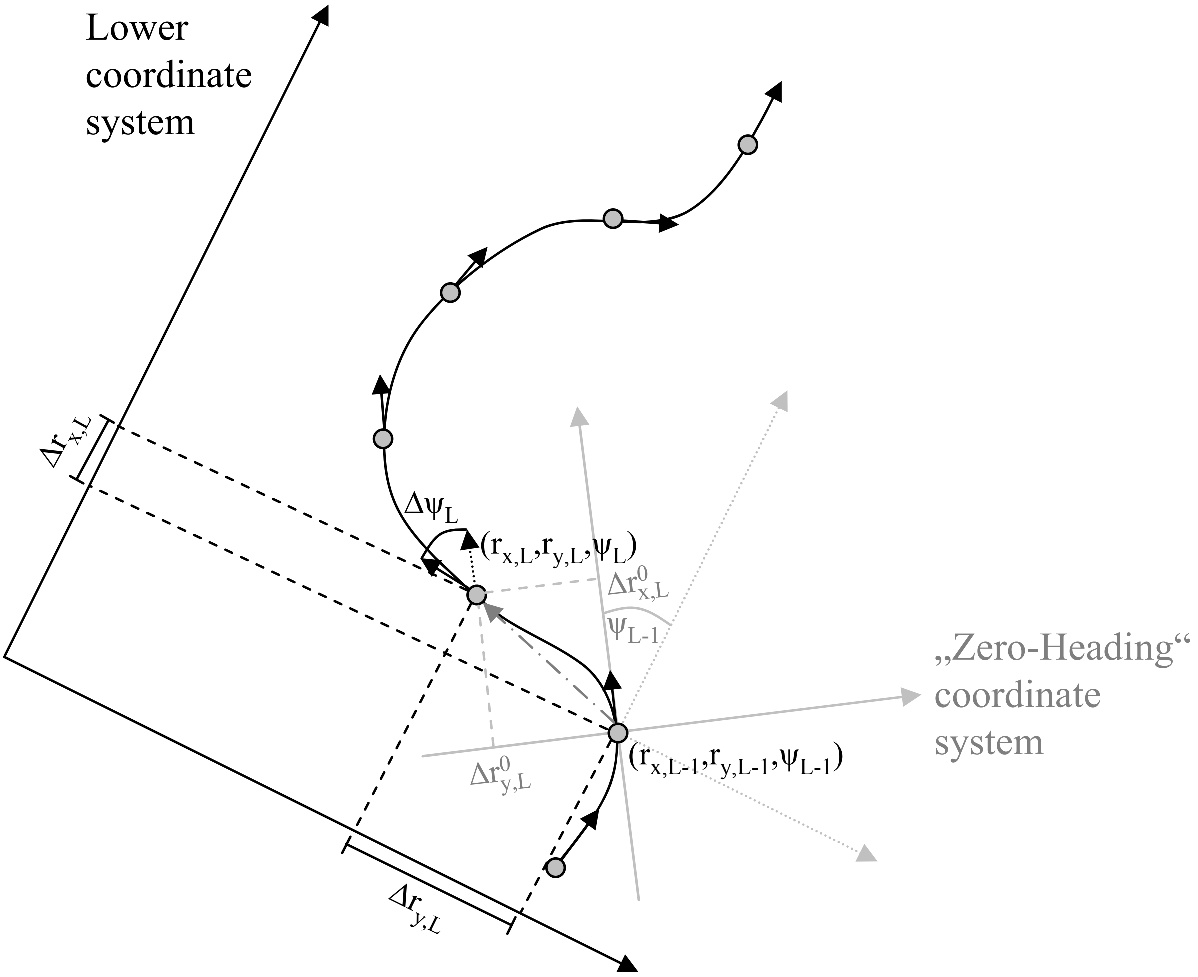
Lower coordinate system
$\Delta r_{x,L}$
$\Delta r_{y,L}$
$\Delta\psi_L$
$(r_{x,L}, r_{y,L}, \psi_L)$
$\Delta r^0_{x,L}$
ψ_{L-1}
„Zero-Heading“ coordinate system
$(r_{x,L-1}, r_{y,L-1}, \psi_{L-1})$
$\Delta r^0_{y,L}$

Figure 4.7: Illustration of the track that is computed by the lower filter. At each step the displacement $\Delta\mathbf{r}_L = [\Delta r_{x,L}, \Delta r_{y,L}]^T$ and the change in heading $\Delta\mathbf{\Psi}_L$ is computed. The final measure that is provided to the upper filter is the displacement $\Delta\mathbf{r}^0_L = [\Delta r^0_{x,L}, \Delta r^0_{y,L}]^T$, which expresses $\Delta\mathbf{r}_L$ with respect to the ”Zero-Heading” coordinate system. Since only changes of position and heading are reported the alignment of the lower filter coordinate system can be performed arbitrarily.

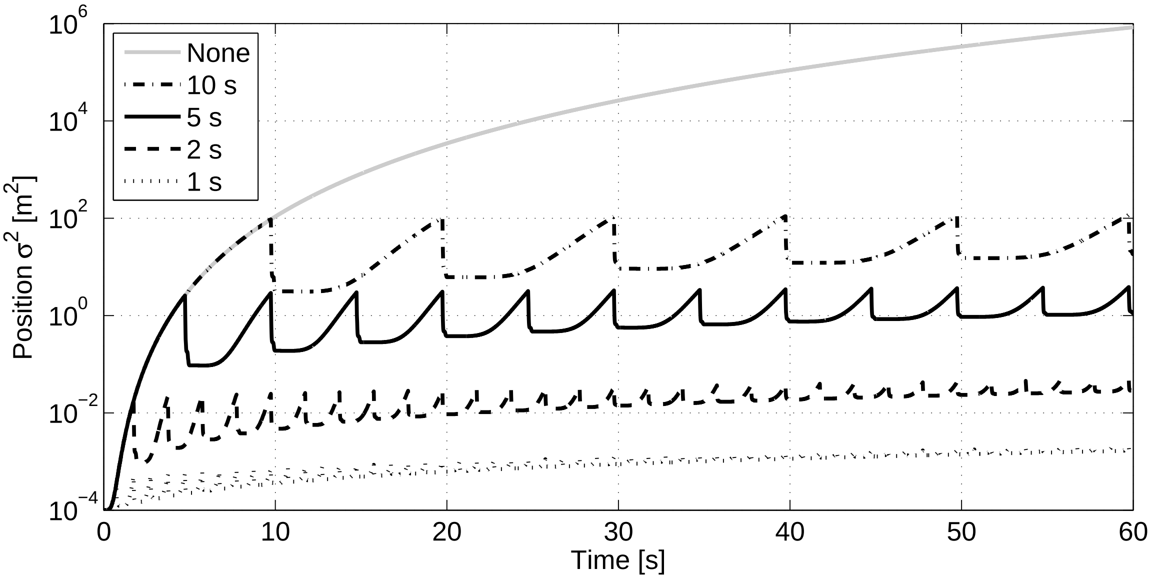

Figure 4.8: Performance of a resting foot-mounted INS comprising state-of-the-art low-cost inertial MEMS depending on the interval between two successively applied ZUPTs. With more frequent ZUPTs the drift gets reduced significantly.

Drift Analysis

As the system dynamics of an inertial navigator model are nonlinear (see (2.31), (2.32), and (2.33)), a general performance analysis is difficult. Nevertheless an approximate analysis is feasible when the magnitude of the errors is restricted. Given the errors are small, the system dynamics can be linearized for a given state to obtain the linear small-scale error dynamic equations. A truncated Taylor-series expansion of the full system equations is generally used for the linearization procedure [TW04]. Given a linear error model the system can be analysed using the well known framework of Kalman filtering [May79]. According to [TW04] the inertial error propagation may be performed in a similar fashion as the implementation of the previously introduced error space EKF in this case. In difference to the online calculation of the EKF covariances the large-scale trajectory is not computed from the inertial measurements, but from a predefined true state trajectory $\mathbf{X}_l \widehat{=} \{\mathbf{x}_q, q = 1, \ldots, l\}$. Given this true state trajectory the error covariances, which equal the PCRB [RAG04], can be computed recursively using (4.18) and (4.23). The results of such a system analysis are shown in Figure 4.8, where the impact of the frequency of ZUPT is shown, and in Figure 4.9, where the impact of the quality of the inertial sensors is illustrated.

4.2.3 Choice of an Appropriate Proposal Density

The selection of the proposal density is crucial for the performance of the particle filter algorithm and it showed up to be an apparent problem for the design of the upper filter in the cascaded estimation framework. If it is not possible to use the optimal proposal density a suitable choice is often the transition density. In this case the update step of particle filtering essentially incorporates the latest sensor evidence at each step in the form of the particles weights

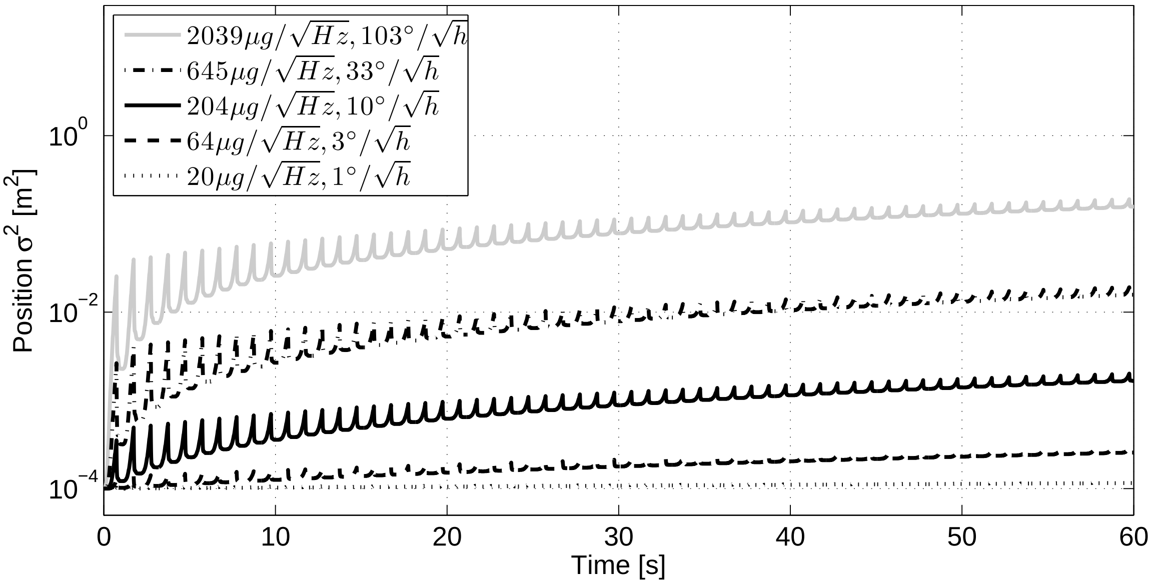

Figure 4.9: Performance of different classes of inertial sensors when applying regular ZUPTs with a rate of 1 Hz to a resting inertial platform. As it can be seen the development of improved sensors will enable an increase of the inertial dead-reckoning performance in the near future.

through the likelihood function (SIR particle filter [AMGC02]). As the optimal choice has been shown to be not appropriate in many situation due to complexity reasons the SIR particle filter is commonly the most widespread approach. Despite the transitional density $p(\mathbf{x}_k|\mathbf{x}_{k-1}^{\mu})$ is a convenient choice, there can be situations where it is not favorable, as the latest evidence $\mathbf{z}_k$ is not incorporated. For instance if the likelihood function is narrow compared to the density after the prediction step, then only a few ”lucky” particles will receive significant weights. The result is usually sample impoverishment which degrades accuracy significantly for a given number of particles. As the likelihood function for the step-measurements is comparatively narrow due to the high accuracy of the step measurement, it is crucial to choose the proposal density other than the state transition density in order to avoid the above mentioned problem. In other words it should be avoided to draw particles that do not follow the accurate step-measurement, because they will receive low weight from the step likelihood function during the update step anyway and hence are a waste of computational resources. To circumvent this drawback the auxiliary particle filter was proposed [PS99]. But especially for more extreme situations, where the likelihood function is much tighter than the a priori PDF, the optimal proposal comes very close to the likelihood function itself. Here the situation is similar, the step sensor is quite accurate, whereas the movement model is influenced mainly by the surrounding walls. Hence it is more efficient to draw according to the step likelihood function. Recalling the weight equation (2.73) the likelihood function cancels out with the proposal if the displacement is drawn from $q(\Delta\mathbf{r}_k, \Delta\Psi_k|\mathbf{z}_k)$, since the likelihood function (4.3) does not depend on $\mathbf{r}_k$, Ψ_k and the states $\mathbf{r}_k$, Ψ_k are computed deterministic using (4.5), (4.6). Using the more efficient likelihood proposal the weight update becomes

$$w_k^{\mu} \propto w_{k-1}^{\mu} p(\mathbf{x}_k^{\mu}|\mathbf{x}_{k-1}^{\mu}) \ . \tag{4.32}$$

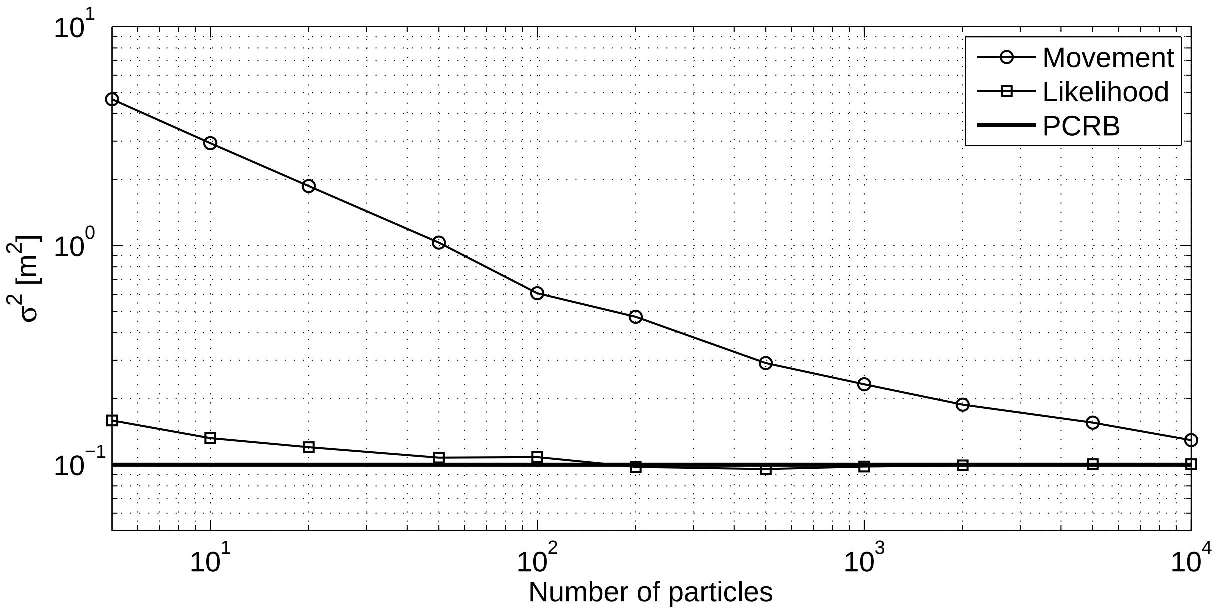

Figure 4.10: Comparison of the conventional movement proposal of the SIR PF and the likelihood proposal after 10 s of walking. With the likelihood proposal much less particles (approx. 100) are needed to attain the a posteriori Cramer-Rao bound.

In this case the particles follow the step measurement and for each particle a disturbance of small Gaussian noise is superimposed at every step. The weight is then calculated from the movement model corresponding to (4.32). This strategy ensures that enough particles survive at each step and impoverishment is avoided. The benefit of the improved proposal density is illustrated in Figure 4.10. A similar approach referred to as likelihood particle filter was proposed in [AMGC02] for a different application scenario.

4.2.4 Integration of a Pair of Platforms

An obvious extension for the integration of foot-mounted inertial sensors is to take benefit of a pair of platforms, with one mounted on each of the pedestrian's feet respectively. Unlike the conventional integration approach, which is based on a single Kalman filter, the cascaded architecture is flexible with respect to the use of a further foot-mounted platform. To integrate the pair of platforms for each of the two feet a Kalman filter may be used to estimate the stepwise position displacement and heading change respectively, such that the lower part of the cascaded architecture shown in Figure 4.1 is just doubled. In this case both lower filters provide their step-measurements to the upper particle filter. Due to the nature of a pedestrian movement the step measurements of the lower filters normally arrive asynchronous. To solve this issue the use of a simple mechanical pedestrian model is proposed now. So far it was assumed that the position of the pedestrian's foot coincides with its body position. If two platforms are used it needs to be addressed with respect to which initial state the displacement estimates are sensed respectively. To ease these considerations a simple physical interpretation is proposed. As illustrated in Figure 4.11 the body center may be assumed to be on the center of a line connecting the centers of both feet. It can be derived easily by geometrical considerations that during travel and turn

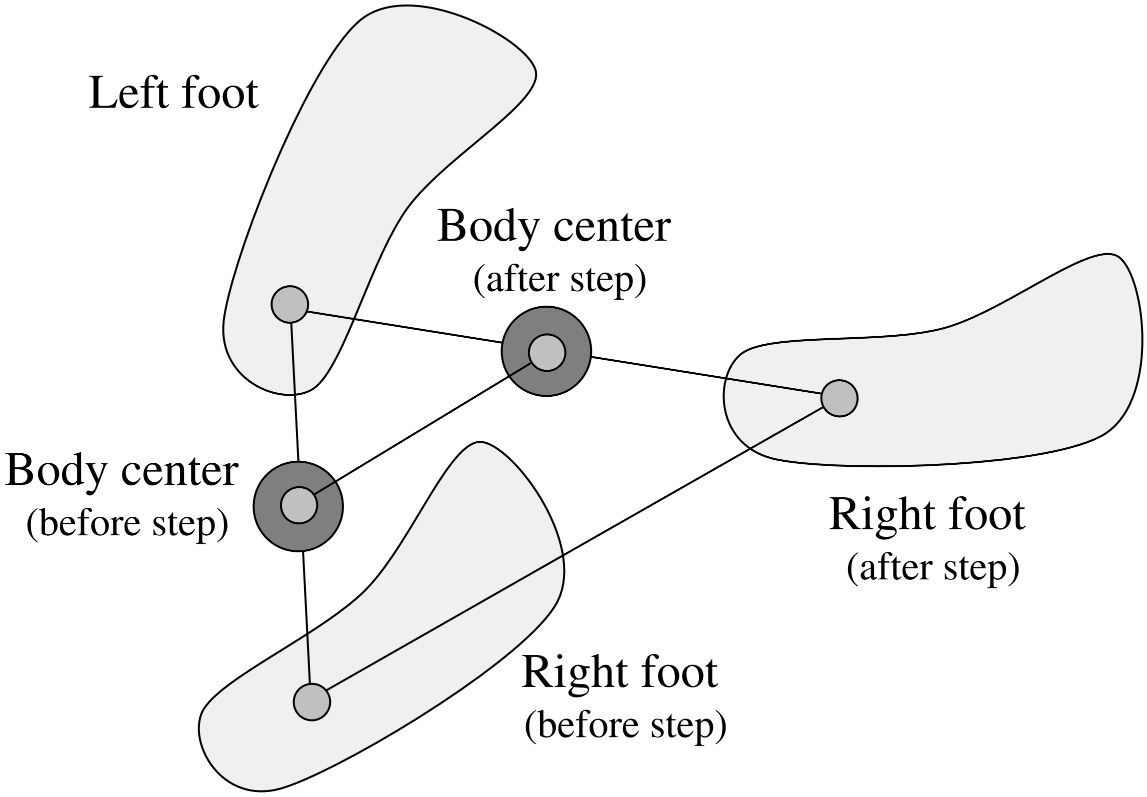

Figure 4.11: Mechanical pedestrian model. The body center is assumed to be centered on the connecting line of the two feet. Due to geometrical constraints at each step the body center experiences half the movement of the respective foot.

of each of the two feet the body center and heading undergoes a change of exact the half of the feet ones. Thus each of the step-measurements provided by the lower filters actually senses the doubled displacement and heading change with respect to the body center. Hence the extended vector of measurements is

$$\mathbf{z}_k = \left[\mathbf{z}_k^r, \mathbf{z}_k^l\right]^T \quad , \tag{4.33}$$

and the right foot measurements may be written as

$$\mathbf{z}_k^r = 2\begin{pmatrix} \Delta\mathbf{r}_k \\ \Delta\Psi_k \end{pmatrix} + \mathbf{n}_\Delta \quad , \tag{4.34}$$

and correspondingly as well for the left side

$$\mathbf{z}_k^l = 2\begin{pmatrix} \Delta\mathbf{r}_k \\ \Delta\Psi_k \end{pmatrix} + \mathbf{n}_\Delta \quad . \tag{4.35}$$

4.2.5 Joint System Error Analysis

As the step measurements are assumed to be superimposed by Gaussian noise according to (4.3) and (4.34), (4.35) respectively, an analysis of the achievable dead-reckoning performance may be carried out analytically. For the analysis a free space scenario is assumed, at which the step-measurement likelihood functions are far tighter than the dynamic restrictions that are given by the probabilistic pedestrian movement model. As already performed for the lower filter an analysis of the performance threshold of the joint system, namely the corresponding PCRB, can be performed based on a linearized system model. Assuming $\Psi_\varepsilon = 0$ the transition equation for the small-scale error state space $\delta\mathbf{x}$ of the upper filter is given according to (4.5), (4.6), (4.10), and (4.11) by

$$\delta\mathbf{x}_k = \underbrace{\begin{pmatrix} 1 & 0 & g_1 & c_{11} & c_{12} & 0 \\ 0 & 1 & g_2 & c_{21} & c_{22} & 0 \\ 0 & 0 & 1 & 0 & 0 & 1 \\ 0 & 0 & 0 & 0 & 0 & 0 \\ 0 & 0 & 0 & 0 & 0 & 0 \\ 0 & 0 & 0 & 0 & 0 & 0 \end{pmatrix}}_{\mathbf{F}_{k-1}} \delta\mathbf{x}_{k-1} \quad . \tag{4.36}$$

The elements $c_{i,j}$ denote the respective element at row i and column j of the matrix $\mathbf{C}(\Psi_{k-1})$. The terms g_1 and g_2 are the respective elements of the vector

$$\mathbf{g} = \mathbf{C}'(\Psi_{k-1})\Delta\mathbf{r}_k \quad , \tag{4.37}$$

with the derivative of the rotation matrix

$$\mathbf{C}'(\Psi) = \frac{\partial\mathbf{C}(\Psi)}{\partial\Psi} \quad . \tag{4.38}$$

According to the EKF framework the incoming step-measurement at time step k affects the covariance through

$$\mathbf{P}_k = (\mathbf{I} - \mathbf{K}_k\mathbf{H})\mathbf{P}_k^- \quad , \tag{4.39}$$

with the Kalman gain

$$\mathbf{K}_k = \mathbf{P}_k^-\mathbf{H}^T(\mathbf{H}\mathbf{P}_k^-\mathbf{H}^T + \mathbf{R})^{-1} \quad . \tag{4.40}$$

The a priori covariance computes with

$$\mathbf{P}_k^- = \mathbf{F}_{k-1}\mathbf{P}_{k-1}\mathbf{F}_{k-1}^T + \mathbf{Q} \quad , \tag{4.41}$$

where the transition matrix $\mathbf{F}_k$ follows from (4.36). The other matrices are defined as

$$\mathbf{H} = \begin{bmatrix} \mathbf{0}_{3\times3} & \mathbf{I}_{3\times3} \end{bmatrix} \quad , \tag{4.42}$$

$$\mathbf{R} = \text{diag}(\begin{bmatrix} \sigma_{\Delta x}^2 & \sigma_{\Delta y}^2 & \sigma_{\Delta\Psi}^2 \end{bmatrix}) \quad , \tag{4.43}$$

$$\mathbf{Q} = \begin{bmatrix} \mathbf{0}_{3\times3} & \mathbf{0}_{3\times3} \\ \mathbf{0}_{3\times3} & \mathbf{Q}_{3\times3}^{ped} \end{bmatrix} \quad . \tag{4.44}$$

Note that $\mathbf{Q}^{ped} = \mathrm{diag}([\sigma_x^2, \sigma_y^2, \sigma_\Psi^2])$ is matched to pedestrian movement. Whenever $\mathbf{Q}_{i,j}^{ped} >> \mathbf{R}_{i,j}$ for all matrix elements i, j, the influence of $\mathbf{Q}^{ped}$ on the error performance is almost negligible. In other words in this case the influence of the movement model becomes negligible, and the the error performance is driven almost solely by the noise of the step-measurements and the pedestrian's trajectory. For the analysis of the double-platform scenario the same approach is still viable. Nevertheless it has to be taken into account that in this case the step-measurements follow (4.34) and (4.35). Thus the measurement matrix becomes for the extended scenario

$$\mathbf{H} = \left[\begin{array}{cc} \mathbf{0}_{3\times3} & 2\mathbf{I}_{3\times3} \end{array} \right] \ . \tag{4.45}$$

4.2.6 Integration of Additional Sensors

The integration of any further available sensors as conceptually shown in Figure 4.1 can be done intuitively pleasing, given their errors are mutually independent. Using the likelihood proposal derived in Section 4.2.3, the weight update may incorporate additional sensors according to (2.38) and (2.73) via

$$w_k^\mu \propto w_{k-1}^\mu p(\mathbf{x}_k^\mu|\mathbf{x}_{k-1}^\mu) \prod_{j=1}^{M} p(\mathbf{z}_{j,k}|\mathbf{x}_k) \ . \tag{4.46}$$

Hence (4.46) just extends (4.32) by the contributions through the factors of the likelihood functions of the additional sensors.

4.3 Results

The performance achievements of shoe-mounted INS as stand-alone or coupled with GNSS and / or magnetometer has been widely reported in the literature [GM99, CG05, GLC06]. Here results are presented that consider the incorporation of nonlinear map-matching as well as the extension towards a pair of foot-mounted platforms, including computer simulation and experimental results.

4.3.1 Simulation

The performance advance with a pair of platforms is assessed by computer simulations. The simulation scenario is the following: Two pedestrians, one of them using a single shoe-mounted platform and the other a pair of them, start dead-reckoning from a known initial position and with known initial heading. The step-measurements are assumed to arrive with a rate of 1 Hz respectively, and the measurements of the second platform are delayed by 0.5 s. An error analysis corresponding to 4.2.5 is carried out along. The advantage of the double platform approach is shown in Figure 4.12(a). For the step-measurement noise $\mathbf{n}_\triangle$ standard deviations of $\sigma_{\triangle x} = \sigma_{\triangle y} = 0.1\,\mathrm{m}$ and $\sigma_{\triangle\Psi} = 2°$ are assumed. The true state trajectory is static. As the number of available measurements is doubled effectively for the double platform approach, the variance is reduced by a factor of 2 compared to the single platform case. An alternative interpretation of the result is given as follows: As it may be derived from the mechanical pedestrian model, the effective variance of the step-measurement noise with respect to the body movement is decreased by a factor of four compared to the foot movement. Along the use of a second platform doubles the number of required filter recursions due to the additional measurements, leading to a variance increase by a factor of two in turn, such that as final advance a performance gain by a factor of two is reached. Figure 4.12(b) shows the result of the corresponding error analysis. As illustrated the simulation results are very close to the behavior that is expected from the error analysis. This implies that the loss due to the suboptimal particle filter implementation is small.

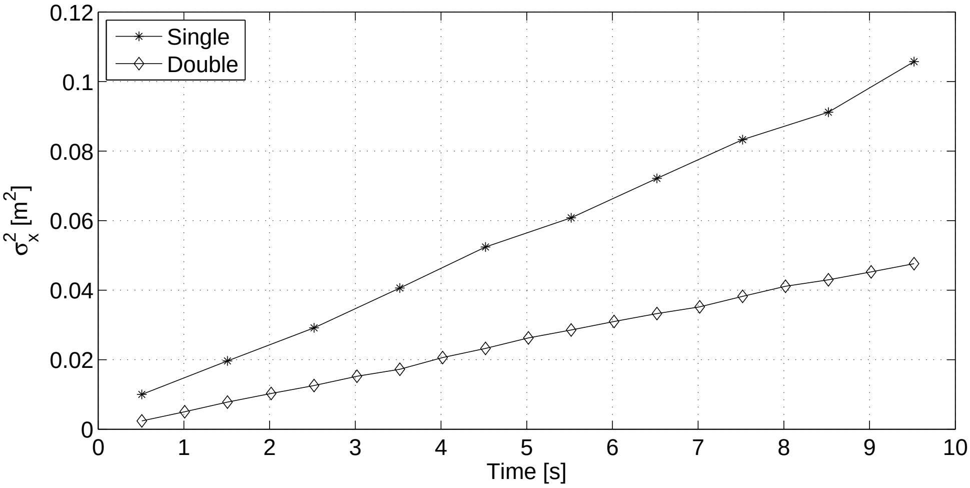

(a) Particle filter

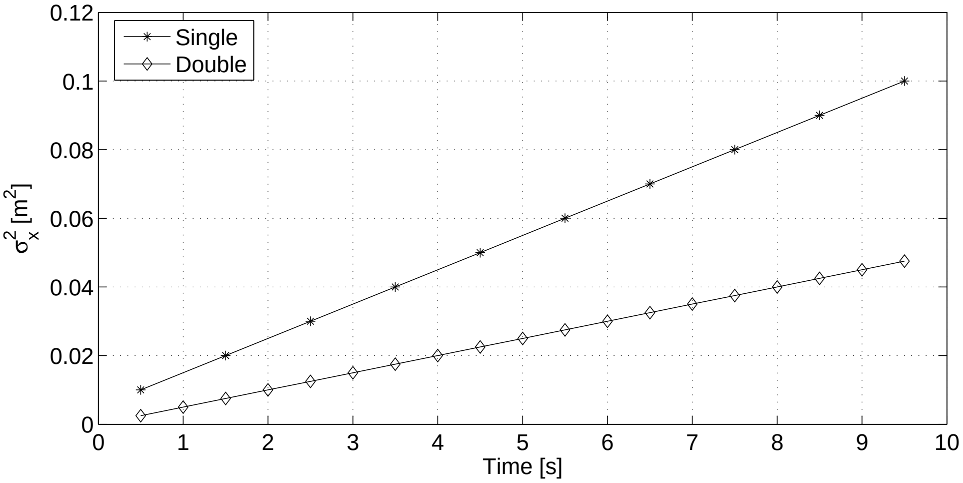

(b) Error analysis, PCRB

Figure 4.12: Comparison of the particle filter performance and the approximate analytical solution for the single and double platform approach during first 10 s of dead-reckoning. The simulation results shown in 4.12(a) are averaged over 750 Monte-Carlo runs using $N_p = 2000$ particles respectively. The results of the Monte-Carlo simulations match the analytical results quite well, where as expected an additional platform improves the performance by a factor of two.

4.3.2 Experiment

The chosen experimental scenario is the following: a pedestrian moves through a building, using only the shoe-mounted INS. The initial position is unknown, and no source of absolute

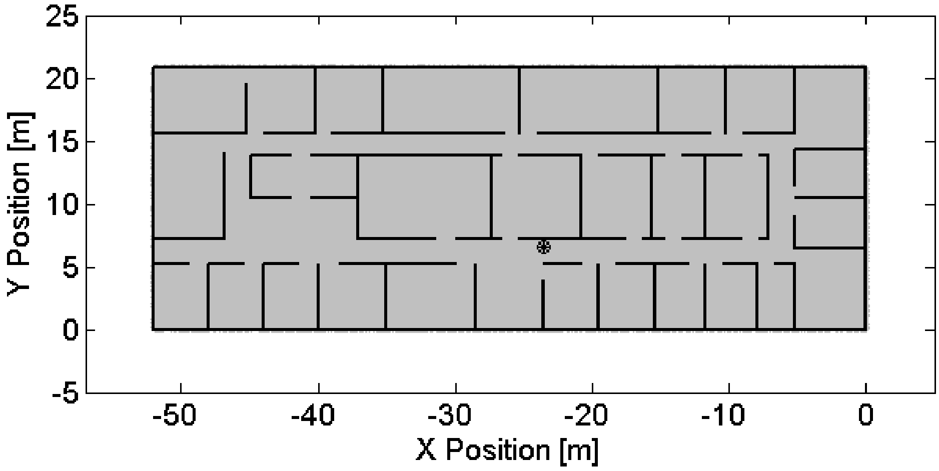

Figure 4.13: Integration with map-matching in the upper particle filter: Initially the location hypotheses (gray) are distributed uniformly across the building. The true position of the pedestrian is indicated by the cross-filled dot.

position information such as GNSS is used. The only other information available to the upper fusion filter is the building layout (floor-plan). It is also assumed that the user is within the specified building, and on a certain known floor. As Figure 4.13 shows, the upper fusion filter - the particle filter - starts with a uniform distribution of particles in the known area. Each particle, according to (4.1), includes its location and current heading. As illustrated in Figure 4.14 over time only those particles survive which are compatible with the layout of the floor-plan. In other words, those hypotheses of the state space will survive, which when moved according to the lower fusion filter's estimate, have not crossed a wall. At first there are many such hypotheses, some moving in different directions compared to the true one, but over the course of time, only one hypothesis (the correct one), survives. In the given case this was achieved in roughly one minute of walking. Naturally, the rate of convergence and the reduction of modes will be a function of the actual route which was walked and of its relation to the floor plan restrictions. In a large hall without walls there will only be moderate reduction on the size of the remaining mode compared to the case with many walls. It should be noted that the surviving modes are ”randomly” distributed across the layout and bear no relationship to the correct location (except the true mode, of course). As can be seen from the third time slice (25 s.) the true mode has already achieved its steady-state local uncertainty (of roughly the dimension of the corridor width). This implies that additional position information can be of significant value even if this is quite coarse (e.g. on the order of 10-50 meters).

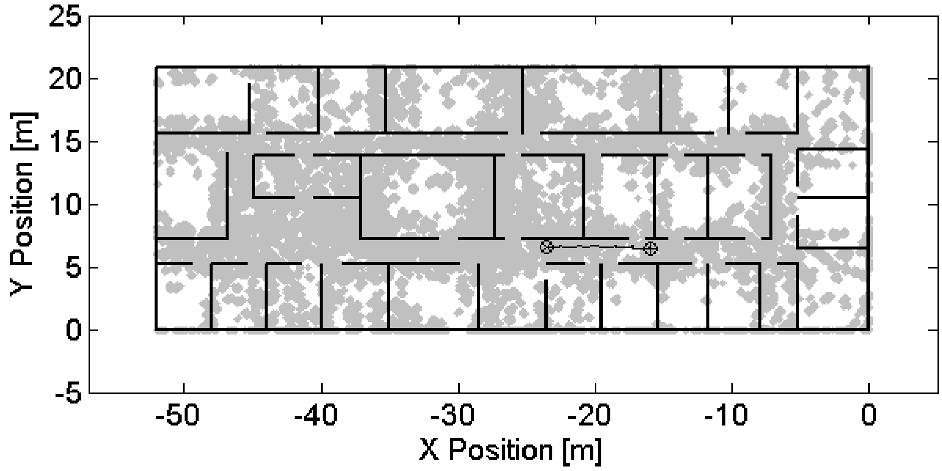

(a) After 10s

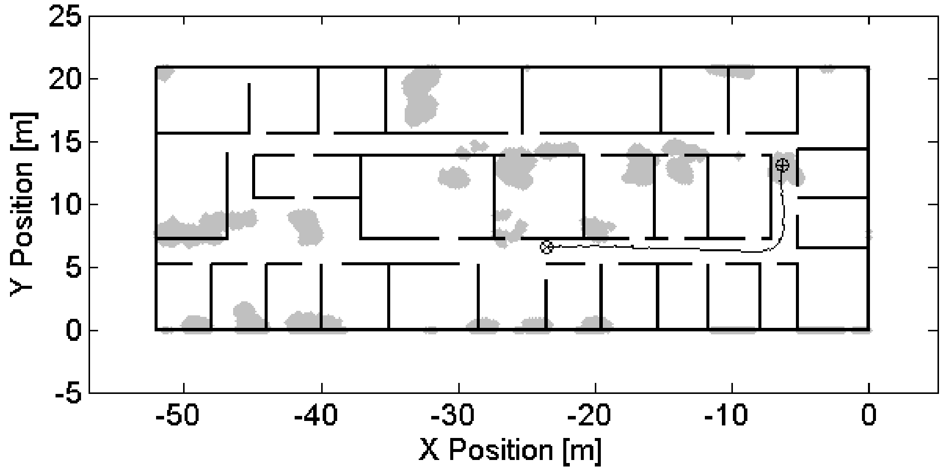

(b) After 25s

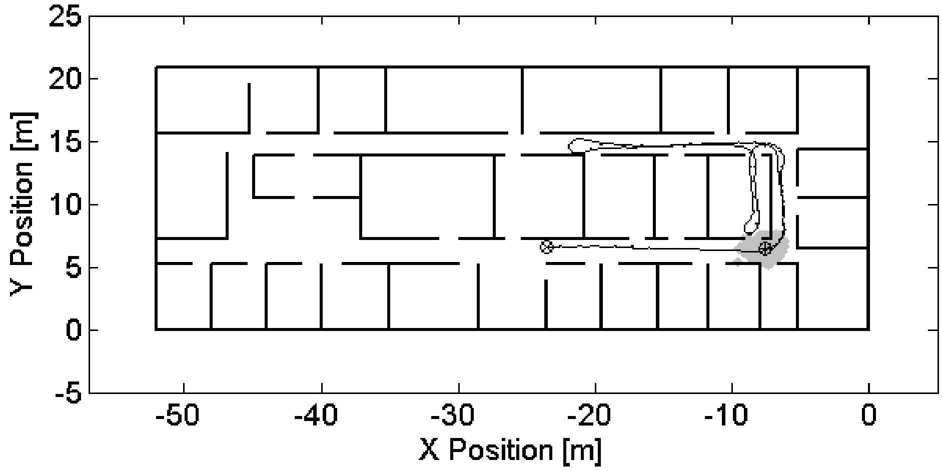

(c) After 80s

Figure 4.14: Integration with map-matching in the upper particle filter: A pedestrian wearing the foot-mounted sensor walked the indicated track (black). As the pedestrian walks the a posteriori position estimate (gray) becomes increasingly accurate, after 80 s it is unimodal.

Chapter 5

Application Examples

In the previous chapters it was shown how the concept of Bayesian filtering can be applied successfully to the problem of multipath mitigation in satellite navigation receivers and to the integration of foot-mounted low-cost inertial sensors. In the following chapter this work will be extended to the design and development of two personal navigation systems and algorithms, which are representative for two real world application examples, which gain advantage from the Bayesian approach. At first it is shown how a foot-mounted inertial navigation system is joined beneficially with a WLAN fingerprinting system via an extended Kalman filter, which is shown to successfully solve the problem of inertial alignment and drift. Subsequently based on the approach discussed in chapter 4 a concept for a modular multi-sensor fusion platform is introduced, which is able to plug in easily any available nonlinear sensor and mobility model due to a flexible particle filter implementation. In both cases real world data is used to assess and to quantify the performance of the proposed sensor fusion algorithms.

5.1 A Joint WLAN/INS Pedestrian Positioning System

In the majority of buildings in which people require personal navigation, for example in airports, public buildings, and company premises (e.g. to be guided to a certain room or office) there now exists a dense installation of WLAN infrastructure [ISO99, IEE99], often operated by different operators, which may be used for localization [ZHD06, KHLH03, RMT$^+$02, QLPD07]. A key enabler for truly ubiquitous personal positioning and navigation will be the capability to be as autonomous as possible, whilst requiring a minimal amount of dedicated infrastructure and whilst building on the rapid advances in portable data processing and sensors. The key idea of this section is to combine an existing WLAN infrastructure with foot mounted inertial sensors [EM06b] based on the concept of hierarchical Bayesian filters as introduced in Chapter 4. A real-time processing system is developed, which employs cascaded extended Kalman filters, one processing the inertial sensor data to obtain step-wise displacement measurements and the other for fusing them with the WLAN data. The federated processing allows to run both filters at their local sampling rates, which reduces overall complexity without suffering from significant loss of final estimation accuracy. The goal is to obtain and process all the sensor data locally, and without any need of registration with the local infrastructure, which is achieved by employing WLAN fingerprinting based on the signal power (e.g. [OBS$^+$05]), where the only information needed at the local device is a fingerprinting database for the local building. The database itself can be maintained and distributed by an entity independent of the local wireless infrastructure domain. The basic approach to use as few calibration locations as possible and to rely on the short-term accuracy of foot mounted inertial PDR ”in between” these points. The role of the WLAN positioning here is therefore to provide long term accuracy in the area of interest. WLAN fingerprinting fulfills the requirement of needing no association with the actual access points and is relatively energy efficient. The fingerprinting itself is a very simple process, requiring per each database location a calibration measurement of the available WLAN stations that lasts just a few seconds. In contrast, in the work of Woodman et al. [WH08] very coarse WLAN positioning was only used to reduce the initial ambiguities of map aided inertial navigation. The work in [SPSS$^+$07] describes how fingerprinting can be simplified by using an INS (not foot mounted) during calibration and how actual performance is enhanced during positioning. The pursued approach using a foot mounted INS is foreseen perform better in situations where WLAN positioning is not available for any significant length of time during which a standard INS approach (no foot mounting; no zero update) would drift too far. It is emphasized that in difference to the work presented in [EM06b, KR08b, KR08a, WH08] and in difference to the approach introduced in Chapter 4 the proposed algorithm does not incorporate any information about the layout of the building, i.e. the building map. After an derivation of the filtering algorithm, in particular for the filter joining the WLAN data with the step displacement estimates, the software and hardware implementation of the real-time positioning system is described. Finally the accuracy of the combined system is quantitatively evaluated in a real building against ground-truth.

5.1.1 WLAN Fingerprinting

Concerning the localization via WLAN RSS two primary methods for location determination can be distinguished. The one class of methods is based on path loss models, where the characteristic signal strength profile over distance in space from the access points is used to derive the location [KHLH03]. The other class relies on previously recorded calibration data upon which an RF map of a building has been created [ZHL$^+$05, ZHD06, YAS03, BP00]. In this case the location information may be inferred through the correlation of the observed RSS measurements with the RF map data, which is commonly denoted as *fingerprinting*. The main drawback of the fingerprinting approach is that generation and maintenance of the RF maps is time-consuming and expensive when performed over wide areas. Nevertheless it typically results in higher accuracy compared to other methods.

A fingerprinting system provides basically two major functional modes, one for the initial calibration, and one for the actual operation, where the localization takes place. The fingerprinting database is established during the calibration procedure via RSS measurements that are taken at a number of topographically referenced calibration points. As depicted in Figure 5.1 for each calibration point the RSS manager collects the readings from the WLAN driver, and establishes a fingerprint that is then stored into the database. Generally the system accuracy increases with the number of calibration points used. However, it has to be taken into account that a too close spacing of the points leads to similar RSS profiles and thus to rather small performance gain, such that an extensive calibration over large areas practically does not always justify the additional efforts. During the operation of the system the continual scans from the

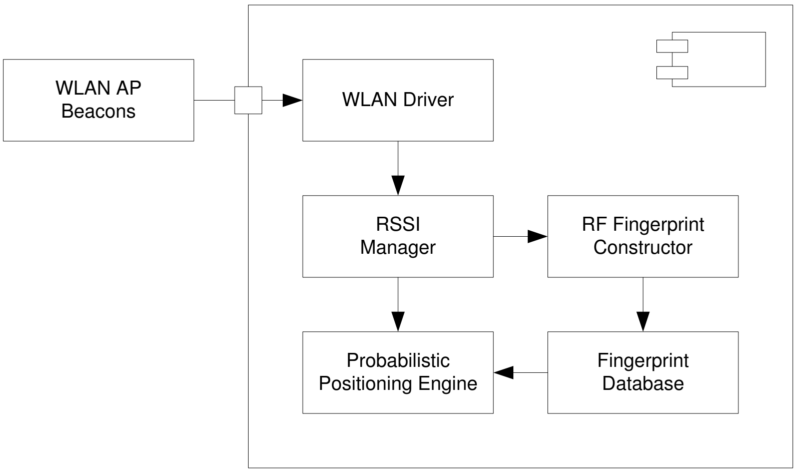

Figure 5.1: System overview of the WLAN fingerprinting component. The previously established fingerprinting database serves as the basis for the location determination during the operational phase.

WLAN driver are passed through the RSS manager to the positioning engine, which computes a distance measure for each of the calibration points, by comparing each one to the observed RSS readings. The distance for each calibration point is defined by the sum over all access points j according to

$$D_p = \sum_j \sum_q \left| \mathbf{z}_j^{\mathrm{RSS}} - \bar{\mathbf{z}}_{j,q}^{\mathrm{RSS}} \right| p_{j,q} \quad , \tag{5.1}$$

where $\mathbf{z}_j^{\mathrm{RSS}}$ is the observed RSS for the access point j, $\bar{\mathbf{z}}_{q,j}^{\mathrm{RSS}}$ is the recorded RSS stored in the fingerprinting database, and $p_{q,j}$ is the likelihood of measuring the reading at the given calibration point. Corresponding to Figure 5.2 the summation over the index q refers to the sum over all database entries per access point. The location estimate is then the calibration point corresponding to the index yielding the minimum distance:

$$\hat{p} = \arg\min_p (D_p) \quad . \tag{5.2}$$

To enhance the stability of the location estimation, a best of three approach is used, where the latest estimate is returned as the current location whenever no dominant location can be determined.

5.1.2 Inertial Step Sensing

To incorporate the foot-mounted inertial sensors the step estimation filter derived in Section 4.2.2 is used to compute the change in position $\Delta \mathbf{r}_k$ and the change in heading $\Delta \Psi_k$ per each step the pedestrian makes. The resulting step-measure is thus

$$\Delta \mathbf{x}_k = \begin{pmatrix} \Delta \mathbf{r}_k \\ \Delta \Psi_k \end{pmatrix} \quad . \tag{5.3}$$

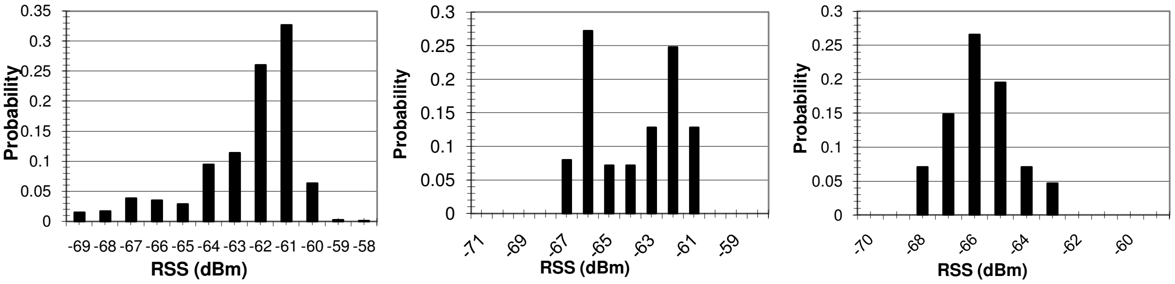

Figure 5.2: Example of likelihood tables of a calibration point for different access points. As shown in Figure 5.1 the likelihood values are provided by the fingerprinting database, where for every calibration point the probability of receiving a specific RSS from each of the access points is stored.

5.1.3 Main Integration Filter

The objective is now to integrate the WLAN-fingerprinting with the inertial step-sensor. This is done via a main integration filter, in which the pedestrian's position $\mathbf{r}_k$ and her heading Ψ_k is tracked. The overall signal processing is illustrated in Figure 5.3. The state vector is written as

$$\mathbf{x}_k = \begin{pmatrix} \mathbf{r}_k \\ \Psi_k \end{pmatrix} . \tag{5.4}$$

In difference to (4.1) the step measures are not considered to be a part of the state vector. Their treatment is addressed subsequently.

Movement Model

The movement model is used to characterize the temporal evolution of the state $\mathbf{x}_k$ in order to reflect the physical constraints that are imposed on the movement of a pedestrian. As it was shown in Chapter 4 this may include in indoor environments as well any restrictions which are imposed by the building layout. Nevertheless in this application scenario the building layout is not known. Hence formally, the new state $\mathbf{x}_k$ is assumed to depend only on the previous state $\mathbf{x}_{k-1}$, the current step-measure $\Delta\mathbf{x}_k$ and a noise term $\mathbf{n}^{\mathrm{d}}_{k-1}$ via the function

$$\mathbf{x}_k = \mathbf{f}_{k-1}(\mathbf{x}_{k-1}, \Delta\mathbf{x}_k) + \mathbf{n}^{\mathrm{d}}_{k-1} \ , \tag{5.5}$$

where in particular the new location and heading depend on the past state and on the step-measure through

$$\mathbf{r}_k = \mathbf{r}_{k-1} + \mathbf{C}(\Psi_\varepsilon)\mathbf{C}(\Psi_{k-1})\Delta\mathbf{r}_k + \mathbf{n}_{\Delta r,k-1} \ , \tag{5.6}$$

$$\Psi_k = \Psi_{k-1} + \Delta\Psi_k + n_{\Delta\Psi,k-1} \ , \tag{5.7}$$

where the rotation matrices $\mathbf{C}(\bullet)$ are defined by (4.7). The vectors $\mathbf{n}^{\mathrm{d}} = [\mathbf{n}^T_{\Delta r}, n_{\Delta\Psi}]^T$ and $\mathbf{n}_{\Delta r} = [n_{\Delta x}, n_{\Delta y}]^T$ comprise realizations of zero-mean uncorrelated Gaussian noise processes of variance $\sigma^2_{\Delta x}$, $\sigma^2_{\Delta y}$, and $\sigma^2_{\Delta\Psi}$ respectively, which are adjusted to reflect the uncertainty of the step-measure. According to Chapter 4 the angle Ψ_ε represents the average misalignment of the foot-mounted IMU with respect to the true body heading.

Measurement Model

The position estimate obtained by the WLAN fingerprinting filter is used as an position measurement $\mathbf{z}_k^{\mathrm{WLAN}}$ in the main integration filter and is assumed to depend only on the current state $\mathbf{x}_k$ and the noise term $\mathbf{n}^{\mathrm{WLAN}}$ via

$$\begin{aligned} \mathbf{z}_k^{\mathrm{WLAN}} &= \mathbf{h}_k(\mathbf{x}_k) + \mathbf{n}_k^{\mathrm{WLAN}} \\ &= \mathbf{r}_k + \mathbf{n}_k^{\mathrm{WLAN}} \quad , \end{aligned} \tag{5.8}$$

with $\mathbf{n}^{\mathrm{WLAN}}$ being zero-mean uncorrelated Gaussian noise of variance σ^2_{WLAN}, which is adjusted to reflect the uncertainty of the fingerprinting-based position estimate.

Filter Design

Since neither the building layout nor further sensors are considered there is no need to incorporate any further nonlinear constraints than the one given by (5.6). But this relation is rather moderate with respect to nonlinearity and thus an extended Kalman filter is adequate to implement the main integration filter, in particular as all relevant noise sources are Gaussian. Given these premises the standard implementation of the EKF may be applied (see Section 2.3.1): Given initial mean $\mathbf{x}_0 = \bar{\mathbf{x}}_0$ and the associated initial covariance $\mathbf{P}_0 = \bar{\mathbf{P}}_0$ at each filter iteration the prediction step computes recursively the parameters of the Gaussian a priori PDF, which are mean

$$\hat{\mathbf{x}}_k^- = \mathbf{f}_{k-1}(\hat{\mathbf{x}}_{k-1}, \Delta\mathbf{x}_k) \quad , \tag{5.9}$$

and covariance

$$\mathbf{P}_k^- = \mathbf{F}_k \mathbf{P}_{k-1} \mathbf{F}_k^T + \mathbf{Q}_k \quad . \tag{5.10}$$

The Jacobian of the system dynamics is given by

$$\begin{aligned} \mathbf{F}_k &= \left. \frac{\partial \mathbf{f}_{k-1}(\mathbf{x}_{k-1}, \Delta\mathbf{x}_k)}{\partial \mathbf{x}_{k-1}} \right|_{\hat{\mathbf{x}}_{k-1}} \\ &= \begin{pmatrix} 1 & 0 & g_1 \\ 0 & 1 & g_2 \\ 0 & 0 & 1 \end{pmatrix} \quad . \end{aligned} \tag{5.11}$$

The terms g_1 and g_2 are the respective elements of the vector

$$\mathbf{g} = \mathbf{C}(\Psi_\varepsilon)\mathbf{C}'(\Psi_{k-1})\Delta\mathbf{r}_k \quad , \tag{5.12}$$

with the derivative of the rotation matrix according to (4.38). In the subsequent update step the parameters of the Gaussian a posteriori PDF are computed recursively at each iteration. The a posteriori mean computes with

$$\hat{\mathbf{x}}_k = \hat{\mathbf{x}}_k^- + \mathbf{K}_k \left(\mathbf{z}_k^{\mathrm{WLAN}} - \mathbf{h}_k(\hat{\mathbf{x}}_k^-) \right) \quad , \tag{5.13}$$

and the a posteriori covariance with

$$\mathbf{P}_k = (\mathbf{I} - \mathbf{K}_k \mathbf{H}_k) \mathbf{P}_k^- \quad , \tag{5.14}$$

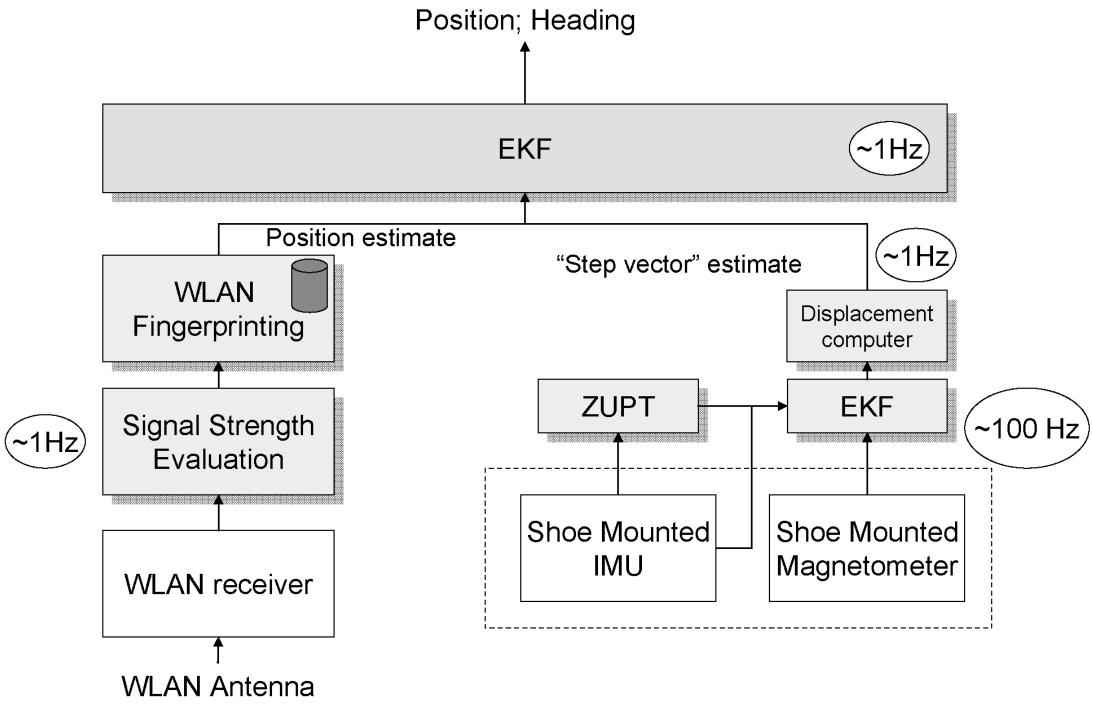
Position; Heading
EKF
~1Hz
Position estimate
"Step vector" estimate
~1Hz
WLAN Fingerprinting
Displacement computer
Signal Strength Evaluation
~1Hz
ZUPT
EKF
~100 Hz
Shoe Mounted IMU
Shoe Mounted Magnetometer
WLAN receiver
WLAN Antenna

Figure 5.3: This figure shows the complete system with two layers of processing: a lower one for the WLAN position estimate and step computation which are then fused in a superordinate EKF.

The Kalman gain is given by

$$\mathbf{K}_k = \mathbf{P}_k^- \mathbf{H}_k^T (\mathbf{H}_k \mathbf{P}_k^- \mathbf{H}_k^T + \mathbf{R}_k)^{-1} \ , \tag{5.15}$$

with the Jacobian of the measurement equation

$$\begin{aligned} \mathbf{H}_k &= \left. \frac{\partial \mathbf{h}_k(\mathbf{x}_k)}{\partial \mathbf{x}_k} \right|_{\hat{\mathbf{x}}_k^-} \\ &= \begin{pmatrix} 1 & 0 & 0 \\ 0 & 1 & 0 \end{pmatrix} \ . \end{aligned} \tag{5.16}$$

The other matrices become

$$\mathbf{R}_k = \mathrm{diag}([\ \sigma^2_{\mathrm{WLAN}} \quad \sigma^2_{\mathrm{WLAN}}\ ]) \ , \tag{5.17}$$

$$\mathbf{Q}_k = \mathrm{diag}([\ \sigma^2_{\Delta x} \quad \sigma^2_{\Delta y} \quad \sigma^2_{\Delta \Psi}\ ]) \ . \tag{5.18}$$

5.1.4 System Evaluation

The purpose of the undertaken system evaluation, whose findings are presented now, is to determine the performance of the standalone WLAN fingerprinting approach and to compare it subsequently to the performance of the joint WLAN/INS system in order to quantify the enhancement by the sensor fusion.

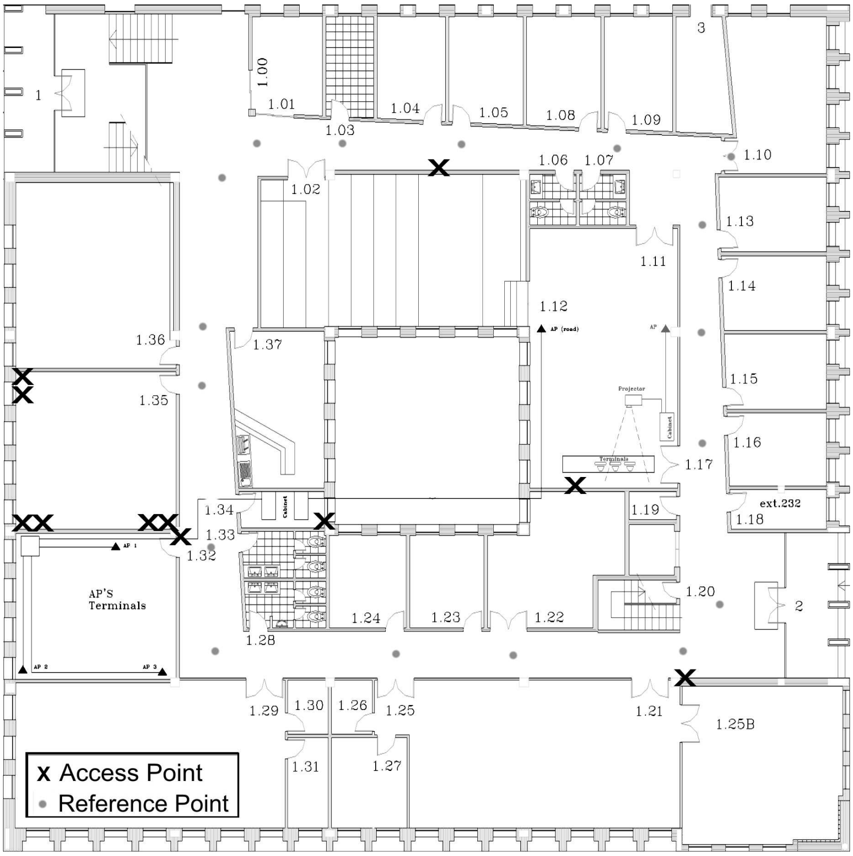
1
1.00
1.01
1.03
1.04
1.05
1.08
1.09
3
1.10
1.06
1.07
1.02
1.13
1.11
1.14
1.12
AP (road)
AP
1.36
1.37
1.15
Projector
1.35
Cabinet
1.16
Terminals
1.17
1.34
ext.232
1.19
1.18
1.33
1.32
AP 1
AP'S
Terminals
1.20
2
1.24
1.23
1.22
1.28
AP 2
AP 3
1.29
1.30
1.26
1.25
1.21
1.25B
1.31
1.27
X Access Point
● Reference Point

Figure 5.4: Floor plan of the test building with eleven access points (black crosses) and 17 ground truth reference points (grey dots), which are distributed evenly on the hallway.

Test Scenario

The system is tested in a university building. As illustrated in Figure 5.4 the building is equipped with eleven WLAN access points on one floor. The detection of different offices and rooms is expected to be fairly easy by WLAN fingerprinting as the infrastructure (in particular walls) is expected to produce room-wise distinct fingerprinting profiles. Hence the test scenario comprises three laps of a circular walk in the hallway. A digital floor plan is used as absolute position reference system, where its pixels coordinates are transformed with a known conversion factor into meter scale. The calibration of the WLAN fingerprinting system was performed on calibration points that were taken approximately every 2.5 m, with the RSS readings being taken once per second. The calibration measurements were taken by holding a laptop at a fixed height (approx. 1.2 m), with slight motion to build up a likelihood database over a small region around the calibration point. The lookup tables were constructed by sets of 60 measurement samples for each of the calibration points respectively. At each calibration point calibration measurements were performed for at least three access points. The coordinates of each calibration point were defined by putting markers on the digital floor plan to designate their topographic location. For the evaluation a set of 17 ground truth reference points (GTRPs) was marked on the digital map and on the floor of the building, which was followed then precisely.

The implementation of the positioning system is realized in three separate subsystems: The

WLAN fingerprinting, the inertial stride estimation, and the joint WLAN/INS fusion filter. The WLAN fingerprinting and the stride estimation modules communicate in client-server mode to the main fusion module, as both sensor connections are implemented in `C` while the higher level Kalman filter is implemented in `Java`. In addition the main fusion features a visualization application. The subsystems are distributed on two laptops. Laptop 1, with a Windows OS (for driver reasons), implements the interface to the IMU, the stride estimation filter, and the client part of the connection to the main filter. Laptop 2 runs Linux with two wireless network cards for the fingerprinting module. One of the two network cards is used to ensure the consistency of the measurement data results during the calibration phase, and to allow for channel hopping without disrupting the network communications. The second wireless card is used to send real-time location updates to other displays for live presentation of the WLAN data. Furthermore the main Kalman filter is executed on laptop 2 as well, where it receives the WLAN and step data via its implemented connection server. After the fusion filter has calculated a new position, the estimate is stored in a file and passed to the visualization application. To reduce network related delays, both laptops are connected by an ethernet cable. The collected sensor data is stored together with the actual system timestamps at the time of reception, which eases the synchronization of the data during the later evaluation. The raw inertial sensor data is stored on on laptop 1. The input from the WLAN fingerprinting and from the low level inertial filter as well as the output of the sensor fusion is stored on laptop 2. Furthermore the system timestamps are recorded on laptop 2 along with the result of the sensor fusion whenever a reference point is passed.

Results

For evaluation of the gathered data the solely WLAN fingerprinting-based position and the fused WLAN/INS position are compared with the true position as given by the track over the sequence of reference points. The performance measure used is the absolute distance from the actual estimated position to the position of reference point that temporally corresponds to this estimate. Figure 5.5(a) shows the results for each of the 49 recorded estimation points, which were passed during the three laps of the experimental walk. The results for WLAN standalone are presented by the dashed line and the fused position error is shown with the solid line. Computing the arithmetic mean error during the test track for both techniques yields:

- 3.2 meters for pure WLAN fingerprinting
- 1.5 meters for the fusion of fingerprinting and inertial data.

In comparison the fused result is more stable and smooth than the fingerprinting approach, since the INS prevents big jumps that happen occasionally with pure fingerprinting, particularly whenever a wrong sample point is considered as current position. On the other side the fingerprinting partially provides very good results, specifically when the GTRPs are very close to correctly determined fingerprinting sample points. This is also revealed by Figure 5.5(b), which shows the normalized cumulative error histogram: The WLAN Fingerprinting provides more than 20% of errors below half a meter, but also 20% of errors over 4 meters - which appear in the fused results only with a frequency below 5%. The majority of the errors of the joint WLAN/INS estimate is around one meter. An illustration of the sensor fusion is given in Figure 5.6

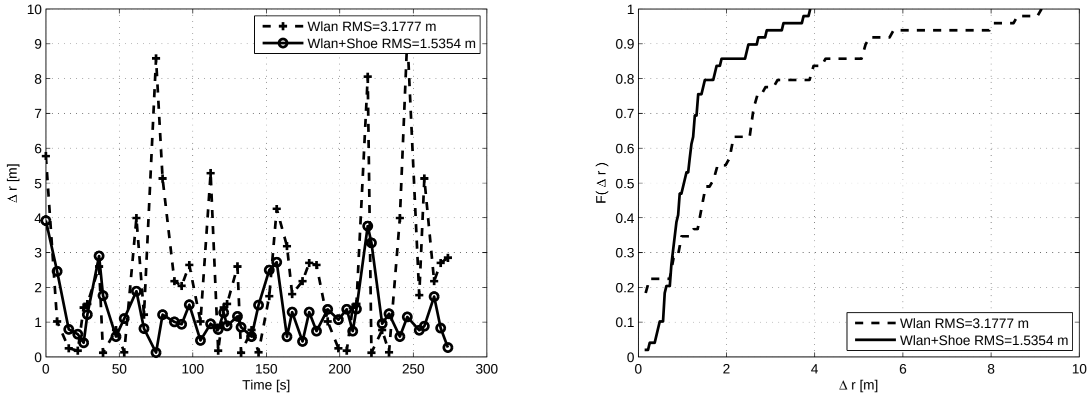

(a) Error over time

(b) Normalized cumulative error histogram

Figure 5.5: Position error over walking time (Figure 5.5(a)) and cumulative probability distribution of errors (Figure 5.5(b)). The errors of the joint WLAN/INS system are significantly smaller than those of the sole WLAN fingerprinting thanks to the sensor fusion, which joins two complementary sensors: Noisy but long-term-stable WLAN fingerprinting and smooth but drifting INS.

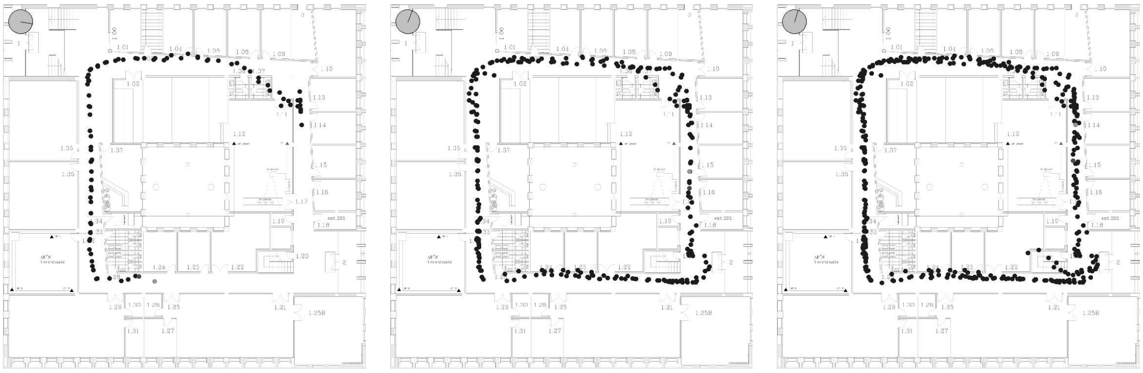

(a) 1st lap fusion

(b) 2nd lap fusion

(c) 3rd lap fusion

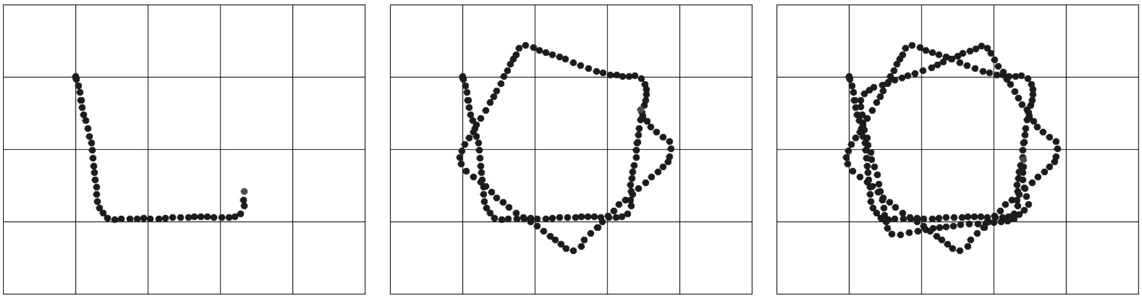

(d) 1st lap PDR

(e) 2nd lap PDR

(f) 3rd lap PDR

Figure 5.6: Illustration of the joint WLAN/INS estimate (Figures 5.6(a), 5.6(b), 5.6(c)) and the sole inertial PDR solution (Figures 5.6(d), 5.6(e), 5.6(f)) during the three laps walked. The continuous update of the joint filter by the WLAN measurements compensates for the drift of the INS.

5.2 A Multi-Sensor Framework for Pedestrian Navigation

In this section the architectural sensor fusion approach introduced in Chapter 4 is pursued further. Specifically the framework is extended by incorporating additional valuable sensors that are suitable for pedestrian navigation. A GNSS receiver is added for enhancing the navigation outdoors, where it may be regarded as the most valuable sensor. To aid the navigation in indoor environments an active RFID-based localization system is added, which operates via distributed tags and user-worn RFID reader. Furthermore an electronic compass is incorporated to aid the navigation through improved directional information. Finally a baro-altimeter is included to allow for the detection of floor transitions when moving indoors. Since the approach introduced in Chapter 4 is basically preserved, the architecture of the sensor fusion system, which is depicted in Figure 5.7, is actually quite similar to the one shown in Figure 4.1, except for the novel sensors, which previously were optionally and not specified further. To study the performance of the particle filtering approach compared to the fusion via a simpler and computationally less demanding algorithm, the Kalman filter introduced in Section 5.1 is adapted to the novel sensors as well by omitting the WLAN component and by adding measurement models for the data that is provided by the new sensors.

5.2.1 Incorporation of Sensors

The incorporation of additional sensors can be performed easily for both, the particle filter and the Kalman filter, since the determination of the relevant state space and the modeling of the system dynamics has been addressed already within the previous chapters and sections of this thesis. As already discussed in Section 4.2.6 the employed particle filter, which uses a proposal density according to the provided step-estimates, may incorporate the novel sensors according to (4.46) by multiplying the particles' weights by the product of the additionally available likelihood values, given the joint likelihood value over all novel sensors can be written in the product form (2.38). Since the Kalman filter represents the Gaussian a posteriori and a priori PDFs and the likelihood function analytically by mean and covariance, the incorporation of additional sensors is not as convenient as for the particle filter, but still feasible. Either the Kalman filter switches its measurement matrix depending on the available sensor data, or a modular approach is selected, which carries out the update equations separately for each available measurement. In the modular solution the mean after incorporation of sensor j equals

$$\hat{\mathbf{x}}_k^j = \hat{\mathbf{x}}_k^{j-} + \mathbf{K}_{j,k}\left(\mathbf{z}_{j,k} - \mathbf{h}_k^j(\hat{\mathbf{x}}_k^{j-})\right) \quad , \tag{5.19}$$

and the corresponding covariance becomes

$$\mathbf{P}_k^j = (\mathbf{I} - \mathbf{K}_{j,k}\mathbf{H}_{j,k})\mathbf{P}_k^{j-} \quad , \tag{5.20}$$

with the Kalman gain

$$\mathbf{K}_{j,k} = \mathbf{P}_k^{j-}\mathbf{H}_{j,k}^T(\mathbf{H}_{j,k}\mathbf{P}_k^{j-}\mathbf{H}_{j,k}^T + \mathbf{R}_{j,k})^{-1} \quad . \tag{5.21}$$

In this case $\hat{\mathbf{x}}_k^{j-}$ and $\mathbf{P}_k^{j-}$ denote mean and covariances before the filter has been updated by the data of sensor j. Thus, given after a prediction step there is the measurement data $\mathbf{z}_{j,k}$, $j = 1, \ldots, M$ available, (5.19), (5.21), and (5.20) are computed M times successively, with each time using $\mathbf{z}_{j,k}$ according to the measurement received from sensor j and $\mathbf{H}_{j,k}$, $\mathbf{R}_{j,k}$, and $\mathbf{h}_k^j(\mathbf{x}_k)$ corresponding to the characterization of the respective sensor.

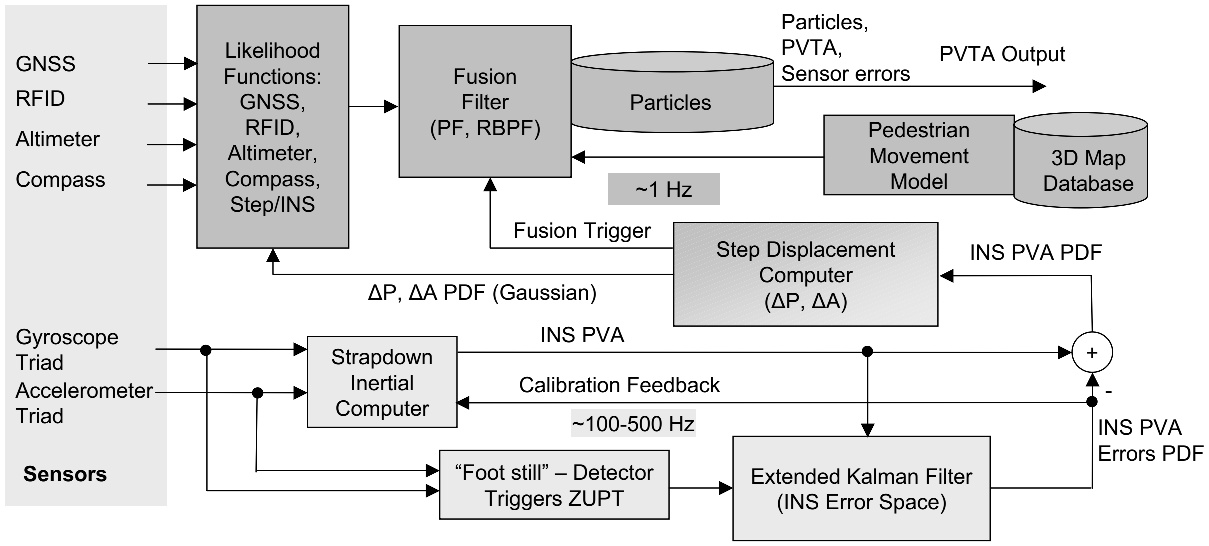
GNSS
RFID
Altimeter
Compass
Gyroscope Triad
Accelerometer Triad
Sensors
Likelihood Functions: GNSS, RFID, Altimeter, Compass, Step/INS
Fusion Filter (PF, RBPF)
Particles
Particles, PVTA, Sensor errors
PVTA Output
Pedestrian Movement Model
3D Map Database
~1 Hz
Fusion Trigger
Step Displacement Computer (ΔP, ΔA)
INS PVA PDF
ΔP, ΔA PDF (Gaussian)
Strapdown Inertial Computer
INS PVA
+
-
Calibration Feedback
~100-500 Hz
INS PVA Errors PDF
"Foot still" – Detector Triggers ZUPT
Extended Kalman Filter (INS Error Space)

Figure 5.7: Architecture of the sensor fusion framework, which now integrates GNSS, compass, altimeter, RFID, inertial sensors, and a map-based mobility model.

5.2.2 Characterization of Sensors

Subsequently for each of the newly incorporated sensors the measurement model is specified, including a Gaussian approximation that can be used by the extended Kalman filter.

GPS Receiver

In Chapter 3 advanced state space and measurement models for satellite navigation were introduced, specifically addressing the use of signal level likelihood functions (3.3). Within the scope of this chapter a much simpler model will be used, at first due to complexity reason, and secondly since todays commercially available GPS receivers do not yet provide the appropriate interfaces to obtain the required data. Thus here the most simple measurement model that can be used for a GNSS receiver is employed corresponding to the loosely coupled integration approach (see Section 2.3.2), in which the position solution of the GNSS receiver is treated as a measurement that is assumed to be affected by Gaussian noise. Consequently the measurement model for the GPS receiver may be expressed as

$$\begin{aligned} \mathbf{z}_k^{\mathrm{GPS}} &= \mathbf{h}_k^{\mathrm{GPS}}(\mathbf{x}_k) + \mathbf{n}_k^{\mathrm{GPS}} \\ &= \mathbf{r}_k + \mathbf{n}_k^{\mathrm{GPS}} \quad , \end{aligned} \tag{5.22}$$

with $\mathbf{n}_k^{\mathrm{GPS}} = [n_{x,k}^{\mathrm{GPS}}, n_{y,k}^{\mathrm{GPS}}]^T$ being zero-mean white Gaussian noise of variance σ_{GPS}^2 respectively. Obviously this assumption is practically questionable, since GNSS positioning errors are often temporally correlated, e.g. due to multipath effects. Since approaches to circumvent this problem have been discussed extensively in Chapter 3 of this thesis, an attempt to model this kind of correlated noise is omitted here. Using (5.22) the likelihood function for the GPS data can be expressed as

$$p(\mathbf{z}_k^{\mathrm{GPS}}|\mathbf{x}_k) = \frac{1}{\sqrt{2\pi\sigma_{\mathrm{GPS}}^2}} \exp\left(-\frac{(\mathbf{z}_k^{\mathrm{GPS}} - \mathbf{r}_k)^H(\mathbf{z}_k^{\mathrm{GPS}} - \mathbf{r}_k)}{2\sigma_{\mathrm{GPS}}^2}\right) \quad . \tag{5.23}$$

Since (5.23) is already linear and Gaussian the derivation of both measurement and the measurement noise matrix is quite simple:

$$\mathbf{H}_k^{\mathrm{GPS}} = \left.\frac{\partial \mathbf{h}_k^{\mathrm{GPS}}(\mathbf{x}_k)}{\partial \mathbf{x}_k}\right|_{\hat{\mathbf{x}}_k^-} = \begin{pmatrix} 1 & 0 & 0 \\ 0 & 1 & 0 \end{pmatrix} \quad , \tag{5.24}$$

$$\mathbf{R}_k^{\mathrm{GPS}} = \begin{pmatrix} \sigma_{\mathrm{GPS}}^2 & 0 \\ 0 & \sigma_{\mathrm{GPS}}^2 \end{pmatrix} \quad . \tag{5.25}$$

Compass

For the compass, which provides a measurement of the current heading, a simple linear Gaussian measurement model is assumed as well, which may be expressed via

$$\begin{aligned} z_k^{\mathrm{COM}} &= \mathbf{h}_k^{\mathrm{COM}}(\mathbf{x}_k) + n_k^{\mathrm{COM}} \\ &= \Psi_k + n_k^{\mathrm{COM}} \quad , \end{aligned} \tag{5.26}$$

with n_k^{COM} being zero-mean white Gaussian noise of variance σ_{COM}^2. Again this is generally a quite coarse assumption, since it does not take into account the temporal and spatial correlation of the compass error, which often occurs in indoor environments due to nearby disturbing materials and current-carrying structures such as cables or wires. Nevertheless due to a lack of an improved compass noise model (5.26) is assumed to hold and the corresponding likelihood function may be written as

$$p(z_k^{\mathrm{COM}}|\mathbf{x}_k) = \frac{1}{\sqrt{2\pi\sigma_{\mathrm{COM}}^2}} \exp\left(-\frac{(z_k^{\mathrm{COM}} - \Psi_k)^2}{2\sigma_{\mathrm{COM}}^2}\right) \quad . \tag{5.27}$$

Practically the problem of correlated compass noise can be tackled to a certain extent by assuming a pessimistic value for σ_{COM}^2, such that on average the impact of the correlated noise is reduced. Since (5.27) is again already linear and Gaussian the correpsonding measurement and measurement noise matrix for the Kalman filter update compute with:

$$\mathbf{H}_k^{\mathrm{COM}} = \left.\frac{\partial \mathbf{h}_k^{\mathrm{COM}}(\mathbf{x}_k)}{\partial \mathbf{x}_k}\right|_{\hat{\mathbf{x}}_k^-} = \begin{pmatrix} 0 & 0 & 1 \end{pmatrix} \quad , \tag{5.28}$$

$$\mathbf{R}_k^{\mathrm{COM}} = \sigma_{\mathrm{COM}}^2 \quad . \tag{5.29}$$

RFID

The location inference via the employed active UHF RFID system is done by means of the RSS value of the received tags. Each tag transmits its unique ID upon an interrogation of the reader. Associated to each tag ID its location is stored in a database, such that the reader position can be inferred from the characteristic RSS profile, which varies with the distance between reader and tag. Specifically the measurement model is

$$\begin{aligned} z_{n,k}^{\mathrm{RFID}} &= \mathbf{h}_{k,n}^{\mathrm{RFID}}(\mathbf{x}_k, \mathbf{n}_k^{\mathrm{RFID}}) \\ &= \mathbf{h}_k^{\mathrm{RFID}}(|\mathbf{r}_n^{\mathrm{RFID}} - \mathbf{r}_k|, \mathbf{n}_k^{\mathrm{RFID}}) \ , \end{aligned} \tag{5.30}$$

in which $\mathbf{r}_n^{\mathrm{RFID}}$ is the location of the received tag as stored along with its ID. Specifically it is thus assumed that the measurement depends only on the distance between tag and the receiver $|\mathbf{r}_n^{\mathrm{RFID}} - \mathbf{r}_k|$ and the noise term $\mathbf{n}_k^{\mathrm{RFID}}$, which is not specified further. The corresponding likelihood function is constructed empirically from measurement data and practically realized via the lookup table function g:

$$p(z_{n,k}^{\mathrm{RFID}}|\mathbf{x}_k) = g(z_{n,k}^{\mathrm{RFID}}, |\mathbf{r}_n^{\mathrm{RFID}} - \mathbf{r}_k|) \ . \tag{5.31}$$

Since independent measurement noise is assumed for the received tags, the joint likelihood value over all received tags $\mathbf{z}_k^{\mathrm{RFID}} = [z_{1,k}^{\mathrm{RFID}}, \ldots, z_{N_\mathrm{D},k}^{\mathrm{RFID}}]^T$ can be computed by the product

$$p(\mathbf{z}_k^{\mathrm{RFID}}|\mathbf{x}_k) = \prod_{n=1}^{N_\mathrm{D}} g(z_{n,k}^{\mathrm{RFID}}, |\mathbf{r}_n^{\mathrm{RFID}} - \mathbf{r}_k|) \ . \tag{5.32}$$

Since the RFID measurement model (5.30) is neither linear nor Gaussian a Gaussian approximation is needed to allow for the incorporation into the Kalman filter. Though a power level-based likelihood function may be feasible for simplicity just an ID-based likelihood function is used for the Kalman filter. Assuming now Gaussian noise n_k^{RFID} of variance σ_{RFID}^2 the RFID measurement model is approximated by

$$\begin{aligned} \mathbf{z}_k^{\mathrm{RFID}} &= \mathbf{h}_k^{\mathrm{RFID}}(\mathbf{x}_k) + \mathbf{n}_k^{\mathrm{RFID}} \\ &= \mathbf{r}_k + \mathbf{n}_k^{\mathrm{RFID}} \ , \end{aligned} \tag{5.33}$$

where the measurement $\mathbf{z}_k^{\mathrm{RFID}}$ corresponds to $\mathbf{r}_n^{\mathrm{RFID}}$ when tag n was detected. Hence the Kalman measurement matrices can be expressed as

$$\mathbf{H}_{n,k}^{\mathrm{RFID}} = \begin{pmatrix} 1 & 0 & 0 \\ 0 & 1 & 0 \end{pmatrix} \ , \tag{5.34}$$

$$\mathbf{R}_{n,k}^{\mathrm{RFID}} = \begin{pmatrix} \sigma_{\mathrm{RFID}}^2 & 0 \\ 0 & \sigma_{\mathrm{RFID}}^2 \end{pmatrix} \ . \tag{5.35}$$

Baro-Altimeter

The baro-altimeter measurements are treated differently from the other sensors. Contrary to the Bayesian philosophy the received data is used to take a hard decision on the floor level on which the pedestrian is currently located. Though a straightforward incorporation via a true likelihood function is feasible and expected to be beneficial in a future full 3D sensor fusion system, it appeared to be sufficient for the 2.5D approach pursued here, where mainly the exact horizontal position is of interest, and the vertical information needs to be only correct up to floor level accuracy, which is approximately around 3 meters. Thus the altimeter data is just used to switch the floor, whenever applicable, and to select properly the map-data that corresponds to this floor.

5.2.3 Movement Model

In difference to the movement model used in (4.10) now the displacement is assumed to depend on the previous one according to

$$\Delta\mathbf{r}_k = \Delta\mathbf{r}_{k-1} + \mathbf{n}_r \; . \tag{5.36}$$

This is to introduce a stronger memory within the model, i.e. to consider it to be more likely that a pedestrian will keep on heading with the same speed instead of changing it completely randomly.

5.2.4 Performance Evaluation

Scenario and Data

To assess the performance of the algorithmic approach two sets of publicly available real world data are used [AFK$^+$09]. To compare the result of the sensor fusion against the true pedestrian position the data includes ground truth reference points (GTRPs) that have been carefully measured to sub-centimeter accuracy with a total station, employing differential GPS, optical distance and angular measurements. The collected measurement data features a wide range of sensors that were worn by a moving pedestrian, namely triads of foot-mounted accelerometers and gyroscopes, an electronic compass, a barometer, a GPS receiver, and an RFID reader, which could detect RFID tags that were deployed throughout the building. The locations of the distributed tags are stored in a database and the building geometry has been made available as vector data representing walls on each of the buildings floor levels. In order to cover a wide range of application scenarios, the measurements specifically include the important transitions from outdoor to indoor and vice versa. Furthermore, the data includes passages with explicit three-dimensional character, such as ramps, stairs and elevators. In Figure 5.8 a selection of the data is illustrated. The sensors and devices used for the measurements are listed in Appendix C.

Data Set 3 Data set 3 starts from outside the building with good GPS coverage and already acquired GPS-receiver. After a short walk the person enters the office building. The person then walks through the corridor in the lower floor and subsequently climbs the stairs to the second floor. After a similar walk on the second floor, the person reaches the elevator. The elevator goes up to the third floor (picking up another passenger), then goes down to the garage level. The person leaves the elevator and then performs a short meandering walk in the garage. Finally the person leaves the garage via the ramp and returns to the starting position.

Data Set 5 Data set 5, which is a pure 1D set, starts from outside the building with good GPS coverage and already acquired GPS-receiver. After a short walk the person enters the office building. The person then walks two laps through the corridors in the ground floor whilst entering some of the offices. Finally the person leaves the building and returns to the starting position.

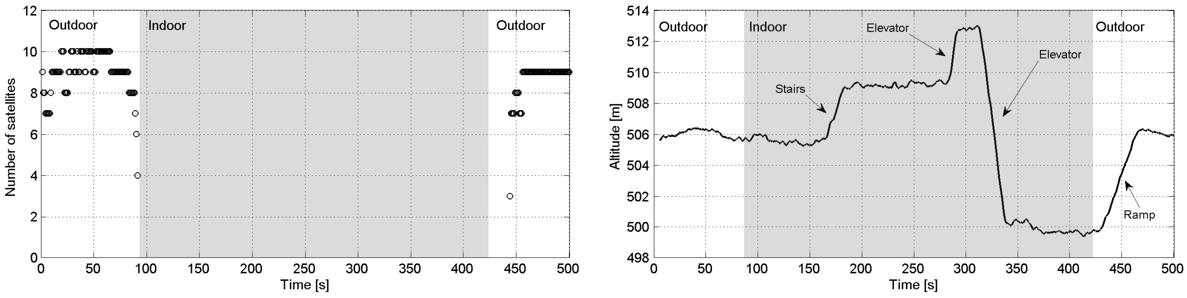

(a) Number of available satellites (b) Baro-altimeter

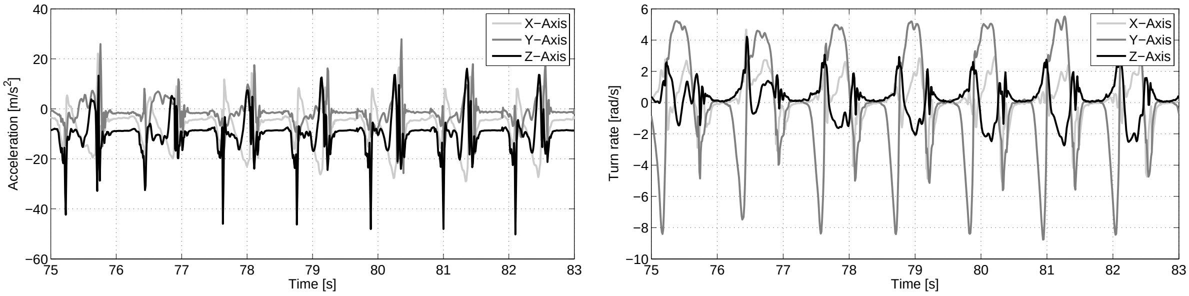

(c) Accelerations (d) Turn rates

Figure 5.8: An example of the sensor data of data set 3: According to Figure 5.8(a) the satellite navigation is completely unavailable during the indoor period. The altimeter data shown in Figure 5.8(b) indicates the important vertical transitions through the staircase, the elevator, and the garage drive-up. Figure 5.8(c) and Figure 5.8(d) illustrate accelerations and turn rates at the foot-mounted IMU during a short walk sequence. The rest phases of the foot are clearly visible in both signatures.

Results

Stride Estimation Since the step estimation is performed independently from the main fusion only via the inertial sensors, a sole inertial PDR track can be computed from the collected inertial data. Figure 5.9 illustrates the PDR track for two scenarios, each lasting approximately 500 seconds. Since in both scenarios the start point coincides with the stop point the accumulated PDR error is just the difference between start and stop. As Figure 5.9(a) and 5.9(b) reveal the drift accumulates to some few tens of meters during the entire duration of both experiments respectively.

Comparison of Algorithms A qualitative and comparative analysis of the sensor fusion via the particle filter and the extended Kalman filter is given in Figure 5.10 for two mixed indoor/outdoor scenarios. In both scenarios the pedestrian is equipped with GPS, altimeter, compass, a foot-mounted IMU, and a building map and starts outdoor with GPS being available. Outdoors both filter perform quite similar, but as soon as the indoor environment prevents the reception of GPS the only source of absolute position information, namely GPS, is not available any more. This may generally cause a temporally increasing degradation, nevertheless the PF is able to constrain the movement due to the map information, which can not be exploited by the EKF due to its nonlinear nature. As a consequence the EKF is drifting freely indoors and

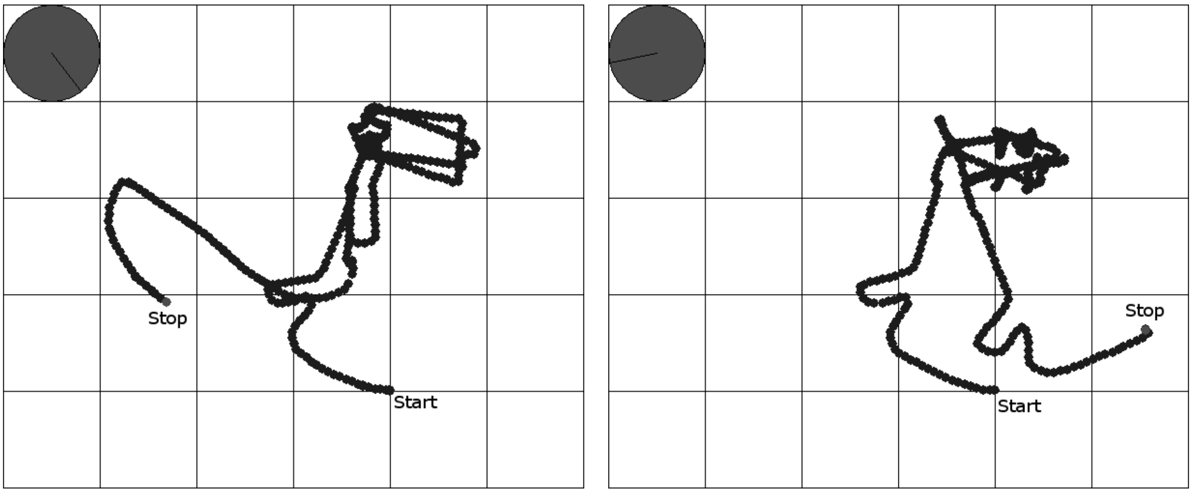

(a) Data set 3

(b) Data set 5

Figure 5.9: PDR track reconstructed from the foot-mounted inertial sensors for two scenarios. In both scenarios the start points coincide with the stop points. The major errors arise due to the angular drift in the heading angle, which is only weakly observable when only inertial sensors are used. The underlying coordinate grid is spaced by 20 meters per line.

accumulates large errors over time, which are not compensated until GPS becomes available again. From that moment both filter algorithms perform almost equally again. Most notably as already observed in Section 4.3.2 the map provides in both scenarios sufficient information to compensate the inherent system drift, which would arise typically indoors due to the lack of absolute position information. Thus the PF algorithm achieves in both scenarios an average accuracy of less than 2 meters, whereas the EKF performs significantly worse.

Complexity The findings of an analysis of the achievable performance of the particle filter are depicted in Figure 5.11, at which the measure of interest is the number of required particles. Again the considered sensors are GPS, altimeter, compass, a foot-mounted IMU, and the map of the building. For each data point the average performance is plotted. Thereby the average value itself is averaged over ten successive simulations using different random seeds while keeping the set of sensor data. Corresponding to the results shown in Figure 5.10 the average performance of the PF is better than 2 meters, given that the number of employed particles is sufficient. The results reveal that for the given scenario a range of 100-1000 particles is sufficient.

Value of Sensors Now the impact and the value of specific sensors is investigated. For that purpose it is assumed that the pedestrian carries at least those sensors, which may be regarded as the rather easily available ones, namely the autonomous sensors. Within this context autonomous means that there is no need for locally deployed infrastructure and that there is no use of specific environmental information, i.e. specifically an indoor map. In that case it may be assumed that the pedestrian is equipped with GPS, compass, baro-altimeter, and a foot-mounted IMU. This suite of autonomous sensors is a quite likely combination, at least for professional application, since all of these sensors are already available today. Nevertheless local infrastructure may not be available as well as detailed map information. As shown in Figure 5.12(a) RFID

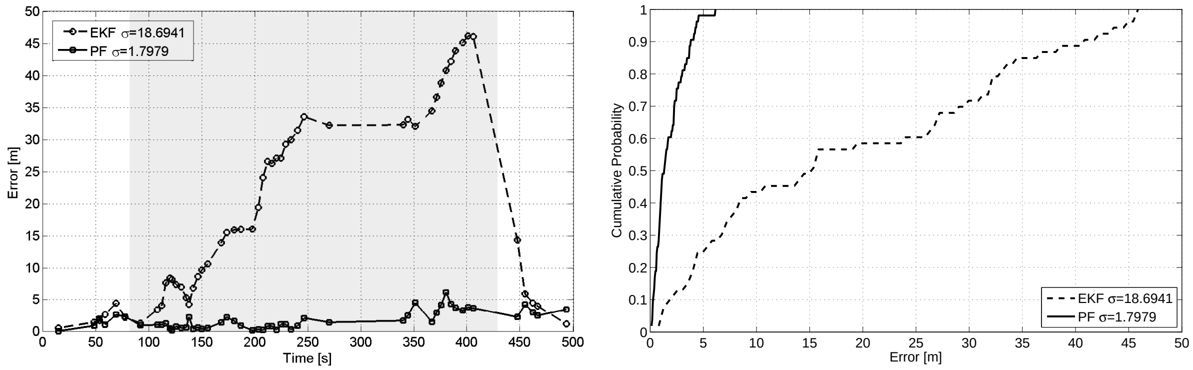

(a) Positioning error, data set 3 (b) Cumulative normalized error histogram, data set 3

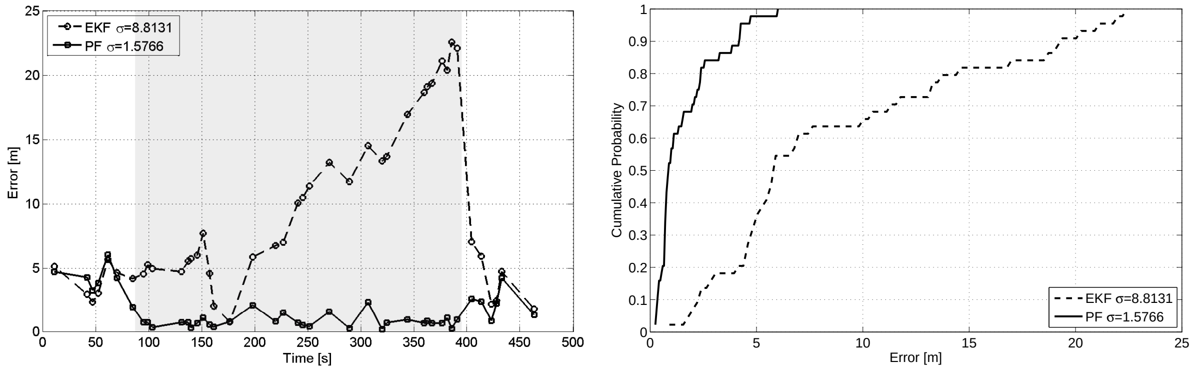

(c) Positioning error, data set 5 (d) Cumulative normalized error histogram, data set 5

Figure 5.10: Comparison of the particle filter and the extended Kalman filter in two mixed indoor/outdoor scenarios. In both scenarios the pedestrian enters the building after approximately 90 seconds. The indoor periods are indicated by the gray shading. Unlike the PF the EKF is not able to exploit the map-based movement model, and thus it accumulates drift errors until the pedestrian leaves the building and GPS becomes available again (Figure 5.10(a) approx. after 450 s and Figure 5.10(c) approx. after 400 s). Thanks to the map-based movement model the errors of the PF do not increase during the indoor period, notably though there is no source of absolute position information. As depicted in Figure 5.10(b) and 5.10(d) the error statistics of the EKF are consequently much worse compared to the PF.

is only of little value when the map is available, since the system performs already quite well, in particular thanks to the fusion of the inertial step estimation and the map, which achieves in combination with the other sensors an average performance around 2 meters and better. If the map is not available the RFID helps to constrain the location estimate and achieves in conjunction with the sensor fusion an improved average performance of around 3–4 meters. If neither RFID nor the map is used the average performance is degraded down to 6–7 meters. The error statistics shown in Figure 5.12(b) reflect these basic trends as well.

The estimated track of the particle filter is depicted in Figure 5.13. It can be clearly seen that the particle filter is able to cope well with the vertical transitions, including the staircase, the elevator, and the walk along the garage ramp. In the subsequent Figure 5.14 the operation of the fusion algorithms is illustrated in some particular characteristic scenarios and transitions. In Figure 5.14(a) a typical outdoor scenario is shown. The particle cloud is well constrained by

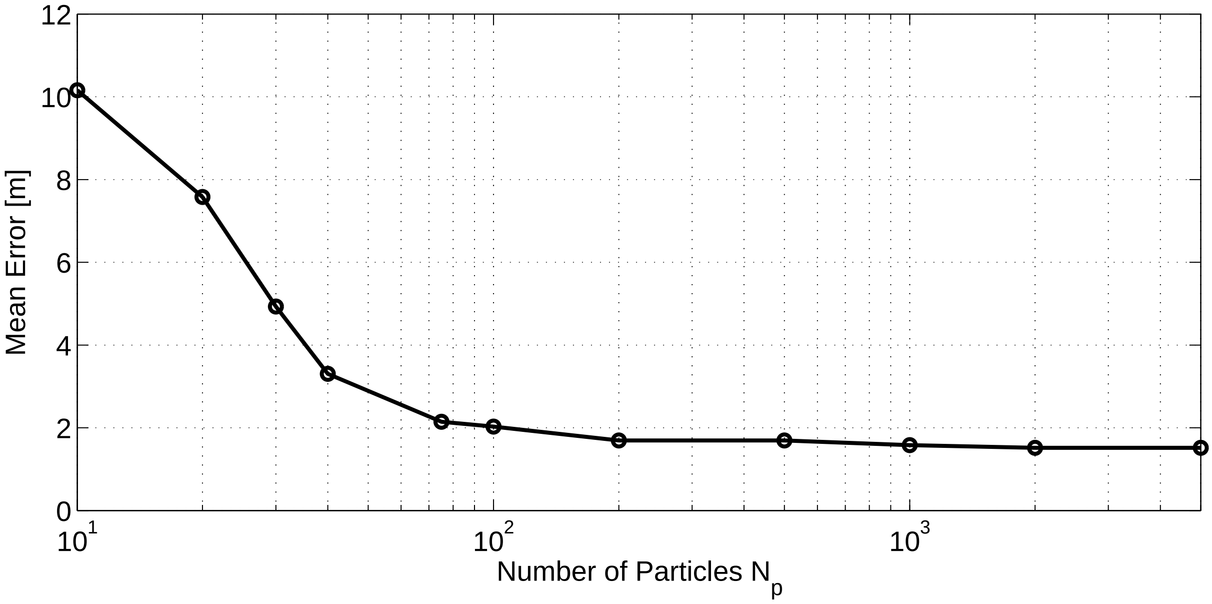

Figure 5.11: Average performance depending on the number of particles used. For more than 100 particles the performance improves only slightly, for more than 1000 particles it is saturated completely.

the absolute position information that is provided by the GPS and by the contributions of the other sensors. In the phase where the building is entered, which is depicted in Figure 5.14(b), the particles resemble a clearly non-Gaussian PDF, since the walls intersect and constrain them. Figure 5.14(c) shows the typical operation in a corridor where the map constrains the particles to a small cloud, whose magnitude is in the order of the corridor's width. In such a scenario basically the step measurements drive the movement of the cloud, whereas the compass aids the heading and the map-based movement model prevents the movement through the walls. As shown in Figure 5.14(d) the walls may also be less restrictive, e.g. in the garage, where the spread of the cloud has become significantly larger compared to the corridor. The longer the system lacks of constraining information, the bigger the particle cloud gets, e.g. when the garage is left after some time as illustrated in Figure 5.14(e), where obviously several slightly dispersed modes are tracked. As soon as restraining sensor information is available, e.g. when GPS becomes available again, the particles collapse again to a unimodal Gaussian shape, as it is shown in Figure 5.14(f).

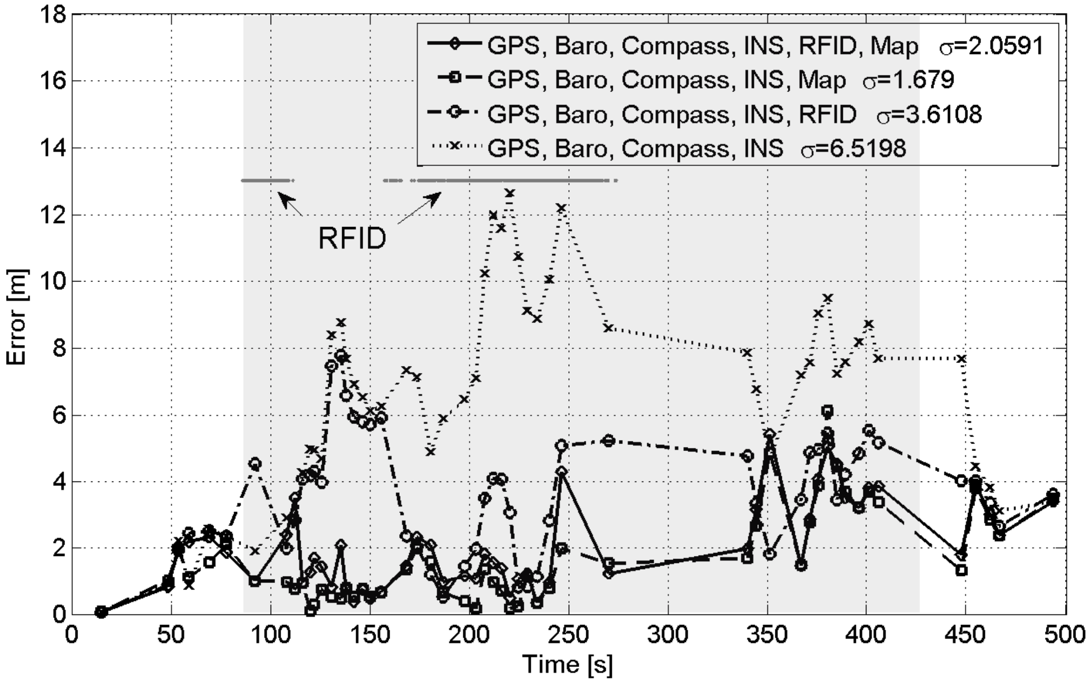

(a) Positioning error

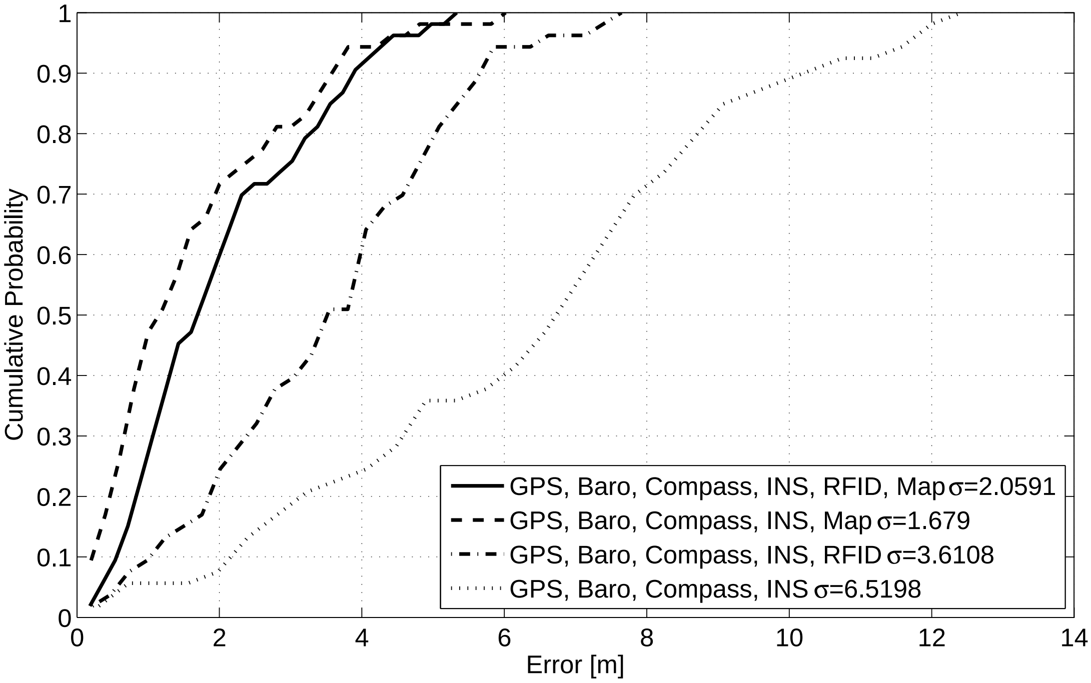

(b) Cumulative normalized error histogram

Figure 5.12: Impact of RFID and the building map in conjunction with the autonomous sensors GPS, baro-altimeter, compass, and foot-mounted IMU. If both RFID and the map are used, the performance is quite similar to the map only, since the rather inaccurate RFID does not contribute much to the already quite well performing system. When the map is not used the benefit of the RFID becomes more obvious: In the periods that are indicated by the gray markers RFID is available and constrains the estimates, such that the average performance is improved.

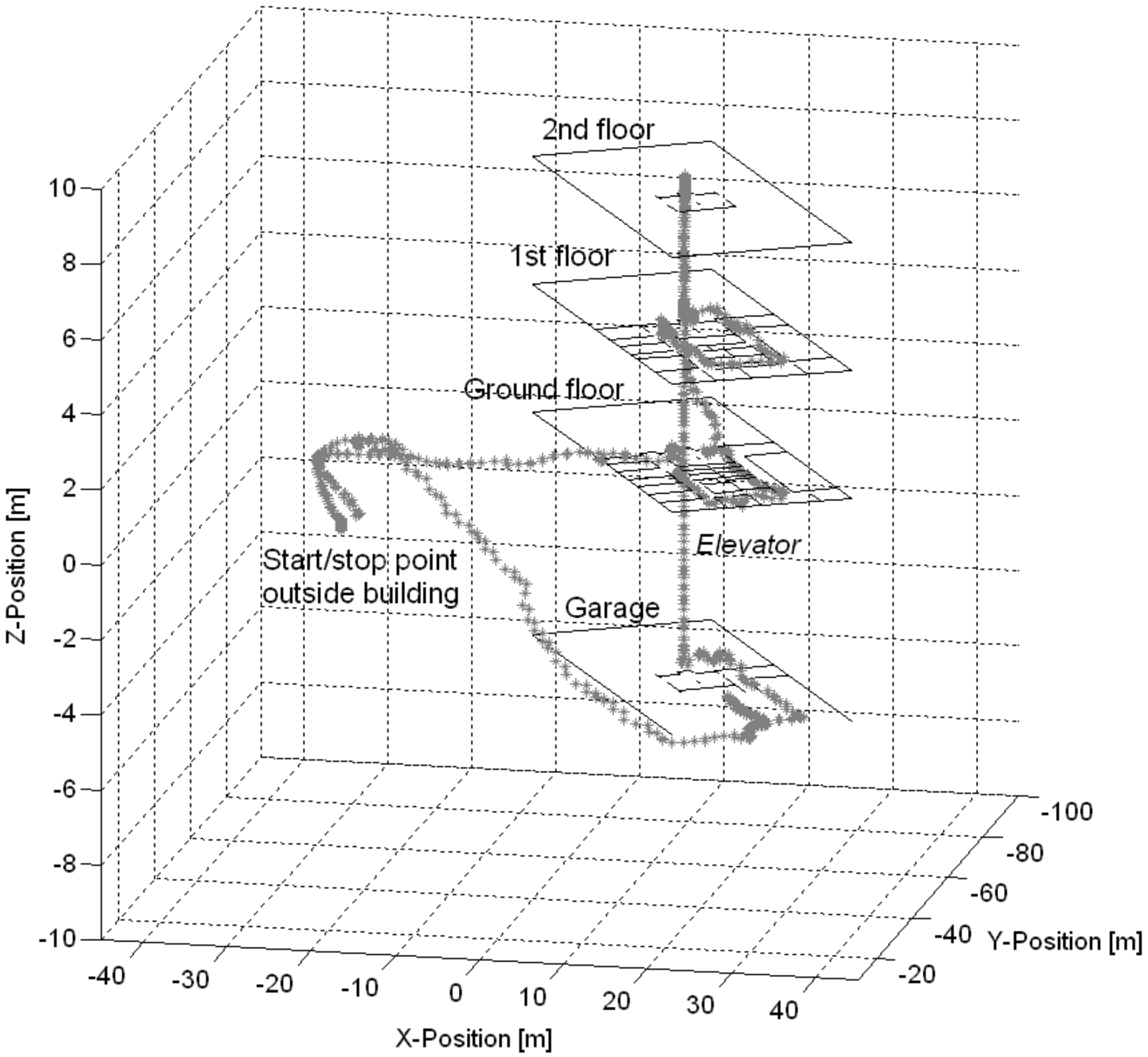

Figure 5.13: Illustration of the particle filter track for data set 3. The vertical transitions are resolved very well thanks to the barometric aiding.

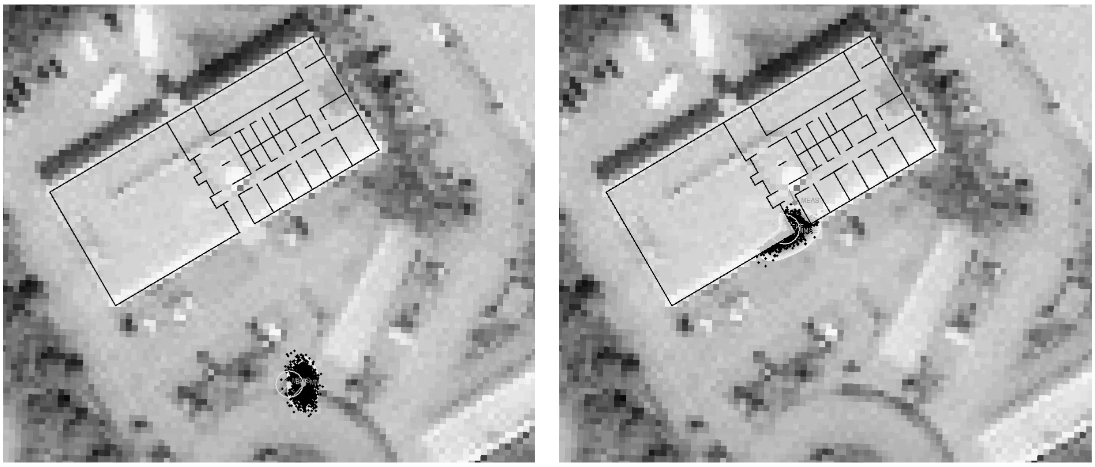

(a) Outdoor (b) Entering the building

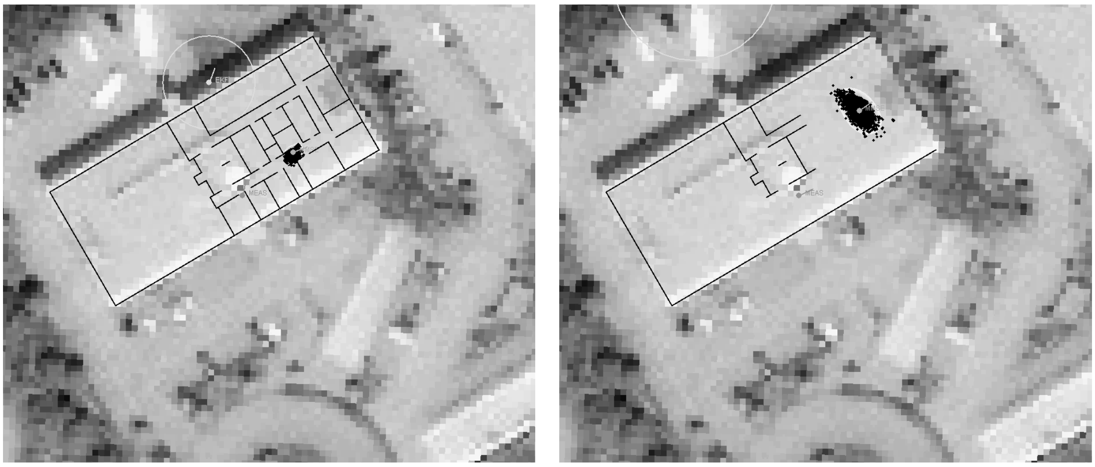

(c) In the 1st floor corridor (d) In the garage

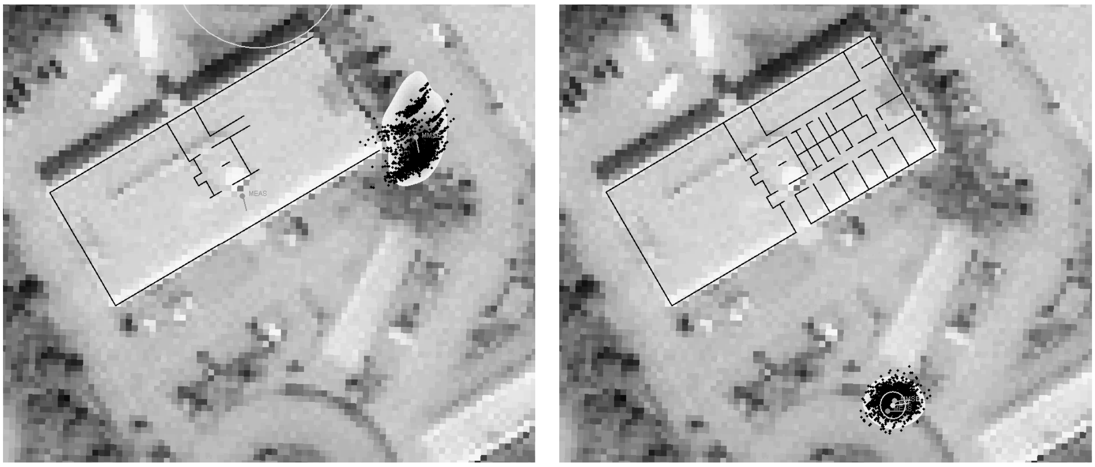

(e) Leaving the garage (f) Reacquiring GPS outdoors

Figure 5.14: Result of the sensor fusion using GPS, compass, baro-altimeter, a foot-mounted IMU, and the building map under various characteristic indoor and outdoor conditions.

Chapter 6

Conclusions

Within this thesis the framework of Bayesian filtering has been applied to enhance pedestrian navigation by joining a variety of complementary personal navigation sensors and other related sources of navigational information. In Chapter 2 the underlying fundamentals were presented as far as relevant for this thesis. The thesis was motivated basically by the idea to establish signal processing concepts with the objective to support pedestrians navigating seamlessly in both indoor and outdoor environments, which may be considered as the next step in the evolution of personal navigation systems. To achieve this the combination of sensors via optimal sensor fusion algorithms is mandatory from today's point of view, since in the mid-term future a singular technical solution is not expected.

6.1 Summary of Contributions

The scope of Chapter 3 was the application of Bayesian filtering to solve the crucial problem of multipath propagation in pedestrian satellite navigation. Two novel approaches were introduced in this context: The range-based and the position-based estimator. To facilitate their integration into receivers it was suggested to make use of reduced complexity techniques, which previously have been considered only for ML estimators. The complexity reduction allows to reduce the efforts needed for the calculation of the likelihood functions, which are the computationally most demanding parts in the proposed filter algorithms. For both introduced approaches new two-fold marginalized Bayesian filters were derived, which allow to estimate the state space efficiently with conditional optimal estimators where possible. Specifically it was shown that the number of impinging multipath signals as well as their complex amplitudes can be estimated optimally using grid-based and Kalman filters, and thus only a reduced set of states needs to be estimated by the computationally more demanding and sub-optimal particle filter. For the more elaborated position-based formulation of the Bayesian filter it was revealed that the joint estimation problem may be partially separated based on the Soft-Location concept, whenever the likelihood function can be factorized into the contributions of the respective received satellites. It was shown that in the introduced partially separated estimator the number of grid-based and Kalman filters is not increased compared to the simpler range-based estimator formulation. Additionally it was proposed to aid the construction of an improved proposal density for the high-dimensional position-domain state space by combining the a posteriori PDFs of an accompanying set of range-based estimators. The presented simulation results for various channel conditions, including the latest available pedestrian channel model as well as a stored measured channel profile revealed the benefit of the Bayesian approach compared to the conventional receiver signal processing. Specifically it was shown that the more advanced position-based estimator outperforms the range-based method. The results revealed that under realistic propagation conditions the performance of the introduced Bayesian filters tends to saturate rapidly for more than two simultaneous replica being considered. An assessment of novel modulation schemes such as the BOC(1,1) or the CBOC, which both are candidates to be used in the Galileo system, confirmed their superior performance compared to the conventional BPSK modulation.

In Chapter 4 a novel method for integrating shoe-mounted inertial sensors into a Bayesian location estimation framework was presented. The approach is characterized by a cascaded filter architecture, which allows to exploit the synergy between a conventional shoe-mounted INS and a nonlinear pedestrian movement model in an indoor scenario. An advantage of the proposed integration algorithm is that each level of the cascaded architecture can operate at an update rate appropriate to the scale: at 100 Hz or higher for the stride estimation and roughly at step-rate for the upper fusion layer. It was shown that the use of a pair of platforms improves the dead-reckoning: the variance is reduced by a factor of two thanks to a newly introduced pedestrian model. Based on experimental data it was shown that a moving pedestrian can be localized in a building just by using a foot-mounted 6DOF inertial platform and map-matching without using any additional sensors and without the need to determine the pedestrian's initial position or heading in an alignment procedure. Furthermore, the experiment revealed that due to the implicit map-matching the uncertainty about the pedestrian's location decreases if the movement and the building layout is suitable, which can lead to long-term stability in an indoor navigation scenario.

The content of Chapter 5 covered two examples for real world application scenarios. In Section 5.1 an indoor positioning system for pedestrians combining WLAN fingerprinting with foot mounted inertial sensors was presented. The approach requires no processing outside of the local device and minimal a priori fingerprinting effort. A hierarchical Bayesian filtering approach using cascaded extended Kalman filters was implemented to achieve a real-time capability. The accuracy of the combined system was quantitatively evaluated in a real building and shows that it is much higher than that of the WLAN fingerprinting alone; in addition it also provides an estimate of the orientation of the user. In the experiment an average positioning error of roughly 1.5 meters was achieved. The approach allows to minimize the fingerprinting effort since the high accuracy is achieved by the support of the inertial-based step estimation in the overall estimation process.

Within Section 5.2 the concepts introduced in Chapter 4 were pursued further and additional sensors were integrated: a GPS receiver, an electronic compass, a baro-altimeter, and an RFID system. Based on experimental data covering a mixed indoor/outdoor scenario including important vertical transitions such as stairs, ramps, and elevators, the algorithm was assessed and the benefit of the respective sensors was investigated. This data was then made publicly available [AFK$^+$09]. The particle filtering approach was compared to the much simpler Kalman filter algorithm introduced in Chapter 5.1. The results clearly show the advantage of the map-based mobility model, which can not be exploited by the Kalman filter algorithm, and give an indication about the number of particles that is required to reach convergence and about the achievable performance with various sensor and algorithm combinations. As real data is used the results basically prove the feasibility of the selected sensor fusion approach, and show that an average accuracy around 2 meters or even better is feasible without deployed infrastructure in a representative indoor environment, given the map-information is available.

6.2 Future Work

The topics addressed in this thesis offer various possibilities for future work. In the context of satellite navigation receiver signal processing the adjustment of algorithm parameters could be addressed in more detail and extended to navigating objects other than pedestrians. A promising approach could be to exploit the mutual correlations between the LOS delay rate (Doppler) and the echo delay rates, which are strongly correlated in practice due to the surrounding environment, in particular in urban scenarios, where echoes depart and approach in a quite characteristic manner. Also an adaptive steering of the echo activity transition probabilities based on the receiver speed could be considered, since for a stationary or slowly moving receiver the likelihoods of emerging and disappearing echoes are much smaller than for a fast moving receiver. Though the introduced algorithms have been assessed under simulation conditions as realistic as possible by using latest channel models and measured channels, an essential step in the further development of these concepts is their evaluation under real world conditions. Thus the implementation of a prototype receiver is certainly a major topic for future work. From a theoretical point of view the concept of a probabilistic navigation receiver raises interesting questions concerning the reliability and integrity of Bayesian filtering algorithms, e.g. when these algorithms are used in safety critical applications such as aviation. Though the Bayesian approach provides inherently the best possible reliability measure, namely the a posteriori probability density function, it is practically just an estimate of the true density, in particular for those filtering approaches that are based on Monte-Carlo methods.

Concerning personal inertial navigation a major benefit in indoor scenarios is due to the enhancement by the map information, which was shown to tackle the problem inertial drift. Practically the availability of indoor map information is not ubiquitous. Though, even if it was not addressed here, an interesting challenge for future work is to join the location estimation with a simultaneous estimation and learning of maps and movement models, which may be performed by classical simultaneous localization and mapping (SLAM) approaches [MTKW02], which are widely used in the robotics community. Furthermore the introduced modular estimation concept could be extended by further location sensor such as UWB, which is foreseen to play a major role for some professional applications, or to assess the benefit of the incorporation of mobile communication signals, in particular when considering the evolution of systems and standards towards higher bandwidths, which will certainly improve the navigation capabilities of these systems. A further topic that has not been addressed in this thesis is the use of optical and visual sensors, such as laser scanners or video cameras, which allow for the detection, recognition, and tracking of environmental features, which is the basis for many of the common SLAM approaches.

Appendix A

Proof of the Factorized Bayesian Estimator

The factorization of the likelihood function for the Bayesian estimator in a multi-sensor scenario plays an important role for the topics discussed in this thesis, in particular for the concept of *Soft-Location* (SoLo). Therefore in this appendix an inductive proof for the factorized expression of the estimator is given.

Proof of the Factorized Bayesian Estimator. Assuming the entire vector of the current observations $\mathbf{z}_k$ is composed by the observations associated to each of the $j = 1, \ldots, M$ sensors via $\mathbf{z}_k \widehat{=} \{\mathbf{z}_{j,k}, j = 1, \ldots, M\}$, the a posteriori PDF at time k can be expressed as

$$\begin{aligned} p(\mathbf{x}_k|\mathbf{Z}_k) &= p(\mathbf{x}_k|\mathbf{z}_k, \mathbf{Z}_{k-1}) \\ &= p(\mathbf{x}_k|\mathbf{z}_{1,k}, \ldots, \mathbf{z}_{M,k}, \mathbf{Z}_{k-1}) \ , \end{aligned} \tag{A.1}$$

where $\mathbf{Z}_k \widehat{=} \{\mathbf{z}_q, q = 1, \ldots, k\}$ denotes the entire history of observations up to time k. Applying the Bayes rule with respect to $\mathbf{z}_{1,k}$ gives

$$p(\mathbf{x}_k|\mathbf{Z}_k) = \frac{p(\mathbf{z}_{1,k}|\mathbf{x}_k, \mathbf{z}_{2,k}, \ldots, \mathbf{z}_{M,k}, \mathbf{Z}_{k-1}) p(\mathbf{x}_k|\mathbf{z}_{2,k}, \ldots, \mathbf{z}_{M,k}, \mathbf{Z}_{k-1})}{p(\mathbf{z}_{1,k}|\mathbf{z}_{2,k}, \ldots, \mathbf{z}_{M,k}, \mathbf{Z}_{k-1})} \ . \tag{A.2}$$

Assuming the observations $\mathbf{z}_{1,k}$ depend only on $\mathbf{x}_k$ and not on any other observations, in other words assuming that the noise affecting $\mathbf{z}_{1,k}$ is independent of the noise affecting the other measurement, the equality $p(\mathbf{z}_{1,k}|\mathbf{x}_k, \mathbf{z}_{2,k}, \ldots, \mathbf{z}_{M,k}, \mathbf{Z}_{k-1}) = p(\mathbf{z}_{1,k}|\mathbf{x}_k, \mathbf{Z}_{k-1})$ may be used and the a posteriori PDF may be expressed as

$$\begin{aligned} p(\mathbf{x}_k|\mathbf{Z}_k) &= \frac{p(\mathbf{z}_{1,k}|\mathbf{x}_k) p(\mathbf{x}_k|\mathbf{z}_{2,k}, \ldots, \mathbf{z}_{M,k}, \mathbf{Z}_{k-1})}{p(\mathbf{z}_{1,k}|\mathbf{z}_{2,k}, \ldots, \mathbf{z}_{M,k}, \mathbf{Z}_{k-1})} \\ &= C_{1,k} p(\mathbf{z}_{1,k}|\mathbf{x}_k) p(\mathbf{x}_k|\mathbf{z}_{2,k}, \ldots, \mathbf{z}_{M,k}, \mathbf{Z}_{k-1}) \ , \end{aligned} \tag{A.3}$$

with $C_{1,k} = [p(\mathbf{z}_{1,k}|\mathbf{z}_{2,k}, \ldots, \mathbf{z}_{M,k}, \mathbf{Z}_{k-1})]^{-1}$. Introducing the term $m = 1$ the previous expression for the a posteriori PDF may be rewritten as

$$p(\mathbf{x}_k|\mathbf{Z}_k) = p(\mathbf{x}_k|\mathbf{z}_{m+1,k}, \ldots, \mathbf{z}_{M,k}, \mathbf{Z}_{k-1}) \prod_{j=1}^{m} C_{j,k} p(\mathbf{z}_{j,k}|\mathbf{x}_k) \ . \tag{A.4}$$

Applying the Bayesian rule to the first expression on the right hand side and assuming again $p(\mathbf{z}_{m+1,k}|\mathbf{x}_k, \mathbf{z}_{m+2,k}, \ldots, \mathbf{z}_{M,k}, \mathbf{Z}_{k-1}) = p(\mathbf{z}_{m+1,k}|\mathbf{x}_k, \mathbf{Z}_{k-1})$ the preceding equation can be transformed into

$$\begin{aligned} p(\mathbf{x}_k|\mathbf{Z}_k) &= \frac{p(\mathbf{z}_{m+1,k}|\mathbf{x}_k)p(\mathbf{x}_k|\mathbf{z}_{m+2,k}, \ldots, \mathbf{z}_{M,k}, \mathbf{Z}_{k-1})}{p(\mathbf{z}_{m+1,k}|\mathbf{z}_{m+2,k}, \ldots, \mathbf{z}_{M,k}, \mathbf{Z}_{k-1})} \prod_{j=1}^{m} C_{j,k} p(\mathbf{z}_{j,k}|\mathbf{x}_k) \qquad \text{(A.5)} \\ &= p(\mathbf{x}_k|\mathbf{z}_{m+2,k}, \ldots, \mathbf{z}_{M,k}, \mathbf{Z}_{k-1}) C_{m+1,k} p(\mathbf{z}_{m+1,k}|\mathbf{x}_k) \prod_{j=1}^{m} C_{j,k} p(\mathbf{z}_{j,k}|\mathbf{x}_k) \ , \end{aligned}$$

with $C_{m+1,k} = [p(\mathbf{z}_{m+1,k}|\mathbf{z}_{m+2,k}, \ldots, \mathbf{z}_{M,k}, \mathbf{Z}_{k-1})]^{-1}$, which is thus equivalent to

$$p(\mathbf{x}_k|\mathbf{Z}_k) = p(\mathbf{x}_k|\mathbf{z}_{m+2,k}, \ldots, \mathbf{z}_{M,k}, \mathbf{Z}_{k-1}) \prod_{j=1}^{m+1} C_{j,k} p(\mathbf{z}_{j,k}|\mathbf{x}_k) \ . \qquad \text{(A.6)}$$

Since replacing the expression $m + 1$ by m in (A.6) leads to (A.4) the Bayesian rule can be applied successively for all further $\mathbf{z}_{q,k}, q = 3, \ldots, M$ without loss of generality, given that $p(\mathbf{z}_{q,k}|\mathbf{x}_k, \mathbf{z}_{q+1,k}, \ldots, \mathbf{z}_{M,k}, \mathbf{Z}_{k-1}) = p(\mathbf{z}_{q,k}|\mathbf{x}_k, \mathbf{Z}_{k-1})$ holds for all q, and the a posteriori PDF may be finally expressed via

$$p(\mathbf{x}_k|\mathbf{Z}_k) = p(\mathbf{x}_k|\mathbf{Z}_{k-1}) \prod_{j=1}^{M} C_{j,k} p(\mathbf{z}_{j,k}|\mathbf{x}_k) \ . \qquad \text{(A.7)}$$

□

Appendix B

Simulation Parameters

This appendix lists the parameters, which have been used in the simulations and computations that have been performed for this thesis.

B.1 Chapter 3

B.1.1 Section 3.4.3: PCRB Computation

- Space segment: Four satellites at elevation 67, 27, 51, 39 degrees and at azimuth 58, 65, 135, 195, degrees respectively.
- Navigation signals: BPSK modulation, chip rate T_c=1.023 MChips/s, Gold code of length 1023, two-sided signal bandwidth 20 MHz, carrier frequency f_0=1.575 GHz
- Receiver: noise level 45 dB-Hz, sampling period T_s=50 ns, coherent observation period 10 ms corresponding to L=200 kSamples and an amplitude filter update rate of 100 Hz, number of incoherent blocks N_b=10 corresponding to a delay, delay rate, position, velocity, clock, and clock drift update rate of 10 Hz, user dynamics $\sigma_x = 0.1\,\mathrm{m}$, $\sigma_y = 0.1\,\mathrm{m}$, $\sigma_z = 0.1\,\mathrm{m}$, $\sigma_\tau = 0.1\,\mathrm{m}$, $\sigma_{\dot{x}} = 0.1\,\mathrm{m/s}$, $\sigma_{\dot{y}} = 0.1\,\mathrm{m/s}$, $\sigma_{\dot{z}} = 0.1\,\mathrm{m/s}$, $\sigma_{\dot{\tau}} = 0.1\,\mathrm{m/s}$, $\sigma_a >> 1$, number of considered multipath signals $N_m = 0$.

B.1.2 Section 3.5.1: AWGN Channel

- Space segment: Four satellites at elevation 67, 27, 51, 39 degrees and at azimuth 58, 65, 135, 195, degrees respectively.
- Navigation signals: BPSK modulation, chip rate T_c=1.023 MChips/s, Gold code of length 1023, two-sided signal bandwidth 20 MHz, carrier frequency f_0=1.575 GHz
- Receiver: noise level 45 dB-Hz, 2nd order DLL with loop bandwith 2 Hz and damping factor 0.7, narrow DLL correlator spacing of $\Delta\tau$=0.1 chips, correlator bank with $N_{cc} = N_{pc} = 25$ signal matched correlators spaced symmetrically around the DLL inphase correlator at a distance of 0.05 chips, sampling period T_s=50 ns, coherent observation period 10 ms corresponding to L=200 kSamples and an amplitude filter update

rate of 100 Hz, number of incoherent blocks N_b=10 corresponding to a delay, delay rate, position, velocity, clock, and clock drift update rate of 10 Hz, user dynamics $\sigma_x = 0.1\,\mathrm{m}$, $\sigma_y = 0.1\,\mathrm{m}$, $\sigma_z = 0.1\,\mathrm{m}$, $\sigma_\tau = 0.1\,\mathrm{m}$, $\sigma_{\dot{x}} = 0.1\,\mathrm{m/s}$, $\sigma_{\dot{y}} = 0.1\,\mathrm{m/s}$, $\sigma_{\dot{z}} = 0.1\,\mathrm{m/s}$, $\sigma_{\dot{\tau}} = 0.1\,\mathrm{m/s}$, $\sigma_a >> 1$, number of considered multipath signals $N_m = 0$, interpolation pulse length $N_g = 64$.

B.1.3 Section 3.5.2: Static Multipath Channel

- Space segment: Four satellites at elevation 67, 27, 51, 39 degrees and at azimuth 58, 65, 135, 195, degrees respectively.
- Navigation signals: BPSK modulation, chip rate T_c=1.023 MChips/s, Gold code of length 1023, two-sided signal bandwidth 20 MHz, carrier frequency f_0=1.575 GHz
- Receiver: noise level 45 dB-Hz, 2nd order DLL with loop bandwith 2 Hz and damping factor 0.7, narrow DLL correlator spacing of $\Delta\tau$=0.1 chips, correlator bank with $N_{cc} = N_{pc} = 25$ signal matched correlators spaced symmetrically around the DLL inphase correlator at a distance of 0.05 chips, sampling period T_s=50 ns, coherent observation period 10 ms corresponding to L=200 kSamples and an amplitude filter update rate of 100 Hz, number of incoherent blocks N_b=10 corresponding to a path activity, delay, delay rate, position, velocity, clock, and clock drift update rate of 10 Hz, user dynamics $\sigma_x = 0.1\,\mathrm{m}$, $\sigma_y = 0.1\,\mathrm{m}$, $\sigma_z = 0.1\,\mathrm{m}$, $\sigma_\tau = 0.1\,\mathrm{m}$, $\sigma_{\dot{x}} = 0.1\,\mathrm{m/s}$, $\sigma_{\dot{y}} = 0.1\,\mathrm{m/s}$, $\sigma_{\dot{z}} = 0.1\,\mathrm{m/s}$, $\sigma_{\dot{\tau}} = 0.1\,\mathrm{m/s}$, $\sigma_a = 0.1$, $p_{\text{offon}} = 10^{-6}$, $p_{\text{onoff}} = 1 - 10^{-6}$, number of considered multipath signals $N_m = 1$, interpolation pulse length $N_g = 64$, signal-to-multipath ratio SMR=6 dB, number of particles $N_p = 100$.

B.1.4 Section 3.5.3: Pedestrian Channel Model

- Space segment: Four satellites at elevation 67, 27, 51, 39 degrees and at azimuth 58, 65, 135, 195, degrees respectively.
- Navigation signals: BPSK modulation, chip rate T_c=1.023 MChips/s, Gold code of length 1023, two-sided signal bandwidth 20 MHz, carrier frequency f_0=1.575 GHz
- Channel model configuration: 10 degrees elevation, default parameters according to [LS09].
- User movement: To create the pedestrian channel corresponding to a typical pedestrian scenario the environmental parameters of the channel model are set according to Table B.1. The elevation is set to a fixed value of 10 degrees. The relative azimuth with respect to the satellite is varied through the simulation in the entire range from 0360 degrees by keeping the absolute azimuth constant at 0 degreees and varying the heading of the user, which in accordance varies the geometry of the surrounding artificial scenery. The time series input function for speed, heading and vertical are generated from a base pattern of 20 seconds duration, which is repeated 90 times. The pattern functions are depicted in B.1. The speed pattern resembles a typical pedestrian movement in an urban environments, including regular periods of walk and rest phases. During each pattern the heading angle is continuously incremented by 4 degrees per repetition. The vertical of 1.2 meters

is slightly varied during the walk phases in order to model the impact of the pedestrians strides. The duration of the simulation corresponds to 30 minute real-time, such that the entire azimuthal range is covered.

- Receiver: noise level 45 dB-Hz, 2nd order DLL with loop bandwith 1 Hz and damping factor 0.7, narrow DLL correlator spacing of $\Delta\tau$=0.1 chips, correlator bank with $N_{cc} = N_{pc} = 25$ signal matched correlators spaced symmetrically around the DLL in-phase correlator at a distance of 0.05 chips, sampling period T_s=50 ns, coherent observation period 10 ms corresponding to L=200 kSamples and an amplitude filter update rate of 100 Hz, number of incoherent blocks N_b=10 corresponding to a path activity, delay, delay rate, position, velocity, clock, and clock drift update rate of 10 Hz, user dynamics $\sigma_x = 0.1\,\mathrm{m}$, $\sigma_y = 0.1\,\mathrm{m}$, $\sigma_z = 0.1\,\mathrm{m}$, $\sigma_\tau = 0.1\,\mathrm{m}$, $\sigma_{\dot{x}} = 0.1\,\mathrm{m/s}$, $\sigma_{\dot{y}} = 0.1\,\mathrm{m/s}$, $\sigma_{\dot{z}} = 0.1\,\mathrm{m/s}$, $\sigma_{\dot{\tau}} = 0.1\,\mathrm{m/s}$, $\sigma_a = 0.1$, $p_{\mathrm{offon}} = 10^{-6}$, $p_{\mathrm{onoff}} = 1 - 10^{-6}$, interpolation pulse length $N_g = 64$, number of particles $N_p = 100$.

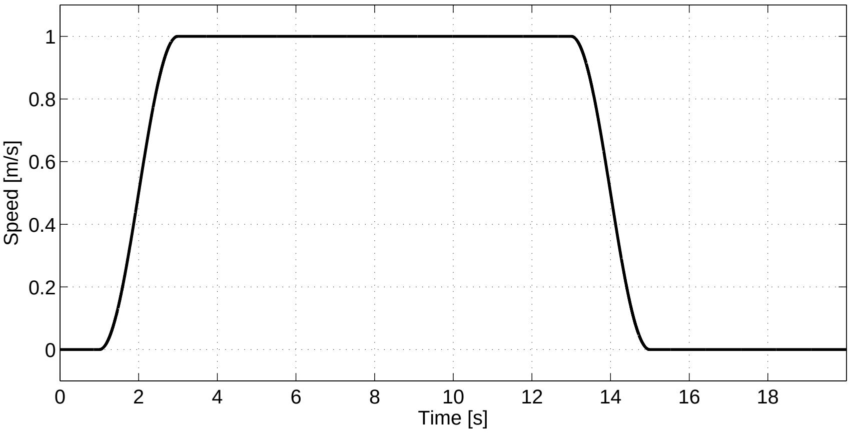

(a) Speed profile

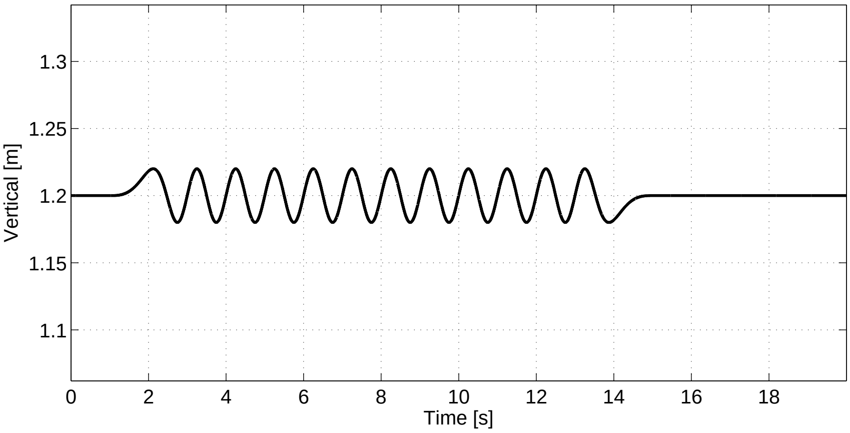

(b) Vertical profile

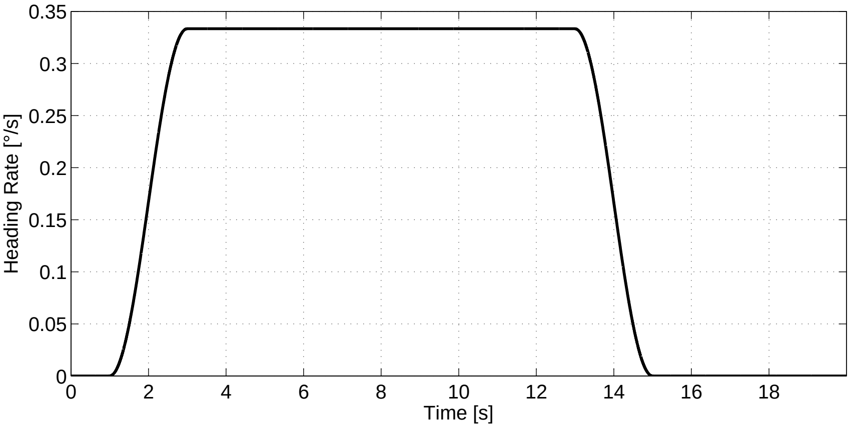

(c) Heading rate profile

Figure B.1: Movement pattern used to drive the generation of the pedestrian channel model. It resembles a pedestrian user moving slowly with regular rest phases (Figure B.1(a)). The pattern is repeated 90 times, such that the entire azimuth range is covered, since per each pattern there is a change of four degrees in the user heading with respect to the satellite direction (Figure B.1(c)). During the movement the variation in the vertical profile (Figure B.1(b)) reflects the slight vertical receiver movement that is induced by each of the steps the pedestrian makes.

Parameter	Value
CarrierFreq	1575420000
SampFreq	1000
EnableDisplay	0
EnableCIRDisplay	0
UserType	Pedestrian
Surrounding	Urban
AntennaHeight	1.2
MinimalPowerdB	-40
DistanceFromRoadMiddle	-6.5
GraphicalPlotArea	50
ViewVector	-60 20
RoadWidth	10
BuildingRow1	1
BuildingRow2	1
BuildingRow1YPosition	-8
BuildingRow2YPosition	8
HouseWidthMean	22
HouseWidthSigma	25
HouseWidthMin	10
HouseHeightMin	4
HouseHeightMax	50
HouseHeightMean	16
HouseHeightSigma	6.4
GapWidthMean	27
GapWidthSigma	25
GapWidthMin	10
BuildingGapLikelihood	0.18
TreeHeight	6
TreeDiameter	3
TreeTrunkLength	2
TreeTrunkDiameter	0.2
TreeAttenuation	1.1
TreeRow1Use	1
TreeRow2Use	1
TreeRow1YPosition	-6
TreeRow2YPosition	6
TreeRow1YSigma	0.5
TreeRow2YSigma	0.5
TreeRow1MeanDistance	60
TreeRow2MeanDistance	40
TreeRow1DistanceSigma	20

TreeRow2DistanceSigma	20
PoleHeight	10
PoleDiameter	0.2
PoleRow1Use	1
PoleRow2Use	0
PoleRow1YPosition	-6
PoleRow2YPosition	0
PoleRow1YSigma	0.5
PoleRow2YSigma	0.5
PoleRow1MeanDistance	25
PoleRow2MeanDistance	10
PoleRow1DistanceSigma	10
PoleRow2DistanceSigma	10

Table B.1: Parameters for the pedestrian channel model.

B.1.5 Section 3.5.4: Measured Pedestrian Channel

- Navigation signals: chip rate T_c=1.023 MChips/s, Gold code of length 1023, two-sided signal bandwidth 16 MHz, carrier frequency f_0=1.575 GHz

- Receiver: noise level 45 dB-Hz, 2nd order DLL with loop bandwith 2 Hz and damping factor 0.7, narrow DLL correlator spacing of $\Delta\tau$=0.1 chips, correlator bank with $N_{cc} = N_{pc} = 35$ signal matched correlators spaced symmetrically around the DLL inphase correlator at a distance of 0.0625 chips, sampling period T_s=62.5 ns, coherent observation period 10 ms corresponding to L=160 kSamples and an amplitude filter update rate of 100 Hz, number of incoherent blocks N_b=10 corresponding to a path activity, delay, delay rate, position, velocity, clock, and clock drift update rate of 10 Hz, user dynamics $\sigma_x = 0.1\,\mathrm{m}$, $\sigma_y = 0.1\,\mathrm{m}$, $\sigma_z = 0.1\,\mathrm{m}$, $\sigma_\tau = 0.1\,\mathrm{m}$, $\sigma_{\dot{x}} = 0.1\,\mathrm{m/s}$, $\sigma_{\dot{y}} = 0.1\,\mathrm{m/s}$, $\sigma_{\dot{z}} = 0.1\,\mathrm{m/s}$, $\sigma_{\dot{\tau}} = 0.1\,\mathrm{m/s}$, $\sigma_a = 0.1$, $p_{\mathrm{offon}} = 10^{-6}$, $p_{\mathrm{onoff}} = 1 - 10^{-6}$, interpolation pulse length $N_g = 128$, signal-to-multipath ratio SMR=6 dB, number of particles $N_p = 100$.

B.2 Chapter 4

B.2.1 Section 4.2.3: Proposal Density

Step rate 1 Hz, step measurement noise $\sigma_{\Delta x} = \sigma_{\Delta y} = 0.1\,\mathrm{m}$, $\sigma_{\Delta\Psi} = 2°$, movement model $\sigma_x = \sigma_y = 1\,\mathrm{m}$, $\sigma_\Psi = 45°$.

B.2.2 Section 4.3.1: Error Analysis

Step rate per foot 1 Hz, step measurement noise $\sigma_{\Delta x} = \sigma_{\Delta y} = 0.1\,\mathrm{m}$, $\sigma_{\Delta\Psi} = 2°$, movement model $\sigma_x = \sigma_y = 1\,\mathrm{m}$, $\sigma_\Psi = 45°$.

B.2.3 Section 4.3.2: Experiment

Lower filter settings $\sigma_{a,x} = \sigma_{a,y} = \sigma_{a,z} = 5 \cdot 10^4\,\mathrm{m/s^2}$, $\sigma_{\omega,x} = \sigma_{\omega,y} = \sigma_{\omega,z} = 0.014°$, movement model $p_{\mathrm{cross}} = 0$.

B.3 Chapter 5

B.3.1 Section 5.1: Filter Settings

Process noise $\sigma_{\Delta x} = \sigma_{\Delta y} = 0.5\,\mathrm{m}$, $\sigma_{\Delta\Psi} = 10°$, measurement noise $\sigma_{\mathrm{WLAN}} = 5\,\mathrm{m}$, initial covariance $\sigma_{x,0} = \sigma_{y,0} = 10\,\mathrm{m}$, $\sigma_{\Psi,0} = 1°$, lower filter settings $\sigma_{a,x} = \sigma_{a,y} = \sigma_{a,z} = 5 \cdot 10^4\,\mathrm{m/s^2}$, $\sigma_{\omega,x} = \sigma_{\omega,y} = \sigma_{\omega,z} = 0.014°$.

B.3.2 Section 5.2: Filter Settings

Step measurement noise $\sigma_{\Delta x} = \sigma_{\Delta y} = 0.02\,\mathrm{m}$, $\sigma_{\Delta\Psi} = 10°$, movement model $\sigma_x = \sigma_y = 1\,\mathrm{m}$, $\sigma_{\Psi} = 45°$.

Appendix C

Sensors and Devices

Table C.1 lists the sensors that were employed for collecting the measurement data sets that were published in [AFK$^+$09] and which were used within the scope of Chapter 5.2 of this thesis.

Sensor	Manufacturer, Type, URL
GPS Receiver	ublox EVK-5 `http://www.u-blox.com/`
Electronic Compass	OceanServer OS-5000 `http://www.ocean-server.com/`
Baro-Altimeter	Intersema MS55490 `http://www.intersema.ch/`
RFID	Indentec Solutions i-CARD2 reader and tags `http://www.identecsolutions.com/`
IMU	Xsens MTx-28A53G25 `http://www.xsens.com/`

Table C.1: Personal navigation sensors and manufacturers with their website URLs.

Bibliography

[AERNU05] F. Antreich, O. Esbri-Rodriguez, J. Nossek, and W. Utschick. Estimation of synchronization parameters using SAGE in a GNSS receiver. In *Proceedings of the 18th International Technical Meeting of the Satellite Division of the Institute of Navigation (ION GNSS 2005)*, pages 2124–2131, Long Beach, California, USA, 2005.

[AFK$^+$09] M. Angermann, A. Friese, M. Khider, B. Krach, K. Krack, and P. Robertson. A reference measurement data set for multisensor pedestrian navigation with accurate ground truth. In *Proceedings of the 2009 European Navigation Conference - Global Navigation Satellite Systems (ENC-GNSS 2009)*, Naples, Italy, May 2009.

[AKR$^+$01] M. Angermann, J. Kammann, P. Robertson, A. Steingass, and T. Strang. Software representation for heterogeneous location data sources using probability density functions. In *Proceedings of the International Symposium on Location Based Services for Cellular Users 2001 (LOCELLUS 2001)*, pages 107–118, Munich, Germany, February 2001.

[AMGC02] S. Arulampalam, S. Maskell, N. Gordon, and T. Clapp. A tutorial on particle filters for online nonlinear/non-Gaussian Bayesian tracking. *IEEE Transactions on Signal Processing*, 50(2):174–188, February 2002. doi:10.1109/78.978374.

[ANU08] F. Antreich, J. A. Nossek, and W. Utschick. Maximum likelihood delay estimation in a navigation receiver for aeronautical applications. *Aerospace Science and Technology*, 12(3):256–267, April 2008. doi:10.1016/j.ast.2007.06.005.

[ARHW$^+$07] J. Avila-Rodriguez, G. Hein, S. Wallner, J. Issler, L. Ries, L. Lestarquit, A. De Latour, J. Godet, F. Bastide, T. Pratt, and J. Owen. The MBOC modulation: The final touch to the Galileo frequency and signal plan. In *Proceedings of the 20th International Technical Meeting of the Satellite Division of the Institute of Navigation (ION GNSS 2007)*, Fort Worth, Texas, USA, September 2007.

[AS01] B. Azimi-Sadjadi. *Approximate Nonlinear Filtering with Applications to Navigation*. PhD thesis, University of Maryland, May 2001.

[Bea07] S. Beauregard. Omnidirectional pedestrian navigation for first responders. In *Proceedings of the 4th Workshop on Positioning, Navigation and Communication, 2007, WPNC07*, pages 33–36, Hannover, Germany, March 2007.

[BP00] P. Bahl and V. N. Padmanabhan. RADAR: An in-building RF-based user location and tracking system. In *Proceedings of the 19th Annual Joint Conference of the IEEE Computer and Communications Societies (INFOCOM 2000)*, pages 775–784, Tel Aviv, Israel, March 2000.

[BRPT04] T. Bertozzi, D. L. Ruyet, C. Panazio, and H. V. Thien. Channel tracking using particle filtering in unresolvable multipath environments. *EURASIP Journal on Applied Signal Processing*, 15:2328–2338, 2004.

[BvD99] M. Braasch and A. van Dierendonck. GPS receiver architectures and measurements. In *Proceedings of the IEEE*, volume 87, pages 48–64, January 1999.

[BWK08] S. Beauregard, Widyawan, and M. Klepal. Indoor PDR performance enhancement using minimal map information and particle filters. In *Proceedings of the 2008 IEEE/ION Position, Location, and Navigation Symposium, PLANS 2008*, Monterey, California, USA, May 2008.

[CFPFR06] P. Closas, C. Fernandez-Prades, and J. Fernandez-Rubio. Bayesian DLL for multipath mitigation in navigation systems using particle filters. In *Proceedings of the IEEE International Conference on Acoustics, Speech and Signal Processing 2006 (ICASSP 2006)*, Toulouse, France, May 2006.

[CFPFR07a] P. Closas, C. Fernandez-Prades, and J. Fernandez-Rubio. Maximum likelihood estimation of position in GNSS. *IEEE Signal Processing Letters*, 14(5):359–362, May 2007. doi:10.1109/LSP.2006.888360.

[CFPFR07b] P. Closas, C. Fernandez-Prades, and J. Fernandez-Rubio. ML estimation of position in a GNSS receiver using the SAGE algorithm. In *Proceedings of the IEEE International Conference on Acoustics, Speech and Signal Processing 2007 (ICASSP 2007)*, volume 3, pages 1045–1048, Honolulu, Hawaii, USA, April 2007.

[CFPFR08] P. Closas, C. Fernandez-Prades, and J. A. Fernandez-Rubio. A particle filtering tracking algorithm for GNSS synchronization using Laplace's method. In *Proceedings of the IEEE International Conference on Acoustics, Speech and Signal Processing 2008 (ICASSP 2008)*, pages 3409–3412, Las Vegas, Nevada, USA, March 2008.

[CFPFRRG06] P. Closas, C. Fernandez-Prades, J. Fernandez-Rubio, and A. Ramirez-Gonzalez. Multipath mitigation using particle filtering. In *Proceedings of the 19th International Technical Meeting of the Satellite Division of the Institute of Navigation (ION GNSS 2006)*, pages 1733–1740, Fort Worth, Texas, USA, September 2006.

[CG05] A. Cavallo, F.and Sabatini and V. Genovese. A step toward GPS/INS personal navigation systems: real-time assessment of gait by foot inertial sensing. In *Proceedings of the IEEE/RSJ International Conference on Intelligent Robots and Systems 2005 (IROS 2005)*, pages 1187–1191, August 2005.

[CML03] J. Collin, O. Mezentsev, and G. Lachapelle. Indoor positioning system using accelerometry and high accuracy heading sensors. In *Proceedings of the 16th International Technical Meeting of the Satellite Division of the Institute of Navigation ION GPS/GNSS 2003*, Portland, Orgeon, USA, September 2003.

[Col06] J. Collin. *Investigations of Self-Contained Sensors for Personal Navigation*. PhD thesis, Tampere University of Technology, September 2006.

[DdFG01] A. Doucet, N. de Freitas, and N. Gordon, editors. *Sequential Monte Carlo Methods in Practice*. Springer, New York, 2001.

[DdFMR00] A. Doucet, N. de Freitas, K. Murphy, and S. Russell. Rao-Blackwellised particle filtering for dynamic Bayesian networks. In *Proceedings of the 16th Annual Conference on Uncertainty in Artificial Intelligence (UAI 2000)*, pages 176–183, San Francisco, California, USA, 2000.

[DMS98] C. Drane, M. Macnaughtan, and C. Scott. Positioning GSM telephones. *IEEE Communications Magazine*, 36(4):46–54, April 1998. doi:10.1109/35.667413.

[EM06a] P. Enge and P. Misra. *Global Positioning System: Signals, Measurements, and Performance*. Ganga-Jamuna Press, Lincoln, Massachusetts, second edition, 2006.

[EM06b] F. Evennou and F. Marx. Advanced integration of WiFi and inertial navigation systems for indoor mobile positioning. *EURASIP Journal on Applied Signal Processing*, 2006, January 2006. doi:10.1155/ASP/2006/86706.

[Fea98] P. Fearnhead. *Sequential Monte Carlo methods in filter theory*. PhD thesis, University of Oxford, 1998.

[FH94] J. Fessler and A. Hero. Space-alternating generalized expectation-maximization algorithm. *IEEE Transactions on Signal Processing*, 42(10):2664–2677, October 1994. doi:10.1109/78.324732.

[FJ05] P. Fenton and J. Jones. The theory and performance of NovAtel Inc.'s Vision Correlator. In *Proceedings of the 18th International Technical Meeting of the Satellite Division of the Institute of Navigation (ION GNSS 2005)*, pages 2178–2186, Long Beach, California, USA, September 2005.

[Fox05] E. Foxlin. Pedestrian tracking with shoe-mounted inertial sensors. *IEEE Computer Graphics and Applications*, 25(6):38–46, November 2005. doi:10.1109/MCG.2005.140.

[GGB$^+$02] F. Gustafsson, F. Gunnarsson, N. Bergman, U. Forssell, J. Jansson, R. Karlsson, and P.-J. Nordlund. Particle filters for positioning, navigation, and tracking. *IEEE Transactions on Signal Processing*, 50(2):425–437, February 2002. doi:10.1109/78.978396.

[GLC06] S. Godha, G. Lachapelle, and M. E. Cannon. Integrated GPS/INS system for pedestrian navigation in a signal degraded environment. In *Proceedings of the 19th International Technical Meeting of the Satellite Division of the Institute of Navigation ION GNSS 2006*, Fort Worth, Texas, USA, September 2006.

[GM99] V. Gabaglio and B. Merminod. Real-time calibration of length of steps with GPS and accelerometers. In *Proceedings of the 1999 European Navigation Conference - Global Navigation Satellite Systems (ENC-GNSS 1999)*, pages 599–605, Genova, Italia, October 1999.

[GPL$^+$07] P. D. Groves, G. W. Pulford, C. A. Littlefield, D. L. J. Nash, and C. J. Mather. Inertial navigation versus pedestrian dead reckoning: Optimizing the integration. In *Proceedings of the 20th International Technical Meeting of the Satellite Division of the Institute of Navigation ION GNSS 2007*, pages 2043—2055, Fort Worth, Texas, USA, September 2007.

[GT05] A. Giremus and Y.-Y. Tourneret. Joint detection/estimation of multipath effects for the Global Positioning System. In *Proceedings of the IEEE International Conference on Acoustics, Speech, and Signal Processing 2005 (ICASSP 2005)*, Philadelphia, Pennsylvania, USA, March 2005.

[GTG$^+$05] S. Gezici, Z. Tian, G. Giannakis, H. Kobayashi, A. Molisch, H. Poor, and Z. Sahinoglu. Localization via ultra-wideband radios: a look at positioning aspects for future sensor networks. *IEEE Signal Processing Magazine*, 22(4):70–84, 2005. doi:10.1109/MSP.2005.1458289.

[GvDR96] L. Garin, F. van Diggelen, and J. Rousseau. Strobe and Edge correlator multipath mitigation for code. In *Proceedings of the 9th International Technical Meeting of the Satellite Division of the Institute of Navigation (ION GPS 1996)*, pages 657–664, Kansas City, Missouri, USA, 1996.

[GWA01] M. Grewal, L. Weill, and A. Andrews. *Global Positioning Systems, Inertial Navigation, and Integration*, volume 5 of *IEE Radar, Navigation and Avionics Series*. John Wiley & Sons, Inc., New York, second edition, 2001.

[Hag94] J. Hagenauer. Soft is better than hard. *Comunications and Cryptology - Two Sides of One Tapestry*, pages 155–171, 1994.

[HKDA08] A. Hornbostel, A. Konovaltsev, H. Denks, and F. Antreich. Simulation of multi-element antenna systems for navigation applications. *IEEE Systems Journal*, 2(1):7–19, March 2008. doi:10.1109/JSYST.2007.916048.

[IARH05] M. Irsigler, J. Avila-Rodriguez, and G. Hein. Criteria for GNSS multipath performance assessment. In *Proceedings of the 18th International Technical Meeting of the Satellite Division of the Institute of Navigation (ION GNSS 2005)*, Long Beach, California , USA, September 2005.

[IEE99] IEEE 802.11b-1999. Supplement to IEEE 802.11 standard, higher-speed physical layer extension in the 2.4 GHz band, 1999.

[IHE04] M. Irsigler, G. Hein, and B. Eissfeller. Multipath performance analysis for future GNSS signals. In *Proceedings of the 2004 National Technical Meeting of the Satellite Division of the Institute of Navigation (ION NTM 2004)*, San Diego, California, USA, January 2004.

[Ilt90] R. Iltis. Joint estimation of PN code delay and multipath using the extended Kalman filter. *IEEE Transactions on Communications*, 38(10):1677–1685, 1990. doi:10.1109/26.61437.

[IR03] ITU-R/P.681-6. Propagation data required for the design of earth-space land mobile telecommunication systems, 2003.

[IR07] ITU-R/P.682-2. Propagation data required for the design of earth-space aeronautical mobile telecommunication systems, 2007.

[ISO99] ISO/IEC 8802-11. Wireless lan medium access control (MAC) and physical layer (PHY) specifications, 1999.

[Jaz70] A. H. Jazwinski. *Stochastic Processes and Filtering Theory*. Academic Press, New York, 1970.

[JFS04] J. Jones, P. Fenton, and B. Smith. Theory and performance of the Pulse Aperture Correlator. In *NovAtel Technical Report, NovAtel Inc.*, Calgary, Alberta, Canada, 2004.

[Kal60] R. E. Kalman. A new approach to linear filtering and prediction problems. *Transactions of the ASME–Journal of Basic Engineering*, 82(Series D):35–45, 1960.

[Kap96] E. D. Kaplan. *Understanding GPS: Principles and Applications*. Artech House Publishers, Boston, London, 1996.

[Kay93] S. M. Kay. *Fundamentals of Statistical Signal Processing - Estimation Theory*. Prentice Hall, New Jersey, 1993.

[KF97] M. Kayton and W. R. Fried. *Avionics Navigation Systems*. John Wiley & Sons, Inc., New York, 2nd edition, 1997.

[KHLH03] A. Kotanen, M. Hännikäinen, H. Leppäkoski, and T. D. Hämäläinen. Positioning with IEEE 802.11b wireless LAN. In *Proceedings of the 14th IEEE Personal, Indoor and Mobile Radio Communications Symposium (PIMRC 2003)*, pages 2218–2222, Beijing, China, 2003.

[Kin98] A. D. King. Inertial navigation - forty years of evolution. *General Electric Company Review*, 13(2):140–149, 1998.

[KKRA08] M. Khider, S. Kaiser, P. Robertson, and M. Angermann. A novel movement model for pedestrians suitable for personal navigation. In *Proceedings of the Institute of Navigation National Technical Meeting 2008*, San Diego, California, USA, January 2008.

[KLR08a] B. Krach, M. Lentmaier, and P. Robertson. Bayesian detection and tracking for joint positioning and multipath mitigation in GNSS. In *Proceedings of the 5th Workshop on Positioning, Navigation and Communication (WPNC 2008)*, pages 173–180, Hannover, Germany, March 2008.

[KLR08b] B. Krach, M. Lentmaier, and P. Robertson. Joint Bayesian positioning and multipath mitigation in GNSS. In *Proceedings of the IEEE International Conference on Acoustics, Speech and Signal Processing 2008 (ICASSP 2008)*, pages 3437–3440, Las Vegas, Nevada, USA, March 2008.

[KMM05] D. Kubrak, C. Macabiau, and M. Monnerat. Performance analysis of MEMS based pedestrian navigation systems. In *Proceedings of the 18th International Technical Meeting of the Satellite Division of the Institute of Navigation ION GNSS 2005*, Long Beach, California, USA, September 2005.

[KMM06] D. Kubrak, C. Macabiau, and M. Monnerat. Real time pedestrian navigation system. In *Proceedings of the 19th International Technical Meeting of the Satellite Division of the Institute of Navigation ION GNSS 2006*, Fort Worth, Texas, USA, September 2006.

[KR08a] B. Krach and P. Robertson. Cascaded estimation architecture for integration of foot-mounted inertial sensors. In *Proceedings of the 2008 IEEE/ION Position, Location, and Navigation Symposium (PLANS 2008)*, pages 112–119, Monterey, California, USA, May 2008.

[KR08b] B. Krach and P. Robertson. Integration of foot-mounted inertial sensors into a Bayesian location-estimation framework. In *Proceedings of the 5th Workshop on Positioning, Navigation and Communication (WPNC 2008)*, pages 55–61, Hannover, Germany, March 2008.

[Kub07] D. Kubrak. *Hybridisation of a GPS Receiver with Low-Cost Sensors for Personal Positioning in Urban Environment*. PhD thesis, Ecole Nationale Superieure des Telecommunications Paris, 2007.

[KW09] B. Krach and R. Weigel. Markovian channel modeling for multipath mitigation in navigation receivers. In *Proceedings of the 3rd European Conference on Antennas and Propagation (EUCAP 2009)*, Berlin, Germany, March 2009. VDE Verlag.

[Lad00] Q. Ladetto. On foot navigation: continuous step calibration using both complementary recursive prediction and adaptive Kalman filtering. In *Proceedings of the 13th International Technical Meeting of the Satellite Division of the Institute of Navigation ION GPS 2000*, 2000.

[Leh07] A. Lehner. *Multipath Channel Modelling of Satellite Navigation Systems*. PhD thesis, University of Erlangen-Nuremberg, April 2007.

[LKR08] M. Lentmaier, B. Krach, and P. Robertson. Bayesian time delay estimation of GNSS signals in dynamic multipath environments. *International Journal of Navigation and Observation*, 2008, March 2008. doi:10.1155/2008/372651.

[LKRT07] M. Lentmaier, B. Krach, P. Robertson, and T. Thiasiriphet. Dynamic multipath estimation by sequential monte carlo methods. In *Proceedings of the 20th International Technical Meeting of the Satellite Division of the Institute of Navigation (ION GNSS 2007)*, pages 1712–1721, Fort Worth, Texas, USA, September 2007.

[LS05] A. Lehner and A. Steingass. A novel channel model for land mobile satellite navigation. In *Proceedings of the 18th International Technical Meeting of the Satellite Division of the Institute of Navigation (ION GNSS 2005)*, Fort Worth, Texas, USA, September 2005.

[LS09] A. Lehner and A. Steingass. A location and movement dependent gnss multipath error model for pedestrian applications. In *Proceedings of the 2009 European Navigation Conference - Global Navigation Satellite Systems (ENC-GNSS 2009)*, Naples, Italy, May 2009.

[Lui02] H. Luinge. *Inertial Sensing of Human Movement*. PhD thesis, Twente University, October 2002.

[Mas04] S. Maskell. *Sequentially Structured Bayesian Solutions*. PhD thesis, Cambridge University, February 2004.

[May79] P. Maybeck. *Stochastic Models, Estimation and Control, Volume I*, volume 141 of *Mathematics in Science and Engineering*. Academic Press, Inc., New York, 1979.

[MB99] G. MacGraw and M. Brasch. GNSS multipath mitigation using gated and high resolution correlator concepts. In *Proceedings of the ION National Technical Meeting*, San Diego, California, USA, 1999.

[MM93] G. Minkler and J. Minkler. *Theory and Application of Kalman Filtering*. Magellan Book Company, Palm Bay, 1993.

[MTKW02] M. Montemerlo, S. Thrun, D. Koller, and B. Wegbreit. Fastslam: a factored solution to the simultaneous localization and mapping problem. In *Eighteenth national conference on Artificial intelligence*, pages 593–598, Menlo Park, CA, USA, 2002. American Association for Artificial Intelligence.

[Nat04] Advances in navigation sensors and integration technology. NATO RTO Eductional Notes, RTO-EN-SET-064, AC/323(SET-064)TP/43, February 2004.

[NSL07] F. D. Nunes, F. M. G. Sousa, and J. M. N. Leitao. Gating functions for multipath mitigation in GNSS BOC signals. *IEEE Transactions on Aerospace and Electronic Systems*, 43(3):951–964, 2007. doi:10.1109/TAES.2007.4383585.

[OBS^{+}05] M. Ocana, L. Bergasa, M. Sotelo, J. Nuevo, and R. Flores. Indoor robot localization system using wifi signal measure and minimizing calibration effort. In *Proceedings of the IEEE International Symposium on Industrial Electronics, 2005.*, pages 1545–1550, June 2005.

[PCB00] N. B. Priyantha, A. Chakraborty, and H. Balakrishnan. The cricket location-support system. In *Proc. of the Sixth Annual ACM International Conference on Mobile Computing and Networking (MOBICOM) 2000*, August 2000.

[PDF04] E. Punskaya, A. Doucet, and W. J. Fitzgerald. Particle filtering for joint symbol and code delay estimation in DS spread spectrum systems in multipath environments. *EURASIP Journal on Applied Signal Processing*, 15:2306–2314, 2004. doi:10.1155/S1110865704408063.

[PS96] B. W. Parkinson and J. J. Spilker Jr., editors. *Global Positioning System: Theory and Applications*. Number 163 in Progress in Astronautics and Aeronautics Series. AIAA, 1996.

[PS99] M. K. Pitt and N. Shephard. Filtering via simulation: Auxiliary particle filters. *Journal of the American Statistical Association*, 94(446), 1999. doi:10.2307/2670179.

[QLPD07] I. J. Quader, B. Li, W. Peng, and A. G. Dempster. Use of fingerprinting in Wi-Fi based outdoor positioning. In *Proceedings of the International Global Navigation Satellite Systems Society (IGNSS) Symposium 2007*, Sydney, Australia, December 2007.

[RAG04] B. Ristic, S. Arulampalam, and N. Gordon. *Beyond the Kalman Filter - Particle Filters for Tracking Applications*. Artech House, Boston-London, 2004.

[Raj08] S. Rajagopal. Personal dead reckoning system with shoe mounted inertial sensors. Master's thesis, Royal Institute of Technology, Stockholm, Sweden, 2008. XR-EE-SB 2008:013.

[RMT^{+}02] T. Roos, P. Myllymäki, H. Tirri, P. Misikangas, and J. Sievänen. A probabilistic approach to WLAN user location estimation. *International Journal of Wireless Information Networks*, 9:155–164, 2002.

[Roe06] D. Roetenberg. *Inertial and Magnetic Sensing of Human Motion*. PhD thesis, Twente University, May 2006.

[SA06a] M. Sahmoudi and M. Amin. Fast iterative maximum-likelihood algorithm (FIMLA) for multipath mitigation in next generation of GNSS receivers. In *Proceedings of 40th Asilomar Conference on Signals, Systems and Computers (ACSSC 2006)*, pages 579–584, Pacific Grove, California, USA, October 2006.

[SA06b] M. Sahmoudi and M. Amin. Improved maximum-likelihood time delay estimation for GPS positioning in multipath, interference and low SNR environments.

In *Proceedings of the IEEE/ION Position Location and Navigation Symposium (PLANS 2006)*, pages 876–882, San Diego, California, USA, April 2006.

[SB01] D. Salmond and H. Birch. A particle filter for track-before-detect. In *Proceedings of the 2001 American Control Conference*, volume 5, pages 3755–3760, Arlington, Virginia, USA, June 2001.

[Sch03] T. Schön. *On Computational Methods for Nonlinear Estimation*. Licentiate thesis no. 1047, Department of Electrical Engineering, Linköping University, SE-581 83 Linköping, Sweden, October 2003.

[Sel04a] J. Selva. Newton-type methods in array processing. *IEEE Signal Processing Letters*, 11(2):2036–2045, February 2004. doi:10.1109/LSP.2003.821651.

[Sel04b] J. Selva. Complexity reduction in the parametric estimation of superimposed signal replicas. *Signal Processing*, 84(12):2325–2343, 2004. doi:10.1016/j.sigpro.2004.07.026.

[Sel04c] J. Selva. *Efficient Multipath Mitigation in Navigation Systems*. PhD thesis, Universitat Politecnica de Catalunya, February 2004.

[Sel05] J. Selva. An efficient Newton-type method for the computation of ML estimators in a uniform linear array. *IEEE Transactions on Signal Processing*, 53(6):2036–2045, June 2005. doi:10.1109/TSP.2005.847842.

[Sel06] J. Selva. Interpolation of bounded bandlimited signals and applications. *IEEE Transactions on Signal Processing*, 54(11):4244–4260, November 2006. doi:10.1109/TSP.2006.880231.

[SFL05] R. Stirling, K. Fyfe, and G. Lachapelle. Evaluation of a new method of heading estimation for pedestrian dead reckoning using shoe mounted sensors. *The Journal of Navigation*, 58:31–45, 2005. doi:10.1017/S0373463304003066.

[SG00] G. Seco-Granados. *Antenna Arrays for Multipath and Interference Mitigation in GNSS Receivers*. PhD thesis, Universitat Politecnica de Catalunya, December 2000.

[SGFRFP05] G. Seco-Granados, J. Fernandez-Rubio, and C. Fernandez-Prades. ML estimator and hybrid beamformer for multipath and interference mitigation in GNSS receivers. *IEEE Transactions on Signal Processing*, 53(3):1194–1208, March 2005. doi:10.1109/TSP.2004.842193.

[SGN05] T. Schön, F. Gustafsson, and P. J. Nordlund. Marginalized particle filters for mixed linear/nonlinear state-space models. *IEEE Transactions on Signal Processing*, 53(7):2279–2289, 2005. doi:10.1109/TSP.2005.849151.

[SL03] A. Steingass and A. Lehner. Land mobile satellite navigation - characteristics of the multipath channel. In *Proceedings of the 16th International Technical Meeting of the Satellite Division of the Institute of Navigation (ION GNSS 2003)*, Portland, Oregon, USA, September 2003.

[SL04] A. Steingass and A. Lehner. Measuring the navigation multipath channel - a statistical analysis. In *Proceedings of the 17th International Technical Meeting of the Satellite Division of the Institute of Navigation (ION GNSS 2004)*, pages 1157–1164, Long Beach, California, USA, September 2004.

[SLF$^+$04] A. Steingass, A. Lehner, P.-F. F., K. E., M. M.J., and A.-R. B. The high resolution aeronautical multipath navigation channel. In *Proceedings of the 2004 National Technical Meeting of the Satellite Division of the Institute of Navigation (ION NTM 2004)*, San Diego, California, USA, January 2004.

[Spa07] I. Spassov. *Algorithms for Map-Aided Autonomous Indoor Pedestrian Positioning and Navigation*. PhD thesis, Ecole Polytechnique Federale de Lausanne, November 2007.

[SPSS$^+$07] J. Seitz, L. Patio-Studencka, B. Schindler, S. Haimerl, J. G. Boronat, S. Meyer, and J. Thielecke. Sensor data fusion for pedestrian navigation using WLAN and INS. In *Symposium Gyro Technology 2007*, Karlsruhe, Germany, September 2007.

[SSL04] P. Stoica, Y. Selen, and J. Li. On information criteria and the generalized likelihood ratio test of model order selection. *IEEE Signal Processing Letters*, 11(10):794–797, 2004. doi:10.1109/LSP.2004.835468.

[Ste02] A. Steingass. *Simulation von Navigationssystemen*. PhD thesis, University of Essen, May 2002.

[TW04] D. H. Titterton and J. L. Weston. *Strapdown inertial navigation technology*, volume 5 of *IEE Radar, Navigation and Avionics Series*. Peter Peregrinus Ltd., London, second edition, 2004.

[vDFF92] A. van Dierendonck, P. Fenton, and T. Ford. Theory and performance of narrow correlator spacing in a GPS receiver. In *Proceedings of the ION National Technical Meeting*, San Diego, California, USA, 1992.

[vdMW04] R. van der Merwe and E. A. Wan. Sigma-point Kalman filters for integrated navigation. In *Proceedings of the 60th Annual Meeting of the Institute of Navigation*, June 2004.

[Ver05] S. Verhagen. *The GNSS integer ambiguities: estimation and validation*. PhD thesis, Technical University Delft, January 2005.

[vNSFT94] D. van Nee, J. Siereveld, P. Fenton, and B. Townsend. The multipath estimating delay lock loop: Approaching theoretical accuracy limits. In *Proceedings of the IEEE Position Location and Navigation Symposium (PLANS 1994)*, pages 246–251, Las Vegas, Nevada, USA, 1994.

[vT68] H. L. van Trees. *Detection, Estimation, and Modulation Theory*. John Wiley & Sons, New York, London, Sydney, 1968.

[Wei95] L. Weill. Achieving theoretical accuracy limits for pseudoranging in the presence of multipath. In *Proceedings of the 8th International Technical Meeting of the Satellite Division of the Institute of Navigation (ION GPS 1995)*, pages 1521–1530, Palm Springs, California, USA, 1995.

[Wei06] L. Weill. Achieving theoretical bounds for receiver-based multipath mitigation using Galileo OS signals. In *Proceedings of the 19th International Technical Meeting of the Satellite Division of the Institute of Navigation (ION GNSS 2006)*, pages 1035–1047, Fort Worth, Texas, USA, September 2006.

[WH08] O. Woodman and R. Harle. Pedestrian localisation for indoor environments. In *Proceedings of the 10th International Conference on Ubiquitous Computing, UbiComp 2008*, pages 114–123, Seoul, South Korea, September 2008.

[WKAR06] K. Wendlandt, M. Khider, M. Angermann, and P. Robertson. Continuous location and direction estimation with multiple sensors using particle filtering. In *Proceedings of the 2006 International Conference in Multisensor Fusion and Integration for Intelligent Systems, MFI 2006*, September 2006.

[WKB08] Widyawan, M. Klepal, and S. Beauregard. A backtracking particle filter for fusing building plans with PDR displacement estimates. In *Proceedings of the 5th Workshop on Positioning, Navigation and Communication, 2008, WPNC08*, Hannover, Germany, March 2008.

[WRK$^+$07] K. Wendlandt, P. Robertson, M. Khider, M. Angermann, and K. Sukchaya. Demonstration of a realtime active-tag RFID, Java based indoor localization system using particle filtering. In *Adjunct Proceedings of the 9th International Conference on Ubiquitous Computing, UbiComp 2007*, September 2007.

[YAS03] M. A. Youssef, A. Agrawala, and A. U. Shankar. WLAN location determination via clustering and probability distributions. In *Proceeding of the 1st IEEE International Conference on Pervasive Computing and Communications (PerCom 2003)*, Fort Worth, Texas, USA, March 2003.

[ZHD06] V. Zarimpas, B. Honary, and M. Darnell. Indoor 802.1x based location determination and real-time tracking. In *Proceedings of the 1st IET International Conference on Wireless, Mobile and Multimedia Networks (ICWMMN 2006)*, Hang Zhou, China, November 2006.

[ZHL$^+$05] V. Zarimpas, B. Honary, D. Lund, C. Tanriover, and N. Thanopoulos. Location determination and tracking using radio beacons. In *Proceedings of the 6th IEE International Conference on 3G and Beyond*, pages 207–211, Washington, Columbia, USA, November 2005.

List of Abbreviations

6DOF	Six degrees of freedom
AGPS	Assisted GPS
AHRS	Attitude and heading reference systems
BPSK	Binary phase shift keying
BOC	Binary offset carrier
CBOC	Composite binary offset carrier
CDF	Cumulative density function
CDMA	Code division multiplex access
CIR	Channel impulse response
DFT	Discrete Fourier transformation
DGPS	Differential GPS
DLL	Delay lock loop
DLR	Deutsches Zentrum für Luft- und Raumfahrt / German Aerospace Center
FIR	Finite impulse response
FLL	Frequency lock loop
GBAS	Ground-based augmentation system
GNSS	Global navigation satellite system
GPS	Global Positioning System
GSM	Global System for Mobile Communications
GTRP	Ground truth reference point
ID	Identification number
IDFT	Inverse DFT
IIR	Infinite impulse response
INC	Inertial navigation computer
IMU	Inertial measurement unit
INS	Inertial navigation system
LOS	Line-of-sight
LS	Least squares
MEDLL	Multipath estimating DLL
MEMS	Micro-electro-mechanical system
NCO	Numerically controlled oscillator
PDA	Personal digital assistant
PDF	Probability density function
PDR	Pedestrian dead-reckoning
PLL	Phase lock loop

RF	Radio frequency
RFID	Radio frequency identification
RSS	Received signal strength
SBAS	Satellite-based augmentation system
SLAM	Simultaneous localization and mapping
SMP	Static multipath
SMR	Signal-to-multipath ratio
SNR	Signal-to-noise ratio
SoLo	Soft-Location
TED	Timing error detector
TOA	Time-of-arrival
TTFF	Time-to-first-fix
UMTS	Universal Mobile Telecommunications System
UWB	Ultra-wideband
WLAN	Wireless Local Area Network
ZUPT	Zero velocity update

List of Symbols

Operators

$\lvert \bullet \rvert$	Magnitude/Determinant of $\bullet$
$\Vert \bullet \Vert$	Magnitude of the determinant of $\bullet$
$[\bullet\times]$	Skew symmetric form of the vector $\bullet$
$\bullet_{[a:b,c:d]}$	Sub-matrix of $\bullet$ from row a to b and column c to d
$\mathrm{diag}(\bullet)$	Diagonal matrix of the vector $(\bullet)$
$\bullet^H$	Hermitian of the matrix or vector $\bullet$
$\bullet^T$	Transpose of the matrix or vector $\bullet$

Constants

c	Speed of light
e	Euler Number
j	Imaginary unit
π	Pi

Indices

c	Compressed quantity
i	Path index
j	Sensor index
k	Temporal block index
l	Temporal sub-block index
μ	Particle index

Indicators

$\hat{\bullet}$	Estimate of $\bullet$
$\hat{\bullet}^-$	A priori estimate of $\bullet$
$\delta\bullet$	Deviation from $\bullet$
$\bullet_{N\times M}$	Matrix $\bullet$ of dimension $N \times M$

Functions

Scalars

a	Complex amplitude
e	Binary path activity
n	Noise
s	Navigation signal
t	Time
z	Measurement
D	Discriminator
ε	Residual travel time errors
ϕ	Phase of complex amplitude
ρ	Pseudorange
σ	Standard deviation
τ	Delay / Signal travel time
τ^0	Initial delay hypothesis
τ^g	Geometrical travel time
τ^r	Receiver clock error
τ^{iono}	Ionospheric delay
τ^{tropo}	Tropospheric delay
τ_ϵ	Timing error
ω	Turn rate

Vectors

$\mathbf{a}$	Complex amplitude
$\mathbf{a}^i, \mathbf{a}^b$	Acceleration in inertial/body frame
$\mathbf{e}$	Binary path activity
$\mathbf{f}^i, \mathbf{f}^b$	Acting force in inertial/body frame
$\mathbf{g}^i, \mathbf{g}^b$	Gravity in inertial/body frame
$\mathbf{n}$	Noise
$\mathbf{n}^d$	Dynamic/Process noise
$\mathbf{n}^m$	Measurement noise
$\mathbf{s}$	Navigation signal
$\mathbf{r}$, $\mathbf{r}^i$	Position (in inertial frame)
$\mathbf{r}^r$	Receiver position
$\mathbf{r}^t$	Transmitter position
$\mathbf{y}$	Signal vector at nominal level
$\mathbf{v}, \mathbf{v}^i$	Velocity (in inertial frame)
$\mathbf{x}$	State
$\mathbf{y}$	Signal including amplitudes
$\mathbf{z}$	Measurement
δ	Pulse
$\boldsymbol{\tau}$	Delay

$\boldsymbol{\tau}_0$	Initial delay hypothesis
$\boldsymbol{\tau}^b$	Delays of correlator bank
$\boldsymbol{\Psi}$	Attitude
$\boldsymbol{\omega}$	Turn rate vector
$\boldsymbol{\omega}_{ib}^b$	Rotation vector of body frame with respect to inertial frame expressed in body frame
$\Omega(\tau)$	Vandermonde vector

Matrices

$\mathbf{0}$	Null matrix
$\mathbf{1}$	Ones matrix
$\mathbf{C}$	Direction cosine matrix
$\mathbf{C}_b^i$	Direction cosine matrix rotating from body to inertial frame
$\mathbf{D}$	Satellite geometry matrix
$\mathbf{F}$	Kalman process matrix
$\mathbf{H}$	Kalman measurement matrix
$\mathbf{I}$	Identity matrix
$\mathbf{K}$	Kalman gain matrix
$\mathbf{Q}$	Kalman process noise matrix
$\mathbf{R}$	Kalman measurement noise matrix
$\mathbf{S}$	Navigation signal matrix
$\mathbf{W}$	Diagonal weighting matrix
$\mathbf{Z}$	Measurement including history
$\boldsymbol{\Omega}_{ib}^b$	Skew symmetric angular rate matrix
$\mathbf{M}_{s_c}$	Matrix for signal interpolation
$\Omega(\boldsymbol{\tau})$	Vandermonde matrix

Variables

f_0	Carrier frequency of navigation signal
B_{pre}	Pre-correlation bandwidth
M	Number of sensors
N_g	Pulse length
N_m	Number of considered multipath signals
N_p	Number of particles
N_{cc}	number of canonical components
N_{pc}	number of principal components
T_s	Sampling interval
τ_m	Mean delay
$\Delta\tau$	Correlator spacing

List of Figures

1.1 Personal navigation sensors and their properties: Each sensor has its individual characteristics. The combination of complementary sensors via an optimal sensor fusion algorithm allows to exploit synergetic effects and improves the overall navigation performance. 4

2.1 2D illustration of TOA positioning: The measured travel time ρ_j is different from the true geometrical travel time $\tau_j^g = \left|\mathbf{r}_j^t - \mathbf{r}^r\right| c^{-1}$ due to the asynchronous receiver clock. The receiver position is at the intersection of the three dashed circles. 10

2.2 Synchronization in a navigation receiver: A combination of a DLL and a FLL/PLL is used to track the delay of the received signal with respect to a local replica signal. 12

2.3 Illustration of multipath due to a reflection at a house front. The LOS path may be shadowed or even blocked simultaneously. 13

2.4 Tracking bias envelopes for BPSK (2.4(a)) and BOC(1,1) (2.4(b)) modulation, early/late TED with $\Delta\tau = 0.5$ chips (outer dotted line), $\Delta\tau = 0.1$ chips (middle dashed line), and double-delta TED with $\Delta\tau = 0.1$ chips (inner solid line), SMR=6 dB, rectangular modulation pulses, 16 MHz two-sided precorrelation signal bandwidth, chip rate 1023 MHz, Gold code of length 1023. As evident the DLL suffers much less from the multipath when the BOC(1,1) modulation is used. Additionally the advantage of the more complex TED functions becomes obvious. 14

2.5 Principle of a gimbaled platform (left) and a strapdown platform (right). In the gimbaled variant the gimbals keep the platform leveled and aligned with respect to the navigation coordinate frame. The strapdown platform is attached rigidly to the host vehicle. 16

2.6 Tilt of two coordinate systems. The transformation of a vector from one into another coordinate system is performed through a multiplication of the vector with a rotation matrix. 17

2.7 Illustration of the strapdown navigation computer in inertial frame mechanization. For each set of arriving gyroscope measurements the attitude computer is updated. The latest attitude matrix is used to resolve the measured accelerations from the vehicle's body frame to the inertial navigation frame. After subtraction of the earth acceleration position and velocity are computed by numerical integration. 18

2.8 Illustration of the hidden Markov estimation process for three time instances. The measurements are the sequence $\mathbf{z}_q, q = 0, \ldots, k\}$, and the parameters to be estimated are $\mathbf{x}_q, q = 0, \ldots, k\}$ 21

2.9 Illustration of the recursive Bayesian estimator. The operations prediction and update can be carried recursively, since the computation of the a posteriori PDF $p(\mathbf{x}_k|\mathbf{Z}_k)$ requires beside the likelihood function $p(\mathbf{z}_k|\mathbf{x}_k)$ as well the a priori PDF $p(\mathbf{x}_k|\mathbf{Z}_{k-1})$, which can be computed from the previous a posteriori PDF $p(\mathbf{x}_{k-1}|\mathbf{Z}_{k-1})$. 22

2.10 State-of-the-art implementation of the Bayesian estimator for a joint satellite and inertial navigation system. The inertial navigation computations are performed in parallel to a Bayesian estimator, commonly an EKF, which estimates the errors of the inertial navigation. 29

2.11 Information fusion in a GNSS/INS navigation system as it is used in aeronautics. Since there is no information that constrains the movement of the vessel a sole INS solution degrades over time, thus the uncertainty about its location increases continuously (2.11(a)). The information provided by the GNSS constrains the possible locations, which allows to correct the joint estimate (Figure 2.11(b)). 30

3.1 Classification of multipath mitigation approaches. The genuine mitigation approaches actually mitigate the impact of multipath, whereas the estimation approaches estimate and compensate the multipath at a later processing stage. . . 34

3.2 Signal model using blocks and sub-blocks. The complex amplitudes $\mathbf{a}$ are allowed to vary with a higher rate than the path activity indicators $\mathbf{e}$ and the delays $\boldsymbol{\tau}$. 36

3.3 Architecture for efficient evaluation of the likelihood function in navigation receivers [Sel04c]. A bank of conventional correlators provides the reduced data set $\mathbf{z}_{c,j,k,l}$, which is sufficient to compute the likelihood function and to estimate the signal parameters. 38

3.4 Output of correlator banks that can be used for data size reduction in navigation receivers for a BPSK and a BOC(1,1) signal with 1.023 MChips/s respectively. The obtained samples need to cover at least a chip interval around the main peak. 39

3.5 Structure of the range-based (3.5(a)) and the position-based estimator (3.5(b)). In the range-based formulation there is a separate particle filter for each received satellite, and each particle (black dots) carries a grid-based filter and several Kalman filters. In the position-based formulation there is only a single particle filter, in which each of the particles carries several grid-based filters with associated Kalman filters. 54

3.6 PCRB of the range-based and the position-based estimator. The position-based approach outperforms the range-based approach, since it omits the intermediate step of range-wise independent time delay estimation before the position computation. 56

3.7 Performance comparison of the range-based and the position-based approach in a four satellite scenario. Due to the smaller state space only few ($\approx$100) particles are needed for the range-based approach to reach convergence, since with more particles its performance does not improve further. Nevertheless for more than 1.000 particles the position-based approach is able to outperform the range-based estimator as it is expected theoretically by the PCRB (see Figure 3.6). With more than 10.000 particles there is no further improvement for the position-based estimator. 57

3.8 Positioning error for the conventional receiver using narrow spaced DLLs and LS estimation, the range-based and the position-based estimator in a static multipath scenario with four received satellites. For very short echoes ($\tau_{\mathrm{m}p} < 7$ m) the mitigation algorithms are not able to resolve the two paths any more. Once the paths can be resolved the advanced estimation methods perform much better than the conventional approach. Thereby the position-based estimator is superior with respect to the error performance. 58

3.9 Average a posteriori multipath detection probability $p(e_{1,1,k}|\mathbf{Z}_k)$ for the the range-based and the position-based estimator in a static multipath scenario with four received satellites. For very short echoes ($\tau_{\mathrm{m}p} < 7$ m) the mitigation algorithms are not able to detect the multipath component any more. 59

3.10 Structure of the pedestrian channel model according to [LS09] 60

3.11 Cumulative normalized histogram of the LOS delay estimation error of the range-based approach in comparison with a conventional narrow correlator DLL using the pedestrian channel model. Already without considering multipath the advanced approach is significantly superior. Considering more simultaneously echoes (via N_m) leads to a further improved performance, which tends to saturate rapidly for more than one additional path. 61

3.12 Comparison of a conventional narrow correlation receiver and the range- and position-based estimator in a four satellite scenario using the pedestrian channel model. The advanced algorithms allow for a significant improvement of accuracy. The position-based implementation is even more advanced than the range-based approach, in particular for errors that are larger than 10 m. 62

3.13 Figure 3.13(b) illustrates the impulse response of a channel, which was measured for a pedestrian moving in the urban environment shown in Figure 3.13(a), where the pedestrian's track is indicated by the arrows (Picture by Google Earth). The view on the scenery corresponds to the direction of the transmitter station. Typical properties of the channel are the long correlation times in the multipath echoes and their clearly observable binding to the user dynamics and the surrounding environment, where reflections at house fronts cause echo traces that persist, approach and depart along with the occasionally shadowed LOS path. 63

3.14 Comparison of LOS delay estimation error for the BPSK signal 3.14(a), the BOC(1,1) signal 3.14(b) and the CBOC signal 3.14(c) for the measured pedestrian channel scenario corresponding to Figure 3.13(b). The advanced modulations significantly outperform the conventional BPSK signal and the range-based estimators are superior compared to the narrow correlator DLL. As already observed for the channel model an increase of the number of considered paths N_m improves the performance. 64

3.15 The channel estimation algorithm has to cope with several simultaneous multipath replica. The DLL receiver shows the typical multipath errors, whose magnitude varies due to the fading processes of the path amplitudes. If the multipath replica are not taken account by the estimator ($N_m = 0$, Figure 3.15(a)), there are still significant errors, but their magnitude is smaller than the DLL errors, since the dynamic model used in the estimator helps to constrain variation of the LOS estimate. With $N_m = 1$ (Figure 3.15(b)) the number of considered paths is to small to track all replica and thus the multipath delay estimates tend to jump between the respective multipath signals. Once the number of considered replica is sufficient to take into account all present signals ($N_m > 1$, Figures 3.15(c) and 3.15(d)), the estimation algorithm detects and tracks properly the channel. 66

3.16 In the illustrated scenario there is a partially shadowed LOS path that is superimpose by a heavy multipath component. During some periods with weak LOS the DLL receiver tracks the multipath signal instead of the true LOS, which leads to high errors in the order of 100 meters. Comparable to the scenario shown in Figure 3.15 the estimation algorithm is still slightly biased, if the multipath replica is not taken account by the estimator ($N_m = 0$, Figure 3.16(a)). Nevertheless the magnitude of the errors is much smaller than the DLL errors, since the dynamic model of the estimator prevents fast variations of the LOS estimate. Once the number of considered replica is sufficient to take into account both present signals ($N_m > 0$, Figures 3.16(b), 3.16(c), and 3.16(d)), the estimation algorithm detects and tracks properly the additional replica and thus successfully mitigates the multipath errors. 67

4.1 Illustration of the cascaded estimator: The high rate inertial computations for the stride estimation are performed in the lower extended Kalman filter (light gray). For each step the pedestrian makes the displacement computer calculates a displacement estimate, which is used at a reduced rate along with all other measurements in the upper main particle filter (dark gray). 72

4.2 Illustration of the foot displacement vector $\Delta\mathbf{r}$ and the change in heading $\Delta\Psi$ for each step the pedestrian makes. 73

4.3 Dynamic Bayesian network illustration of the pedestrian model used in the upper particle filter. The current position depends on the previous position and the current displacement, which is observable through the measurement (4.3). . . . 75

4.4 Movement of particles in the upper filter. The displacement $\Delta\mathbf{r}_k = [\Delta r_{x,k}, \Delta r_{y,k}]^T$ corresponds to the movement with respect to the "Zero-Heading" coordinate system that is associated to each particle according to its heading. The particle movement with respect to the upper filter navigation coordinate system is thus for each particle given by the vector $\Delta\mathbf{r}'_k = [\Delta r'_{x,k}, \Delta r'_{y,k}]^T$, which is according to (4.5) just the result of a rotational transformation on $\Delta\mathbf{r}_k$. 76

4.5 Magnitude of acceleration vector subtracted by gravity g during the beginning of a walk sequence. ZUPT triggers and k-cycle triggers are shown along. Each time a novel step is detected a fusion at the upper filter is triggered. 78

4.6 Relation between upper and lower filter scheduling. The time instances where the lower index l corresponds to the index L indicate a cycle a the k-rate. 79

4.7 Illustration of the track that is computed by the lower filter. At each step the displacement $\Delta\mathbf{r}_L = [\Delta r_{x,L}, \Delta r_{y,L}]^T$ and the change in heading $\Delta\mathbf{\Psi}_L$ is computed. The final measure that is provided to the upper filter is the displacement $\Delta\mathbf{r}^0_L = [\Delta r^0_{x,L}, \Delta r^0_{y,L}]^T$, which expresses $\Delta\mathbf{r}_L$ with respect to the "Zero-Heading" coordinate system. Since only changes of position and heading are reported the alignment of the lower filter coordinate system can be performed arbitrarily. 80

4.8 Performance of a resting foot-mounted INS comprising state-of-the-art low-cost inertial MEMS depending on the interval between two successively applied ZUPTs. With more frequent ZUPTs the drift gets reduced significantly. 81

4.9 Performance of different classes of inertial sensors when applying regular ZUPTs with a rate of 1 Hz to a resting inertial platform. As it can be seen the development of improved sensors will enable an increase of the inertial dead-reckoning performance in the near future. 82

4.10 Comparison of the conventional movement proposal of the SIR PF and the likelihood proposal after 10 s of walking. With the likelihood proposal much less particles (approx. 100) are needed to attain the a posteriori Cramer-Rao bound. 83

4.11 Mechanical pedestrian model. The body center is assumed to be centered on the connecting line of the two feet. Due to geometrical constraints at each step the body center experiences half the movement of the respective foot. 84

4.12 Comparison of the particle filter performance and the approximate analytical solution for the single and double platform approach during first 10 s of dead-reckoning. The simulation results shown in 4.12(a) are averaged over 750 Monte-Carlo runs using $N_p = 2000$ particles respectively. The results of the Monte-Carlo simulations match the analytical results quite well, where as expected an additional platform improves the performance by a factor of two. . . 87

4.13 Integration with map-matching in the upper particle filter: Initially the location hypotheses (gray) are distributed uniformly across the building. The true position of the pedestrian is indicated by the cross-filled dot. 88

4.14 Integration with map-matching in the upper particle filter: A pedestrian wearing the foot-mounted sensor walked the indicated track (black). As the pedestrian walks the a posteriori position estimate (gray) becomes increasingly accurate, after 80 s it is unimodal. 89

5.1 System overview of the WLAN fingerprinting component. The previously established fingerprinting database serves as the basis for the location determination during the operational phase. 93

5.2 Example of likelihood tables of a calibration point for different access points. As shown in Figure 5.1 the likelihood values are provided by the fingerprinting database, where for every calibration point the probability of receiving a specific RSS from each of the access points is stored. 94

5.3 This figure shows the complete system with two layers of processing: a lower one for the WLAN position estimate and step computation which are then fused in a superordinate EKF. 96

5.4 Floor plan of the test building with eleven access points (black crosses) and 17 ground truth reference points (grey dots), which are distributed evenly on the hallway. 97

5.5 Position error over walking time (Figure 5.5(a)) and cumulative probability distribution of errors (Figure 5.5(b)). The errors of the joint WLAN/INS system are significantly smaller than those of the sole WLAN fingerprinting thanks to the sensor fusion, which joins two complementary sensors: Noisy but long-term-stable WLAN fingerprinting and smooth but drifting INS. 99

5.6 Illustration of the joint WLAN/INS estimate (Figures 5.6(a), 5.6(b), 5.6(c)) and the sole inertial PDR solution (Figures 5.6(d), 5.6(e), 5.6(f)) during the three laps walked. The continuous update of the joint filter by the WLAN measurements compensates for the drift of the INS. 99

5.7 Architecture of the sensor fusion framework, which now integrates GNSS, compass, altimeter, RFID, inertial sensors, and a map-based mobility model. 101

5.8 An example of the sensor data of data set 3: According to Figure 5.8(a) the satellite navigation is completely unavailable during the indoor period. The altimeter data shown in Figure 5.8(b) indicates the important vertical transitions through the staircase, the elevator, and the garage drive-up. Figure 5.8(c) and Figure 5.8(d) illustrate accelerations and turn rates at the foot-mounted IMU during a short walk sequence. The rest phases of the foot are clearly visible in both signatures. 105

5.9 PDR track reconstructed from the foot-mounted inertial sensors for two scenarios. In both scenarios the start points coincide with the stop points. The major errors arise due to the angular drift in the heading angle, which is only weakly observable when only inertial sensors are used. The underlying coordinate grid is spaced by 20 meters per line. 106

5.10 Comparison of the particle filter and the extended Kalman filter in two mixed indoor/outdoor scenarios. In both scenarios the pedestrian enters the building after approximately 90 seconds. The indoor periods are indicated by the gray shading. Unlike the PF the EKF is not able to exploit the map-based movement model, and thus it accumulates drift errors until the pedestrian leaves the building and GPS becomes available again (Figure 5.10(a) approx. after 450 s and Figure 5.10(c) approx. after 400 s). Thanks to the map-based movement model the errors of the PF do not increase during the indoor period, notably though there is no source of absolute position information. As depicted in Figure 5.10(b) and 5.10(d) the error statistics of the EKF are consequently much worse compared to the PF. 107
5.11 Average performance depending on the number of particles used. For more than 100 particles the performance improves only slightly, for more than 1000 particles it is saturated completely. 108
5.12 Impact of RFID and the building map in conjunction with the autonomous sensors GPS, baro-altimeter, compass, and foot-mounted IMU. If both RFID and the map are used, the performance is quite similar to the map only, since the rather inaccurate RFID does not contribute much to the already quite well performing system. When the map is not used the benefit of the RFID becomes more obvious: In the periods that are indicated by the gray markers RFID is available and constrains the estimates, such that the average performance is improved. 109
5.13 Illustration of the particle filter track for data set 3. The vertical transitions are resolved very well thanks to the barometric aiding. 110
5.14 Result of the sensor fusion using GPS, compass, baro-altimeter, a foot-mounted IMU, and the building map under various characteristic indoor and outdoor conditions. 111

B.1 Movement pattern used to drive the generation of the pedestrian channel model. It resembles a pedestrian user moving slowly with regular rest phases (Figure B.1(a)). The pattern is repeated 90 times, such that the entire azimuth range is covered, since per each pattern there is a change of four degrees in the user heading with respect to the satellite direction (Figure B.1(c)). During the movement the variation in the vertical profile (Figure B.1(b)) reflects the slight vertical receiver movement that is induced by each of the steps the pedestrian makes. . 122

List of Tables

B.1 Parameters for the pedestrian channel model. 124

C.1 Personal navigation sensors and manufacturers with their website URLs. 127